INVESTIGATIONS OF SHOCKS IN NOVAE WITH EVOLVED COMPANIONS

By

Isabella Stephanie Molina

A DISSERTATION

Submitted to
Michigan State University
in partial fulfillment of the requirements
for the degree of

Astrophysics and Astronomy — Doctor of Philosophy

2026

ABSTRACT

Novae are thermonuclear eruptions on the surfaces of white dwarfs in binary systems. These eruptions result in a sudden increase in brightness and material being ejected from the binary at high speeds. This binary survives and multiple eruptions can be observed in the same system, these systems are known as recurrent novae. Of the known Galactic recurrent novae there is a prevalence of novae with evolved companions. While novae with main sequence companions are well studied, there remains much to be learned about novae with evolved companions. In this dissertation I give an introduction of our current understanding of novae, the binary structure, the eruption evolution and emission mechanisms. Then, I delve into the recurrent symbiotic nova V745 Sco, modelling its radio light curves and determine that the shock is abruptly emerging from a dense circumstellar medium (CSM) unveiling multi-frequency radio emission. I then investigate the recurrent symbiotic nova V3890 Sgr, producing Very Long Baseline Array (VLBA) images of the 2019 eruption and modelling the radio and γ-ray emission. Then I analyse 11 novae with evolved companions, examining their radio, γ -ray, optical and binary features and characterizing their radio emission. I conclude with future work, including utilizing 3-dimensional hydrodynamical simulations to model the complex CSM of V745 Sco and using X-ray observations to constrain the CSM density of the 11 novae with evolved companions.

To my family

ACKNOWLEDGMENTS

This work was done by the perseverance of ants [1]. I would like to sincerely thank everyone who helped make this work possible.

I thank my advisor Laura Chomiuk for giving me the opportunity to conduct astrophysics research and for her guidance, mentorship, and support. I also want to thank my thesis committee Jay Strader, Seth Jacobson, Wolfgang Kerzendorf and Nathan Whitehorn for their support. Thank you to Justin Linford and Evangelia Tremou for being my mentors at NRAO.

I am very grateful for my collaborators Peter Craig, Justin Linford, Montana Williams, Kirill Sokolovsky, Miriam Nyamai, Elias Aydi, Koji Mukai, Amy Mioduszewski, and Jennifer L. Sokoloski. I loved discussing novae with you all and learned so much from you. Thank you for answering my stupid questions.

I also thank past and present members of my research group for you support and friendship: Teresa Panurach, Ryan Urquhart, Chelsea Harris, Peter Craig, Thomas Do, Kwangmin Oh, Elias Aydi, Esha Kundu, Rebecca Kyer, Allison Crossland, Grace Showerman, Ashley Stone, Atticus Chong, Wilhelm Hawes, Brandon Benavente. Thank you to the many great people around the physics and astronomy department. Thank you to Steve and Mackenzie my teaching certification buddies and Emily Elizondo and Rebecca Kyer my PAREDS pals.

Thank you to Rique Campa, Stephanie Baier and my cohort of FAST fellows, Maria Cruciani, Tessa Jordan, Maura Philippone, Jordon Parker, Ian McCrary, Chandler Hendrickson, Farnaz Tajik, Shashini Marasinghe, Ayesha Bundy. Thank you Allison Crossland and Cassidy Walker for helping me with my FAST project.

Also I want to thank all of the staff that helped me: Kim Crosslan, Jennifer Roberts, Cathy Coords, Brenda Wenzlick, Susie Harwood Brown and Jessica Dellinger.

I would like to thank Jocelyn Read, Geoffrey Lovelace, Josh Smith, Marissa Walker, Michael Loverude and the Gravitational Wave Physics and Astronomy Center at California State University, Fullerton. You helped me believe I could actually be a scientist and encouraged me to continue in research. Thank you to Denyz, Teresa, Montana, Celeste, Toko, Esther, Peter, and Scott for steadying me and bringing joy in a difficult time.

I thank my family for getting me where I am today, thank you for your perseverance, your sacrifice, your hard work and your faith that it would all be worth it. To my mom Margie, my dad, Mark, Joan, Zoë, Jonathan, Malachi, Sophia and Micah, thank you for your chaos, your color, your music, your love. Thank you for reminding me who I am while I navigate the alien world of academia. Thank you Harvey, Steve, Salvador, Carlos, Aisha, Laura, Martha, Salvador, Deborah, Helena and Xavier. You all defined who I am today, my success is yours too. Last, but certainly not least, I thank my fiancé Eric who supported me and believed in me even, when I didn't. I am so grateful to have you on this journey with me.

TABLE OF CONTENTS

LIST OF TABLES

LIST OF FIGURES

Chapter 1. Introduction

Stella novae or "new stars" were observed as unusual bright sources in the night sky, suddenly appearing and eventually fading away. Originally thought to be newly formed stars, they are now known to be the result of powerful eruptions occurring on the surface of accreting white dwarfs in binary systems, leading to a sudden burst of light that we observe here on Earth. These eruptions blow off massive amounts of material ranging from $10^{-7} - 10^{-3}$ $M_{\odot}$ at speeds varying between 500 km s^{-1} and 10000 km s^{-1} [2].

The white dwarf survives this eruption and multiple eruptions can be observed from the same binary system, these are called "recurrent novae". All novae, theoretically, are recurrent—however as our human timescales are rather short, we have not observed multiple eruptions from all known novae. Currently, there are 10 confirmed recurrent novae in the Milky Way [3] and a similar amount of recurrent novae candidates [4]. Nova eruption properties, like recurrence time and ejecta mass, are thought to mainly depend on the mass of the white dwarf and the accretion rate [2, 5, 6]. It is estimated that 26 novae erupt each year in the Milky Way [7] and about 10-15 novae are discovered, mainly by amateur astronomers.

The mechanisms of this eruption, characteristics of the stars in the binary, properties of the blast, and the impact the nova has on the surrounding environment are all active areas of study. Since the first observed nova, astronomers have increased the depth and range of nova observations. Using radio data from the Very Long Baseline Array (VLBA) we have been able to image novae with high angular resolution, illustrating the detailed structure of the blast and how it changes over time. Through observations of classical and recurrent novae with the Fermi Gamma-ray Space Telescope, novae have been established as GeV γ-ray sources. [8]. X-ray observations with the *Neil Gehrels Swift Observatory* have shown that the vast majority of novae undergo a supersoft X-ray phase, resulting from residual

nuclear burning after thermonuclear runaway [9–11]. Additionally, using X-ray monitoring to determine the duration of the supersoft emission, we can estimate how much mass was ejected in the nova [12]. Infrared (IR) observations are used to indicate dust formation during novae eruptions. Dust particles absorb optical radiation and re-emit it as IR radiation [13]. Dust formation in novae has been shown to correlate with detectable γ-ray emission with 86 % of γ-ray detected novae forming dust [14]. UV observations of novae can be used to determine the temperature and density of the ejecta as well as the elemental abundances [15].

Joint observations with different instruments provide multi-wavelength insight into novae allowing us to investigate the high energy shocks in the system and the physics of the ejecta mechanisms. From the theoretical side, astronomers have modelled nova eruptions, particle acceleration, blast evolution and shocks (see Refs. [16–21] for reviews). Using astronomical observations of recurrent novae, we can verify these models. Recurrent novae in particular provide a unique opportunity to observe multiple nova eruptions and observe the effects these eruptions have on their local environment.

1.1 Why Study Novae

Novae offer us a valuable opportunity to study several avenues of astrophysics including the physics of shocks, high energy particle acceleration [22], circumstellar medium (CSM; [23]), and the potential to model and test the formation of Type Ia supernova progenitors [24]. Novae are routinely detected in γ-rays providing a unique opportunity to study real time particle acceleration in shocks. 3D hydrodynamic simulations can be tested by real observations allowing us to determine if our physical understanding is correct [16, 25]. CSM studies, like those done by [26] and [27] investigate absorption lines in some Type Ia SNe

and determine if they can be produced by systems like RS Oph, further establishing a link between symbiotic recurrent novae and Type Ia SNe.

In our galaxy there numerous bright novae that can be observed with the whole electromagnetic spectrum resulting in high resolution imaging and multi-wavelength analysis. Additionally, recurrent novae allow us to observe multiple eruptions in the same system and see how it changes as a whole over time. Recurrent novae, especially those with evolved companions, are also thought to be potential Type Ia supernovae (SNe Ia) progenitors, producing SNe Ia through the single degenerate scenario. SNe Ia are supernovae occurring in a binary system with a carbon oxygen white dwarf and a companion star [28, 29]. Unlike in a nova, the white dwarf does not survive a SN Ia.

In the single degenerate progenitor scenario a companion star, often an evolved companion, transfers material onto the surface of the white dwarf. As the white dwarf nears Chandrasekhar mass, electron degeneracy pressure is no longer able to prevent the white dwarf from collapsing in on itself and the white dwarf becomes unstable and collapses, causing the SN Ia [30]. The double degenerate scenario is actually a family of scenarios in which the binary system consists of two white dwarfs, at least one of them being a carbon oxygen white dwarf. The white dwarfs do not need to reach Chandrasekhar mass to erupt for example, through the dynamically driven double degenerate double detonation method (D6 method) [31].

The dominant scenario that leads to SNe Ia is unknown; observations suggest that both the single and double degenerate scenarios are at play (see Refs. [32–35] for review). Through studying recurrent novae with evolved companions, we can further test the single degenerate scenario as accretion rates tend to be higher with these novae and less material is blown off of the white dwarf during novae, leading to it growing in mass over time [2]. As we are able

to observe multiple eruptions from recurrent novae we can also determine if the white dwarf is growing in mass (like in the case of RS Oph; [36]). Additionally, we can make estimates on the environment surrounding the nova (e.g., CSM density) to see if they are consistent with our constraints on SN Ia CSM [23].

Novae are also laboratories for shock physics. Internal shocks are common amongst classical and symbiotic novae and occur when a fast moving outflow collides with a slow moving outflow, leading to reverse and forward shocks [21, 37]. External shocks occur when the nova ejecta collide with the CSM. Both shocks can result in particle acceleration leading to detectable radio synchrotron emission and γ-ray emission [8, 38–40]

Novae also provide research opportunities in neutrino physics. GeV – TeV neutrinos from novae are thought to occur alongside γ-ray emission. Searches for these neutrinos have been carried out by the IceCube Neutrino Observatory but so far with no success [41]. However, the upcoming eruption of the symbiotic recurrent nova T Coronae Borealis (T CrB) is a promising opportunity to continue the search. T CrB is only 895^{+22}_{-23} pc away [42], has a high optical flux and is located in a region of the sky where IceCube is highly sensitive. For these reasons, T CrB is expected to have neutrino signals much stronger than what was predicted for RS Oph [43].

1.1.1 Context of This Work

This work aims to add to our knowledge of novae by exploring recurrent novae and novae with evolved companions. There already exists extensive knowledge on novae with main sequence companions [37] but significantly less on novae with evolved companions (sub-giants, giants and AGB stars). In the M31 galaxy it is estimated that 30 % of the novae have red giant companions [44]. Contrast that with the Milky Way, where there are only seven novae

with evolved companions out of the 291 listed in [45]. The total number of Galactic novae with evolved companions is uncertain, as the ones listed in [45] are well known novae with measured orbital periods.

Evolved companions have a significant impact on the surrounding CSM, the accretion rate and the dynamics of the blast, with AGB stars having the greatest impact. The novae studied here are observed in several wavelengths including optical, radio, γ-ray and X-ray, with an emphasis on radio wavelengths. Each wavelength offers us unique insight into the physics of these systems, with radio being able to traverse unobstructed through dust, optical presenting elemental emission lines and γ-rays indicating the presence of high energy shocks and particle acceleration. Emission lines are also used to give velocity information from line profiles. X-rays are used to estimate the density of shocked gas.

Two in-depth studies focus on the recurrent novae V745 Sco and V3890 Sgr with a broader study focusing on 11 novae with evolved companions in our Galaxy. Our V745 Sco study chapter 2, published in the *Monthly Notices of the Royal Astronomical Society (MNRAS)* as *Molina et al. 2024*, modelled the CSM as a simple spherical wind and found that this model could not explain the radio observations. Instead a better model for the CSM consists of a dense close-in component and a lower density outer CSM. As the shock breaks out of the dense CSM, all frequencies in the radio become optically thin in succession leading to the radio light curve we see. We also found that, based on CSM properties alone, we cannot rule out V745 Sco as a possible Type Ia SN progenitor.

In our V3890 Sgr study chapter 3, submitted to *MNRAS* as *Molina et al. 2026*, we presented Very Long Baseline Interferometric (VLBI) radio imaging and *Fermi*/LAT GeV γ-rays. The radio and γ-ray emission were found to be produced from different regions in the shock, with the γ-ray emission coming from dense CSM in the orbital plane and the

radio coming from the more spherical component. The density of the spherical component of the CSM was found to be more dense than other symbiotic recurrent novae.

The broader study in chapter 4 aims to characterize the properties of novae with evolved companions, covering a wide range of the electromagnetic spectrum. This includes estimating CSM densities using radio observations of the novae in quiescence and a comparison between radio and binary properties as well as determining if the majority of radio emission is thermal or non thermal.

The remainder of this introduction discusses the components of the host binary: white dwarfs and their companion stars. This leads to a discussion of binary properties and how the companion shapes these properties. We then delve into the nova eruption itself and discuss the CNO cycle and thermonuclear runaway. The stages of the blast are described as well and an overview of shocks. We then hone in on recurrent novae and explore how we find novae. Lastly, we discuss radio emission, the Karl G. Jansky Very Large Array (VLA) and the VLBA, and give a brief outline of the following chapters.

1.2 Binary Hosts to Nova Eruptions

1.2.1 White Dwarfs

As stars age, they go through different stages in their lives. A map of this stellar evolution is seen in the Hertzsprung-Russell diagram in Figure 1.1. A main sequence star burns hydrogen into helium via nuclear fusion, where two or more atomic nuclei combine to form a larger nucleus. Four H nuclei merge to form a He nucleus. This process releases energy that heats the star and creates pressure that pushes outward. The outward force from these nuclear reactions is balanced by the inward force of the star's gravity. High mass stars evolve into

supergiants where they can burn helium into heavier elements like carbon and oxygen. Lower to intermediate mass stars ($M \lesssim 1-9\ M_\odot$) will burn hydrogen into helium and then reach the Red Giant Branch, the phase before helium burning begins. While the star is transitioning from the main sequence to the Red Giant Branch it is considered a sub giant. Once in the red giant phase the star increases in size ($\sim 10 - 100\ R_\odot$) and luminosity and cools. H is burned into He in a shell around the He core.

A low mass star ($\leq 2\ M_\odot$) will next undergo a helium flash (a quick episode of thermal nuclear fusion in the star's core where helium is fused into carbon) lifting the degeneracy of the material and allowing it to expand. Next the star enters the horizontal branch, all of the hydrogen in the core has been fused into helium, and helium fusion into heavier elements begins. In the shell around the core hydrogen is burned into helium.

From here low-to-intermediate mass stars evolve to the Asymptotic Giant branch (AGB), where the stars are cool and luminous. The star's envelope can have a radius of 1AU. For low to intermediate mass stars that have reached the AGB stage, the core is carbon and oxygen, and a helium shell around the core is burning helium into carbon. A shell around this shell is fusing hydrogen into helium and mass is lost through stellar winds. Periodic pulsations in the optical or near infrared may also take place. Over time, this cloud will dissipate revealing a white dwarf [46, 47].

White dwarfs are the final stage in the evolution of stars that were not massive enough to become black holes or neutron stars ($M< 10\ M_\odot$). Low mass stars ($< 0.6\ M_\odot$) will result in a white dwarf with a helium core (He white dwarfs). A $\sim 1-9\ M_\odot$ star burning hydrogen into helium will result in a white dwarf that is abundant in carbon and oxygen (a CO white dwarf). A star near $10\ M_\odot$ will eventually form heavier elements including carbon, neon and oxygen, resulting in a white dwarf rich in oxygen and neon (a ONe white dwarf). These

dense compact objects have a size on the order of the Earth's size and a mass on the order of the Sun's mass. To give a sense of scale, the Sun has a mass equal to $333,000$ times that of the Earth. They come in a range of colours with surface temperatures ranging from less than 5000K to over $80,000$K. They start out hot and cool over time, unless there is some interaction with a binary companion that prevents this. White dwarfs do not fuse nuclei in their cores and are held together with electron degeneracy pressure which keeps them from collapsing in on themselves. This is explained by the Pauli exclusion principle which states that two or more identical fermions (in this context, electrons) cannot both occupy the same quantum state at the same time. The compactness of the white dwarf forces the electrons to fill all available energy levels, and since they cannot occupy the same ones they are pushed to fill higher energy levels creating a pressure known as electron degeneracy pressure. However, this pressure has its limits and is not able to withstand the gravitational force of the white dwarf if it reaches a mass of ~ 1.44 $M_{\odot}$ also known as Chandrasekhar mass. If a CO white dwarf surpasses this mass limit, the increase in pressure and temperature will spark carbon-oxygen fusion further increasing the temperature. Ultimately, this will lead to thermonuclear runaway and the explosion of the star as a SN Ia [48, 49]. If the white dwarf is an ONe white dwarf, exceeding this mass limit will result in it collapsing in on itself to a neutron star.

1.2.2 Companion Stars

Novae can have a range of companion stars including main sequence stars, subgiants, giants or AGB stars. Evolved companions are stars that have evolved past the main sequence stage, including subgiants and red giants. Based on the companion star, Ref. [50] suggests we classify novae in one of three categories: MS-Novae are novae with main sequence companions, SG-Novae are novae with subgiant companions, and RG-Novae are novae with red giant

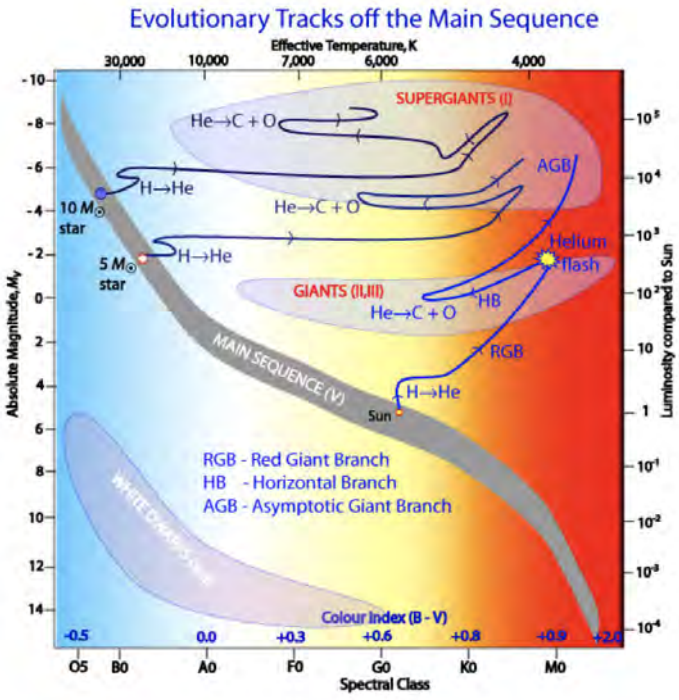

Figure 1.1 Hertzsprung-Russell Diagram showing the evolutionary track of three different stars (a 10 $M_\odot$ star, a 5 $M_\odot$ star, and 1 $M_\odot$ star). White dwarfs lie beneath the main sequence. Image Credit: Robert Hollow, Commonwealth Science and Industrial Research Organization (CSIRO), Australia, adapted by Carin Cain

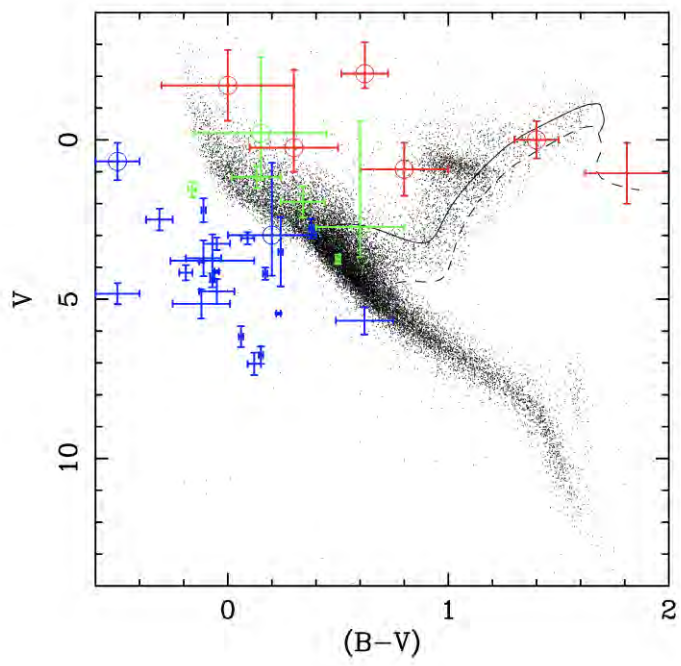

Figure 1.2 Colour magnitude diagram from [50] showing the companions of Galactic novae. The blue marks are main sequence companions, the green are subgiants and the red evolved companions. The majority of companions in Galactic novae are main sequence.

companions. These categories delineate different mass transfer rates and methods, orbital separations and periods, amplitude of the eruption, ejecta mass and ejecta velocity.

MS-Novae have the smallest orbital separation and thus have orbital periods on the order of hours, SG-Novae have orbital periods on the order of days, and the RG-Novae have the greatest orbital separation and so have orbital periods on the order of years [50]. Giant companions strongly impact the environment of the binary. Winds from the companion can be shaped into structures of gas called “circumstellar medium" or CSM, which leave observable effects on the nova eruption. Sub giants may lead to CSM but with lower density, in fact not much is know about the environments of subgiant binaries.

Figure 1.2 from [50] shows the companions of Galactic novae, with most novae having main sequence companions. [45] catalogues 291 Galactic novae listing their orbital periods.

From this list, only seven have orbital periods over 100 days (implying a giant companion). There are extensive studies of novae with main sequence companions [51] in optical wavelengths [45], X-rays [52], γ-rays [53] and radio wavelengths [37]. While there are a handful of novae with giant companions that are extensively studied like RS Oph ([19, 54–56]) overall there are not many population studies of novae with evolved companions.

1.2.3 Cataclysmic variables and Symbiotic binaries

Cataclysmic variables are close binary systems consisting of a companion star and a white dwarf. Their orbital periods tend to range between $\sim$ 77 minutes and 12 hours, and there is a distinct lack of cataclysmic variables with orbital periods within the range of $\sim 2-3$ hours [57, 58].

Roche Lobe overflow is the primary method of mass transfer for cataclysmic variables. The Roche Lobe is a tear drop shaped region surrounding each star in a binary system. Any material that is within this region is gravitationally bound to the star. Material outside the companion's Roche Lobe will either leave the system, orbit the system, or fall onto the white dwarf. When the companion fills its Roche Lobe, then material will overflow through the Lagrangian point and transfer to the white dwarf [59]. Mass transfer through Roche Lobe overflow is thought to be quite conservative, and most of the transferred material ends up on the white dwarf. Cataclysmic variables have temporary increases in brightness caused by eruption, which can be powered by nuclear reaction or accretion.

There are several sub classes of cataclysmic variables including classical novae and dwarf novae among others. Dwarf novae have outbursts that are powered by accretion. Classical novae are a subclass of cataclysmic variables that have main sequence companions, and have experienced eruptions on the surfaces of white dwarfs triggered by nuclear reactions, with some eruptions being somewhat regular and recurring within human timescales. The

accreted material is usually hydrogen rich and accumulates as an envelope of material on the surface of the white dwarf. The eruption can peak to luminosities of $10^5 - 10^6$ $L_\odot$ [60]. All cataclysmic variables are predicted to host novae at some point in their lives, however the timescales are enormously long (on order of Myr - Gyr).

Like cataclysmic variables, symbiotic binaries also consists of a primary star and a companion star; however, the orbital periods are much longer ($P \sim 1 - 100$ yr) [61]. One of the stars is a hot small star—either a white dwarf, subdwarf, or low mass main sequence star—and the other is a cooler giant companion star. In the case of the symbiotic binaries being studied here (and in most cases), the small star is a white dwarf. The binary is embedded in CSM, made up of gas from the giant companion and ionized by the white dwarf [62]. There are two subclasses of symbiotic binaries: D-type, in which the IR emission shows signs of dust, and S-type, in which the IR emission is characteristic of a red giant atmosphere. D-type symbiotics are also known to have orbital periods of over 20 years and S-types have orbital periods of about 1-15 years [63].

Wind-fed accretion tends to occur when the companion star is more evolved, and the orbital period/separation is much larger. Winds from the companion carry material to the white dwarf. Mass loss rates for red giants are in the range of 10^{-8} – 10^{-6} $M_\odot$ yr^{-1} and typically have wind velocities on the order of 10 km s^{-1} [64]. Roche Lobe overflow may not be unusual for symbiotic binaries with orbital periods less than 1000 days [63]. Wind fed Roche Lobe overflow is described in [65] where material is blown off by the winds of the giant companion and fills the Roche Lobe and is then transferred to the white dwarf. Accretion rates for evolved companions tend to be higher since accretion is driven by the companion's winds or a combination of wind accretion and Roche Lobe overflow. Wind fed Roche Lobe accretion rates can be 100 times more than just wind fed accretion rates. These

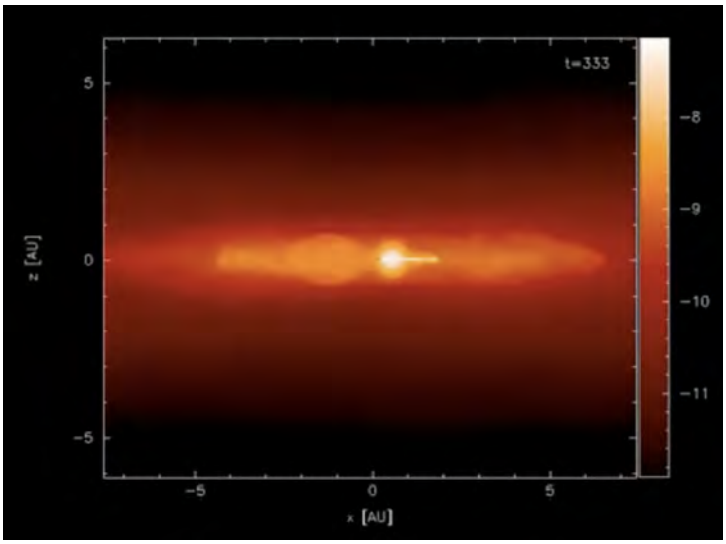

Figure 1.3 3D hydrodynamic simulation of RS Oph taking a side view of pre-eruption CSM. The colour bar shows a log density scale with higher density material appearing more lightly coloured. The binary is in the centre of the field, there is a giant companion and an accreting white dwarf, with mass accumulating in the binary plane. Image courtesy of Shazrene Mohamed.

high accretion rates lead to gentler eruptions blowing off less accreted material, potentially leading to the white dwarf growing in mass over time [2]. Recurrence times are also shorter for higher accretion rates and greater white dwarf mass, leading to a prevalence of observed recurrent novae with evolved companions.

Wind fed accretion is much messier than Roche Lobe overflow, and material accumulates in the environment as CSM. Wind fed Roche Lobe overflow is less messy but still leads to some material falling into the environment. This method of mass transfer also tends to lead to material building up in the binary plane [65]. This build up of material in the orbital plane is seen in Figure 1.3, a 3D simulation of RS Oph.

Estimates of the CSM density can be made using radio observations of the symbiotic system in quiescence. Quiescence occurs when the star's accretion, mass loss and ionization are in equilibrium. The radio flux is assumed to be only thermal emission coming from the red giant wind as it is ionized and heated to 10^4 K by the accreting white dwarf [62, 64].

The CSM is modelled as a simple spherical r^{-2} wind [66]. Assuming a constant red giant mass loss rate of ($\dot{M}_w$) and wind velocity (v_w) the density in the wind is given by:

$$\rho_{CSM} = \frac{\dot{M}_w}{4\pi v_w} r^{-2} \tag{1.1}$$

This assumes that all of the CSM is ionized, leading to radio thermal emission from the entire CSM, which may not be the case and thus provides a lower limit on $\dot{M}_w/v_w$ from the radio flux density (Equation 2 of [62]). Because we are assuming the flux is coming from an ionized stellar wind we would get a radio flux density that corresponds to frequency (ν) as $S_\nu \propto \nu^{0.6}$ [66, 67]. Using the mass loss rates described above and assuming a constant wind velocity of 10 km s^{-1} we use Equation 1.2

$$\dot{M} = 3.4 \times 10^{-9} \left(\frac{v_w}{km\ s^{-1}}\right) \left(\frac{D}{kpc}\right)^{\frac{3}{2}} \left(\frac{S_5}{mJy}\right)^{\frac{3}{4}} M_\odot\ yr^{-1} \tag{1.2}$$

from [62] where v_w is the velocity of the giant wind, D is the distance in kpc and S_5 is the flux density in the 4.9 GHz frequency band. The resulting mass loss rates are plotted in Figure 1.4 showing D type symbiotics mainly with $\dot{M}_w$ values around 10^{-5}– 10^{-6} $M_\odot$ yr^{-1}. S type symbiotics mainly have mass loss rates of the range 10^{-8}– 10^{-6} $M_\odot$ yr^{-1}. Data from Ref. [68] which catalogues symbiotic stars of both S and D-type is used in Fig. 1.5. The symbiotic measurements and upper limits on $\dot{M}/v_w$ come from thermal radio emission from ionized CSM. These data are displayed in the top panel of Figure 1.5 along with a log-normal distribution fit. These values give us estimates on the CSM density that we can then use to study novae shocks, particle acceleration and possible multi-messenger (neutrino) signal. The symbiotic measurements of $\dot{M}/v_w$ fall within the range of $10^{-5} \sim 10^{-9}$ $M_\odot$ yr^{-1} assuming

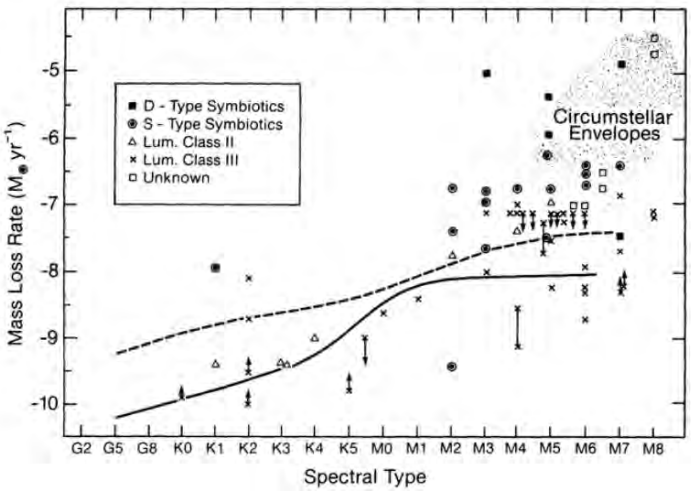

Figure 1.4 Mass loss rates in relation to star's spectral type, assuming $v_w = 10$ km s^{-1}. Figure from Ref.[62]. Symbiotic binary companions are shown as filled in squares or circles and tend to be of cooler spectral types, like M giants.

a $v_w = 10$ km s^{-1}.The bottom two panels are upper limits on the CSM density surrounding SNe Ia, derived from radio observations and assuming different ϵ_B values [24]. These values can be used to compare with nova CSM measurements to determine their potential as Type Ia SN progenitors. For example, V745 Sco's CSM can be described as having a denser close in CSM and a less dense CSM farther out from the binary. At typical radii probed by SN Ia radio observations, $\dot{M}_{out} = 7 \times 10^{-9}$ M$_\odot$ yr^{-1} assuming $v_w = 10$ km s^{-1} and $\epsilon_B = 0.01$. This would fall well within the constraints in the bottom panel and CSM constraints alone could not rule out this nova as a Type Ia SN progenitor [23].

1.3 Nova Eruption

Hydrogen rich material accreted onto the surface of the white dwarf builds up over time, increasing in temperature. The bottom layer compresses from the weight of this new material and increases in density. The accreted material is confined to a thin shell preventing the material from expanding quickly. Temperatures will rise due to an increase in pressure and as a result of nuclear reactions.

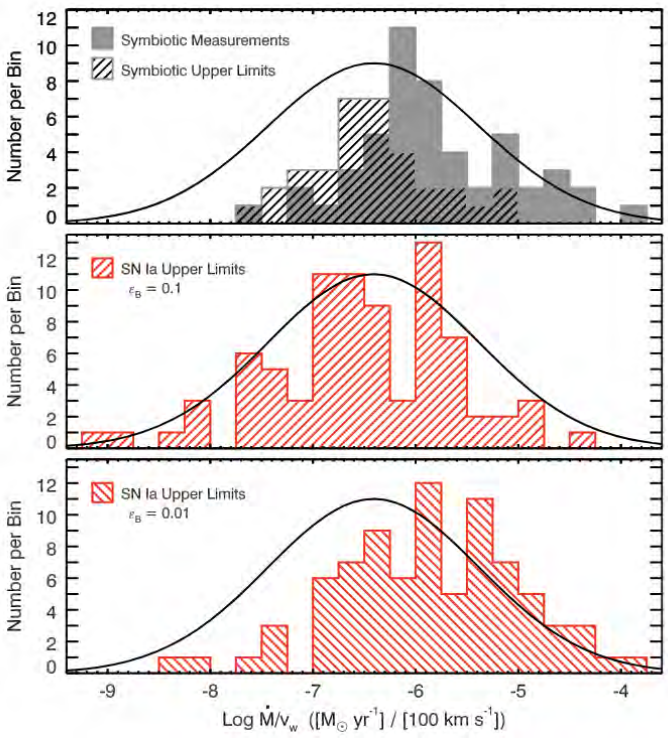

Figure 1.5 Histogram from [24]. The top panel shows the measurements (solid histogram) and upper limits (hatched histogram) on $\dot{M}/v_w$ for symbiotic binaries (normalized to $v_w = 100$ km s^{-1}). The solid line is a fitted log-normal distribution of these data. The bottom two panels show $\dot{M}/v_w$ upper limits for SNe Ia assuming $\epsilon_B = 0.1$ and 0.01.

Two temperature dependent fusion mechanisms are at play here: the proton - proton chain reaction and the Carbon-Nitrogen-Oxygen cycle or CNO cycle. These reactions occur, increasing the temperature until the eruption happens. When the temperature of the accreted material reaches 10^6 K, the proton - proton chain reaction begins which results in the formation of helium nuclei [69].

As temperatures continue to rise, more nuclear reactions begin to occur. Once the temperature reaches 10^7K the CNO cycle starts. Figure 1.6 illustrates this cycle showing the fusion of four H nuclei using CNO isotopes as catalyst. The CNO nuclei absorb protons creating radioactive nuclei which dominantly decay through β^+ emission. The rate of energy production from these decays results in convection. This convection pushes CNO nuclei to higher temperature regions of the accreted material, further increasing the rate of CNO cycles. Material from the white dwarf can get mixed in with the accreted material, increasing the amount of carbon and oxygen available. When the temperature has reached 2×10^7 K, the CNO cycle is the dominant channel of energy release (more so than the proton - proton chain reactions). At temperatures above 10^8 K the half lives of the $\beta+$ decay nuclei limit the number of nuclear reactions and thus the amount of energy that can be generated.

Runaway keeps going and finally the accreted and mixed in white dwarf material can expand (this is later called the ejecta, the material ejected in the eruption). The energy from these reactions is enough to puff up the accreted envelope into a red giant like atmosphere. In many cases, this envelope is ejected with enough speed to escape the white dwarf. Residual nuclear burning continues on the white dwarf after thermonuclear runaway for days to years (depending on the mass ejected) and and is seen as supersoft X-ray emission.

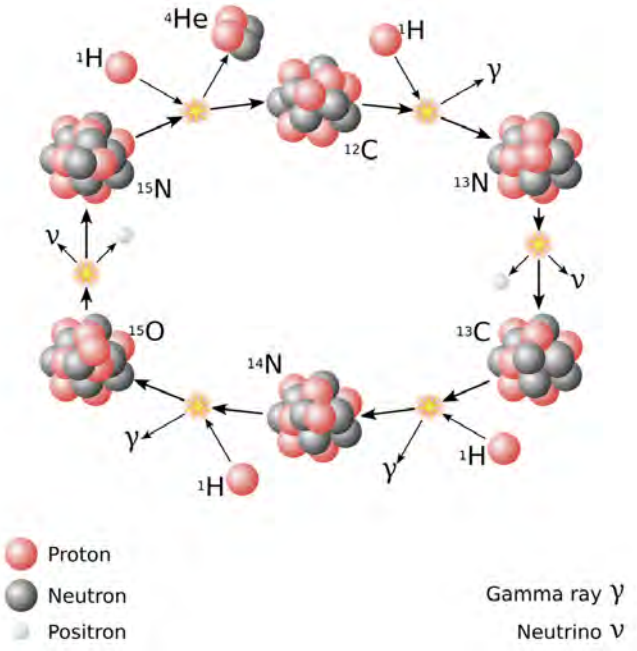

Figure 1.6 Diagram of CNO-cycle showing CNO nuclei being used as catalyst for H fusion. Image Credit: Wikipedia

1.3.1 Stages of the Blast

A nova with a red giant companion may have its local environment polluted with CSM from the red giant wind [e.g. 62]. As the ejecta expand into the CSM, mass is swept up and the ejecta slow down. We can describe the evolution of the nova blast as a small scale version of a supernova remnant, as the ejecta mass and velocities are much lower than in SNe. The first phase of the blast is called the free expansion phase where the velocity is decreasing as the blast moves away from the binary with a nearly constant velocity. This ends around the 'Sedov time' when the swept up CSM mass equals the mass of the ejected material. The next phase is the Sedov-Taylor phase or the adiabatic phase, where the velocity is decreasing as $v \sim t^{-2/5}$. The energy at the front of the shock goes from kinetic to thermal energy, but the amount of energy stays relatively the same. The last phase is the radiative phase, when the time it takes for radiative cooling is shorter than the expansion time. Either the density

of the shock is very high or the velocity of the shock has decreased enough that the post shock gas is only heated to $\sim 10^{5.5}$ K, a regime that cools rapidly [70–72]. Another take on this phase is described in Ref. [73] where energy from the shock is lost by particles being accelerated to relativistic speeds via diffusive shock acceleration and then escape the shock

1.3.2 Shocks

Novae can have both internal and external shocks. When the ejected material hits up against either earlier outflows or pre-existing CSM, the shock wave accelerates particles and can lead to high energy emission seen as radio synchrotron emission [74, 75] or γ-rays [8]. In the case of internal shocks there is an initial low velocity outflow focused in the orbital plane [76, 77]. These slow ejecta are referred to as a dense external shell by [18]. This is followed by a higher velocity wind resulting in a collision between the two outflows causing internal shocks. External shocks are caused by the ejecta colliding with the dense wind from the evolved companion.

The observation of TeV and GeV γ-rays and synchrotron radio emission implies that relativistic particles are accelerated through diffusive shock acceleration. Diffusive shock acceleration is a phenomena where charged fermions are repeatedly reflected back and forth across the shock by magnetic mirroring leading to an increase in energy [78, 79]. Additionally, the post-shock magnetic field is amplified by the streaming instability [80]. The energy density in the post shock magnetic field (U_B) and in the relativistic electrons (U_e) are given by

$$U_B = \epsilon_B \, \rho_{CSM} \, v_s^2 \tag{1.3}$$

$$U_e = \epsilon_e \, \rho_{CSM} \, v_s^2 \tag{1.4}$$

Here v_s is the velocity of the shock, ϵ_B is the fraction of the post shock energy density in the magnetic field and ϵ_e is the fraction of the shock power in relativistic leptons. Both ϵ_B and ϵ_e are uncertain and can depend on the Mach number of the shock, inclination angle, and strength of the magnetic field [75]. In novae, a reasonable range of these values would be $\epsilon_e = 0.01 - 0.08$ and $\epsilon_B = 0.01$ [75] or lower like in the case of V3890 Sgr which was found to have ϵ_B and ϵ_e on the order of $10^{-3} - 10^{-4}$ (see Ch. 3).

1.3.3 Recurrent Novae

There are ten observed recurrent novae in the Milky Way [3]. Their recurrence timescales are on the order of decades. Higher mass white dwarfs and higher accretion rates ($\sim 10^{-7}$ $M_\odot$ yr^{-1}) yield these shorter recurrence times [81, 82]. Of these ten known recurrent novae, four of them are 'symbiotic' binaries with giant companions [61], suggesting that evolved companions are more common amongst recurrent novae than classical novae. Classical novae, with white dwarf masses in the range of $0.6 - 1$ $M_\odot$ with lower accretion rates, are predicted to have recurrence times on the order of hundreds or thousands of years

1.4 How Do We Observe Novae?

Nova eruptions emit in all electromagnetic wavelengths, each giving different insights into the physics of the system. Amateur astronomers regularly spot novae in optical wavelengths. IR observations monitor dust formation [13]. X-ray observations monitor sustained nuclear burning and thermal-emission from shocks[52, 83]. Radio and γ-ray observations have proved that high energy particle acceleration is taking place in novae and have led to the idea that shocks contribute to the emission [8, 84].

A great deal of work has been put into finding new novae. The majority of nova discoveries are done by amateur astronomers and citizen scientists. An early pursuit to survey the entire

sky was embarked on by the All-sky Automated Survey (ASAS-3; [85]). This endeavour led to the discovery of many novae in the early 2000s. Another large sky survey started in 2010. The Optical Gravitational Lensing Experiment (OGLE-IV, [86]) resulted in even more nova discoveries, with many being in the Galactic bulge [87]. The New Milky Way Survey (NMW, [88]) started high cadence observations in 2011. The All Sky Automated Survey for Super-Novae (ASAS-SN, [89]) was the first survey to observe the entire sky with consistent cadence [90]. These observations revealed quickly evolving novae that we otherwise may have missed.

1.4.1 Radio Emission

This dissertation primarily focuses on radio emission from nova eruptions, which can be categorized as either thermal or non-thermal emission. Thermal emission (free-free emission) is produced by electrons in thermodynamic equilibrium passing by ions and accelerating due to the Coulomb force. Non-thermal (synchrotron) emission is caused by relativistic electrons spiralling in magnetic fields [91]. Radio emission can travel through dust and gas and provides information on the evolution and morphology of the blast, the density of the ejecta, and the total mass ejected [51, 92].

The first radio observations of novae were the classical novae HR Del and FH Ser by Hjellming and Wade in 1970. Since then, radio observations of novae have exploded. Radio telescopes and telescope arrays were constructed around the world including the VLA in Socorro, New Mexico, MeerKAT in South Africa and the Australia Telescope Compact Array in Narrabri, Australia. The two main radio telescope arrays used in this work are the VLA and the VLBA.

Thermal emission comes from ionized gas and is the acceleration of free electrons scattering off ions. The absorption coefficient increases as the inverse square of the frequency

for thermal emission. At lower frequencies the emission can be optically thick and at higher frequencies optically thin. Optical depth can be defined as

$$\tau_\nu = N\sigma_\nu \tag{1.5}$$

where N is the column density and σ_ν is the cross section of the region the emission is travelling through. If τ_ν is large than the medium is optically thick; if the absorbing region lets no radiation through then $\tau_\nu = \infty$. If τ_ν is small then the medium is optically thin, if $\tau_\nu = 0$ then the medium is completely transparent. Optical depth tells us how opaque or transparent the surrounding medium is that the emission is travelling through. Intensity can be related to optical depth as:

$$I_\nu = I_\nu^0 exp(-\tau_\nu) \tag{1.6}$$

where I_ν is the specific intensity of the radiation traversing an absorbing medium and τ_ν is the optical depth. The intensity of the radiation diminishes as optical depth increases.

Radio synchrotron emission is caused by relativistic particles gyrating along magnetic fields. The energy spectrum of relativistic electrons is given as $N(E) \propto E^{-p}$. In the case of optically thin synchrotron emission, the radio spectral index (α) is related to the electron spectrum as $\alpha = (1-p)/2$. Spectral index illustrates how much flux density (S) depends on frequency (ν) and is defined as $S \propto \nu^\alpha$. Spectral index values expected for diffusive shock acceleration range from $\alpha = -0.5$ to -1 [78, 79].

Regardless of whether the emission is thermal or synchrotron, optical depth increases at lower frequencies. As seen in Fig. 1.7 frequencies less than ν_{abs} are optically thick. In Figure 1.8 shows how radio emission can change over time.

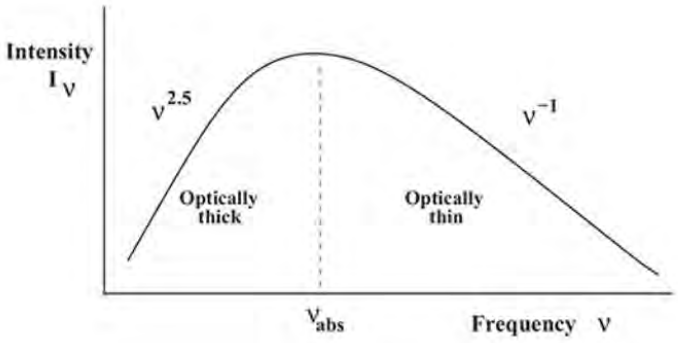

Figure 1.7 Image from Ref. [91] showing a synchrotron radio spectrum with intensity on the y-axis and frequency on the x-axis. Past the absorbing frequency the spectrum goes from optically thick to optically thin.

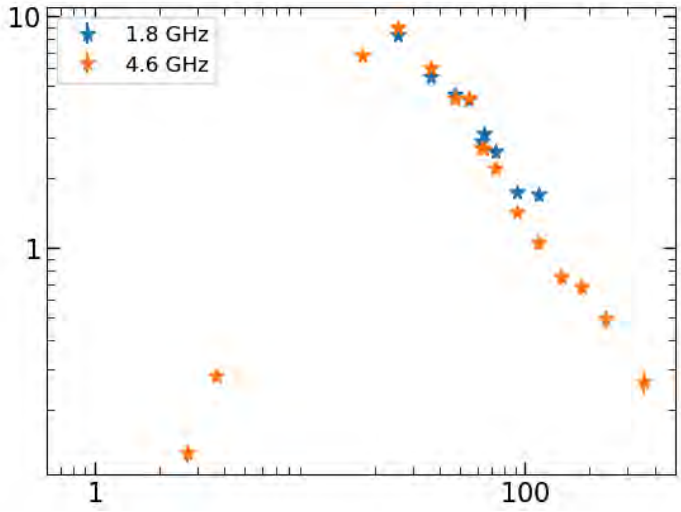

Figure 1.8 Radio light curve of V745 Sco over time showing how the brightness of the radio emission changes over time.

Prior to radio peak, the emission is optically thick and radio luminosity increases as the optically thick region expands. At radio peak $\tau \sim 1$. Then τ decreases and the emission becomes optically thin. For thermal emission τ decreases because the density and emission measure of the ejecta are decreasing with time as they expand. Emission measure is the integral of n_e^2 (where n_e is the number of electrons) along the line of sight. For synchrotron emission, τ declines over time as the shock expands and decelerates and the surrounding region decreases in density [93]. Radio emission observed from novae is likely a combination of thermal and non thermal emission. This mix of emissions can lead to different α values or more complex spectral shapes in novae (for example V1345 Sco [94] and V3890 Sgr [95]).

1.4.1.1 The Karl G. Jansky Very Large Array

The VLA is an interferometer located in Socorro, New Mexico. It consists of 28 radio dishes that are each 25 meters across, arranged in a "Y" configuration. The telescopes are on tracks and can be moved closer and farther apart. In A-configuration the telescopes span a range of 22.62 miles and in D-configuration they are 0.64 miles across. This range in size of the telescope array allows for a difference in angular resolution (for the range of frequencies we use the angular resolution ranges from 0.043– 46 arcseconds). The VLA is able to observe thermal and non-thermal radio emission, giving us the total radio flux density. Our observations lie within the frequency range of 1–40 GHz. In A configuration we can sometimes image nova ejecta (e.g. QU Vul, V959 Mon) [96, 97].

1.4.1.2 The Very Long Baseline Array

The VLBA is an interferometer consisting of ten radio telescopes with locations spread throughout the USA: in Saint Croix, Virgin Islands; Hancock, New Hampshire; North Liberty, Iowa; Fort Davis, Texas; Los Alamos, New Mexico; Pie Town, New Mexico; Kitt Peak, Arizona; Owens Valley, California; Brewster, Washington; and Mauna Kea, Hawaii. The longest baseline is between the telescopes located in Mauna Kea and Saint Croix (8600 km). Each telescope has a 25 meter diameter dish and observes wavelengths in the range of 90 cm to 3mm. The VLBA can be used to image radio sources with brightness temperatures that exceed 10^5 K (non-thermal emission). At 8.4 GHz, the VLBA has an angular resolution of 0.8 milliarcseconds, or a physical resolution of 6 AU at a distance of 8 kpc.

1.5 Dissertation Organization

This dissertation is focused on novae with evolved companions and the shocks that result from these novae interacting with CSM. The dissertation is organized as follows: In Ch. 2 we overview the symbiotic recurrent nova V745 Sco in a range of wavelengths with an emphasis on the radio. We give a real world example of what a shock looks like when it collides with CSM and what happens when we scale that up to SN levels. In Ch. 3 we discuss the recurrent nova V3890 Sgr in radio, optical and γ-ray wavelengths. Here we present VLBI images of V3890 Sgr and *Fermi*/LAT γ-ray emission, and model the radio and γ-ray emission determining that they are produced in different regions of the shock. In Ch. 4 we compare and analyse 11 novae with evolved companions in radio, γ-ray and optical wavelengths. Finally, conclusions and future work are outlined in Ch. 5.

Chapter 2. Radio Observations of V745 Sco

2.1 The Symbiotic Recurrent Nova V745 Sco at Radio Wavelengths

V745 Sco is a Galactic symbiotic recurrent nova with nova eruptions in 1937, 1989 and 2014. We study the behaviour of V745 Sco at radio wavelengths (0.6–37 GHz), covering both its 1989 and 2014 eruptions and informed by optical, X-ray, and γ-ray data. The radio light curves are synchrotron-dominated. Surprisingly, compared to expectations for synchrotron emission from explosive transients such as radio supernovae, the light curves spanning 0.6–37 GHz all peak around the same time ($\sim$18–26 days after eruption) and with similar flux densities (5–9 mJy). We model the synchrotron light curves as interaction of the nova ejecta with the red giant wind, but find that simple spherically symmetric models with wind-like circumstellar material (CSM) cannot explain the radio light curve. Instead, we conclude that the shock suddenly breaks out of a dense CSM absorbing screen around 20 days after eruption, and then expands into a relatively low density wind ($\dot{M}_{out} \approx 10^{-9} - 10^{-8}$ $M_\odot$ yr^{-1} for $v_w = 10$ km s^{-1}) out to $\sim$1 year post-eruption. The dense, close-in CSM may be an equatorial density enhancement or a more spherical red giant wind with $\dot{M}_{in} \approx [5-10]\times10^{-7}$ $M_\odot$ yr^{-1}, truncated beyond several $\times10^{14}$ cm. The outer lower-density CSM would not be visible in typical radio observations of Type Ia supernovae: V745 Sco cannot be ruled out as a Type Ia progenitor based on CSM constraints alone. Complementary constraints from the free–free radio optical depth and the synchrotron luminosity imply the shock is efficient at accelerating relativistic electrons and amplifying magnetic fields, with ϵ_e and $\epsilon_B \approx 0.01-0.1$.

2.2 Introduction

A nova is a thermonuclear explosion that ignites at the bottom of a layer of accreted material on a white dwarf (WD) in a binary system [37, 98, 99]. The companion star is usually a main-sequence star, but is occasionally a more evolved sub-giant or giant star. The companion transfers H-rich gas onto the WD, accumulating an envelope of accreted material on its surface. As this material is compressed, the pressure and temperature at the base of the accreted layer increase, and nuclear reactions accelerate, until conditions are reached for thermonuclear runaway [100]. This leads to a sudden increase in luminosity, and the accreted layer is expelled from the WD at velocities of $\sim 500 - 5000$ km s^{-1}. Some material from the WD may be mixed into the accreted envelope and also expelled in the eruption [101–103]. The binary survives this nova eruption, and the accretion process can continue, implying that multiple nova eruptions may recur over time in a given binary. The properties of nova eruptions, including recurrence time and ejecta mass ($\sim 10^{-7} - 10^{-3}$ M$_\odot$), are thought to primarily depend on the WD mass and accretion rate [2, 5, 6]. While most novae have recurrence times significantly longer than human time-scales, if the WD is massive enough and the accretion occurs at a fast enough rate, then the recurrence time between nova eruptions can shorten to decades, years, or even months [2, 82, 104]. Systems where multiple nova eruptions have been observed are called 'recurrent novae', with 10 recurrent novae confirmed in the Milky Way [3] and a similar number of recurrent novae candidates [4]. Four of these ten are 'symbiotic' binaries with giant companions [61], implying that evolved companion stars may be over-represented amongst recurrent novae (compared to classical novae with longer recurrence times (for example [45]); although we note that the symbiotic fraction remains poorly constrained amongst novae; (see [44] for a pioneering study). The

prevalence of giant companions amongst recurrent novae is often explained by accretion fed by red giant winds reaching higher rates than accretion fed by a dwarf companion filling its Roche Lobe [105, 106].

2.2.1 Recurrent Novae as Potential SN Ia Progenitors

Recurrent novae are potential candidate progenitors of Type Ia supernovae (SNe Ia). A SN Ia is a type of supernova that takes place in a binary system with a carbon-oxygen WD and a companion star [28, 29]. In contrast with a nova, when a SN Ia occurs, the WD is completely destroyed. The companion star may be either an evolved star (the single degenerate channel; [30]) or another WD (the double degenerate channel; [107]). In the single-degenerate scenario, the companion star transfers material onto the WD, causing it to grow in mass and density. Electron degeneracy pressure prevents the WD from collapsing due to gravity until the WD approaches Chandrasekhar mass, when it becomes unstable and collapses, producing a SN Ia. In the double-degenerate class of scenarios, the binary system consists of two WDs, at least one of which must be composed of carbon-oxygen, but neither of which needs to grow near the Chandrasekhar mass. The dominant channel producing most SNe Ia remains an open question, but observational tests imply that both single and double degenerate scenarios likely produce SNe Ia of various subtypes [28, 29].

Classical novae are challenging to the single degenerate scenario for SNe Ia because they make it very difficult for the WD to retain the mass it has accreted, and may actually lead to the WD shrinking in mass [100, 108]. However, models predict that recurrent novae tend to eject less accreted material, allowing the WD to grow over time [2] potentially near Chandrasekhar mass. The WDs in most recurrent novae have been observed to be massive, approaching the Chandrasekhar mass. Using the effective temperature of the WD, V745 Sco

was found to have a $M_{WD} > 1.3 M_{\odot}$ ([109]; see [82] for the relationship between WD effective temperature and mass). The effective temperatures of the WDs in two other recurrent novae, RS Oph and V3890 Sgr also suggest high masses. V3890 Sgr has a $M_{WD} = 1.25 - 1.3 M_{\odot}$ and RS Oph was found to have a $M_{WD} = 1.2 M_{\odot}$ [11, 110].

While these results support massive WDs as the hosts of recurrent novae, it is an open question if these massive WDs are composed of carbon-oxygen or oxygen-neon (a ONe WD will likely collapse into a neutron star rather than exploding as a SN Ia; [111–113]). Still, recurrent novae with evolved companions remain compelling candidates for SN Ia progenitors—and are also some of the most testable candidate progenitors. For symbiotic recurrent novae with giant companions, the giant drives a dense wind, polluting the circumbinary environment. Red giant mass loss rates range from $\dot{M} \approx 10^{-8} - 10^{-6}\ M_{\odot}\, yr^{-1}$ [62] with velocities of the order, $10 - 100$ km s^{-1} [114, 115]. Recurrent nova eruptions can then sweep up and shape this wind into a series of shells and cavities [116], potentially leading to parsec-scale nova super-remnants [117, 118]. This dense, structured circumstellar material (CSM) is detectable, both shaping how a symbiotic recurrent nova appears and also leaving observable signatures in SNe Ia, should these systems be SN Ia progenitors. The SN Ia–CSM interaction might be detectable as radio synchrotron emission [24, 119, 120], X-ray emission [121, 122], optical absorption lines [123, 124], or even as features in the optical light curve [33]. By observing nearby recurrent novae and measuring the density and distribution of their CSM, we can obtain a real-world benchmark for this SN Ia progenitor scenario, which can in turn be compared with observations of SNe Ia. A goal of this paper is to make progress on these questions with a detailed study of one Galactic symbiotic recurrent nova, V745 Sco.

2.2.2 V745 Sco

V745 Sco is a symbiotic recurrent nova with eruptions observed on May 10, 1937 [125], July 30.08, 1989 [126], and February 6.69, 2014 [127]. The companion star was determined to be an M6 III giant based on TiO bands [128] or an M4 III giant using CO absorption features in infrared spectra [129]. [3] used photometry to estimate the orbital period to be around 510 days. However, [130] show with higher cadence, long-term photometry from OGLE [131] that a period of 510 days (or 255 days) is not significant, and instead the optical light curve of V745 Sco during quiescence is dominated by pulsations of the giant component. These semi-regular pulsations of the red giant have periods of 136.5 and 77.4 days.

V745 Sco erupts with a relatively short recurrence time, with only 25 years between the 1989 and 2014 eruptions. The optical light curve of V745 Sco's 2014 eruption is presented in Figure 2.1, created using publicly available data reported to the American Association of Variable Stars (AAVSO; [132]). The data consist of V-band photometry and visual estimates. The nova reached optical peak at $V_{\rm peak} = 8.66\,$mag on 2014 Feb 06.77, a few hours after discovery (2014 Feb 06.69, which we take as t_0). The optical light curve shows a rapid evolution with the time for the nova to decline two magnitudes from optical peak, $t_2 = 2.5\,$days, making it a very fast nova. The 1989 V-band light curve starts at $V = 9.7$ mag and declined slower than the 2014 light curve with a $t_2 = 5$ days [3, 133], perhaps indicating that the peak of the light curve was not observed. The rapid optical decline of V745 Sco's eruptions increases the likelihood that observers may have missed one eruption or more.

The 2014 eruption was detected at X-ray, UV, optical, near-IR and radio wavelengths [73, 109, 130, 134–137]. In addition, marginal detections of GeV γ-rays were obtained with *Fermi*/LAT on 2014 Feb 6 and 7, at 2.4 and 2.5σ level significance [138]. *Swift* observed

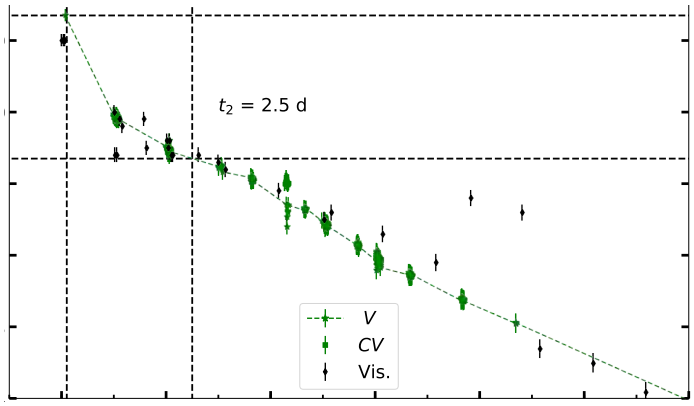

Figure 2.1 The AAVSO optical light curve of V745 Sco during the first 12 days of the 2014 eruption (t_0 = 2014 Feb 6.69). The vertical dashed lines represent $t_{\rm peak}$ and t_2. The horizontal dashed lines represent $V_{\rm peak}$ and $V_{\rm peak} - 2$.

the nova soon after eruption, obtaining X-ray light curves with XRT as well as UV coverage with UVOT [109].

Single-epoch X-ray observations were obtained with *Chandra* grating spectrometers and *NuSTAR*, and showed that the temperature of the shock-heated gas was decreasing over time [134, 135]. This drop in temperature was interpreted as the shock wave decelerating as the expanding ejecta sweep up CSM [16, 73, 134, 135]. [135] and [16] determined that the shocks producing the observed X-ray emission are the result of collisions with an aspherical CSM, characterized by an equatorial density enhancement. [135] estimated the mass that is lost during the eruption to be $M_{ej} = 10^{-7}$ M$_\odot$ (see also [109]) and concluded that this is less than the ignition mass, implying that the WD may be growing in mass over the course of the accretion–eruption cycle.

[136] analysed near IR data taken with the Mount Abu Infrared Observatory starting 1.3 days after discovery of the 2014 eruption. The Paβ line profiles narrowed rapidly and were used to estimate the ejecta velocity via their full width at half maximum (FWHM). These FWHM values do not fit a $t^{-1/3}$ decline, as expected for the Sedov Taylor phase of nova

ejecta interacting with CSM, which they claim further supports the idea that the CSM is asymmetric. [137] presented low-frequency radio observations (610 MHz and 235 MHz) of V745 Sco's 2014 eruption obtained with the Giant Metrewave Radio Telescope (GMRT) and compared them to 1.4 GHz observations of the 1989 eruption.

The goal of this paper is to revisit the radio behaviour of V745 Sco over the course of its 1989 and 2014 eruptions, using newly published data of unprecedented quality from the Very Large Array (VLA; both before and after its upgrade to the Karl G. Jansky VLA) covering frequencies from 1–37 GHz. In §2 we present the observations used in our analysis. In §3 we detail the distance measurements made for V745 Sco based on high-resolution optical spectroscopy and three-dimensional dust maps. In §4 we present the optical spectroscopic data and discuss whether they can be used to estimate the velocity and radius of the nova shock. In §5 we present the radio behaviour of V745 Sco: the multi-frequency radio light curves, brightness temperature evolution, and spectral evolution. In §6 we model the radio synchrotron emission from the nova using the formalism of [93], and discuss whether a V745 Sco-like progenitor would be detectable, given current progenitor constraints on Type Ia supernovae. We summarize our results and discuss future steps in §7.

2.3 Observations and Data Reduction

2.3.1 Optical Spectroscopy of the 2014 Eruption

We revisit the spectroscopic evolution of V745 Sco using publicly available optical spectra obtained using the Small and Moderate Aperture Research Telescope System (SMARTS) 1.5m telescope and its CHIRON optical spectrograph [139]. The observations covered the wavelength range of $4080 - 8900$ Å with a resolution of $R = 27,800$. Observations began

February 9, 2014 (3 days after eruption) and ended May 13, 2014 (96 days after eruption), and were obtained with near-daily cadence. In Table 2.2 we present dates of the observations, along with the measured line width values as well as the integrated flux of the Hα line (see §2.5 for more details).

2.3.2 Radio Observations of the 1989 Eruption

Observations with the VLA started on September 1.9 1989 (about 34 days after eruption) and ended February 15 1990 (200 days after eruption). Observations were obtained under VLA program codes AL202 (PI W. Lewin), AH383, AH389, and AH390 (all three with PI R. Hjellming). The observations were obtained before the 2010 Expanded VLA upgrade, and were conducted in full-Stokes 'continuum mode' with two closely spaced spectral windows each providing 43 MHz of bandwidth. The frequency bands observed were L band (1.50 GHz), C band (4.86 GHz), X band (8.44 GHz), and U band (14.94 GHz). 3C286 was used as the absolute flux density calibrator, and $1733-130$ and $1743-038$ as complex gain calibrators.

We edited, calibrated and imaged these data using standard routines in AIPS [140]. The data from 1990 Feb 2 were obtained during 'move time' between D and A configurations, and without an absolute flux calibrator. For this epoch, we took the flux density of the complex gain calibrator $1733-130$ from the subsequent epoch, and restricted the uv range in imaging, but the data quality remained poor and the nova was not detected.

Flux densities were measured by fitting a Gaussian with width fixed to that of the synthesized beam, and we use a 3σ detection threshold (upper limits for non-detected epochs are 3σ significance). Radio flux densities are listed in Table 2.1 and the multi-frequency radio light curve is plotted in Figure 2.2. For lower frequency observations (<10 GHz), we

assumed a calibration error of 5 per cent, while for higher frequency observations (>10 GHz) we assumed 10 per cent calibration errors. These calibration errors were not considered when determining which measurements were detections (significant at $> 3\sigma$ level), but are quoted in Table 2.1 as part of the uncertainty in flux density measurements.

We note that the 1.5 GHz data were presented in [137], but the data presented here represent an independent reduction. Our measurements generally agree with theirs within the uncertainties, with the exception of the 1989 Oct 20 epoch, where our flux measurement is more than twice as bright as [137]. This discrepancy can be easily understood, because one of the spectral windows was not fringing on the calibrator and target on this day; we flagged this spectral window and only used the one good window, but if we had not, the resulting flux would have been erroneously low. For this reason, we prefer the value listed in Table 2.1. This is the first time the higher frequency data of the 1989 eruption have been published.

During the last observation on day 200, the VLA was in its extended A configuration, which yields the highest angular resolution. While Galactic novae are occasionally resolved in this configuration (e.g. QU Vul- [96]; V959 Mon- [97]), V745 Sco had already faded significantly and a resolved image could not be produced from the data.

2.3.3 Radio Observations of the 2014 Eruption

The upgraded VLA monitored the 2014 eruption of V745 Sco from February 8, 2014 (2.6 days after the discovery of the 2014 eruption) to February 1, 2015 (day 360) under program code 13B-057 (PI L. Chomiuk). The data were collected in Full Stokes continuum mode in L (1–2 GHz), C (4–8 GHz), Ku (12–18 GHz) and Ka (26.5–40 GHz) bands. The L-band

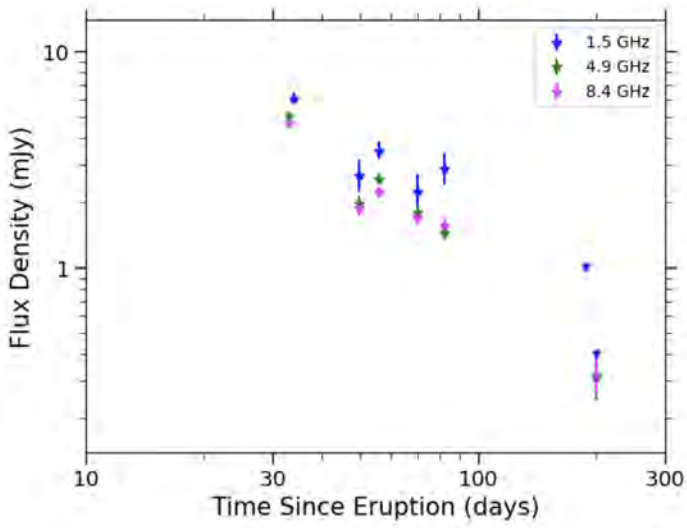

Figure 2.2 Multi-frequency radio light curve of V745 Sco's 1989 eruption. We took the day of discovery, July 30.08 1989, as t_0. Non detections are shown as downward-facing triangles.

Table 2.1 Radio Observations of V745 Sco's 1989 Eruption

UT Date	$t - t_0$ (days)	Freq (GHz)	Flux $\pm$ Error (mJy)	Config
1989 Sep 1.9	34	1.49	6.13 ± 0.38	CnB
1989 Sep 1.9	34	4.86	5.06 ± 0.27	CnB
1989 Sep 1.9	34	8.44	4.69 ± 0.24	CnB
1989 Sep 17.9	50	1.49	2.69 ± 0.44	CnB
1989 Sep 17.9	50	4.86	1.98 ± 0.17	CnB
1989 Sep 17.9	50	8.44	1.88 ± 0.14	CnB
1989 Sep 24.0	56	1.49	3.50 ± 0.32	CnB
1989 Sep 24.0	56	4.86	2.58 ± 0.14	CnB
1989 Sep 24.0	56	8.44	2.24 ± 0.12	CnB
1989 Oct 7.9	70	1.49	2.26 ± 0.46	DnC
1989 Oct 7.9	70	4.86	1.79 ± 0.15	DnC
1989 Oct 7.9	70	8.44	1.70 ± 0.12	DnC
1989 Oct 20.0	82	1.51	2.90 ± 0.48	DnC
1989 Oct 20.0	82	4.86	1.45 ± 0.12	DnC
1989 Oct 20.0	82	8.44	1.57 ± 0.11	DnC
1990 Feb 2.7	187	1.49	< 1.00	D$\rightarrow$A
1990 Feb 15.5	200	1.49	< 0.40	A
1990 Feb 15.5	200	4.86	0.31 ± 0.07	A
1990 Feb 15.5	200	8.44	0.32 ± 0.07	A
1990 Feb 15.5	200	14.94	< 0.19	A

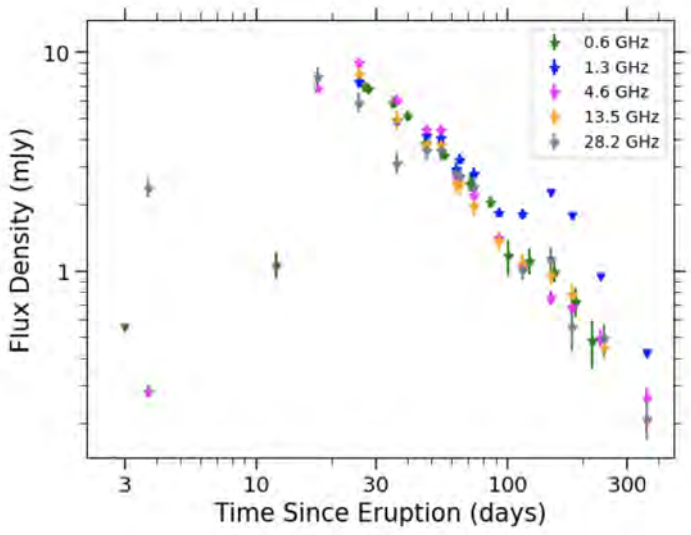

Figure 2.3 The multi-frequency VLA light curve of the 2014 eruption of V745 Sco, including 610 MHz data from [137]. We take 2014 Feb 6.7 as t_0. Flux density measurements are plotted as stars with error bars, and 3σ upper limits are plotted as downward-facing triangles. Note that all frequency bands appear to peak at similar flux densities and at similar times (day $\sim$18–26). Given the strong overlap in light curves at different frequencies, we only plot a representative sub-sample of frequencies here.

observations yielded 1 GHz of bandwidth sampled with 1 MHz-wide channels, while the other bands are sampled with two independently tunable 1-GHz wide windows, providing 2 GHz of bandwidth total sampled with 2 MHz wide channels. A typical scheduling block was 1.5 hours in duration, and observations are obtained in all four receiver bands. The absolute gain calibrator 3C286 is visited for several minutes in each band, in order to calibrate the bandpass and flux density scale. Observations are made of V745 Sco in each receiver band in sequence, toggling back and forth between the nova and a complex gain calibrator (J1744−3116 at C, Ku, and Ka bands, and J1751−2524 at L band). Typical on-source times in each receiver band are 5–15 minutes.

The VLA data were edited, calibrated, and imaged using standard routines in AIPS, IRAF, and DIFMAP [140–142]. Data were imaged using a Briggs weighting with a robust value of 1. The cleaned images showed the nova as consistent with a point source in all

epochs, and flux densities were measured by fitting a Gaussian with width fixed to the image synthesized beam. Flux density values are listed in Table 2.3, and the multi-frequency light curve is plotted in Figure 2.3. Figure 2.3 also shows the GMRT 610 MHz data overplotted [137]. Calibration errors were set using the same procedure as explained in §2.3.2 for the 1989 eruption.

2.4 The Distance to V745 Sco

The distance of 7.8 ± 1.8 kpc that is commonly employed for V745 Sco is based on a flawed assumption: that the orbital period is 510 days [3, 143]. As stated in §1.2, [130] has shown that no such stable periodicity is detectable in extant photometry, calling into question the orbital period of V745 Sco. We therefore revisit the distance to V745 Sco using a different technique: combining absorption measurements from high-resolution optical spectroscopy with three dimensional dust maps of the Galaxy.

We use high-resolution optical spectra obtained with SMARTS/CHIRON (see §2.3.1), to measure the equivalent width (EWs) of several absorption features associated with diffuse interstellar bands (DIBs), which trace dust along the line of sight. We focused on the DIB absorption lines at 5487.7, 5705.1, 5780.5, 5797.1, 6196.0, 6204.5, 6283.8, and 6613.6 Å (see Figure 2.4 for a sample). We combine these measurements with the relations from [144] to derive $E(B-V) = 0.69 \pm 0.20$ mag and $A_V = 2.14 \pm 0.6$ mag, assuming $R_V = 3.1$. Uncertainties are informed by the uncertainty in the EW measurements and the scatter in the relationships between EW and $E(B-V)$ from [144], following the method in Craig et al. (2024, in preparation). This A_V value is consistent with the total extinction along the line of sight, $A_V = 2.2$ mag, as measured by [145]. This corresponds to an ISM column density

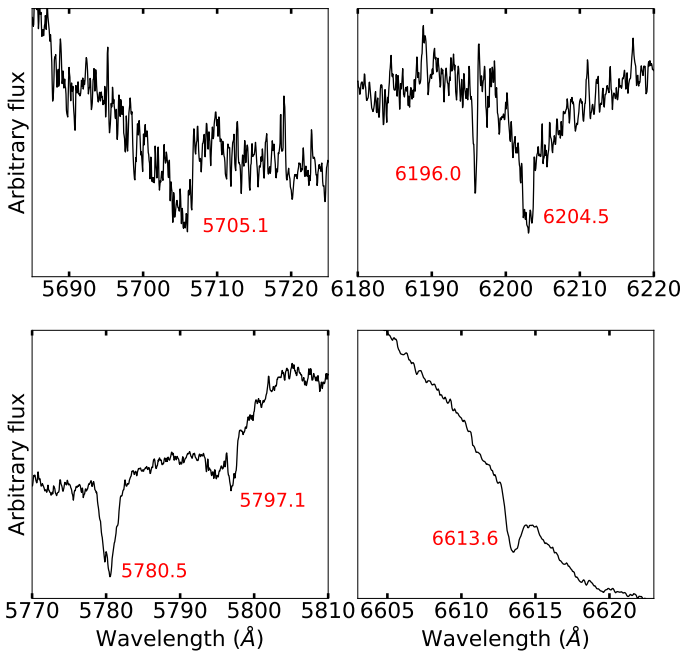

Figure 2.4 A sample of DIB absorption features from used to derive the reddening towards V745 Sco. DIB absorption lines are labelled in red.

of $N_H = 6 \times 10^{21}$ cm^{-2} [146].

We use the extinction derived from the DIB absorption features to constrain the distance to V745 Sco, by comparing it with the Galactic reddening maps of [147]. These maps use measurements from the *Gaia* DR2, 2MASS, and WISE surveys, so we use the reddening laws of [148] to convert $E(B-V) = 0.71$ mag to $E(G-K_s) = 1.56$ mag, $E(G_B-G_R) = 0.91$ mag, and $E(H-K_s) = 0.11$ mag. Using these values and the maps from [147] we derive a distance of at least 3.2 kpc. Beyond this distance, the extinction in the three-dimensional dust maps no longer increases, and instead flattens out to the integrated value [145]. This is not surprising, as at V745 Sco's Galactic latitude ($b = -4°$), a distance of 3.2 kpc implies a location 220 pc above the plane, or ∼twice the scale height of dust in the Milky Way's plane [149]. Therefore, based off the extinction and 3D dust maps alone, we can only constrain V745 Sco's distance to > 3.2 kpc.

To further constrain the distance to V745 Sco, we implemented a novel strategy based on the Galactic model described by [7, 150]. We generated a population of 10^7 simulated novae in this model, distributed in proportion to stellar mass as described by a realistic three-dimensional model of the Milky Way [151]. Then for each simulated nova, we calculated its foreground V-band extinction using a composite three-dimensional dust model as implemented in `mwdust` [152], which combines several three-dimensional dust maps [153–155]. As in [7], we assume that the simulated novae have peak absolute magnitudes normally distributed with mean $M_V = -7.2\,\mathrm{mag}$ and standard deviation $\sigma = 0.8\,\mathrm{mag}$ [156], but the absolute magnitude distribution is truncated at higher luminosities for longer t_2 values (not relevant for V745 Sco, where the time to decline by two magnitudes from optical peak is just $t_2 = 2.5$ days for the 2014 eruption). For each simulated nova, the simulated absolute magnitude is combined with the distance and line-of-sight extinction to infer simulated peak apparent V magnitudes. We find the 300 simulated novae that are the nearest angular matches to V745 Sco. These have a median offset of 3.5 arcmin, which is lower than the typical resolution of the dust maps. Of the 300 simulated novae, we then select those that have peak V magnitudes within 0.5 mag of the actual observed peak ($V_{\mathrm{peak}} = 8.66$ mag). This helps account for the uncertain measurement of V_{peak} for most observed novae and allows for reasonable statistics without a more computationally intensive simulation. The resulting distance is $8.2^{+1.2}_{-1.0}$ kpc for V745 Sco, in close alignment with distances commonly used in the literature (e.g. [73, 109, 133]). We use this distance throughout the remainder of this paper.

2.5 Hα Line Profile Evolution

2.5.1 Optical Spectral Evolution during the 2014 Eruption

The spectral evolution of the 2014 eruption of V745 Sco is presented in Figure 2.5, highlighting a sample of the spectral epochs covering the first ∼100 days of the eruption. Since the first epoch, taken 3 days into the eruption, the spectra show strong emission lines of H I Balmer, He I, He II, N III with weak Fe II lines per the universal spectral evolution of novae described by [157]. The Balmer, He and N emission lines remain the dominant lines in the spectra throughout the first 100 days of the eruption. This means that the nova was first observed during a transition from the Fe II phase to the second He/N phase.

2.5.2 Line Width Estimates

The optical spectroscopic data for the 2014 eruption were used to measure the full width at zero intensity (FWZI) and FWHM of the Hα emission line. Figures 2.6 and 2.7 show the line profile evolution of Hα throughout the first 96 days of the eruption. The Hα line starts out broad and complex; the first 15 days are the epochs that motivated [136] to fit the line profile with a combination of a narrow and broader Gaussian, but their lower spectral resolution (∼300 km s^{-1} resolution) glossed over much of the observed complexity. Also visible in the earliest epochs is a bright, very narrow spike centered at $v = -134$ km s^{-1} with a width of $\sim$ 65 km s^{-1}, which has been interpreted as originating in unshocked CSM [56, 136, 158, 159]. Subsequently, the line profile narrows while the very narrow spike becomes less visible.

For each spectroscopic epoch, the FWZI was measured by estimating the continuum level surrounding the line and measuring the full extent of Hα emission where it converges with the continuum. The He I line at 6678 Å complicated this process by obscuring where the

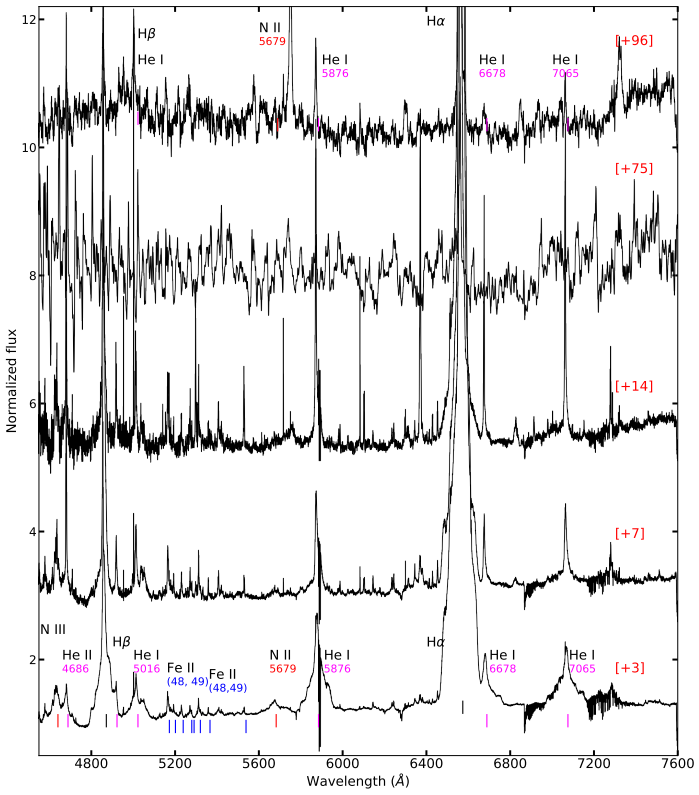

Figure 2.5 A sampling of optical spectra covering V745 Sco's 2014 eruption and demonstrating its spectral evolution. The red numbers between brackets are days after t_0. An offset to the normalized spectra is added for visualization purposes. Line identifications marked with vertical lines colour-coded to the element producing them are added to assist the reader.

Hα line ended on the red side. To get around this we mirrored the curve of the blue side of the Hα line on to the red side of the curve. To measure the FWHM we used the deblending function in IRAF `splot` to fit a Lorentzian profile to the Hα emission line. In all epochs, the Hα line only appears in emission with no notable absorption components or P Cygni profiles, which is unsurprising given its rapid optical decline time [160].

In fitting the Lorentzian profile to the earliest epochs, we excluded the bright very narrow spike and only fit the broader underlying line. By day $\sim$10, the observed line profile has relaxed to a simpler shape reasonably well fit by a Lorentzian function. The peak of the Lorentzian during day 10–21 was mildly but consistently lower than the observed line profile, at the $\sim$5-10 per cent level. By around day 60, the spectra had become significantly noisier and had to be smoothed in order to more accurately determine the continuum level. When smoothed, it was typically down to $R = 2700$, with the resulting velocity resolution less than the line width in all cases; smoothed spectra are shown in Figure 2.7.

Figure 2.8 shows how the width of the Hα line changes over time, and measurements are tabulated in Table 2.2. The line is broadest at early times, with FWZI = 8910 km s^{-1} and FWHM = 2230 km s^{-1} on day 3. FWZI is relatively constant at early times (FWZI $\propto t^{-0.2}$ for day $\sim 3 - 10$), and then declines faster after day $\sim$14 (FWZI $\propto t^{-0.8}$). The behaviour of FWHM is almost the inverse of FWZI; it declines rapidly at early times (FWHM $\propto t^{-0.9}$ for day 3–14) and then more gradually at later times (FWHM $\propto t^{-0.2}$). The discrepant FWHM and FWZI evolution can be explained if, in the first $\sim$10 days, the wings of the line are relatively constant in width, while the core of the line narrows. At later times, this behaviour must flip, and the core of the line has a relatively constant width, while the wings narrow. It is difficult to compare our results with those of [136], because they fit their line profiles with two Gaussians, but do not give the relative intensities of these dual components.

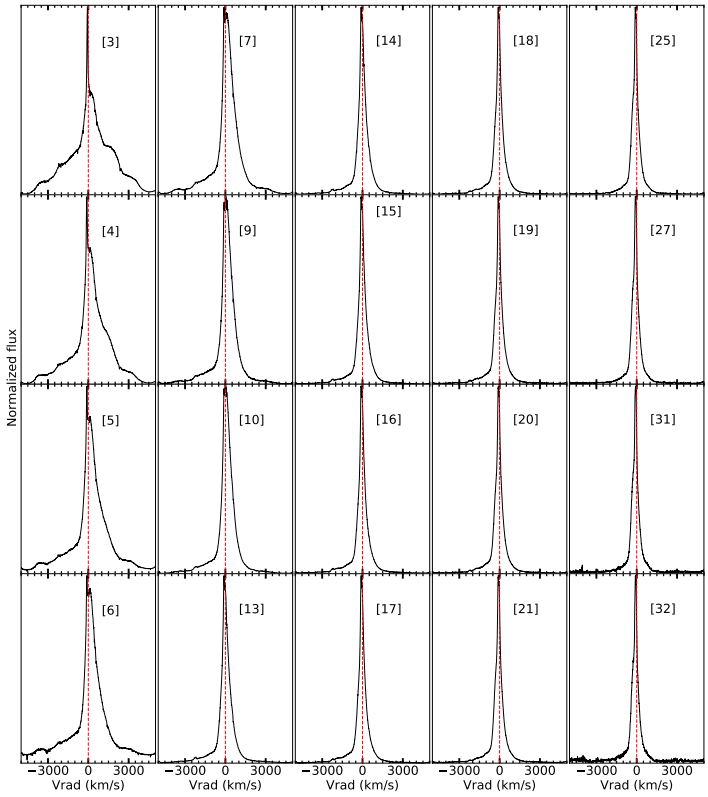

Figure 2.6 Evolution of the Hα line profiles, covering 3–32 days into the 2014 eruption. In each panel, rest velocity is marked with a vertical dashed line. The line rapidly decreases in width over the first seven days. The first three epochs show multiple components in the line profile that smooth out by around day 6.

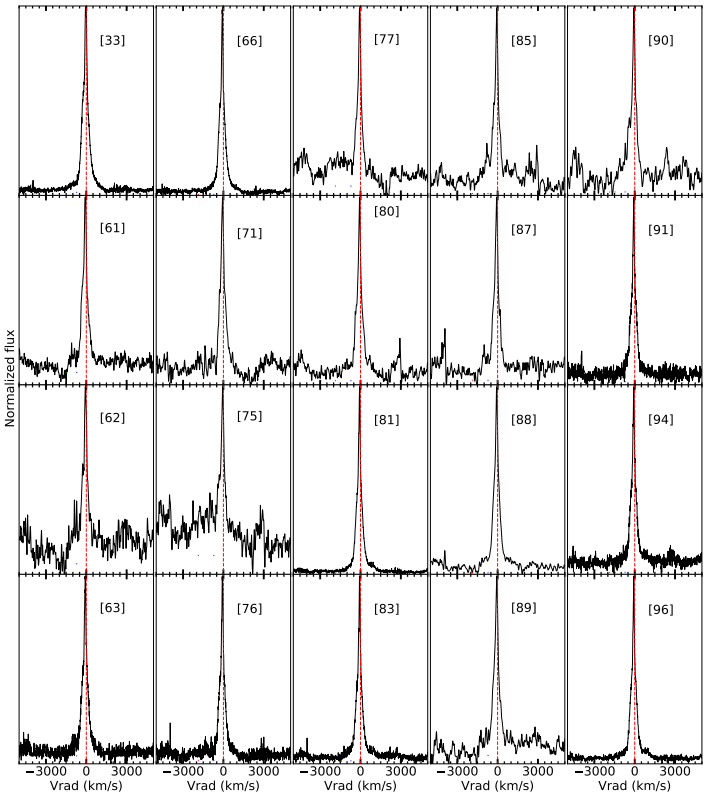

Figure 2.7 Hα line profiles at later times, covering 33–96 days following the discovery of the 2014 eruption.

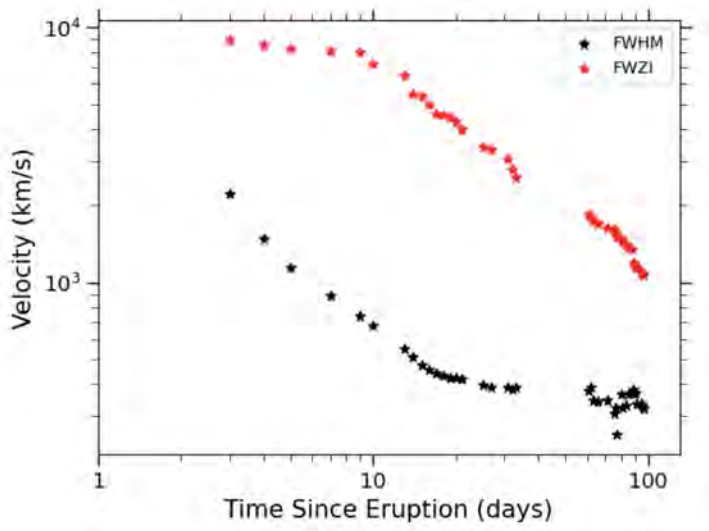

Figure 2.8 Width of the Hα line (in km s^{-1}) as a function of time (days since eruption) for the 2014 eruption. The line profile's FWHM is shown as black stars, and FWZI as red stars.

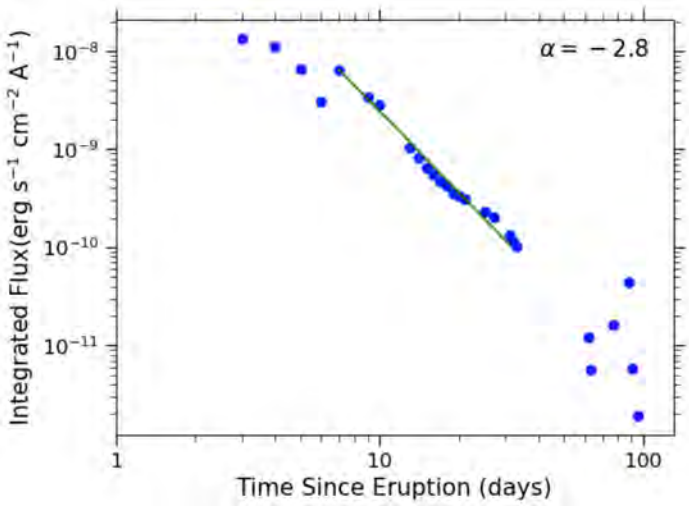

Figure 2.9 The integrated flux of the Hα emission line after flux calibration as a function of time during V745 Sco's 2014 eruption. Between days 7 and 31 the flux is declining with a slope of $t^{-2.8}$.

The early narrowing of FWHM (while FWZI is nearly constant) suggests strong asymmetry, in line with the simulations of [16]. If the CSM is concentrated in an equatorial density enhancement, we expect early deceleration of ejecta in the equatorial directions, with strong Hα emission coming from this region. Meanwhile, FWZI is measuring the largely un-decelerated polar ejecta (at least for the first $\sim$10 days or so, before the wings of the Hα line start to fade significantly).

We use the early line width measurements to estimate the initial kinetic energy of the ejecta by assuming an ejecta density profile, $\rho_{ej} \propto r^{-2}$, a 'Hubble flow' or homologous velocity distribution $v \propto r$, and a maximum velocity of 4450 km s^{-1} (matching our initial FWZI/2 measurements). We consider ejecta masses of $M_{ej} = 10^{-6}$ M$_\odot$ or 10^{-7} M$_\odot$ [109], as expected for fast novae with short recurrence times [2]. Using the equations of [72] (see discussion in §2.7.1), the resulting kinetic energies are $KE = 5 \times 10^{43}$ erg and $KE = 5 \times 10^{42}$ erg, respectively.

2.5.3 Rapid Deceleration or Dropping Density?

As V745 Sco is a nova with a red giant companion, its immediate surroundings are polluted with CSM accumulated from the red giant wind [62]. When the nova ejecta expand into this CSM, mass is swept up and the ejecta decelerate, acting as a scaled-down version of a supernova remnant. The early evolution of the blast is characterized by a free expansion phase, when the velocity decreases slowly. This phase ends around the 'Sedov time', when the blast wave has swept up a mass of CSM equivalent to the mass of the ejecta. The next phase is the Sedov-Taylor or adiabatic phase, which is characterized by a more rapid deceleration than in the free expansion phase. During this phase, as in the free expansion phase, the energy of the shock front is transferred from kinetic to internal (thermal) energy, but the total amount of energy roughly stays the same. The final phase of blast wave evolution is the radiative phase, wherein the time-scale for radiative cooling becomes shorter than the expansion time. A revised take on the radiative phase is proposed by [73], wherein energy is efficiently lost from the shock by particles that are accelerated to relativistic speeds through diffusive shock acceleration and then escape the shock.

[73] revisit the Paβ line profiles of V745 Sco's 2014 eruption from [136], and note the very rapid decline in line width, $\propto t^{-0.5}$. Such a rapid deceleration cannot be explained in either the free expansion or Sedov Taylor phase (for reasonable CSM profiles, e.g. $\rho_{\rm CSM} \propto r^{-2}$; [72]), and they conclude that the blast wave evolves from the free expansion phase straight to the radiative phase. They suggest that this rapid cooling and the quick decline in velocity is driven by very efficient particle acceleration and γ-ray radiation (see also [161]).

Another possibility to explain the observed drastic decline in FWZI is that the ejecta and shock are dropping in density, rather than decelerating. In this case, the emission lines

appear to narrow simply because their flux and signal-to-noise ratio (S/N) are dropping rapidly, swamping the faint wings of the lines with noise. As pointed out by [162], if the ejecta expand into empty space, the diameter of the ejecta (l) will grow with time ($l \propto t$), and the density of the ejecta will drop as $\rho \propto l^{-3} \sim t^{-3}$. The H$\alpha$ emission measure scales as $EM \propto \rho^2 l$, and the integrated flux in the Hα line is $f_{H\alpha} \propto (l/D)^2\, EM$, where D is the distance. Hence, we expect the flux of the Hα line to decline with time as $f_{H\alpha} \propto t^{-3}$ [162]. On the other hand, if the ejecta were sweeping up CSM, the density in the shock would drop less quickly and we would expect the decline of $f_{H\alpha}$ to be more gradual.

Novae with evolved companions show a range of behaviours; for some, the evolution of emission line profiles is consistent with a decelerating blast wave [158], while in other cases, it appears that the ejecta expand with little deceleration [162]. To test how much the H line profiles are affected by dropping density in the 2014 eruption of V745 Sco, we flux calibrated the optical spectra using contemporaneous photometry in the R band from [139] and analysed the results. These photometry were obtained using the ANDICAM dual channel imager on the SMARTS 1.3m [163]. Figure 2.9 shows the resulting integrated flux of the Hα line over time, and Table 2.2 lists our measurements. Between 7 to 31 days after eruption, the integrated flux declines steeply at a rate of $t^{-2.78}$. These observations of V745 Sco are consistent with $f_{H\alpha} \propto t^{-3}$, implying that it is difficult to use the Hα emission line profile to probe blast wave dynamics.

We therefore conclude that it is likely that the apparent narrowing of the Hα lines is primarily an observational effect driven by dropping density [162] rather than by efficient energy loss due to particle acceleration [73]. In addition to this, the apparent continuum of the line profile is not physical. Chiron uses a single fiber and by about day 30 the sky dominates the continuum in many of the spectra. This further supports the idea that the

rapid Hα line narrowing is an observational effect. Additional reasons for preferring the 'observational effect' scenario are laid out in Appendix A.1. This casts doubt on using the line width measurements to accurately measure the deceleration of the blast wave as a function of time in V745 Sco. We do, however, proceed by using the initial FWZI/2 of the Hα line, as observed on day 3, to estimate the expansion velocity of the fastest ejecta, $v = 4450$ km s^{-1}.

Another complication is pointed out by [136]: instead of being a spherical wind, the CSM is likely to be denser in the orbital plane (perhaps shaped by wind Roche lobe overflow; [164]) and more wind-like in the polar directions. [16] explore this complicated CSM profile with 3D hydrodynamic simulations of V745 Sco's 2014 eruption. They include an equatorial density enhancement in their models to create a bipolar ejecta with higher velocity in the polar directions and lower velocity in the orbital plane. They demonstrate that they can reproduce the Paβ line width evolution observed by [136] in their simulations without requiring efficient particle acceleration and deceleration. This picture implies higher shock densities while the blast is within the equatorial density enhancement, and then a drop in CSM density when the blast expands beyond the equatorial density enhancement. This would explain why the Hα integrated flux declines at such a rapid rate around day 10: the blast is breaking out of the equatorial density enhancement and now moving in a low density region.

2.6 The Behaviour of V745 Sco at Radio Wavelengths

2.6.1 Constraints on Radio Emission in Quiescence

Radio observations of symbiotic stars in quiescence can be used to estimate the density of the CSM, because the radio flux is thermal free-free emission coming from the red giant wind

being ionized and heated by the accreting WD [62, 64]. A wind of constant mass loss rate ($\dot{M}$) and velocity (v_w) yields a density profile:

$$\rho_{CSM} = \frac{\dot{M}}{4\pi v_w} r^{-2} \tag{2.1}$$

Assuming the radio emission is dominated by thermal free-free emission from such a wind-like CSM that is ionized and maintained at 10^4 K, there is a one-to-one mapping between a radio flux density and $\dot{M}/v_w$ (Equation 2 of [62]).

While the VLA archive does not contain any targeted radio observations of V745 Sco out of eruption, the system was observed by the VLA Sky Survey in the S band (2–4 GHz). We downloaded three epochs of observations from the CIRADA cutout server, obtained between 2018 and 2023. Each of these failed to detect V745 Sco down to 3σ upper limits: <0.35 mJy (2018 Feb 11), <0.53 mJy (2020 Nov 6), and <0.38 mJy (2023 Jul 4). From these radio upper limits, we estimate that the giant component of V745 Sco drives a mass-loss rate $\dot{M} < 6 \times 10^{-7}$ M$_\odot$ yr^{-1}, assuming a wind velocity of 10 km s^{-1} [165] and a radio spectrum where flux density S_ν scales with frequency ν as $S_\nu \propto \nu^{0.6}$, as expected for an ionized stellar wind [66, 67].

Our upper limit is comparable to the $\dot{M}_{\rm in}$ of the inner, denser CSM estimated by [73], estimated using N_H values measured from X-ray spectroscopy: $\dot{M}_{\rm in} = [5 - 10] \times 10^{-7}$ M$_\odot$ yr^{-1} (assuming $v_w = 10$ km s^{-1}). However, note that these authors argue that the inner red-giant wind is truncated beyond an outer radius of $\sim$ several $\times 10^{14}$ cm, which would decrease the expected radio emission in quiescence. Studying a sample of symbiotic stars, [62] measure 1×10^{-8} M$_\odot$ yr^{-1} $< \dot{M} < 1 \times 10^{-6}$ M$_\odot$ yr^{-1}, so our V745 Sco upper limit fits within this range, but places V745 Sco as a symbiotic with relatively low density CSM.

2.6.2 Behaviour of the Multi frequency Radio Light Curve—and Comparison across Eruptions

Radio observations of the 1989 eruption began about 34 days after discovery, on September 1, 1989 (Table 2.1 and Figure 2.2). The highest flux densities at all frequencies were measured on day 34, however it is very possible that the peak occurred earlier and was missed. The 1.5 GHz data has slightly higher flux density values than the higher frequencies at all epochs (take, for example, day 50 when the 1.5 GHz flux density is 0.7 mJy, or 35% greater than the 4.9 GHz).

The 2014 eruption is observed with better cadence and frequency coverage, and we see that the higher frequencies (28.2/36.5 GHz) appear to peak around day 17.5 (Figure 2.3 and Table 2.3). All other frequencies peak slightly later, around 25.6 days after eruption. It is possible that the highest frequencies (e.g. 28–36 GHz) peak earlier; we note that there is a rather large observation gap between day 3.6 and 17.5. Because of this, we cannot determine the peak flux densities at these frequencies. At frequencies ranging from 1.3 - 17.4 GHz the light curves peak at the same time and at similar flux densities, around 8 mJy. Subsequently, the radio flux declines monotonically at all frequencies.

The multi-frequency radio light curves of both the 1989 and 2014 eruptions of V745 Sco demonstrate rather unusual behaviour when compared with other novae at radio wavelengths [51]. Classical novae (with main-sequence companions) typically show the higher frequencies peaking earlier and at greater flux densities compared to lower frequencies. This behaviour occurs if the radio luminosity is produced by thermal free-free emission and absorbed by free-free absorption, as expected for warm ($\sim 10^4$ K) ionized expanding nova ejecta [166–

168]. For V745 Sco, we note a similar time and brightness of the light curve's peak across frequencies, suggesting that free-free emission is not what is driving the radio emission in this system. Other novae show more complex structure or multiple peaks in their radio light curves [51, 74, 95, 168–171], which is often attributed to multiple emission mechanisms (perhaps a combination of thermal and synchrotron emission, the relative contributions changing with time).

The 1989 radio light curve does not exactly follow the same path as the 2014 radio light curve, but they are similar. Figure 2.10 compares the radio light curves of the two eruptions as observed ∼4.9 GHz, showing that coverage of the 1989 eruption does not start until after light curve peak. We also have fewer observations for the 1989 eruption and larger error bars. At 4.6 GHz, the 2014 light curve declines from peak at a rate of $S_\nu \propto t^{-1.21\pm0.08}$, while the 1989 light curve declines at a rate of $t^{-1.47\pm0.19}$. For the 4.9 GHz band, we would need to scale the 1989 light curve by 1.2 to get it to align with the 2014 light curve. The discrepancy between the 1989 and 2014 light curves is unlikely to be explained by refining the time of eruption, as the start of eruption is well measured in both cases, with <1 day uncertainty [3, 127]. Similar behaviour is seen at ∼1.5 GHz, with the 1989 data at slightly lower flux densities than the 2014 data (Figure 2.11). The 2014 1.3 GHz light curve declines at a rate of $S_\nu \propto t^{-1.05\pm0.21}$, and the 1989 1.5 GHz light curve declines at a rate of $t^{-1.28\pm0.47}$.

[3] has shown that the optical light curves for subsequent eruptions in recurrent novae are similar, but comparable analyses are sparse at radio wavelengths. [137] compared the 1.4 GHz light curve of V745 Sco's 1989 eruption (similar to what is published here) with a 610 MHz light curve of the 2014 eruption (observed with the GMRT; also plotted in Figure 2.3). Fitting the light curves with a parametric model of synchrotron emission developed for radio supernovae [172], they find that the radio emission becomes unabsorbed and peaks earlier

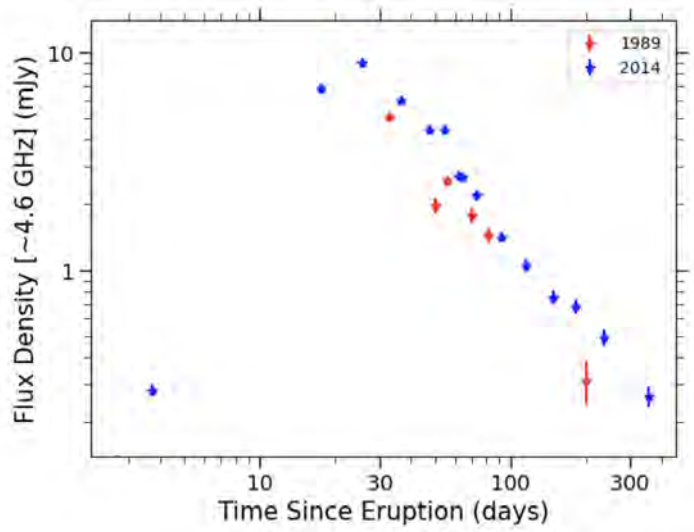

Figure 2.10 A comparison of the radio light curves of the 1989 and 2014 eruptions of V745 Sco, observed at 4.9 GHz in 1989 (red points) and 4.6 GHz in 2014 (blue points). Measured flux densities are plotted as stars with error bars,and 3σ upper limits as upside down triangles.

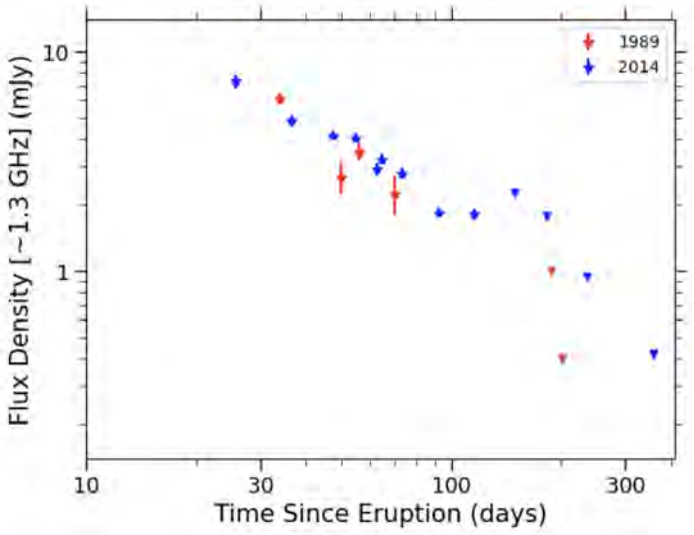

Figure 2.11 A comparison of the radio light curves of the 1989 and 2014 eruptions of V745 Sco, observed at 1.5 GHz in 1989 (red points) and 1.3 GHz in 2014 (blue points). Measured flux densities are plotted as stars with error bars, and 3σ upper limits as upside down triangles.

during the 2014 eruption, as compared to the 1989 eruption. [137] argue that this reflects evolution in the CSM over decades. Our observations improve on this comparison by observing the two eruptions at similar frequencies, enabling a direct comparison without modelling of the eruption. We do not find any evidence of the 2014 light curve peaking earlier than the 1989 light curve. Based on the observations in hand, we can conclude that the period of decline from light curve maximum, $\sim 30 - 200$ days following eruption, was fainter for the 1989 eruption than for the 2014 eruption. This is the period when the radio optical depth should be relatively low, so it is unlikely that changes in the absorbing medium (due to i.e., a different orientation of the binary between the two eruptions) can explain the difference. It is instead likely that the deviation between the radio light curves is reflecting real differences in the energetics of the synchrotron-emitting material between eruptions, either implying a faster shock or denser CSM being shocked in 2014.Similar conclusions were reached by [173], who compared 0.3–1.3 GHz observations of the 2006 and 2021 eruptions of RS Oph, and found that the 2021 eruption was systematically brighter at radio wavelengths.

2.6.3 Brightness Temperature Evolution

We estimated the radio brightness temperature (T_B) of V745 Sco over the course of its 2014 eruption to test if the radio emission is dominated by thermal or non-thermal emission. A brightness temperature exceeding a value of 5×10^4 K cannot be produced by photo-ionized gas [174], and the radio emission expected for thermal emission from the hot shocked X-ray-emitting gas will be optically thin and below the detection threshold of the VLA [170, 171, 175]. The implication is that a measurement of $T_B > 5 \times 10^4$ K indicates non-thermal radio emission [51].

Calculating brightness temperature requires the flux density at a specific frequency and

the angular size of the emitting source:

$$T_B = 1763.1\, K \left(\frac{\nu}{\mathrm{GHz}}\right)^{-2} \left(\frac{S_\nu}{\mathrm{mJy}}\right) \left(\frac{\theta}{\mathrm{arcsec}}\right)^{-2} \tag{2.2}$$

Here, θ represents the angular diameter of the emitting source, assuming the source is disc-shaped. Ideally, θ would be directly estimated from imaging, but Very Long Baseline Array (VLBA) data of V745 Sco's 2014 eruption could not be calibrated due in part to instrumental issues and the source's low elevation which limited what antenna could continuously observe the nova. Unfortunately, radio images were not salvageable. Instead, we inferred angular size measurements for the nova ejecta, assuming a distance of 8.2 kpc and a time-dependent physical diameter of the ejecta, calculated assuming ejection on 2014 Feb 6.7 and a constant expansion velocity of $V = 4450$ km s^{-1} (FWZI/2 for the first Hα observation on day 3). Note that this is almost certainly an upper limit on the diameter of the ejecta, as they will decelerate upon interaction with CSM, so resulting T_B estimates are lower limits (the same thing is true if the synchrotron emission does not originate over the full ejecta, but instead is limited to compact knots; the resulting T_B if imaged with e.g. VLBA would be significantly higher than that estimated here).

Figure 2.12 plots the calculated brightness temperature as a function of time covering the 2014 eruption at three different frequencies. At 0.6 GHz [137], the brightness temperature starts out around 10^8 K, and remains above 5×10^4 K over the course of the eruption, for more than 200 days. This indicates that the emission is synchrotron dominated at all times at the lower frequencies. This is consistent with the analysis of [137], who assume the lower frequency radio emission ($0.2 - 1.4$ GHz) from V745 Sco is synchrotron radiation. Constraints on T_B from higher frequency observations are not as stringent as the 0.6 GHz data

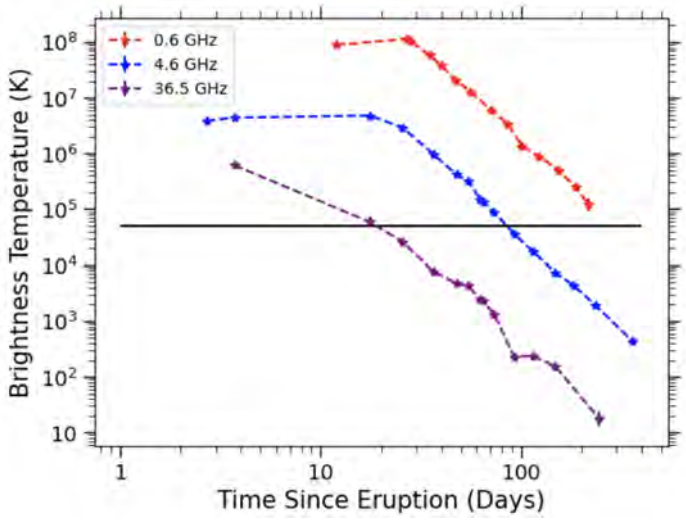

Figure 2.12 Brightness temperature as a function of time following V745 Sco's 2014 eruption. The brightness temperature is estimated at three frequencies: 0.6 GHz (red) [137], 4.6 GHz (blue) and 36.5 GHz (purple). Each point on the dashed lines correspond to an observation obtained in the corresponding frequency band. The horizontal black line indicates where $T_B = 5 \times 10^4$K.

(Figure 2.12); the T_B estimate drops below 5×10^4 K by day 92 at 4.6 GHz, and by day 25 at 36 GHz. Therefore, it is possible that thermal emission contributes to higher frequencies at later times. However, note that the brightness temperature expected for optically-thin thermal gas is significantly lower than the physical temperature of the gas (T), such that $T_B \approx \tau T$, where τ is the optical depth in the optically thin regime. The radio spectrum is optically thin at these late times (§2.6.4), so it is doubtful that thermal emission can be the dominant radio emission mechanism at e.g. 4.6 GHz on day 200.

2.6.4 Radio Spectral Evolution

To assess how the radio emission evolves over time and how long it remains optically thick, we analysed the radio spectral evolution of V745 Sco over the course of its eruptions. Figure 2.13 and Figure 2.14 plot flux density against frequency for each radio epoch during the 2014 eruption. A best fit line (in log–log space) is plotted over the spectra, the slope of which

yields the spectral index. The spectral index α is a measure of how the flux density depends on frequency, given by the relation $S_\nu \propto \nu^\alpha$. For most epochs, a broken power law was used to accommodate different slopes at low and high frequencies, while some observations were better fit with a single power law. The reduced χ^2 value of the fits was used to decide if a single or broken power law fit the data better. The broken power law requires a break point, the frequency at which one power law ends and the other begins. A range of break points were tried, and the best fit determined by minimizing the reduced χ^2 value. α_{high} corresponds to the slope of the frequencies above this break point, and α_{low} corresponds to the slope of the frequencies below the break point. These fits to the spectra were made using LevMarLSQfitter in Astropy, a fitter which uses a Levenberg-Marquardt algorithm to optimize the fit. Flux measurements input into the power law fitter were weighted by $\frac{1}{error^2}$. Upper limits were not included in the broken power law or the fit.

Before radio peak, the ejecta are optically thick and the spectrum rises steeply ($\alpha \approx 1.3$ on day 2). Around radio peak on day 25, the spectrum is relatively flat below $\sim$10 GHz ($\alpha = 0.2$), and decreases with frequency at higher frequencies ($\alpha \approx -0.2$). This behaviour is consistent with radio emission transitioning to an optically thin state, where $\tau \approx 1$ is around 10 GHz. Similar spectral shapes continue for the next three observations, through day 54. Generally, we expect higher frequencies to become optically thin earlier, because it takes more material to be optically thick at high frequencies. Around day 64, the spectrum changes shape from a concave to a convex morphology, with a mildly negative spectral index ($\alpha = -0.2$) at lower frequencies, and a mildly positive spectral index ($\alpha = 0.2$) at higher frequencies. It is possible there is a combination of thermal emission at higher frequencies and non-thermal emission at lower frequencies. This behaviour continues for day 72. For the last five observations, the spectrum is flat for all frequencies ($\alpha \approx 0.0$).

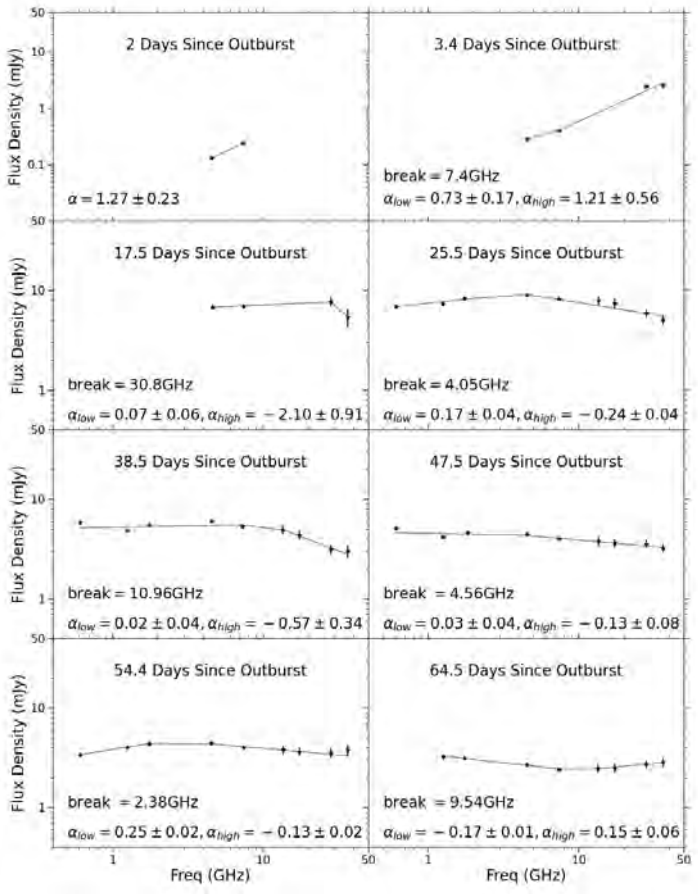

Figure 2.13 Radio spectra observed over 8 early epochs of V745 Sco's 2014 eruption. Each row has a fixed y-axis range. Power-law fits ($S_\nu \propto \nu^\alpha$) to the spectra are overplotted, and the resulting spectral indices are listed in each panel. Data from [137] was included.

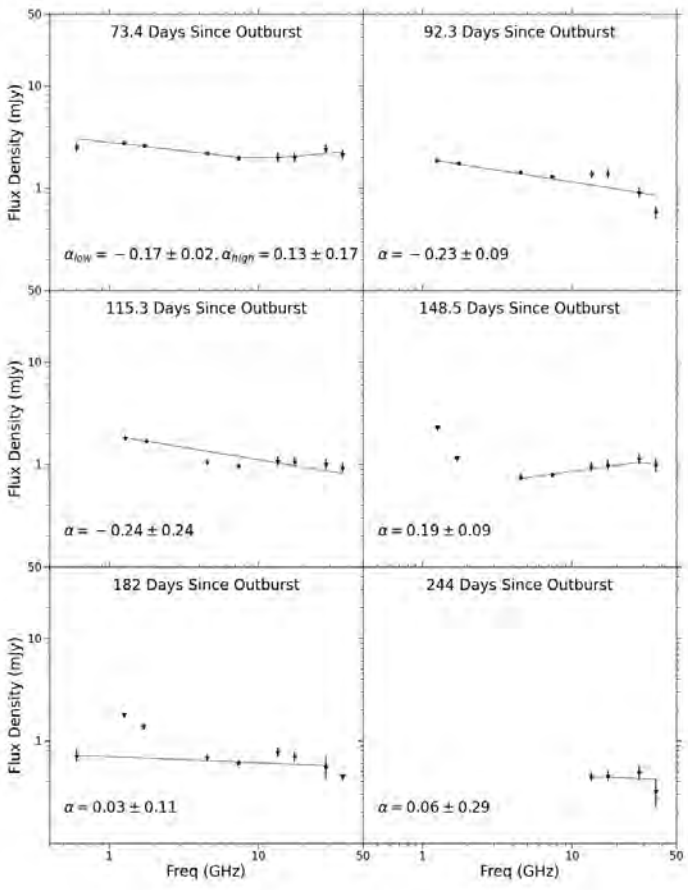

Figure 2.14 Radio spectra observed over 6 later epochs of V745 Sco's 2014 eruption. 3σ upper limits are plotted as black triangles. Each row has a fixed y-axis range. Power-law fits to the spectra are overplotted, and the resulting spectral indices are listed in each panel.

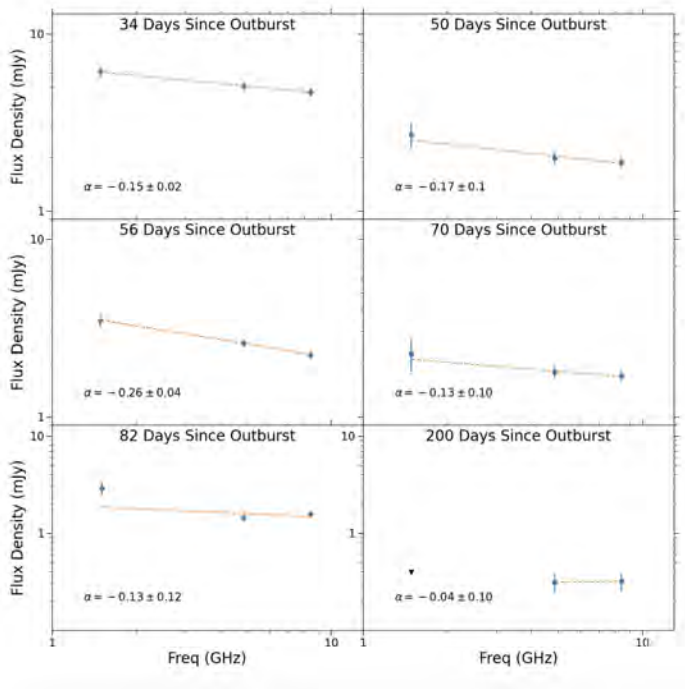

Figure 2.15 Radio spectral evolution of the 1989 eruption. 3σ upper limits are plotted as black triangles. Each row has a fixed y-axis range. Power-law fits to the spectra are overplotted, and the resulting spectral indices are listed in each panel.

Figure 2.15 shows the spectral evolution of V745 Sco's 1989 eruption. The first epoch of the 1989 eruption, 34 days into eruption, shows the lower frequencies peaking at slightly higher flux density values than the higher frequencies, with $\alpha = -0.15 \pm 0.02$. The slope is most steep on day 56 ($\alpha = -0.26$) and then remains relatively flat ($\alpha = -0.13$). There are fewer points in the 1989 spectral index plots so we cannot tell how the spectral index evolves at higher frequencies (> 8.44 GHz). The slope of the lower frequencies remains negative at all times, and like the 2014 spectra, it is flatter at later times. However, the slope between the 1.49 GHz and 4.86 GHz measurements is never positive, as we see for the 2014 eruption before day 64.

The radio spectral evolution of V745 Sco's 2014 eruption is summarized in Figure 2.16, which shows how the spectral index changes over time for high and low frequencies. It is

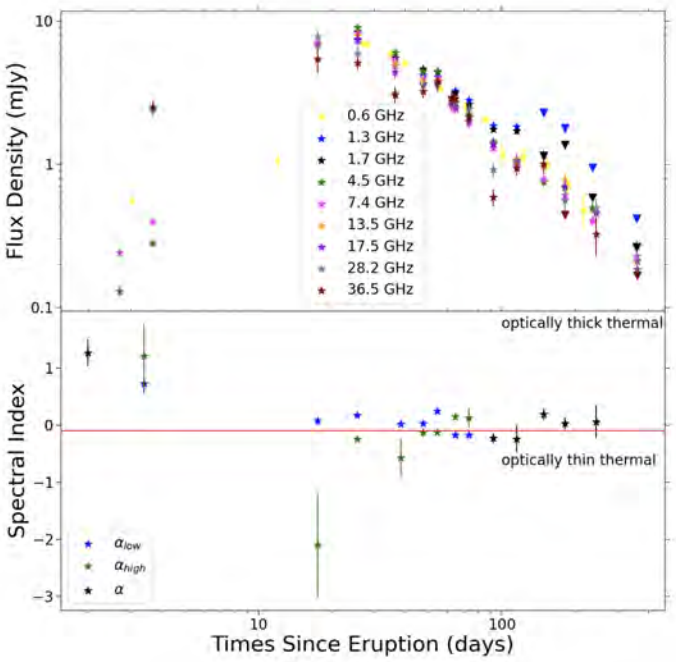

Figure 2.16 Stacked plots of the multi-frequency radio light curve (top panel) and the spectral index as a function of time (bottom panel) for V745 Sco's 2014 eruption. Spectral indices fit to the higher frequencies (α_{high}) are plotted as green stars, fits to lower frequencies (α_{low}) are plotted as blue stars, and epochs where one power law can be fit to the whole frequency have spectral indices (α) plotted as black stars. The alpha value associated with optically thin thermal emission is plotted as a red horizontal line at -0.1.

plotted under the multi-frequency radio light curve to show how the spectral index relates to the radio peak and decline. It shows that the spectral index begins at a value of $\alpha = 1.3$, indicative of optically thick emission. The spectral index then drops quickly and stays around 0, indicative of optically thin thermal emission or partially optically thin synchrotron emission (e.g. [176]).

We can compare V745 Sco's radio spectral evolution with the spectral evolution of other novae with synchrotron-dominated light curves. Before radio peak, the spectrum of the symbiotic recurrent nova V3890 Sgr rises with frequency as $\alpha = 1.3$, much as observed in V745 Sco [95]. After radio peak the spectrum turns over and converges to $\alpha = -0.3$, which [95] interpret as indicative of optically thin synchrotron emission. [94] analysed the spectral evolution of another nova with a giant donor, V1535 Sco. The radio spectrum starts with the flux density decreasing with frequency, as $\alpha \approx -0.9$. After one of the radio peaks (day 23.7), the spectrum switches to $\alpha \approx 1$. It flattens by day 41 ($\alpha \approx 0.2$), and further flattens at later times (day 78.5, $\alpha = -0.06$).

The relatively steeply inverted spectra observed at early times ($\alpha \approx 1$ on days 2 and 3 in V745 Sco) require a radio absorption mechanism. Free-free absorption from warm ionized CSM between the observer and the synchrotron-emitting shock is likely, and is expected to decline as the shock moves outward, sweeping up and shock-heating the CSM. As discussed in §2.7.1, synchrotron self-absorption is unlikely to be important in V745 Sco. Alternatively, [74] suggested the Razin-Tsytovich effect suppressing synchrotron radiation in the presence of thermal plasma [177, 178] may be responsible for a high spectral index of a nova. This effect has also been discussed in the context of colliding-wind binaries [179], synchrotron emission from winds of single hot stars [180, 181] and active galactic nuclei [182, 183].For any absorption mechanism, a gradient in the optical depth across the source may flatten the

spectrum compared to a uniform source affected by this mechanism.

After light curve peak, novae regularly show shallower spectral indices for their synchrotron emission than the $\alpha = -0.5$ to -1 typically expected for diffusive shock acceleration [78, 79] and observed for optically thin synchrotron emission in other astrophysical phenomena (e.g. [172, 184]) and V745 Sco is no exception. However, brightness temperature arguments (§2.6.3) confirm that the emission is in fact non-thermal, at least at the lower frequencies (Figure 2.12). The radio emission we observe in novae is likely a combination of thermal and non-thermal emission. The thermal and synchrotron components may change the slope of the observed spectrum or produce a more complex spectral shape. However, even imaging with Very Long Baseline Interferometry (VLBI), which is sensitive only to high brightness temperature synchrotron emission, reveals relatively flat spectral indices in these novae [55, 94, 97], suggesting that the radio spectrum of synchrotron emission in novae may be unusually flat. If thermal emission contributes to the radio light curve of V745 Sco, it is likely at relatively high frequencies and at relatively late times, perhaps dictating '$\alpha_{\rm high}$' after day 60 (the estimated brightness temperature at 36.5 GHz on day 64 is $\sim 10^4$, which cannot exclude thermal emission).

Very likely, complex optical depth effects are also playing a part in producing the flat radio spectra of non-thermal emission in novae (e.g. [75]). Flat spectral indices are often observed in X-ray binaries in quiescence and many active galactic nuclei (e.g. [185, 186]), and are usually interpreted as partially optically thin synchrotron emission from a self-absorbed compact conical jet [176, 187]. The key difference between a quiescent X-ray binary jet and a nova eruption is that the former can drive a steady outflow of plasma, yielding a self-similar geometry that can maintain a flat radio spectrum over significant frequency and time ranges, while novae confine mass ejection to a relatively short period of time during the eruption.

Because the ejecta in V745 Sco are expanding and the density of the synchrotron-emitting regions (and any absorbing screen) is greatly dropping over the time period covered by our radio observations, one would therefore expect the radio spectrum to converge to an optically thin value at late times. Indeed, when X-ray binaries enter an outbursting state, they are observed to launch synchrotron-emitting blobs with steep radio spectra, as expected for optically thin synchrotron emission [185]but no such transition to a steeper radio spectrum is seen in V745 Sco (or other novae).

There is also the possibility that the energy spectrum of relativistic electrons in novae diverges from the $N(E) \propto E^{-2}$ power law typically expected from diffusive shock acceleration [78, 79], and is instead significantly flatter. Flatter energy spectra for relativistic particles are predicted by non-linear diffusive shock acceleration models, wherein a significant fraction of the post-shock energy density is transferred to relativistic particles, leading to higher shock compression ratios [188].

Another possibility is that there is a low-energy cutoff in the relativistic electron spectrum above the frequencies where the slightly positive α is measured. A spectral index of $\alpha = 0.3$ is expected below the low-energy cutoff frequency, which is the slope of the synchrotron spectrum of a single electron [177, 178].This might explain the concave but relatively flat spectra during days 25–54 and the measured values of $\alpha_{\rm low}$ during this time. In this scenario, the low-energy cutoff moves to lower energies as the eruption evolves, dropping below our observed frequency by day 64.

2.7 Modelling the Radio Light Curve

If we have an estimate of the blast wave dynamics and CSM density profile that the blast is expanding into, it is possible to use the formalism pioneered by [93] to predict the synchrotron emission. Our goal is to compare the synchrotron model with our radio observations of V745 Sco, in order to constrain the properties of the CSM surrounding V745 Sco (§2.7.1). In §2.7.2, we compare V745 Sco's CSM with constraints on CSM around SNe Ia (primarily also from radio observations), in order to test V745 Sco as a viable progenitor system for SNe Ia.

2.7.1 A Model for Synchrotron Emission from V745 Sco

Here, we consider the synchrotron emission that might be expected from a simple nova ejecta interacting with a spherically symmetric wind-like CSM described by Equation 2.1. We set v_w, the wind velocity of the red giant, to 10 km s^{-1} throughout this paper. The ejecta are assumed to expand homologously ($v_{ej} \propto r$) and to have a density profile $\rho_{ej} \propto r^{-2}$ [166, 189]. The dynamics of this interaction are described by [72] over the course of the free expansion and Sedov-Taylor phases. As described in §2.5.2, we take an ejecta kinetic energy of 5×10^{42} erg (5×10^{43} erg) for a $10^{-7} M_\odot$ ($10^{-6} M_\odot$) ejection, to match the early shock velocity to the early Hα FWZI/2.

The model for synchrotron emission is very similar to that applied to the recurrent nova V3890 Sgr by [95]. In the shock between the nova ejecta and CSM, particles are accelerated to relativistic speeds due to the Fermi mechanism [78], and the magnetic field is amplified due to the streaming instability [80]. The energy densities in the post-shock magnetic field (U_B) and in relativistic electrons (U_e) are assumed to be fractions of the post-shock energy

density:

$$U_B = \epsilon_B \, \rho_{CSM} \, v_s^2 \tag{2.3}$$

$$U_e = \epsilon_e \, \rho_{CSM} \, v_s^2 \tag{2.4}$$

Here, ϵ_B is the fraction of the post shock energy density in the magnetic field and ϵ_e is the fraction of the shock power in relativistic leptons. The microphysical parameters ϵ_e and ϵ_B are uncertain, and may depend on the Mach number of the shock, the inclination angle, and strength of the magnetic field [75].

The energy spectrum of relativistic electrons is assumed to be a power law: $N(E) \propto E^{-p}$. For optically thin synchrotron emission, the radio spectral index is related to the electron spectrum as $\alpha = (1-p)/2$. Taking an $\alpha = -0.2$ (measured when the radio emission is optically thin in V745 Sco) gives $p = 1.4$. However, the formalism of [190] is only valid for $p > 2$, and it is not clear at this time if the spectra of relativistic electrons in novae are in fact unusually flat (see discussion in §2.6.4). Therefore, we take $p = 2.1$ in our analysis. The corresponding constants for calculating the synchrotron luminosity are then $C_5 = 1.37 \times 10^{-23}$ and $C_6 = 8.61 \times 10^{-41}$ [191].

As described by [95] (their Equation 3), we use the equations of [190] to predict the radio synchrotron flux density at an arbitrary frequency ν, accounting for synchrotron self-absorption. From Equation 1 of [190] and Equations 2.3 and 2.4 above, the optical depth to synchrotron self absorption is

$$\tau_{\rm SSA} \propto \sqrt{\frac{{\epsilon_e}^2 \epsilon_B^{(p+2)/2} \rho_{\rm CSM}^{(\frac{1}{2}p+3)} v_s^{(p+6)}}{\nu^{(p+4)}}} \tag{2.5}$$

In the case where $p = 2$, the proportionality simplifies to $\tau_{\rm SSA} \propto \epsilon_e \epsilon_B \rho_{\rm CSM}^2 v_s^4 \nu^{-3}$. This

demonstrates that faster shocks and shocks with denser CSM will suffer stronger synchrotron self-absorption. The relatively slow shocks of novae ($\sim$3000 km s^{-1}) compared to e.g. Type Ibc SNe ($\sim$30,000 km s^{-1}) mean that synchrotron self-absorption is usually negligible in novae (while it can be important in Type Ibc SNe; [190, 192]), and this is what our models predict for parameters consistent with V745 Sco.

A much more important source of radio opacity in V745 Sco is free-free absorption from the warm ionized CSM between the shock and the observer. We approximate τ_{ff} by again assuming a spherical wind-like CSM, maintained at a photoionized temperature of 10^4 K, and using Equation 14 from [193]:

$$\tau_{\rm ff} = 0.005 \left(\frac{\dot{M}}{10^{-6}\ {\rm M}_\odot\ {\rm yr}^{-1}} \right)^2 \times \left(\frac{v_{\rm w}}{10\ {\rm km\ s}^{-1}} \right)^{-2} \times \left(\frac{\nu}{1.4\ {\rm GHz}} \right)^{-2} \times \left(\frac{R}{2 \times 10^{16}\ {\rm cm}} \right)^{-3} \tag{2.6}$$

where R is the radius of the shock. The light curves at frequencies, 0.6–17.5 GHz, all peak around day 25 (Figure 2.3), implying that $\tau_{ff} \approx 1$ at this time (at all these frequencies near simultaneously). Running [72] models for reasonable parameters of the inner CSM (constrained by X-ray observations of [73]: $\dot{M} = [5 - 10] \times 10^{-7}$ M$_\odot$ yr^{-1}, $v_w = 10$ km s^{-1}), in combination with $M_{ej} = 10^{-7} - 10^{-6}$ M$_\odot$, and kinetic energies as derived in §2.5.2, the shock radius on day 25 is $[1.3 - 3.2] \times 10^{14}$ cm. Meanwhile, if the CSM is asymmetric (e.g., largely confined in an equatorial density enhancement), the shock may be relatively undecelerated in some directions, and could reach 9.6×10^{14} cm by day 25 (expanding at 4450 km s^{-1}.

From Equation 2.6 and taking the most constraining frequency of 0.6 GHz, we can infer that the CSM external to this radius is characterized by $\dot{M} < [3 - 64] \times 10^{-9}$ M$_\odot$ yr^{-1}

(assuming $v_w = 10$ km s^{-1}). This $\dot{M}$ is one to two orders of magnitude less than the $[5-10] \times 10^{-7}$ M$_\odot$ yr^{-1} implied by the X-ray absorbing column in the eruption's first few days [73], in line with the suggestion by Delgado & Hernanz that the inner dense CSM is truncated beyond several $\times 10^{14}$ cm. The radio and X-ray data can be reconciled if the CSM within this truncation radius is characterized by $\dot{M}_{in} = [5-10] \times 10^{-7}$ M$_\odot$ yr^{-1}, and the outer CSM is significantly less dense: $\dot{M}_{out} \lesssim 6 \times 10^{-8}$ M$_\odot$ yr^{-1}. In this case, $\dot{M}_{out}$ would produce a small amount of absorption in the X-ray, $N_H \lesssim 1 \times 10^{20}$ cm^{-2}, compared to the larger ISM column, $\sim 6 \times 10^{21}$ cm^{-2} (§2.4; see also [109] and [73]).

The need for a truncated inner dense CSM can be seen in Figure 2.17, which shows the modeled synchrotron emission on top of the observed light curves of V745 Sco's 2014 eruption for three representative frequency bands. In this model, we fit the observed light curve peak at 4.6 GHz, which yields $\dot{M} = 10^{-7}$ M$_\odot$ yr^{-1}; meanwhile, relatively low values of $\epsilon_e = \epsilon_B = 0.0028$ are needed to fit the optically thin decline of the light curve with this relatively high $\dot{M}$. At a given frequency, at early times, the model light curve rises steeply as the free-free optical depth decreases (due to the blast moving out into the CSM), and peaks when $\tau_{ff} \approx 1$. The light curve then declines as the shock decelerates and interacts with less dense CSM. As expected from Equation 2.6, we see that the model light curve peaks at 0.6, 4.6, and 28.2 GHz are all distinct from one another, with e.g., 4.6 GHz peaking around day 18, while 0.6 GHz does not peak until after day 100. The observations, on the other hand, show no such behaviour, with 0.6 GHz and 4.6 GHz peaking on day 25, and 28.2 GHz peaking just a bit earlier, on day 17.5.

The simplest way to obtain a light curve where the different frequencies all peak at the same time is if the synchrotron-emitting shock suddenly 'breaks out' from a large absorbing column, so that all frequencies become optically thin in rapid succession. A possible

explanation for this discontinuity in the CSM, with a relatively high $\dot{M}_{in}$ within several $\times 10^{14}$ cm and a lower $\dot{M}_{out}$ external, is that the wind from the RG companion has only had time to extend to a certain radius. [73] suggest that V745 Sco's 1989 eruption swept the environs clean, and the giant has only had $(2014 - 1989) = 25$ years to pollute the surroundings with its wind. In this scenario, we expect the red giant wind to extend out to $7.8 \times 10^{14} \, (v_w / 10 \text{ km s}^{-1})$ cm, which is comparable to within an order of magnitude to the CSM truncation radius estimated here.

Another scenario which could explain the sudden unveiling of synchrotron emission is an asymmetric CSM largely concentrated in the orbital plane [16]; if the synchrotron emission is primarily originating in the fastest ejecta expanding in the polar directions, the shock may suddenly appear unabsorbed as it expands beyond the equatorial density enhancement. To test this idea, in the future we plan to adapt and expand the 3D hydrodynamic model of [16] to yield a simulated multi-frequency radio light curve that can be compared with observations.

Beyond day $\sim$25, interaction is ongoing, as is clear from the prolonged tail of synchrotron emission gradually fading out to at least day $\sim$200 (Figure 2.3). This optically thin tail of the light curve can be explained by interaction with a lower density wind-like CSM ($\dot{M}_{out}$). As our goal is to compare V745 Sco's CSM with constraints on CSM around SNe Ia (§2.7.2), we use $\epsilon_e = 0.1$ and $\epsilon_B = 0.1$ and 0.01 to estimate $\dot{M}_{out}$, as [24] did in their study of SNe Ia at radio wavelengths. Our comparison therefore assumes that SN shocks and nova shocks accelerate particles and amplify B fields with similar efficiency; if ϵ_e and/or ϵ_B depend on shock velocity/Mach number (e.g. [194]), then it would be more appropriate to use lower ϵ values in novae; we provide how CSM density scales with ϵ_e and ϵ_B at the end of this sub-section. This outer wind can be described by $\dot{M}_{out} = 9 \times 10^{-10}$ M$_\odot$ yr^{-1} for $\epsilon_B = 0.1$

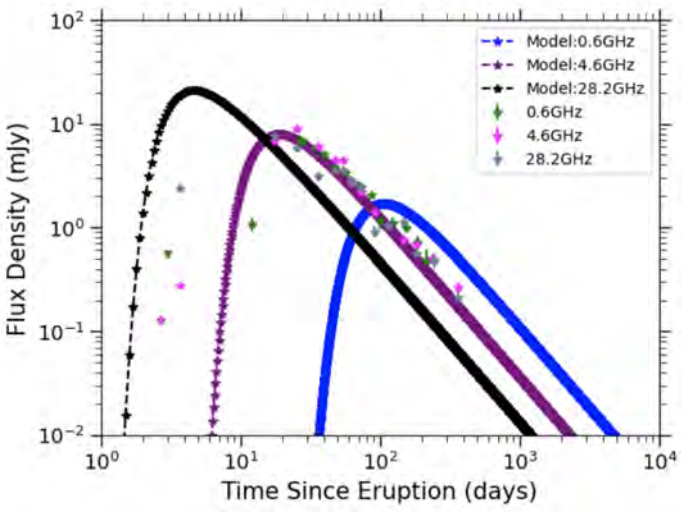

Figure 2.17 Modelled synchrotron emission light curves at three frequencies: 0.6 GHz (blue), 4.6 GHz (purple) and 28.2 GHz (black), superimposed on the observed radio light curve at corresponding frequencies. The model was selected to fit the 4.6 GHz light curve, and takes $\dot{M} = 10^{-7}$ M$_\odot$ yr^{-1}, $M_{ejecta} = 10^{-7}$ M$_\odot$, $\epsilon_e = \epsilon_B = 0.0028$. At different frequencies, this model peaks on different days and at different flux densities, in a matter that is inconsistent with observations.

and $\dot{M}_{out} = 7 \times 10^{-9}$ M$_\odot$ yr^{-1} for $\epsilon_B = 0.01$ (primarily constrained by the luminosity of the radio light curve on the decline; taking $v_w = 10$ km s^{-1}). Figures 2.18 and 2.19 show the synchrotron models superimposed on the observed light curves for $\epsilon_B = 0.1$ and $\epsilon_B = 0.01$, respectively. The models are similar between the two figures, although the transition from the ejecta-dominated phase to the Sedov phase occurs later in Figure 2.18, where $\dot{M}_{out}$ is smaller. The model light curves peak significantly earlier and brighter than the observed light curve peaks, which can be reconciled because, at these early times, the shock is interacting with and being absorbed by the relatively dense $\dot{M}_{in}$ (so this bright emission is being obscured). By the time the shocks breaks out of $\dot{M}_{in}$ around day 25 and begins interacting with the less dense $\dot{M}_{out}$, the light curve models in Figure 2.18 are declining from peak. For the models on the decline from light curve peak, the lower frequencies are brighter than the higher frequencies, as expected for our model selection of $p = 2.1$ (the shallowest particle spectrum

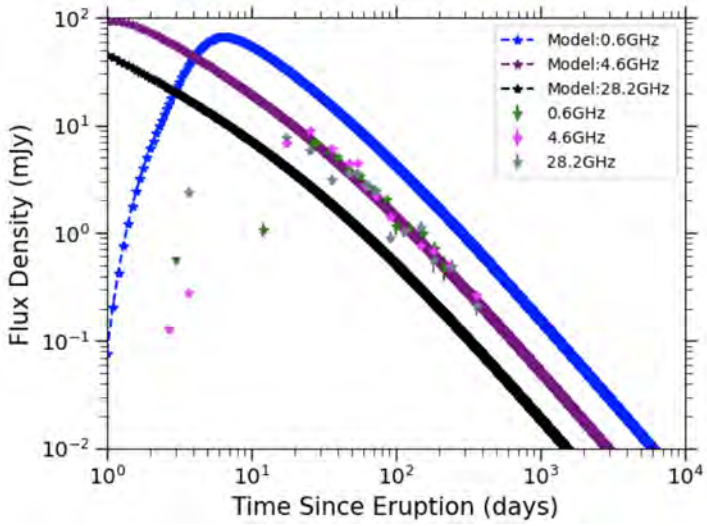

Figure 2.18 As in Figure 2.17, synchrotron light curve models are superimposed on observations at three representative frequencies. This model takes $E = 5 \times 10^{42}$ erg, $M_{ej} = 10^{-7}$ $M_\odot$, $\dot{M} = 9 \times 10^{-10}$ $M_\odot$ yr^{-1}, $v_w = 10$ km s^{-1}, $\epsilon_B = 0.1$ and $\epsilon_e = 0.1$. This model demonstrates that the decline from radio peak can be reasonably well fit by a low $\dot{M}$ and efficient microphysical parameters, if the synchrotron emission until day ∼17–28 is absorbed by additional dense CSM at small radii.

accommodated in the [93, 190] model), which yields $\alpha = -0.55$ (significantly steeper than observed in V745 Sco; §2.6.4). In estimating $\dot{M}_{out}$, we fit the synchrotron model to the data at an intermediate frequency, 4.6 GHz, in an attempt to capture the average behaviour of the multi-frequency light curve.

The optically thin evolution of the radio flux density (valid after radio light curve peak) scales as:

$$S_\nu \propto \frac{R^3}{D^2} \epsilon_e \, \epsilon_B^{(p+1)/4} \, \rho_{CSM}^{(p+5)/4} \, v_s^{(p+5)/2} \, \nu^{(1-p)/2} \tag{2.7}$$

At late times, the blast wave should be in its Sedov Taylor phase, and assuming it is interacting with a $\rho_{CSM} \propto r^{-2}$ wind-like CSM, the evolution of the blast-wave radius scales as $R \propto KE^{1/3}(\dot{M}/v_w)^{-1/3}t^{2/3}$ and the blastwave velocity scales as $v_s \propto KE^{1/3}(\dot{M}/v_w)^{-1/3}t^{-1/3}$[72].

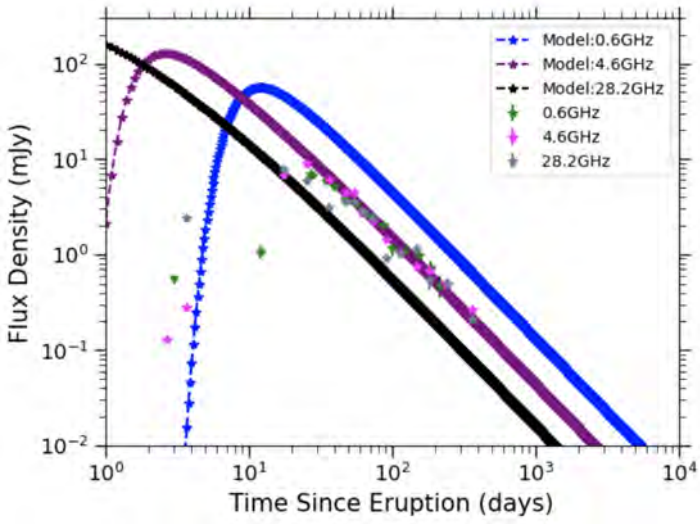

Figure 2.19 As in Figures 2.17 and 2.18, synchrotron light curve models are superimposed on three representative frequencies. This model is identical to that in Figure 2.18, except it takes $\epsilon_B = 0.01$ and $\dot{M} = 7 \times 10^{-9}$ $M_\odot$ yr^{-1}.

Substituting into Equation 2.7, we find:

$$S_\nu \propto \frac{KE}{D^2} \epsilon_e \epsilon_B^{(p+1)/4} \left(\frac{\dot{M}}{v_w} \right)^{(p+1)/4} t^{-(p+1)/2} \nu^{(1-p)/2} \tag{2.8}$$

The implication is that our estimate of the CSM density depends on assumptions about the shock microphysical parameters as $\dot{M}/v_w \propto \epsilon_e^{-4/(p+1)} \epsilon_B^{-1}$. Therefore, for example, if $\epsilon_B \approx 0.001$ and $\epsilon_e = 0.004$ as modelled for radio supernova remnants [195] (rather than the $\epsilon_e = 0.1$ and $\epsilon_B = 0.01/0.1$ assumed above), the $\dot{M}/v_w$ we would infer from the synchrotron luminosity would increase to $\dot{M}_{out} = 5 \times 10^{-6}$ $M_\odot$ yr^{-1}. However, such a high $\dot{M}_{out}$ would imply a higher opacity to free-free absorption (Equation 2.6) and a late light curve peak which is inconsistent with our observations (especially at the lower frequencies). Therefore, the combination of constraints on synchrotron luminosity and τ_{ff} imply relatively efficient microphysical parameters governing particle acceleration and B field amplification, $\epsilon_e \approx 0.1$ and $\epsilon_B \approx 0.01 - 0.1$, in V745 Sco.

2.7.2 V745 Sco in Context: Symbiotic Stars and SN Ia Progenitors

As described in §2.7.1, V745 Sco shows dense, absorbing CSM out to $\sim$ several $\times 10^{14}$ cm, and much lower density CSM at larger radii. It is not currently clear if the dense, close-in CSM is characterized by (a) a disc-like equatorial density enhancement [16], which is presumably the product of wind Roche Lobe overflow and the mass transfer being concentrated in the orbital plane [164], or (b) a more spherical wind that has only had 25 years to fill the environment (the time elapsed between the 1989 and 2014 eruptions). The low-density wind at larger radii has $\dot{M}_{out} = 9 \times 10^{-10} - 7 \times 10^{-9}$ M$_\odot$ yr^{-1} for $v_w = 10$ km s^{-1}. This is significantly lower than the $\dot{M}$ values typically measured for symbiotic stars [62, 68], but note that these works usually assume spherical, continuous, wind-like CSM. A relatively high accretion rate must be sustained on to the white dwarf in V745 Sco to drive the short nova recurrence time, and presumably this mass transfer is far from conservative, but much of the CSM resulting from non-conservative transfer is relatively hidden, tucked in close to the binary.

Is V745 Sco a viable progenitor system for Type Ia supernovae? Its relatively high mass and short recurrence time make it an intriguing candidate, but we can do one better: compare the properties of its CSM with constraints on CSM around SNe Ia, to test if a V745 Sco-like system has been ruled out as a progenitor of most SNe Ia. Constraints on CSM around SNe Ia come from radio observations [24, 119], X-ray measurements [121], and optical observations [124]; see [28] for a review. Here we focus on the radio observations, because they are some of the most constraining and also are in direct analogy to the synchrotron-dominated radio light curve of V745 Sco presented here. Radio observations of SNe Ia are typically obtained $\sim 10 - 100$ days after SN explosion [24], probing the CSM at radii of $\sim 10^{16} - 10^{17}$ cm through synchrotron emission. The nova blast in V745 Sco is $\sim$10 times slower than a SN

Ia, indicating that the radius reached by the nova on day 20 will be reached by a SN Ia blast in just ∼2 days. The implication is that, if a SN Ia interacted with the dense, close-in CSM seen in V745 Sco ($\dot{M}_{in}$), this interaction would only be visible for a few days, and would have been missed by most extant radio observations of SNe Ia.

Radio observations of SNe Ia would instead be probing larger radii, populated by the lower density, extended, wind-like CSM in V745 Sco ($\dot{M}_{out}$. Figure 9 of [24] shows that most radio observations of SNe Ia cannot constrain a wind below $\dot{M} <$ few $\times 10^{-9}$ M$_\odot$ yr^{-1} for $v_w = 10$ km s^{-1}, $\epsilon_e = 0.1$, and $\epsilon_B = 0.1$, and $\dot{M} < 10^{-8}$ M$_\odot$ yr^{-1} for similar parameters except $\epsilon_B = 0.01$. Assuming the ϵ microphysical parameters are similar in novae and SNe Ia, the implication is that most current radio observations of SNe Ia cannot rule out the CSM of V745 Sco, which is characterized by $\dot{M}_{out} = 9 \times 10^{-10}$ M$_\odot$ yr^{-1} for $\epsilon_e = 0.1$, $\epsilon_B = 0.1$, and $\dot{M}_{out} = 7 \times 10^{-9}$ M$_\odot$ yr^{-1} for $\epsilon_e = 0.1$, $\epsilon_B = 0.01$. Even simply using the constraint on $\dot{M}_{out}$ from τ_{ff} ($\dot{M}_{out} < 6 \times 10^{-8}$ M$_\odot$ yr^{-1}; Equation 2.6), which does not depend on ϵ parameters, less than ∼half of SNe Ia with radio observations could rule out V745 Sco's CSM.

We do note that a few of the nearest, best studied SNe Ia (e.g. SN 2011fe, SN 2014J) have unusually deep constraints on CSM [196, 197], and these can rule out a V745 Sco like progenitor. We also note that perhaps more constraining than CSM observations is nebular spectroscopy of SNe Ia to search for material stripped from the companion star [198]. These observations typically find < 0.1 M$_\odot$ of hydrogen can be swept up and remain consistent with spectroscopic limits, while $\gtrsim$0.3 M$_\odot$ of material is expected to be stripped from a giant companion [199, 200]. However, interpretation of nebular spectroscopy is model dependent [201], and multiple constraints should be brought to bear in ruling out a SN Ia progenitor channel. In an era where investigators increasingly think that multiple progenitor channels

contribute to the SN Ia population, and based on CSM properties alone, V745 Sco is allowed as a progenitor system for most SNe Ia.

2.8 Conclusions

We have embarked on a multi-wavelength, but radio forward, investigation of the symbiotic recurrent nova V745 Sco. Our key results are:

- The line of sight to V745 Sco suffers dust extinction of $A_V = 2.14 \pm 0.6$ mag, as constrained by DIBs in optical spectroscopy, consistent with the total Galactic column along that line of sight (§2.4).

- We estimate a distance of $8.2^{+1.2}_{-1.0}$ kpc to V745 Sco, constrained by its peak optical brightness, our extinction measurement, and a realistic three-dimensional map of the Milky Way and its dust (§2.4).

- The apparent narrowing of optical emission lines during V745 Sco's 2014 eruption is likely not dominated by true deceleration due to interaction with CSM, but instead due to a rapid drop in line intensity and S/N. We therefore consider Hα FWZI/2 measurements as lower limits on the shock velocity, except during the first observations, where we use FWZI/2 to measure the maximum ejecta velocity, 4450 km s^{-1} (§2.5.3).

- At radio wavelengths, V745 Sco is not detected during quiescence (2018–2023) by VLASS, consistent with a relatively low density CSM (§2.6.1).

- We find that the radio light curves of V745 Sco's 1989 and 2014 eruptions, constrained at $\sim$1.5 and $\sim$4.9 GHz, are very similar between eruptions. However, the 1989 eruption is $\sim$20 per cent fainter than the 2014 eruption, in contrast with the claim of [137]

(§2.6.2).

- The radio light curve during eruption is dominated by synchrotron emission, as determined from the brightness temperature evolution (§2.6.3).

- We apply a simple [93] model to the 0.6–37 GHz radio synchrotron light curves of V745 Sco in eruption, but find that interaction with a $\rho \propto r^{-2}$ wind-like CSM cannot explain the early portion of the light curves (on the rise to radio peak; the first $\sim$30 days of eruption). Instead, we find relatively dense CSM close-in to the binary ($\dot{M}_{in} = [5-10] \times 10^{-7}$ M$_\odot$ yr^{-1} at $<$ several $\times 10^{14}$ cm, as primarily constrained by X-ray measurements; [73]), and a less dense, extended wind-like CSM at larger radii. The dense close-in CSM may be an equatorial density enhancement [16], or it may be the red giant wind which has only had 25 years since the last nova eruption in which to pollute its environment [73]. We find that the lower density, outer wind can be characterized by $\dot{M}_{out} = 9 \times 10^{-10} - 7 \times 10^{-9}$ M$_\odot$ yr^{-1}, assuming $v_w = 10$ km s^{-1}, $\epsilon_e = 0.1$, and $\epsilon_B = 0.01 - 0.1$. We favor efficient ϵ values such as these, because relatively high values are necessary to reconcile the luminous late-time synchrotron emission and the early radio light curve peak in V745 Sco (§2.7.1).

- It would be relatively easy to hide a V745 Sco-like CSM around a SN Ia, because the dense CSM is confined to near the binary (which would only be constrained by early observations), and the extended wind is lower density than most constraints on SN Ia CSM. This implies that, based on CSM considerations alone, V745 Sco (and symbiotic recurrent novae like it) remains a viable SN Ia progenitor for a significant fraction of SNe Ia (§2.7.2).

In the future, we are excited to extend the simulations of [16] to simulate the multi-

frequency radio light curve predicted for a nova interacting with a complex CSM with an equatorial density enhancement. This will give us a more intricate picture of the blast wave evolution that we can then compare with radio observations, and further elucidate the nature of the dense CSM close in to the binary.

Acknowledgements

IM, LC, EA, KVS, PC, and CEH are grateful for support from NSF grants AST-1751874, AST-2107070, and AST-2205628, and NASA grants 80NSSC23K0497 and 80NSSC23K1247. JS acknowledges support from the Packard Foundation. EA gratefully acknowledges support from the NASA Hubble Fellowship. JLS acknowledges support from NSF grant AST-1816100.

The National Radio Astronomy Observatory is a facility of the National Science Foundation operated under cooperative agreement by Associated Universities, Inc. We acknowledge with thanks the variable star observations from the AAVSO International Database contributed by observers worldwide and used in this research. This work has made use of data from the European Space Agency (ESA) mission *Gaia* (https://www.cosmos.esa.int/gaia), processed by the *Gaia* Data Processing and Analysis Consortium (DPAC; https://www.cosmos.esa.int/web/gaia/dpac/consortium). Funding for the DPAC has been provided by national institutions, in particular the institutions participating in the *Gaia* Multilateral Agreement. This research has made use of the CIRADA cutout service at cutouts.cirada.ca, operated by the Canadian Initiative for Radio Astronomy Data Analysis (CIRADA). CIRADA is funded by a grant from the Canada Foundation for Innovation 2017 Innovation Fund (Project 35999), as well as by the Provinces of Ontario, British Columbia, Alberta, Manitoba and Quebec, in collaboration with the National Research Council of Canada, the

US National Radio Astronomy Observatory and Australia's Commonwealth Scientific and Industrial Research Organisation.

Data Availability

The optical spectra are publicly available at https://www.astro.sunysb.edu/fwalter/SMARTS/NovaAtlas/. All VLA data are publicly available from the NRAO data archive at data.nrao.edu under project codes AL202,AH383, AH389,220 and AH390 (for the 1989 observations) and 13B-057 (for the 2014 observations).

Table 2.2 Spectroscopic Observations of Hα Over the Course of V745 Sco's 2014 Eruption

UT Date	$t - t_0$ (days)	FWHM (km s^{-1})	FWZI (km s^{-1})	Integrated Flux (erg s^{-1} cm^{-2}Å^{-1})
2014 Feb 09	3	2233	8909.3	1.34×10^{-8}
2014 Feb 10	4	1484	8580.9	1.12×10^{-8}
2014 Feb 11	5	1147	8293.6	6.51×10^{-9}
2014 Feb 13	7	889.3	8071.2	6.41×10^{-9}
2014 Feb 15	9	739.1	7335.4	3.37×10^{-9}
2014 Feb 16	10	682.7	5272.0	2.83×10^{-9}
2014 Feb 19	13	552	5452.4	1.05×10^{-9}
2014 Feb 20	14	509.9	4794.1	8.28×10^{-10}
2014 Feb 21	15	476	5084.8	6.44×10^{-10}
2014 Feb 22	16	455.5	4979.0	5.49×10^{-10}
2014 Feb 23	17	439.3	4467.3	4.74×10^{-10}
2014 Feb 24	18	433.3	4513.0	4.21×10^{-10}
2014 Feb 25	19	423.2	4416.8	3.51×10^{-10}
2014 Feb 26	20	424.2	4237.7	3.32×10^{-10}
2014 Feb 27	21	418.4	3995.7	3.13×10^{-10}
2014 Mar 03	25	397.2	3385.6	2.30×10^{-10}
2014 Mar 05	27	387.3	3344.6	2.03×10^{-10}
2014 Mar 09	31	387	3051.6	1.33×10^{-10}
2014 Mar 10	32	380.3	2778.0	1.15×10^{-10}
2014 Mar 11	33	388.6	2583.7	1.02×10^{-10}
2014 Apr 08	61	375.8	1833.6	
2014 Apr 09	62	387.7	1797.1	1.20×10^{-11}
2014 Apr 10	63	343.7	1738.8	5.64×10^{-12}
2014 Apr 13	66	341.1	1706.0	
2014 Apr 18	71	346.5	1643.5	
2014 Apr 22	75	306	1613.5	
2014 Apr 23	76	325.6	1571.4	
2014 Apr 24	77	253.7	1507.9	1.64×10^{-11}
2014 Apr 27	80	362.3	1490.6	
2014 Apr 28	81	323.9	1434.6	
2014 Apr 30	83	330	1410.5	
2014 May 02	85	362.8	1366.5	
2014 May 04	87	366.7	1355.5	
2014 May 05	88	380	1186.5	4.42×10^{-11}
2014 May 06	89	366	1190.3	
2014 May 07	90	366.9	1157.8	
2014 May 08	91	335.1	1139.1	5.82×10^{-12}
2014 May 11	94	332.6	1095.5	
2014 May 12	95	327.1	1080.3	1.92×10^{-12}
2014 May 13	96	319	1072.0	

[a]We take the start of eruption t_0 to be February 6, 2014. The integrated flux was measured after flux calibration.

Table 2.3 Radio Observations of V745 Sco's 2014 Eruption

	$t - t_0^a$	Flux Density ± 1σ Error								Config
	(days)	1.25 GHz (mJy)	1.75 GHz (mJy)	4.6 GHz (mJy)	7.4 GHz (mJy)	13.6 GHz (mJy)	17.5 GHz (mJy)	28.2 GHz (mJy)	36.5 GHz (mJy)	
8.6	2.6			0.13 ± 0.01	0.24 ± 0.02					BnA
9.6	3.6			0.28 ± 0.02	0.40 ± 0.02			2.40 ± 0.24	2.50 ± 0.25	BnA
23.5	17.5			6.80 ± 0.34	7.00 ± 0.35			7.70 ± 0.81	5.40 ± 1.14	A
3.6	25.6	7.33 ± 0.47	8.35 ± 0.44	8.93 ± 0.45	8.26 ± 0.41	7.92 ± 0.80	7.42 ± 0.75	5.90 ± 0.61	5.08 ± 0.54	A
16.5	38.5	4.85 ± 0.25	5.51 ± 0.28	6.00 ± 0.30	5.34 ± 0.27	4.92 ± 0.49	4.37 ± 0.44	3.12 ± 0.34	3.03 ± 0.43	A
25.5	47.5	4.17 ± 0.21	4.59 ± 0.24	4.43 ± 0.22	4.01 ± 0.20	3.80 ± 0.38	3.62 ± 0.36	3.56 ± 0.36	3.22 ± 0.33	A
31.5	54.5	4.04 ± 0.21	4.40 ± 0.28	4.43 ± 0.22	4.00 ± 0.20	3.81 ± 0.38	3.64 ± 0.36	3.55 ± 0.36	3.77 ± 0.53	A
9.4	63.4	2.91 ± 0.18	2.87 ± 0.16	2.73 ± 0.14	2.56 ± 0.13	2.53 ± 0.26	2.61 ± 0.27	2.83 ± 0.30	2.90 ± 0.34	A
11.5	65.5	3.24 ± 0.18	3.13 ± 0.17	2.68 ± 0.14	2.41 ± 0.12	2.48 ± 0.25	2.50 ± 0.25	2.71 ± 0.28	2.86 ± 0.30	A
20.4	74.4	2.78 ± 0.16	2.60 ± 0.14	2.21 ± 0.11	1.96 ± 0.10	1.99 ± 0.20	2.00 ± 0.20	2.42 ± 0.25	2.14 ± 0.24	A
9.3	92.3	1.85 ± 0.10	1.75 ± 0.10	1.43 ± 0.07	1.29 ± 0.07	1.38 ± 0.14	1.38 ± 0.14	0.91 ± 0.10	0.59 ± 0.08	A
1.3	116.3	1.82 ± 0.10	1.70 ± 0.10	1.05 ± 0.07	0.97 ± 0.05	1.08 ± 0.11	1.06 ± 0.11	1.02 ± 0.11	0.93 ± 0.11	A
3.5	148.5	< 2.28	< 1.14	0.76 ± 0.06	0.79 ± 0.04	0.96 ± 0.10	1.00 ± 0.11	1.14 ± 0.14	1.00 ± 0.15	D
7.1	183.1	< 1.78	< 1.36	0.68 ± 0.05	0.61 ± 0.04	0.78 ± 0.09	0.70 ± 0.08	0.56 ± 0.13	< 0.44	D
29.9	236.9	< 0.95	< 0.58	0.49 ± 0.04	0.40 ± 0.03					DnC
8.0	245					0.45 ± 0.05	0.45 ± 0.05	0.49 ± 0.08	0.32 ± 0.10	DnC→C[b]
30.6	359.6	< 0.42	< 0.26	0.27 ± 0.03	0.23 ± 0.02					CnB→B[b]
1.7	361.7					0.21 ± 0.02	0.18 ± 0.02	0.21 ± 0.04	< 0.17	CnB→B[b]

t_0 to be the time of discovery to be February 6.69, 2014.

tions were obtained during 'move time' between VLA array configurations.

Chapter 3. VLBI Images & γ-Rays of V3890 Sgr

3.1 Shocks in the Symbiotic Recurrent Nova V3890 Sgr: VLBI Radio Imaging and Fermi GeV Gamma-Rays

We present very long baseline interferometric (VLBI) radio imaging and *Fermi*/LAT GeV γ-ray observations of the 2019 eruption of the symbiotic recurrent nova V3890 Sgr. The VLBI imaging spans 8 – 51 days after eruption, synchronous with the detected γ-rays. VLBI imaging shows the eruption starts out asymmetric on day 8 with an eastern component brighter than a western component. By day 32 the blast is rather circularly symmetric, and on day 49, the nova shell is brighter along the north–south axis. This morphological evolution is explained by interaction with circumstellar material (CSM) comprised of a spherical wind plus an over-density in the orbital plane. Comparing radio images to optical line widths gives an expansion parallax distance of 6.8 kpc. In the first 32 days or eruption, VLBI images capture >80 % of the integrated flux (as measured by the VLA), implying that synchrotron emission dominates. A second peak in the VLA light curve is explained by an image on day 48 that reveals the nova shell surrounded by a diffuse halo, powered by synchrotron emission from particles that have diffused upstream of the shock. The γ-rays appear around optical maximum and remain detectable for 23 days; marginally significant γ-rays reappear around day 60, concurrent with the second radio peak. Modelling indicates radio and γ-ray emission arise in distinct shock regions: γ-rays from dense CSM in the orbital plane, radio from the more spherical CSM component. X-ray observations constrain the spherical CSM density, which is higher than in other symbiotic recurrent novae. Assuming equipartition, we estimate the fraction of the post-shock pressure in magnetic fields, $\epsilon_B = 3 \times 10^{-4} - 2 \times 10^{-3}$.

3.2 Introduction

Novae are thermonuclear eruptions that occur on the surfaces of accreting white dwarfs in binary systems [37, 98, 99]. The white dwarf accumulates hydrogen rich material on its surface from the companion star, which may range from a main sequence star to a giant. As this material builds up, the bottom layer compresses, temperature increases and the rate of nuclear reactions increase, leading to a thermonuclear runaway, seen as an increase in luminosity [100]. The eruption blows off the accreted envelope mixed with some white dwarf material at velocities ranging from 500-10,000 $\mathrm{km\,s^{-1}}$ [e.g., 2, 45, 202]. As the ejected mass is relatively small [10^{-3} to $10^{-7} M_{\odot}$; 2, 108], the binary system survives the eruption and accretion can continue, accumulating hydrogen-rich matter for the next nova eruption [203, 204].

In some cases, subsequent eruptions have been observed in the same system; these novae are called recurrent novae. The majority of novae have recurrence times longer than a human lifespan and have only had one observed eruption. However, 10 recurrent novae have been observed in the Milky Way [3, 205], with four of them being symbiotic binaries [61], including V3890 Sgr. The prevalence of giant companions among recurrent novae is often explained by accretion fed by red giant winds reaching higher rates than accretion fed by a main sequence companion filling its Roche Lobe [105, 106].

3.2.1 V3890 Sgr

V3890 Sgr is a symbiotic recurrent nova [3] with an M5 III giant companion [129]. It has had three observed eruptions: 2019 August 27.87 [206], 1990 April 27.7 [207, 208] and 1962 June 2 [209, 210]. The recurrence time is short, only about 28 years between eruptions. It is

possible that we have missed an eruption as the nova is behind the sun every December, and the optical light curve shows a rapid decline, $t_3 = 14$ days [211]. The distance is constrained to 6–9 kpc [211], and is discussed further in section 3.4.2. The mass of the white dwarf is estimated at $1.35\,M_\odot$, and the orbital period is 747.6 d [211].

The most recent 2019 eruption of V3890 Sgr was observed in γ-ray, X-ray, UV, optical, IR, and radio wavelengths [40, 212–217]. Here we are focused on high-resolution very long baseline interferometry (VLBI) radio observations and GeV γ-ray observations of the eruption.

Radio observations of the 2019 eruption were reported by [95]. Observations began about 7 days after discovery of the eruption and were done using MeerKAT and the Karl G. Jansky Very Large Array (VLA), with frequencies ranging from $1 - 37$ GHz. The 5 and 7 GHz light curves peak on day 11.2 at $\sim$50 mJy, while the $1.26 - 1.78$ GHz light curves peak around day 15 in the range of 44.2 – 49.0 mJy.

[95] concluded that the radio light curve is dominated by synchrotron emission based on brightness temperature arguments. There is another increase in radio flux density on day 45 seen in frequency bands 1.26 to 7.0 GHz. This second peak in the radio light curve is difficult to explain as thermal emission (as in other novae; [168, 170]). This second bump has been interpreted instead as synchrotron emission resulting from interaction with circumstellar material (CSM) with a complex structure. [95] suggest that the CSM around the nova is complex in shape with perhaps a denser region at a distance from the white dwarf, $\sim 10^{15}$ cm.

V3890 Sgr was also detected in GeV γ-rays by the Large Area Telescope (LAT) on the *Fermi Gamma Ray Space Telescope* shortly after the start of eruption [212]. This makes it the third nova with a giant companion to be significantly detected by *Fermi*, joining the

ranks of V407 Cyg [8] and RS Oph [218] (V745 Sco was also a marginal detection [138]. According to this Astronomer's Telegram on V3890 Sgr, the *Fermi* onset began at the time of optical peak, and lasted 12 days.

3.2.2 Shocks in Nova Eruptions

This paper focuses on the shock signatures from the 2019 eruption of V3890 Sgr, in both radio and γ-ray bands. In the last decade, shocks in novae have been recognized as energetically important and key for shaping their electromagnetic emission [37]. To date, 26 Galactic novae have been detected in GeV γ-rays by *Fermi*/LAT, which signals that novae efficiently accelerate particles to relativistic speeds through diffusive shock acceleration [219]. Most of these novae have main-sequence companions and are surrounded by low-density environments born of conservative mass transfer [84], so the shocks are internal to the nova ejecta [97]. However, a handful of *Fermi*-detected novae have giant companions, where mass transfer is expected to be messier and the environment is polluted by the red giant wind [8, 19]. In these systems, the shock is expected to be external with pre-existing CSM. This dichotomy is further supported by X-ray observations of novae; in *Fermi*-detected novae with main-sequence companions, hot shocked gas is not detected contemporaneous with γ-rays despite numerous observations with *Swift*/XRT, implying high absorption columns [220, 221] or suppression of hot gas behind a radiative shock due to mixing with cooler gas [222–224]. On the other hand, novae with giant companions often show hot X-ray emission from shocked gas from the earliest phases of their eruption [11, 39, 109, 225], implying significantly lower absorption columns.

The CSM is often modelled as a spherical wind with a r^{-2} density profile, and an equatorial density enhancement (EDE) in the orbital plane, driven by gravitational focusing of

the mass loss by the white dwarf [16, 164, 226, 227]. This is the scenario we have in mind in studying V3890 Sgr's 2019 eruption: external shocks between the nova ejecta and CSM, and denser interaction in the orbital plane.

3.2.3 This Paper

Here we present high-resolution radio images and analysis of the 2019 eruption of V3890 Sgr using data obtained with the Very Long Baseline Array (VLBA) and the European VLBI Network (EVN) plus the Enhanced Multi-Element Remotely Linked Interferometer Network (e-MERLIN). We also analyse data from *Fermi*/LAT to characterize the GeV γ-ray light curve. With observations in both wavelengths we are able to compare results, investigate the efficiency of particle acceleration and discuss the evolution of the blast and the structure of the surrounding CSM.

In §**??**, we describe the data sets under consideration. Section 3.4 contains analyses of the VLBA and EVN+e-MERLIN images, using them to test the origin of the radio emission, to measure the magnetic field strength, and to estimate an expansion parallax distance of 6.8 kpc. In §3.5, we analyse the *Fermi* data, presenting the light curve over the first 75 days of eruption and demonstrating a curious-but-marginal reappearance of γ-rays around the time of the second radio bump. We discuss and model our findings in §**??**, estimating the efficiency of magnetic field amplification and particle acceleration, describing efforts to simultaneously model the radio and γ-ray emission, and exploring the origin of the second bump in the radio and γ-ray light curves. We conclude in §**??**.

Table 3.1 VLBI and Corresponding VLA Observations of V3890 Sgr

UT Date	$t - t_0$[a] (days)	Freq (GHz)	Flux ± Error (VLA) (mJy)	Flux ± Error (VLBI)[b] (mJy)	Major Axis[c] (mas)	Minor Axis[d] (mas)	RMS noise (μJy bm^{-1})	Panel[e]
2019 Sep 5.0	8.1	4.87	43.5 ± 2.2	37.75 ± 4.17			115	(a)
2019 Sep 5.0	8.1	8.37	44.6 ± 2.2	36.91 ± 2.37	8.4	8.0	82	(b)
2019 Sep 13.0	16.1	4.87	44.0 ± 2.2	36.42 ± 2.02			116	(c)
2019 Sep 12.9	16.0	8.37	39.9 ± 2.0	32.68 ± 1.75	13.7	13.3	58	(d)
2019 Sep 28.9	32.0	4.87	24.8 ± 1.2	24.61 ± 1.37	22.5	21.5	60	(e)
2019 Oct 15.6	48.7	4.93	17.3 ± 0.9	12.44 ± 0.64[f]	46.0	43.2	31	(g)
2019 Oct 15.6	48.7	4.93	17.3 ± 0.9	17.15 ± 0.94[g]	157	96	31	(h)
2019 Oct 17.9	51.0	4.87	17.3 ± 0.9	14.00 ± 0.80	34.0	31.9	22	(f)

[a] We take the start of eruption t_0 to be 2019 August 27.9 UT.

[b] All VLBI images were obtained with the VLBA, except the 2019 Oct 15 epoch, which was obtained with the EVN+e-MERLIN.

[c] Oriented east–west in all images, except the diffuse flux on 2019 Oct 15, when the major axis has a PA = 50°.

[d] Oriented north–south in images, except the diffuse flux on 2019 Oct 15.

[e] Images are shown in these corresponding panels of Figure 3.3.5.

[f] Measurements for the bright nova shell, equivalent to what is captured in VLBA images.

[g] Measurements including the diffuse emission surrounding the nova shell.

3.3 Observations and Data Reduction

3.3.1 VLBA Radio Observations of the 2019 Eruption

High-resolution imaging observations of V3890 Sgr with the VLBA started on 2019 September 5.0 (8.1 days after start of eruption) and ended 2020 February 8 (164 days after eruption). Nine observations were obtained under VLBA project code BL267 (PI Linford). For observations taken on 2019 September 28 and October 17 in X band (center frequency 8.37 GHz) and February 8 in C band (center frequency 4.87 GHz), we were unable to properly calibrate the data. The phases were scattered and the check source when imaged was not a point source indicating that there was an issue with the calibration, perhaps due to the southerly declination of the source and resulting low elevation of observations. We made several attempts to calibrate the data but unfortunately were unable to get usable results. Because of this we decided to cut out these data and do not include them in any of the following plots, images, or analysis. The six observations that yielded good images are listed in Table 3.1. VLA observations, which are useful for determining V3890 Sgr's integrated flux density, began on August 30th [95]. For each VLBA observation there were near-contemporaneous VLA observations at 5 GHz and 7 GHz.

The September 5 and September 13 observations included both 4.87 GHz and 8.37 GHz, with observations switching between bands on average every 42 minutes. The September 28 and October 17 observations only had usable data at 4.87 GHz. The phase reference calibrator was J1820−2528, and the check source was J1819−2036. For the final two observations a fringe finder (J1924−2914) was included. Each observation has 4 spectral windows, each 128 MHz wide, resulting in a total bandwidth of 512 MHz. There are 128 spectral channels per spectral window. All data were obtained in full Stokes mode. The exposure time of each

epoch was about 1.8 hours on V3890 Sgr, except for the October 17th 4.87 GHz observation which was 3.6 hours. On the September 5 observation, Mauna Kea did not join until about 2 hours after the start of the observation. On the September 28 observation, Brewster was not recording data.

After flagging poor data and radio frequency interference on the calibrator scans, we noticed the phase calibrator J1820−2528 showed complex structure, so we split it into its own FITS file and loaded it into DIFMAP [228] in order to improve our model. There we iteratively self calibrated and imaged the calibrator data, recovering some diffuse flux surrounding a point-like source. This improved model was loaded back into AIPS and then used in the calibration process.

The data were calibrated using standard routines in AIPS 31DEC22 [140]. Instrumental delay calibration and bandpass calibration were performed using J1820−2528 for the observations taken on September 5 and 13. For observations taken on September 28 and October 17 both J1820−2528 and J1924−2914 were used. Global fringe fitting was then carried out with solution intervals of 1 minute over the course of the observation. Again, for the last two observations J1924−2914 was included in the global fringe fitting. Flux calibration was carried out using VLBAAMP in AIPS. In AIPS phase and amplitude self calibration were performed on the calibrator with a solution interval of 0.5 and 1 minute respectively.

The science target was then flagged, calibrated, and split. It was exported into DIFMAP and imaged in Stokes I. We used RADPLOT to further flag the data before cleaning the image. Natural weighting was used for all epochs. Images of all VLBA observations were made with untapered data to obtain maximum angular resolution. We boxed regions with significantly higher flux density than the background and used the CLEAN algorithm to clean the image. This was done repeatedly, applying phase SELFCAL of decreasing integration intervals until

we reached a solution interval of 2 minutes. The final image was viewed in MAPL CLN.

3.3.2 EVN plus e-MERLIN Observations

To reveal more details about V3890 Sgr as it expands and fades, we also performed real-time *e*-VLBI observations (project code: RY008, PI: Jun Yang) with the EVN plus e-MERLIN at 4.9 GHz on 2019 October 15 (48.7 days after the start of eruption). The target-of-opportunity observations lasted about four hours (UT: 14:30–18:30). The participating stations were Jodrell Bank, Westerbork, Effelsberg, Medicina, Onsala, Yebes, Hartesbeesthoek, Zelenchukskaya, Irebene, Cambridge, Darnhall, Pickmere, Defford, and Knockin. The observations used the default frequency setup at C band for the EVN (16 subbands in dual polarization, 32 MHz per subband, 2-bit quantization) and e-MERLIN (2 subbands in dual polarization, 64 MHz per subband, 2-bit quantization) stations.

We used a different source, J1828−2417, as the phase-referencing calibrator during the EVN and e-MERLIN observations of V3890 Sgr. The calibrator is only half degree apart from V3890 Sgr and has a compact core-jet VLBI structure with a correlation amplitude of 21 mJy on the long baselines at 8.4 GHz. The nodding observations used a cycle time of three minutes: 20 s for the calibrator, 100 s for the target, and 60 s for the antenna slewing time. To derive the relative position of J1828−2417 with respect to J1820−2528, i.e. the bright calibrator used in the above VLBA observations, we also observed the pair of calibrators for 11 phase-referencing cycles.

The correlation data were calibrated in AIPS 31DEC22 [140]. When the visibility data were loaded into AIPS discs, we ran AIPS task `ACCOR` to slightly correct cross-correlation amplitudes. Before general a-priori amplitude calibration, the antenna system temperature data were significantly smoothed to minimize their random errors. When antenna system

temperatures and gain curves were not available, we used nominal system equivalent flux densities and a flat gain curve to do a-priori amplitude calibration. The task `TECOR` was used to remove ionospheric dispersive delays calculated according to maps of total electron content provided by Global Positioning System (GPS) satellite observations. The phase errors resulting from the antenna parallactic angle variations were removed. We corrected the instrumental phases and delays across the subbands via running fringe-fitting with the data from the bright fringe finder J1800+3848. After removing the instrumental phase errors, all subband data of were combined to run more accurate fringe fitting with a solution interval of 20 s. The most sensitive telescope Effelsberg was used as the reference station. The solutions were also applied by two-point linear interpolation from J1828−2417 to V3890 Sgr and J1820−2528. The phase connections were also quite smooth at all stations. Bandpass calibration was also performed using the fringe finder J1800+3848.

The deconvolution was performed in DIFMAP [228]. The calibrator J0834−0417 shows a one-sided core-jet structure with a total flux density of ∼38 mJy at 4.93 GHz. With the input image, we re-ran the fringe-fitting and the amplitude and phase self-calibration in AIPS. All of these solutions were also transferred to the target data by linear interpolation. The target V3890 Sgr was imaged without self-calibration. The low-elevation data in the first and last hour hours were excluded in the imaging process. The small positional offset of the weak calibrator J1828−2417 was calculated with respect to the bright calibrator J1820+2528, and was corrected in the VLBI map of V3890 Sgr.

3.3.3 *Fermi*/LAT γ-ray Observations of the 2019 Eruption

V3890 Sgr was observed at GeV γ-ray energies using *Fermi*/LAT. For our γ-ray analysis of V3890 Sgr, we used `Fermitools` (version 2.4.0). Our analysis is based on the binned likeli-

hood tutorial provided by the *Fermi* team[1]. We begin by selecting events based on their class and type, selecting only events with `evclass`=128 and `evtype`=3. We also select for good time intervals using the logical expression `(DATA_QUAL>0)&&(LAT_CONFIG==1)`. The selected observations contain all the Pass 8 (P8R3_V3) γ-ray events from 100 MeV to 300 GeV within 10 degrees of the nova. We use a model including all the known sources in the 4FGL-DR3 catalogue [229] within 20 degrees of V3890 Sgr. Also included are the Galactic diffuse emission and the isotropic emission models (i.e. `gll_iem_v07` and `iso_P8R3_SOURCE_V3_v1`). A point source model for V3890 Sgr is added as well, assuming a power law spectrum with an exponential cutoff, as is frequently used to model the γ-ray spectra of novae [138]. This spectral model is shown in equation 3.1, where N_0 is a normalization parameter, γ_1 is the power law index, E_c is the energy cutoff, and E_0 is an energy scale fixed to 200 MeV.

$$\frac{dN}{dE} = N_0 \left(\frac{E}{E_0}\right)^{-\gamma_1} e^{-\frac{E}{E_c}} \tag{3.1}$$

We analysed the *Fermi*/LAT data to obtain V3890 Sgr's GeV γ-ray flux, fitting this model to data ranging from 2 days before the optical peak to 20 days after the peak. This 22-day window was used to obtain the average flux for this nova, and to obtain spectral parameters. As is typical for a *Fermi* analysis, we estimate our detection significance using the test statistic, which is -2 times the likelihood ratio between the best fitting model including the nova and a background only model. This can be converted to a typical significance level by taking the square root of the test statistic. In our case, this time window yields a $> 5\sigma$ detection, making the detection of γ-ray emission from V3890 Sgr unambiguous. Due to the relatively large distance, and correspondingly small observed γ-ray flux of V3890 Sgr, the

[1] https://fermi.gsfc.nasa.gov/ssc/data/analysis/scitools/binned_likelihood_tutorial.html

spectral parameters remain highly uncertain. We recover a spectral index of $\gamma_1 = 1.4 \pm 1.8$ with a cutoff energy of 2 GeV, though the spectral model is not well constrained.

After obtaining the average flux and associated test statistic for V3890 Sgr we built a light curve starting 60 days before the optical peak, with each point using 15 days of data (as in [138]). The resulting light curve is discussed in §3.5. Throughout this light curve, we fix the spectral parameters to a set that are typical for the γ-ray emission from novae, assuming a power law index of 1.9 and a cutoff energy of 4.3 GeV [138]. In many of the light curve bins the data are insufficient to meaningfully constrain the spectral parameters, so the only model parameter for V3890 Sgr allowed to vary is the normalization.

3.3.4 *Swift* XRT X-ray Observations

X-ray Telescope (XRT) observations with the *Neil Gehrels Swift Observatory* began about 0.7 days after eruption, revealing a bright hard X-ray source [230]. Data were taken from August 28 to September 5, took a brief hiatus for proximity to the Moon, and proceeded at decreasing cadence from September 10 until V3890 Sgr entered solar conjunction on November 11. Once the nova was no longer blocked by the Sun observations resumed on 2020 February 17 until May 4.

Swift data were processed using HEASoft and the most recent calibration files available for late 2019. Here we use the same spectral fits as [231] for constraining the X-ray emission at the epochs of our VLBI imaging. On days 7.7 and 51.4, the spectrum is fit with a single optically thin thermal component (i.e. APEC, which represents hot shocked gas). On day 15.5, the fit is improved by the addition of a second APEC component and also a blackbody component (which represents the supersoft source). By day 31.9, the supersoft source had faded, but the optically thin thermal emission is still better fit by two APEC components

than one. Absorption is held fixed at $N_H = 5.1 \times 10^{21}$ cm^{-2}. The APEC parameters (kT and normalization) are listed in Table 3.3.

3.3.5 Optical Spectroscopy of the 2019 Eruption

As an additional constraint on the ejecta velocities in V3890 Sgr, we considered optical spectroscopy of the 2019 eruption obtained using the Small and Moderate Aperture Research Telescope System (SMARTS) 1.5 m telescope and its CHIRON optical spectrograph [139]. The observations covered the wavelength range $4082 - 8770$ Å with a resolution of $R = 27,800$. Observations post eruption began on August 28, 2019 and ended November 4, 2019, with some spectra obtained pre-eruption.

3.4 VLBI Radio Image Analysis

Our VLBA radio images of V3890 Sgr's 2019 eruption are plotted in panels (a–f) of Figure 3.3.5 in J2000 equatorial coordinates. The EVN+e-MERLIN image is shown in panels (g) and (h) of Figure 3.3.5. In each image, the position derived from *Gaia* Data Release 3 [232, 233] is marked using a white dot and error bars; the *Gaia* position was corrected for proper motion to the observation time of each image. The *Gaia* position at the average observing epoch is RA = 18h30m43.2824s and Dec = $-24°01'08.988''$, and the error bars are smaller than the marker and are not visible in the images. The mean *Gaia* epoch is 2019.81.

The background RMS noise was found in DIFMAP by calculating statistics on a blank image region away from the nova. The rms noise levels in the 8.37 GHz images were 58–82 μJy beam^{-1} and the noise values in the VLBA 4.87 GHz images were 22–116 μJy beam^{-1}. The specific image noise values are listed in Table 3.1. The rms noise in the 4.93 GHz EVN+e-MERLIN image is 31 μJy beam^{-1}. The image RMS values were used to set the contour levels in the images to $-1.5, 1, 3, 5$ and 7σ (Figure 3.3.5). These noise levels can be compared with the theoretical thermal noise of the VLBA, as calculated using the EVN calculator. This led to theoretical noise estimates of 18.1 μJy beam^{-1} at 8.37 GHz with the VLBA, 15.4 μJy beam^{-1} at 4.87 GHz with the VLBA, and 13.0 μJy beam^{-1} for the EVN+e-MERLIN observation. It is not unusual for VLBI images to have observed noise values several times that theoretically expected, and reaching theoretical noise was made unusually difficult by the low elevation of V3890 Sgr as observed by these radio facilities.

All VLBA images are centered at the same location (RA= 18h30m43.2826s, Dec = $-24°01'08.990''$) with the same map size (2048 pixels on a side) and pixel size (0.15 mas). For the 4.87 GHz VLBA images, the average FWHM resolution is $B_{\rm maj} = 4.5$ mas along

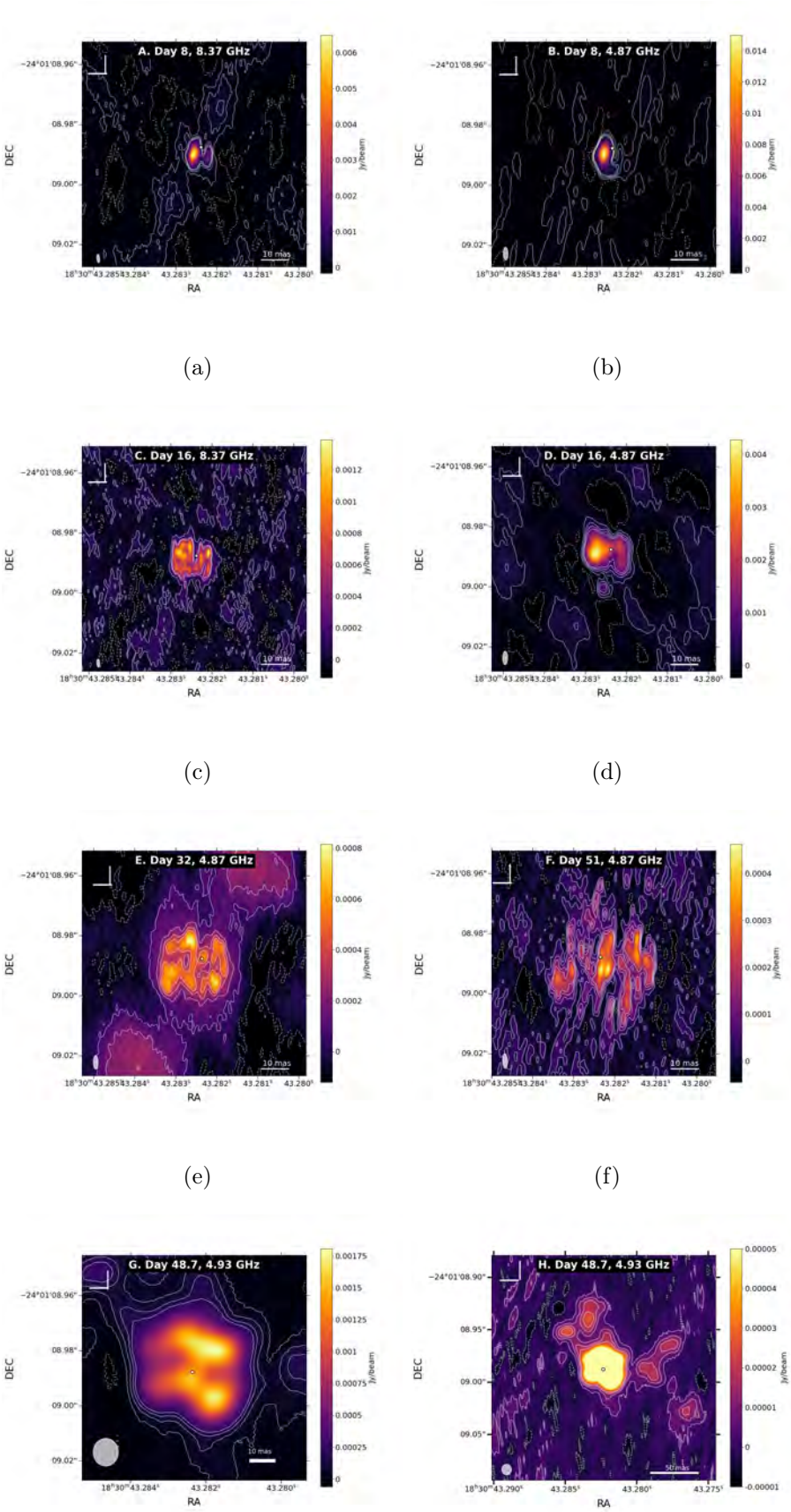

(a) (b)

(c) (d)

(e) (f)

(g) (h)

Figure 3.1 VLBI radio images of the 2019 eruption of V3890 Sgr. The top two panels, (a) and (b), show 4.87 and 8.37 GHz VLBA images on day 8.1. The second row—panels (c)

the major axis and $B_{min} = 1.7$ mas along the minor axis with an average position angle of $PA = -1.3°$. The 8.37 GHz images have an average resolution $B_{\rm maj} = 2.7$ mas and $B_{\rm min} = 1.0$ mas. The 4.93 GHz EVN+e-MERLIN image is restored with a symmetric beam of FWHM = 10 mas.

3.4.1 Morphology and Evolution

The images in Figure 3.3.5 show how the shape of the nova changes over time. Eight days after eruption we see an elliptical compact source offset to the east—likely a lobe of a bipolar outflow—and another small region to the west of source center (panels (a) and (b) of Figure 3.3.5). This fainter western component is more apparent in the 8.37 GHz image than the 4.87 GHz image (panel (b) compared with panel (a)). This likely implies that the western structure is absorbed by intervening CSM in this first epoch.

16 days after eruption, radio emission from V3890 Sgr has become more spread out (panels (c) and (d) of Figure 3.3.5), and both lobes are now more apparent. In the 4.87 GHz image the brightest region remains the eastern lobe. The small structure beneath the nova, located at Dec of about −24:01:09.00 in panel (c), is likely an artefact as we do not see it in later epochs. At 8.37 GHz, the radio emission is noisier, as expected from the higher angular resolution sampling the nova with more synthesized beams. The eastern and western lobes are of more comparable brightness at 8.37 GHz, implying that optical depth continues to affect the western lobe at 4.87 GHz.

The shape of the early radio emission could be explained if the CSM is composed of a spherical wind and a region of increased density in the orbital plane, (i.e., the EDE; [16, 234–236]). The position angle of the EDE could range from 0 to −15° (oriented roughly up–down in Figure 3.3.5). The EDE impedes expansion in the north–south direction and

confines the ejecta into two lobes oriented mostly east–west. The lobes being imaged in VLBA suggest that the synchrotron emission is coming from the lobes and not the central disc. The synchrotron emission would then be coming from interactions with the spherical component of the CSM. The inclination angle of the nova is well constrained to be $67 - 69°$ by [211], and our VLBA imaging shows that the eastern side is tilted towards us, while the western side is tilted away from us and undergoes more absorption from the EDE in early imaging epochs.

During the third epoch, 32 days after eruption (panel (e) of Figure 3.3.5), the radio emitting region continues to expand and now looks quite symmetric east–west. The nova no longer looks so bipolar, and has similar dimensions north–south and east–west (Table 3.1). There are significant deconvolution artifacts visible around the nova in this epoch (visible as blotches at top-right and bottom-left in panel (e)); these should be disregarded.

The time period of day 48–51 is imaged by both the VLBA and EVN; while the VLBA has higher resolution, EVN+e-MERLIN is more sensitive to lower surface brightness emission. The VLBA image from this last epoch is quite noisy, implying that the surface brightness of the radio emission has dropped (panel (f) of Figure 3.3.5). The EVN+e-MERLIN image, however, captures more of the flux at higher significance, and now shows that the nova is brighter along the north–south axis: a $\sim 90°$ flip from what was observed earlier in the eruption (panel (g) of Figure 3.3.5). The radio-emitting shocks therefore seem to be primarily interacting with the EDE at this late epoch.

The EVN+e-MERLIN image from day 48 also shows significant diffuse radio flux external to the primary nova shell (panel (h) of Figure 3.3.5). This emission is patchy, elongated, and asymmetrically distributed around the nova shell, with a position angle of $\sim 50°$.

Compared with RS Oph's 2021 eruption, our VLBA images appear to be missing a central

disc component. In addition to this compact central component, RS Oph shows a bi-lobed structure similar to V3890 Sgr, with one lobe being initially fainter and then increasing in brightness over time, which is attributed to absorption by an EDE [237, 238]. However, RS Oph remains more elongated/bipolar in later epochs (64–65 days after explosion), while V3890 Sgr exhibits more circular symmetry in our later imaging epochs (Figure 3.3.5). V407 Cyg— a 2010 nova that erupted in a longer period symbiotic binary with an asymptotic giant branch companion and the first nova detected in GeV γ-rays [8]— was imaged with VLBI 20 to 203 days after eruption. Images revealed an expanding elliptical shell with no central brightening [239]. They also exhibit radio emission at larger radii than can be attributed to the nova eruption [239], perhaps similar to the extended diffuse emission we observe in V3890 Sgr with the EVN+e-MERLIN.

3.4.2 Angular Size as a Function of Time

We estimated the size of the radio emission from our VLBI images. In the first two epochs, we use the 8.37 GHz images for size determination, as they are both higher resolution and less affected by absorption than the 4.87 GHz images. As the source morphology is complex and not well described by e.g. a Gaussian, we do not fit the source with parametric models in the uv plane; instead, we directly estimate the source size from the image.

For the first epoch the size of the nova was determined using JMFIT in AIPS by fitting two Gaussians to the nova. Both lobes of the nova were resolved, so we used the deconvolved sizes of the components to estimate the 2σ radii of the Gaussians, and then measured the distance between the centres of the Gaussians to get the distance between the two lobes. This was all added together to get the full diameter of the source along the major (roughly east–west) axis. The diameter of the nova along its minor axis was the average of the

two deconvolved Gaussian widths in the ∼north–south direction. For the remaining VLBA epochs the size was determined by measuring the diameter of 3σ contours in CARTA.

In the EVN+e-MERLIN image, there is significant diffuse flux external to the nova shell, and we estimated the size in two different ways: the dimensions of the nova shell estimated from 5σ contours in CARTA, and the larger dimensions of the diffuse flux estimated from 3σ contours. We note that the dimensions of the nova shell estimated from the EVN image are significantly larger than in the VLBA image from day 51 (mean diameter of 44.5 mas, compared to 32.9 mas). This could be caused by a poorly measured diameter in the noisy VLBA image or the lower resolution of the EVN image.We note that if we use the EVN dimensions of the nova shell, we find that the expanding shell would have had to significantly accelerate between day 32 and 48 (§3.4.2), which seems unlikely. We therefore conclude that the EVN dimensions of the nova shell are likely affected by the lower resolution of this image. As the EVN image and day 51 VLBA image yield similar fluxes for the nova shell, but the VLBA image better hones in on the nova shell, we use the VLBA image for estimating the shock velocity and magnetic field (Table 3.2)

The major and minor axes are listed in Table 3.1. Generally, the major axis of the nova shell is oriented east–west and the minor axis north–south, although we note that the source is not greatly elongated in the east–west direction in any of the epochs.

3.4.3 Velocities and Expansion Parallax Distance

If we assume a distance of 9 kpc to V3890 Sgr, as suggested by [211] based on the assumption that the red giant companion is Roche Lobe filling, the diameter of V3890 Sgr's VLBA emission would be 1.1×10^{15} cm on day 8, growing to 4.7×10^{15} cm on day 51. This implies remarkably high expansion velocities of 8080 km s^{-1} over the first 8 days, and ∼5000 km

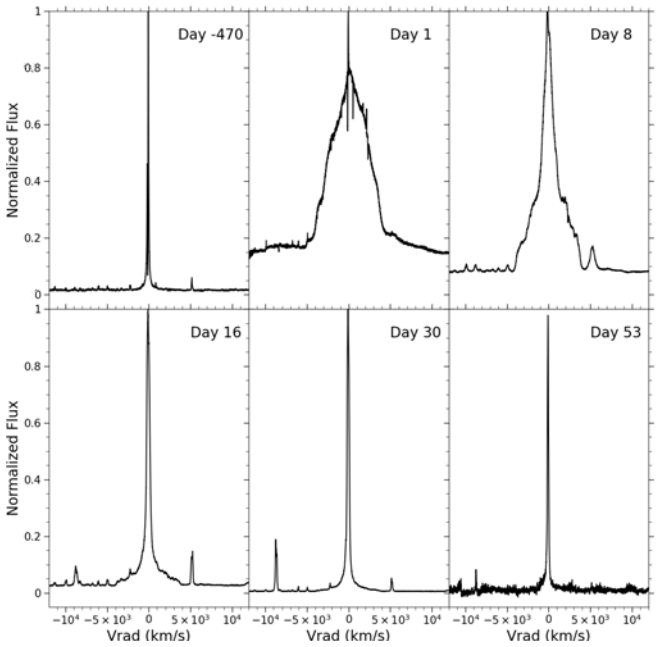

Figure 3.2 The Hα emission line profiles 470 days before V3890 Sgr's 2019 eruption and 1, 8, 16, 30, and 53 days after the eruption.

s^{-1} over the following 43 days.

To test if these high expansion velocities are plausible in V3890 Sgr, we inspected Hα line profiles as observed by SMARTS/CHIRON. Six epochs of Hα line profiles of the 2019 eruption are plotted in Figure 3.2. The full width at zero intensity (FWZI) was estimated for each of the Hα emission lines using SPECPLOT in IRAF. To measure the FWZI we estimated the continuum level of the data and measured where the Hα emission line met that continuum level.

A spectrum obtained more than a year before the 2019 eruption shows a very narrow Hα emission line with no extended wings. This emission emanates from the circumbinary material, ionized by the accreting white dwarf. One day following eruption, the Hα line shows a much broader emission line with a remnant of the narrow emission line superimposed (implying the presence of unshocked circumstellar material; centered at $v = -131$ km s^{-1}).

While the bulk of the emission is confined to $\pm$5000 km s^{-1}, there may be faint wings on day 1 that extend to about $\pm$9600 km s^{-1}. However, these wings are very faint, and sensitive to vagaries of continuum fitting, so we are not certain how reliable the presence of 9600 km s^{-1} gas is in V3890 Sgr. Prior to the eruption there is no evidence of these extended wings. By day 8, the narrow component has broadened and the broad wings have disappeared, giving the profile a near-triangular shape. Although a He I line at 6678 Å makes it difficult to measure the edge of the Hα line profile, we estimate it converges with the continuum around $\pm$4300 km s^{-1}. On day 16, the narrow component is very strong compared to the broad component, and the Hα line reaches $-$3840 km s^{-1} and +3650 km s^{-1}, indicating that the expansion is slowing. The broad component of the Hα line has further narrowed by day 30 with HWZI $v = 2520$ km s^{-1}. By day 53 the line width has decreased to about $v = \pm 1440$ km s^{-1}.

These spectroscopic velocities are lower than what is implied by our VLBA images, if we take a distance of 9 kpc. [211] convincingly argue based on Na I D absorption lines that the distance to V3890 Sgr is at least 6 kpc, and a distance of about 9 kpc is likely an upper limit, as it assumes the red giant companion completely fills its Roche Lobe. We combine the spectroscopic velocities and our VLBA imaging to estimate expansion parallax distances, taking the expansion in the north–south direction, as V3890 Sgr is viewed relatively edge-on ($i \approx 68^\circ$; [211]) and our imaging shows the orbital plane is oriented roughly north–south, so the radial velocity will more closely mirror the north–south expansion than east–west. Assuming that the emission began as a point source on day 0 and expanded to a diameter of 7.9 mas by day 8.1, we find a distance of 11.4 kpc if the 9600 km s^{-1} broad wings are reliable, and a distance of 5.9 kpc if the radio emission is characterized by expansion of 5000 km s^{-1}, more in line with the bulk of the emission line flux.

Between days 8 and 16, we estimate an expansion parallax distance of 6.6 kpc (for an average spectroscopic velocity of 4000 km s^{-1} during this time). Between days 16 and 32, we find 6.9 kpc for an average velocity of 3130 km s^{-1} during this time. Choosing to disregard the first epoch due to ambiguity with the FWZI measurement, we prefer a distance of 6.8 kpc to V3890 Sgr, and use this throughout the rest of this paper. Velocities estimated from our VLBA images, taking $d = 6.8$ kpc and the geometric mean of the major and minor axis of V3890 Sgr, are listed in Table 3.2.

At this distance, the dimensions of the diffuse radio emission detected by EVN+e-MERLIN on day 48 are 8×10^{15} cm by 5×10^{15} cm. If this material was launched on day 0 of the 2019 eruption, it would have needed to expand at ∼15,000 km s^{-1}, much faster than is observed in V3890 Sgr (or in any nova that we know). We therefore conclude that this diffuse emission was caused by a relativistic tracer, like photons or cosmic rays, escaping the nova shell and interacting with the environment. We discuss this scenario more in §3.6.4.

3.4.4 Fraction of Flux 'Resolved Out' by VLBA

In Figure 3.3 the VLA light curve, which measures V3890 Sgr's integrated radio flux density, is plotted using stars and compared to the VLBI light curve plotted as dots. The total flux density of V3890 Sgr in our VLBA and EVN+e-MERLIN images is found by boxing a region around the nova in CARTA. We then estimated the associated uncertainty by determining how many synthesized beams fit into this region, and multiplying the image rms noise by the square root of this number of beams. We added this uncertainty in quadrature with an estimated flux calibration error of 5 %, as all frequency bands are below 10 GHz. The resulting flux densities and errors are listed in Table 3.1.

We see the VLBA light curve is brightest during our first epoch on day 8, and the 4.87

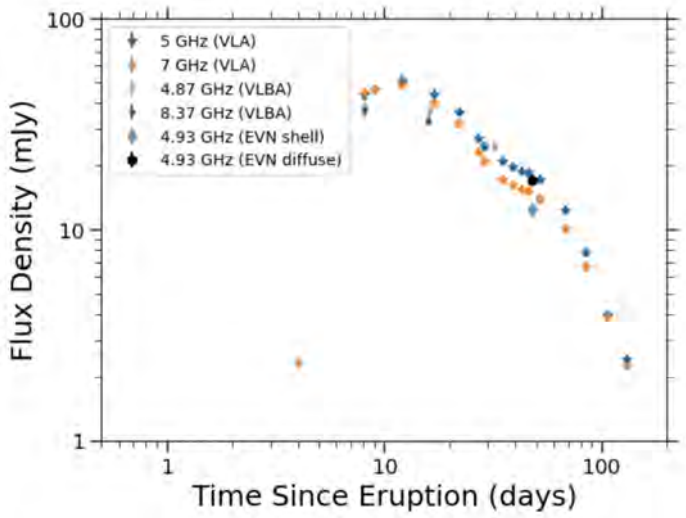

Figure 3.3 Integrated flux densities from our VLBA observations and the EVN+e-MERLIN observation as a function of time following V3890 Sgr's 2019 eruption, compared to the VLA light curve in similar frequency bands (VLA data published in [95]).

GHz flux density then declines with a power-law slope of -0.91 ± 0.45 (excluding the EVN point that detects the diffuse flux). The VLA light curves peak 11 days after discovery; if we measure the power law slope of the 5.0 GHz band from day 9 to day 51 we find a shallower decline than VLBA with power-law slope of -0.67 ± 0.05.

The VLBA observations appear to capture most of the flux density seen in the VLA observations. On day 8 the VLBA captures 87 % of the flux density in 4.87 GHz and on day 16 the VLBA captures 83 %. This confirms that the radio emission is synchrotron dominated, as the VLBA is not sensitive to thermal emission (the theoretical 3σ brightness temperature sensitivity of the VLBA is 3.1×10^5 K at 4.87 GHz and 3.5×10^5 K at 8.37 GHz, for our exposure times; Equation 3.2).

However, the second bump in the VLA light curve, which happens around day 50, is missed by our day 51 VLBA image, detecting only 13.9 mJy of the 17.3 mJy integrated and explaining the steeper decline of the VLBA light curve, compared to VLA. We do note the appearance of two significant compact flux components near the center of the nova in our

Day 51 image (panel (f) of Figure 3.3.5). However, these two components have a combined flux of 1.8 ± 0.13 mJy, which is not enough to explain the increase in flux density in the VLA light curve around this time.

The flux density measured from the nova shell in the day 48 EVN+e-MERLIN image is similar to the day 51 VLBA image, at 12.4 mJy, but EVN+e-MERLIN recovers significant diffuse flux extended over ∼0.1 arcsec which rivals the integrated flux, at 17.2 mJy. We conclude that the origin of the second radio bump is not caused by a brightening at the shock front (as proposed by [95]), but instead by an enhancement of diffuse radio emission upstream of the shock front. We consider possible physical explanations for this emission in §3.6.4.

3.4.5 Brightness Temperature

The brightness temperature was calculated from our VLBA images of the nova shell, assuming a source with a Gaussian shape and the relation from [240]:

$$T_{\rm B} = 1224\,{\rm K}\,\frac{S_\nu}{\rm mJy}\,\left(\frac{\nu}{\rm GHz}\right)^{-2}\,\left(\frac{\theta_{\rm maj}\,\theta_{\rm min}}{\rm arcsec^2}\right)^{-1} \tag{3.2}$$

Here ν is the frequency of the observation, S_ν is the flux density at that frequency, $\theta_{\rm maj}$ is the FWHM major axis of the source and $\theta_{\rm min}$ is the FWHM minor axis. In this case, we estimated the diameter of V3890 Sgr from 3σ contour levels, as listed in Table 3.1.

Figure 3.4 plots the calculated brightness temperature as a function of time following the 2019 eruption. The 4.87 GHz brightness temperature starts at 2.8×10^8 K on day 8 and declines to a value of 2.2×10^6 K by day 51. The 8.37 GHz brightness temperature starts lower at a value of 3.9×10^7 K and declines to 1.2×10^7 K on day 16. At all times the

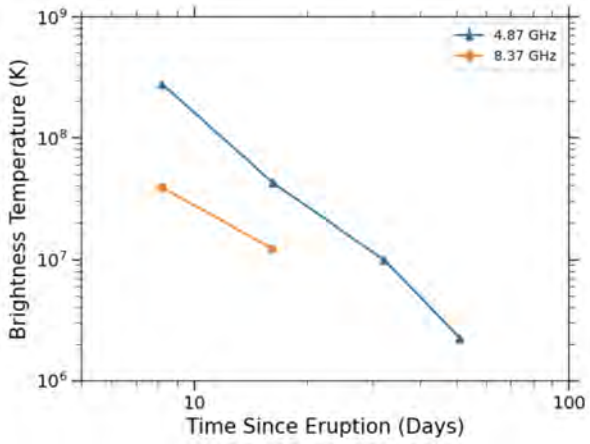

Figure 3.4 Brightness temperature measurements as a function of time following V3890 Sgr's 2019 eruption, measured from our VLBA images in 4.87 GHz (plotted as blue triangles) and 8.37 GHz (plotted as orange circles).

brightness temperature is high, staying well above a thermal expectation of $\lesssim 5 \times 10^4$ K [51]. These $T_{\rm B}$ estimates are consistent with the conclusion in the previous subsection, that the vast majority of the flux is synchrotron emission.

[95] estimated the brightness temperature of V3890 Sgr from VLA observations of the integrated flux, by assuming a spherically symmetric shell expanding at a constant velocity of 4200 km s^{-1} at a distance of 9 kpc. The flux densities used were from the 1.28 GHz VLA observations. Our brightness temperature measurements are similar to [95] on day 8 (2.8×10^8K vs their $\sim 2.5 \times 10^8$ K). However, our brightness temperature decreases much faster (51 days after eruption we have a value 2.2×10^6 K vs their 2×10^7 K). This difference can partially be explained by the negative spectral index and the difference in frequencies used to estimate $T_{\rm B}$. Our initial velocity measurement is also faster than the modelled velocity used in [95] and decelerates faster. Our VLBA estimates of $T_{\rm B}$ are made directly from images, and are therefore more reliable than those estimated from integrated fluxes relying on assumptions about the emitting region size.

We also estimate the brightness temperature of the diffuse flux detected by the EVN+e-

MERLIN on day 48 (panel (h) of Figure 3.3.5). The emission is patchy, and peaks at 0.27 mJy beam^{-1}, which corresponds to a peak brightness temperature of 1.3×10^5 K. Such a high surface brightness makes it unlikely to be thermal emission, as might be expected if circumstellar material is photoionized by the nova; in this case, we would expect $T_{\rm B} \approx 10^4$ K. The relatively high brightness temperature of the diffuse emission and spectral index of the second radio bump (§3.5.2) make it likely that the diffuse emission is synchrotron in origin.

3.4.6 Magnetic Field Strength

The magnetic field strength in V3890 Sgr's synchrotron-emitting nova shell was calculated using the revised equipartition formula from [241]:

$$B_{\rm eq} = \left(\frac{4\pi(1-2\alpha)(K_0+1)I_\nu E_{\rm p}^{1+2\alpha}(\nu/2c_1)^{-\alpha}}{(-2\alpha-1)c_2 l c_4} \right)^{\frac{1}{3-\alpha}} \tag{3.3}$$

Here K_0 is the proton-to-electron number density ratio amongst the relativistic particles, α is the radio spectral index defined as $S_\nu \propto \nu^\alpha$, I_ν is the synchrotron intensity at frequency ν, $E_{\rm p}$ is the proton rest energy (938.26 MeV), and l is the path length through the synchrotron emitting region. $c_1 = 6.264 \times 10^{18}$ erg^{-2}s^{-1}G^{-1} and $c_4 = (2/3)^{(\alpha+1)/2}$, as defined in [241] in Appendix A. c_2 is defined in [241]: for an $\alpha = -0.7$, $c_2 = 1.016 \times 10^{-23}$erg G^{-1} sterad $^{-1}$.

The spectral index of V3890 Sgr is relatively flat compared to other astrophysical synchrotron sources. On Day 16, we estimate $\alpha = -0.25$ from our VLBA images. Even at late times, the spectral index converges to $\alpha \approx -0.4$ [95].

However, Equation 3.3 is only valid for α values steeper than -0.5, so we used $\alpha = -0.7$

Table 3.2 Properties Derived from VLBA Radio Images of V3890 Sgr

Day	Freq (GHz)	l[a] (cm)	$B_{K_0=40}$[b] (G)	$B_{K_0=100}$[b] (G)	v_s (km s^{-1})	$\epsilon_B(K_0=40)$[c]	$\epsilon_B(K_0=100)$[c]
8.1	8.37	8.0×10^{14}	0.13	0.17	5940[d]	2.9×10^{-4}	5.0×10^{-4}
16.0	8.37	1.4×10^{15}	0.08	0.11	3970[e]	6.7×10^{-4}	1.3×10^{-3}
32.0	4.87	2.2×10^{15}	0.05	0.06	3130[f]	1.4×10^{-3}	2.0×10^{-3}
51.0	4.87	3.2×10^{15}	0.03	0.04	3390[g]	1.1×10^{-3}	1.9×10^{-3}

[a] Diameter of the radio emission, assuming a distance of 6.8 kpc.
[b] Magnetic field estimated using $\alpha = -0.7$.
[c] ϵ_B estimated assuming v_s from this Table and n_e from Table 3.3.
[d] Velocity between day 0–8.1, representing the geometric mean of the major and minor axes.
[e] Velocity between day 8.1–16.0.
[f] Velocity between day 16.0–32.0.
[g] Velocity between day 32.0–51.0.

for the magnetic field estimates, as is typical for other synchrotron-emitting astrophysical shocks (e.g., [172, 184]). I_ν was found by dividing the measured flux density by the angular area of the nova, measured from our VLBA images. We set K_0 to be 40 and 100; $K_0 = 100$ comes from measurements of local Galactic cosmic rays and $K_0 = 40$ is expected for strong shocks [241]. The path length l takes a distance of 6.8 kpc and the estimates of the minor axis angular size from Table 3.1.

The resulting magnetic field estimates are listed in Table 3.2. On day 8 the magnetic field is 0.13 G (for $K_0 = 40$) and diminishes to 0.03 G by day 51. For $K_0 = 100$ on day 8 the magnetic field is slightly higher at 0.17 G and declines to 0.04 G by day 51.

These magnetic field strengths in V3890 Sgr are comparable with other novae that have been imaged with the VLBA. In V1535 Sco, [94] estimate magnetic field strengths of 0.13 G for $K_0 = 40$ and 0.17 G for $K_0 = 100$ about 7.7 days after eruption using a path length of $\sim 10^{13}$ cm, comparable to our day 8.1 estimates in V3890 Sgr. In imaging of V1674 Her, M. Williams et al. in prep. estimate the magnetic field on day 20 to be 0.09 G for $K_0 = 40$

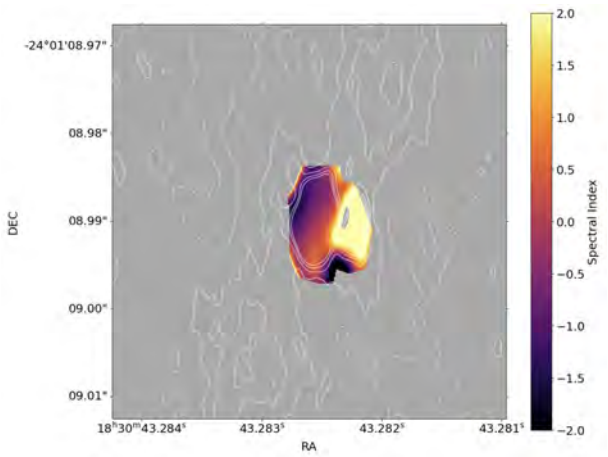

Figure 3.5 Spectral index map of the September 4 observation, 8.1 days after eruption, using 4.87 GHz and 8.37 GHz. The September 4 8.37 GHz image contours are overlaid on the SIM.

and 0.11 G for $K_0 = 100$, very similar to what we find for V3890 Sgr 16 days after eruption. RS Oph was also found to have similar magnetic field values, of 0.09 G for $K_0 = 40$ and 0.11 G for $K_0 = 100$ about 21 days after eruption [55].

We also estimate the magnetic field pressure, given by $P_{\rm B} = \frac{B^2}{8\pi}$. The magnetic field pressures on day 8.1 are 7×10^{-4} dyn cm^{-2} for $K_0 = 40$ and 0.001 dyn cm^{-2} for $K_0 = 100$. On day 16 the magnetic pressure has decreased to 3×10^{-4} dyn cm^{-2} for $K_0 = 40$ and 5×10^{-4} dyn cm^{-2} for $K_0 = 100$. By day 51 the magnetic pressure has further declined to 4×10^{-5} dyn cm^{-2} for $K_0 = 40$ and 6×10^{-5} dyn cm^{-2} for $K_0 = 100$. These magnetic field determinations will be used to estimate the magnetic pressure fraction ($\epsilon_{\rm B}$) in §3.6.2.

3.4.7 Spectral Index Maps

We combine our 4.87 GHz and 8.37 GHz VLBA images to measure the spectral index α across V3890 Sgr on day 8 and 16 of eruption. The spectral index maps (SIMs) use images of the nova made in DIFMAP. Each epoch had identical map and cell sizes. The 4.87 GHz UV data were plotted in RADPL, and the data on the shortest baselines were cut so that the data began at the same minimum UV distance as the corresponding 8.37 GHz data. The

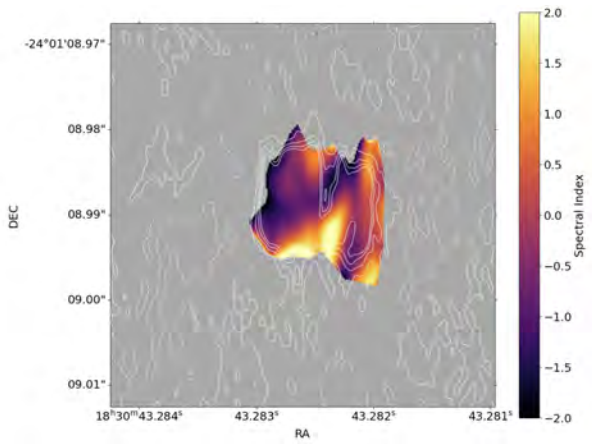

Figure 3.6 Spectral index map of the September 12 observation, 16 days after eruption, using 4.87 GHz and 8.37 GHz. The September 12 8.37 GHz image contours are overlaid on the SIM.

8.37 GHz images were also tapered to have the same beam size as the 4.87 GHz images. This way the UV ranges sampled by the two frequencies are brought into alignment. The fits files were then loaded back into AIPS to make the spectral index maps. Using BLANK the nova was outlined and regions without significant nova emission were blanked out in both frequencies. Then an image cube was made using FQUB which was then transposed using TRANS. The SIM was made using SPIXR.

The SIMs are shown in Figures 3.5 and 3.6. The more yellow regions correspond to a positive spectral index, brighter at higher frequencies. Contours of the 8.37 GHz image flux (identical to those in panels (a) and (c) of Figure 3.3.5) are added to further show how the spectral index is changing over the source.

From the SIM on day 8 (Figure 3.5), we see that the spectral index changes over the source, with the eastern region having a spectral index of around -0.5 to 0.5. The western component is more positive with values of $\alpha \approx 2$. This could be explained by the eastern region being optically thin synchrotron emission and the western region still being optically thick, free-free absorbed by intervening CSM (see Figure 2 of [237] for a nice illustration).

The hole located just to the west of image center is due to a small region with negative flux density in the 4.87 GHz image. At this same location there is significant positive flux from the source in the 8.37 GHz image, ~ 0.0015Jy. When the two images are overlaid, this resulted in a non physical spectral index. The values on the edge of this hole should also be disregarded. Here we have reduced the scale to only allow for a range of $\alpha = -2$ to 2. Due to noise and the differences between the apparent structures in the 4.87 GHz and 8.37 GHz images, the spectral index calculated at the edges of the SIMs should also be disregarded.

In the day 16 SIM the spectral index in the eastern region becomes more negative with values ranging from -1 to 0.5. The western region has become flatter with values ranging from 0.5 to 2. The negative spectral index seen in the eastern region is as expected for synchrotron emission from shocks originating from ejecta hitting up against strong CSM [94]. This is also seen in RS Oph's early radio emission [169].

To attempt to constrain the spectral index of the diffuse emission in the day 48 EVN+e-MERLIN image, we considered the VLA observations published in [95]. High frequency ($\gtrsim$30 GHz) observations obtained in the VLA's A configuration should be able to resolve this diffuse emission. Unfortunately, while the VLA observations obtained on day 45 and 51 were in A configuration, they were limited to <8 GHz, where resolution is poorer. The VLA observation from day 67 did include higher frequency data, but were obtained in A-to-D configuration move time, which made extracting a high-resolution image difficult, with limited baselines probing the small angular scales. We conclude that there is no bright flux at 30 GHz resolvable on $\sim$0.06 arcsec scales, and the VLA data are all consistent with point-like emission. This, along with the fact that the integrated radio spectrum during the second bump maintains a negative spectral index ($\alpha = -0.4$; [95]), leads us to conclude that it is likely that the diffuse emission is brighter at lower frequencies, as expected for synchrotron

emission.

3.5 *Fermi* GeV γ-ray Analysis

3.5.1 LAT Light Curve

V3890 Sgr's >100 MeV γ-ray light curve, as measured by *Fermi*/LAT, is shown in Figure **??** with time bins that are 15 days wide and sampling every 2 days. The displayed light curve spans 2019 June 29 to November 15 with the maximum flux being 2019 Sep 2 (5 days after start of eruption/optical peak). To convert between photon and energy fluxes, we assume a standard spectral model based on V906 Car (currently the highest S/N γ-ray detection of a nova; [242]), which has been found to be reasonable for most novae [138]. For our energy band, this translates to a conversion factor of 1 photon cm^{-2} s^{-1} = 1.2794×10^{-3} erg cm^{-2} s^{-1} (the same one used by [219]). Given the low S/N of the V3890 Sgr detections, the available data are not able to provide better constraints on the γ-ray spectrum of this nova. A maximum flux value of 1.43×10^{-10} erg s^{-1} cm^{-2} with an error of 4.6×10^{-11} erg s^{-1} cm^{-2} were found. A narrower bin, beginning two days before the optical peak to ensure that we capture the start of the γ-ray emission, and ending at the observed maximum in the light curve, with free spectral parameters, yields a somewhat larger flux of 2.4×10^{-10} erg s^{-1} cm^{-2}, with a relatively large uncertainty of 1.5 $\times 10^{-10}$ erg s^{-1} cm^{-2}. We take this to be the maximum γ-ray flux during the eruption to estimate the system's γ-ray luminosity.

At a distance of 6.8 kpc, this *Fermi*/LAT flux corresponds to a peak >100 MeV luminosity of $(1.3 \pm 0.8) \times 10^{36}$ erg s^{-1}, or about 1 % of the white-dwarf Eddington luminosity. This is more luminous than V745 Sco ($< 5.2 \times 10^{35}$ erg s^{-1} at 8.2 kpc; [23, 138]) and V407 Cyg (6.6×10^{35} erg s^{-1} at 3.5 kpc; [8, 37]). V3890 Sgr is significantly less γ-ray luminous than RS Oph at peak (6.7×10^{36} erg s^{-1} at 2.7 kpc; [218, 243]). V3890 Sgr's γ-ray luminosity

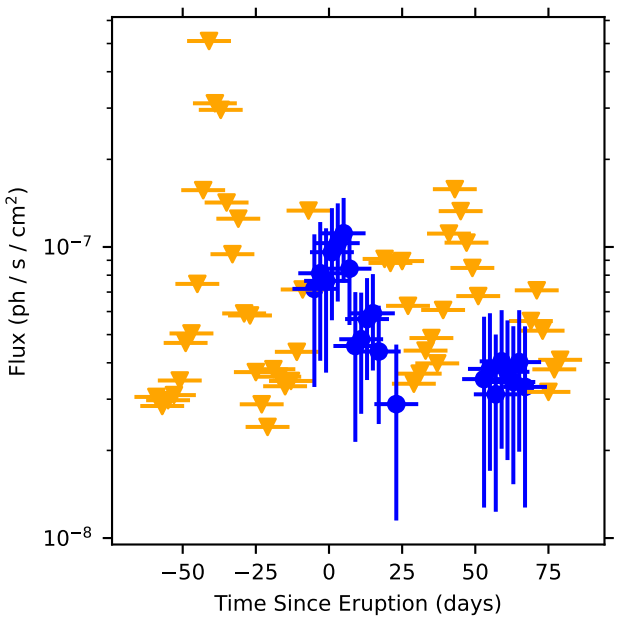

Figure 3.7 γ-ray light curve for V3890 Sgr obtained using *Fermi*/LAT data using a bin width of 15 days. Blue points indicate bins with a test statistic of 4 or greater, corresponding to at least a 2σ detection, while orange triangles show 95 per cent upper limits on the γ-ray flux.

ranks in the top ∼quarter of the classical nova sample of [219], which is focused on novae with main-sequence companions but provides an overview of the state-of-the-art of the population of γ-ray detected novae.

The light curve in Figure 3.7 indicates that V3890 Sgr had a peak in the γ-rays shortly after optical maximum, and emitted significantly until 23 days after optical peak. Interestingly, there is a marginal detection (with a detection defined here as a test statistic of at least 4) around day 60, after a series of non-detections. The timing of this γ-ray reappearance is strikingly similar to the timing of the second radio bump (day ∼40–80; Figure 3.3 and [95]). Possible explanations for this resurgence of γ-rays and radio emission are considered in §3.6.4.

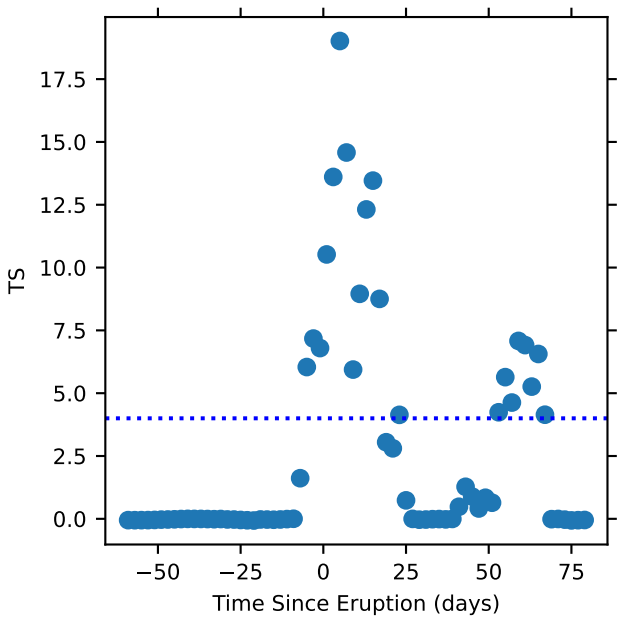

Figure 3.8 *Fermi*/LAT test statistic on V3890 Sgr as a function of time, with windows of 15 days. Time shown is relative to the optical peak. The horizontal dotted line displays the $TS = 4$ significance cutoff adopted for the light curve in Figure 3.7.

3.5.2 LAT Test Statistic

A plot displaying the test statistic throughout our *Fermi*/LAT light curve is shown in Figure 3.8. Each point matches a point in the light curve, so the sampling is again a series of bins with a total width of 15 days, sampled every 2 days. A horizontal line displays the threshold for a significant detection in the light curve, set to the 2-σ level. The highest test statistic recovered in the light curve is 19.0, found on day 5 (also the day with the maximum observed flux), which corresponds to a 4.3σ detection. We note that a larger test statistic can be found with a longer time window, exceeding a 5σ detection. In the secondary peak around day 60, there are a series of several bins with test statistics between 4 and 7, which meet our cutoff for significance in the light curve.

Measuring the duration of the γ-ray emission is tricky in light curves with large, overlapping time windows. Following the methods of [138], we find the test statistic across a

range of start and end times. This includes start times at 1 day intervals ranging from 10 days before the optical peak until 10 days after the peak, and end times at 1 day intervals ranging from 1 to 35 days following optical peak. The exceptions are any start and end time combinations that lead to the start time being the same or after the end time. From this analysis, the maximum TS value is obtained starting 2 days before the optical peak, and continuing until 21 days after the peak, corresponding to a γ-ray duration of 23 days. This solution also corresponds to our maximum TS value of 25.5, a 5σ detection. The assumed spectral model is again a power law with an exponential cutoff (equation 3.1, but here the power law index and energy cutoff are allowed to vary. The resulting grid of TS values is displayed in Figure 3.9.

As the secondary peak around day 60 is only a marginal detection, with the significance peaking at 2.5σ in our light curve, we investigate the rate of false positives at this significance level. The goal is to eliminate the possibility that we are getting false detections due to a poor fit to the background or similar modelling difficulty. In order to make the fairest comparison with our generated light curve, we extend the start time of our light curve to 600 days before the optical peak for this nova. Data more than 60 days before the eruption certainly contain no γ-ray emission from the nova eruption itself, so we repeat our analysis at these times to search for false positives. The distribution of test statistics recovered from this data set is shown in Figure 3.10. The vertical line displays the same cutoff used in our light curve. Out of 266 samples, we find only one that exceeds our significance cutoff. We note that these trials are not independent, as the sampling follows our light curve procedure and therefore nearby points contain some data overlap. However, this low false detection rate leads us to have confidence that the secondary γ-ray peak in V3890 Sgr is real.

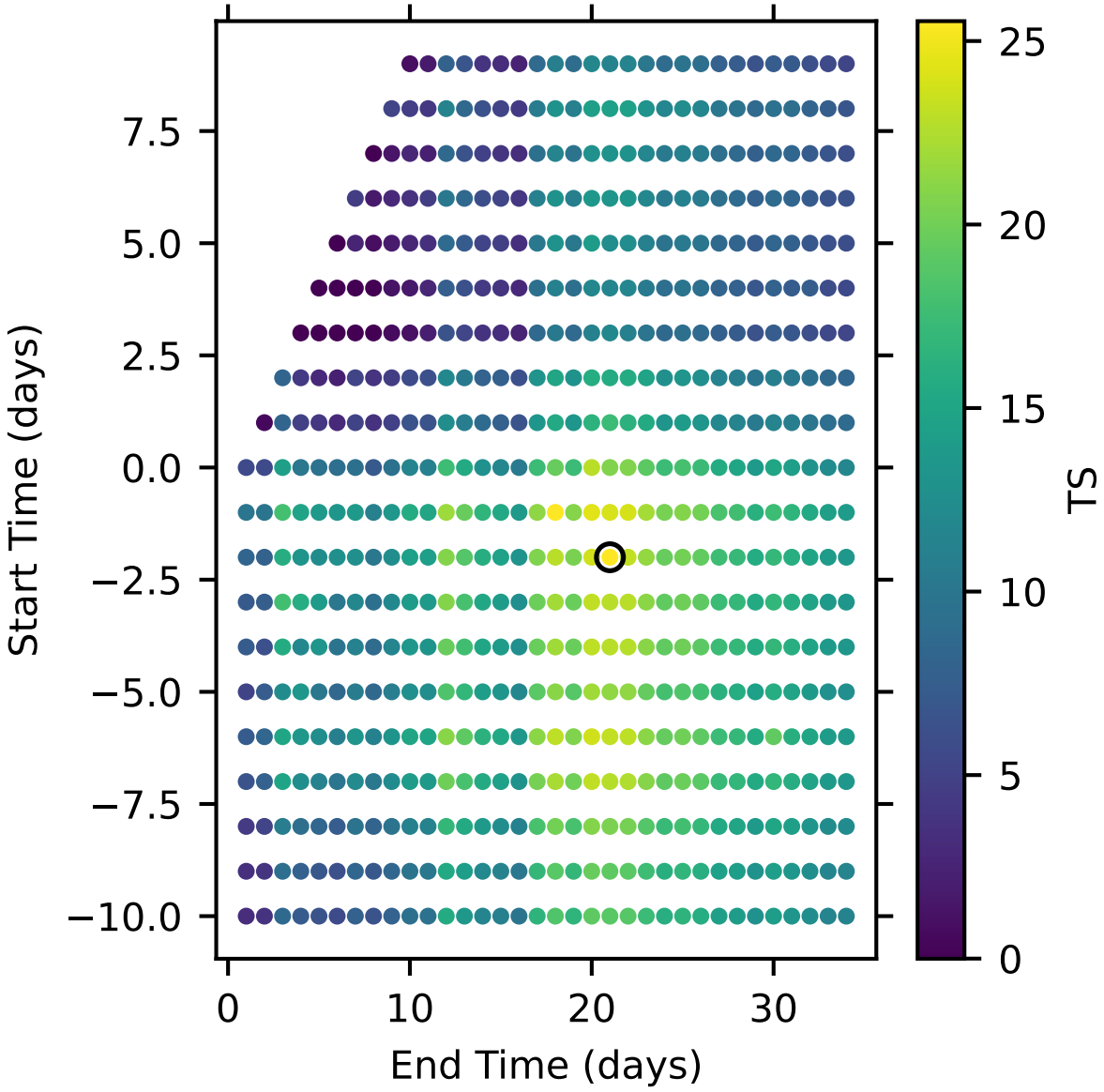

Figure 3.9 Grid of TS values assuming different windows of data selection for V3890 Sgr. The circled point corresponds to the maximum recovered TS value of 25.5, and a duration of 23 days. The upper left corner is blank because in this region the end times would be before the start times, and therefore there are no data.

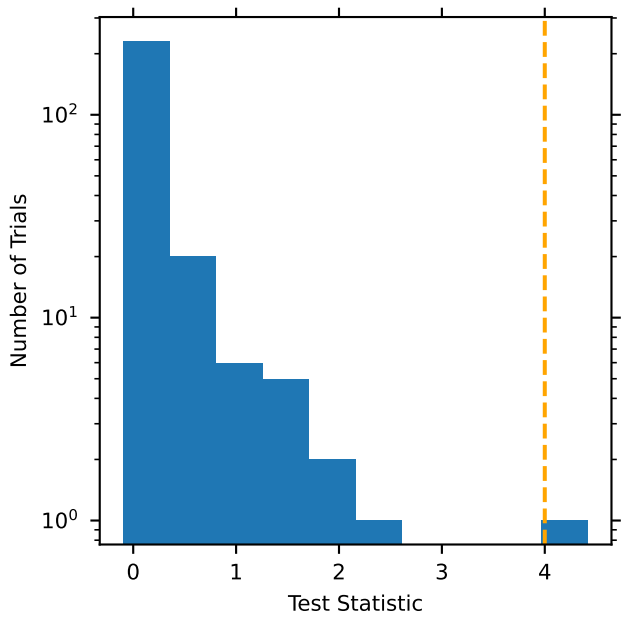

Figure 3.10 Histogram showing the obtained *Fermi*/LAT test statistic values from background sampled regions. The vertical orange line displays the cutoff for a significant detection. Only 0.38 per cent of our background samples would meet this criterion, and none match the significance of the detections during the eruption of V3890 Sgr.

3.6 Modelling the Shock in V3890 Sgr

3.6.1 Density of the Shocked Gas

The density of the gas being shocked, ρ, is a key parameter in determining shock signatures. In V3890 Sgr, ρ is the density of the pre-existing CSM, expelled from the red giant as a wind. Here we assume a spherical wind of constant mass-loss rate $\dot{M}_{\rm w}$ and velocity $v_{\rm w}$,

Table 3.3 Properties Derived from X-ray Spectra of V3890 Sgr

Day	kT_{hot} (keV)	$Norm_{hot}$ (cm^{-5})	kT_{cool} (keV)	$Norm_{cool}$ (cm^{-5})	$n_{\rm H}$(hot) (10^6 cm^{-3})	$\dot{M}_{\rm w}$ ($M_\odot$ yr^{-1})
7.7	$2.8^{+1.1}_{-0.7}$	$0.064^{+0.014}_{-0.010}$	–	–	11.1 ± 1.1	2.2×10^{-7}
15.5	$2.1^{+0.3}_{-0.2}$	$0.041^{+0.003}_{-0.005}$	$0.76^{+0.20}_{-0.15}$	$0.017^{+0.006}_{-0.006}$	4.2 ± 0.2	2.3×10^{-7}
31.9	$1.5^{+5.9}_{-0.3}$	$0.017^{+0.006}_{-0.012}$	$0.62^{+0.37}_{-0.29}$	$0.011^{+0.007}_{-0.005}$	1.3 ± 0.3	1.9×10^{-7}
51.4	< 0.9	$0.008^{+0.001}_{-0.001}$	–	–	0.49 ± 0.03	1.6×10^{-7}

which yields a CSM density profile of:

$$\rho = \frac{\dot{M}_{\rm w}}{4\pi v_{\rm w} r^2} \tag{3.4}$$

While the CSM in V3890 Sgr is likely more complex than a simple spherical wind, our VLBI images show that, at least for the first 32 days, the radio-emitting shock is likely to be interacting with the lower density spherical component (as opposed to the EDE). This shock component, with relatively low absorption (as opposed to the shocks in the orbital plane, which are likely dominating the γ-rays; §**??**), is also most likely to produce the X-rays detectable by *Swift*/XRT.

We therefore estimate ρ from the hard X-ray emission observed by *Swift*/XRT [11]; APEC normalization factors and temperatures from these observations are listed in Table 3.3. While the X-ray plasma temperatures listed in Table 3.3 are rather low, similarly modest X-ray temperatures have been measured in other symbiotic recurrent novae at $\tilde{1}$ week after optical peak (e.g., RS Oph and V745 Sco; [73, 244]). It is possible that the hot X-ray plasma is mixing with cooler gas from behind the shock reducing the temperature.

The APEC normalization factor constrains the number density of electrons and ions as:

$$\text{Norm} = \frac{10^{-14}}{4\pi D^2} \int n_{\rm e} n_{\rm H} dV \tag{3.5}$$

We solve for n_H assuming that $n_{\rm e} = n_{\rm H}$, $D = 6.8$ kpc, and V is the volume of the hot shocked region. We assume the hot APEC component is filling the volume between the forward shock and the contact discontinuity, take the radius of the forward shock from our VLBA images, and estimate the radius of the contact discontinuity ($R_{\rm CD}$) from the formalism described in [72] and [95]: $R_{\rm CD} \approx 0.35\, R_{\rm FS}$ over the time-scale of our VLBA

observations. The resulting densities of the hot shocked gas are listed in Table 3.3.

These $n_{\rm H}$ estimates can be used to estimate ρ, the density of the gas being shocked, assuming a compression ratio of 4 as expected for a strong shock. We estimate the mass-loss rate of the wind $\dot{M}_{\rm w}$ from Equation 3.4, assuming $v_{\rm w} = 10$ km s^{-1} as expected for a red giant, and the radii from our VLBA images, assuming $D = 6.8$ kpc. These $\dot{M}_{\rm w}$ estimates are also given in Table 3.3.

We find that $\dot{M}_{\rm w} = 2 \times 10^{-7}$ M$_\odot$ yr^{-1} in V3890 Sgr, consistently across our four imaging epochs as expected if the CSM truly is distributed as a wind. To sanity check this estimate of $\dot{M}_{\rm w}$, we searched for radio observations of V3890 Sgr in quiescence, when free-free thermal emission is expected to dominate, driven by the CSM ionized by the accreting white dwarf [62]. While there are no targeted observations in the VLA archive, we obtained limits on the radio flux from the VLA Sky Survey (VLASS; [245]). VLASS Epoch 1.1 observed V3890 Sgr on 2018 Feb 17, and reveals a low-significance peak (2.9σ) near the position of V3890 Sgr. We are not confident that this is a detection, and therefore take a 3σ upper limit of $<$0.59 mJy at 3.0 GHz. Using Equation 2 of [62] and assuming $\alpha = 0.6$ in quiescence [66], we estimate an upper limit on $\dot{M}_{\rm w}$ of $< 5 \times 10^{-7}$ M$_\odot$ yr^{-1}, consistent with our X-ray estimates.

$\dot{M}_{\rm w} = 2 \times 10^{-7}$ M$_\odot$ yr^{-1} is typical for a symbiotic star, whose $\dot{M}_{\rm w}$ span $10^{-8} - 10^{-5}$ M$_\odot$ yr^{-1} [62, 68]. However, it is significantly higher than other symbiotic recurrent novae, like V745 Sco ($\dot{M}_{\rm w} = 2 \times 10^{-8}$ M$_\odot$ yr^{-1}; [16, 23]), and T CrB ($\dot{M}_{\rm w} = 2 \times 10^{-9}$ M$_\odot$ yr^{-1}; [227]). The symbiotic recurrent nova RS Oph also has a lower $\dot{M}_{\rm w} \approx 6 \times 10^{-8}$ M$_\odot$ yr^{-1} in the spherical CSM component [227], but $\dot{M}_{\rm EDE} \approx 2 \times 10^{-7}$ M$_\odot$ yr^{-1} in the EDE (for comparable $v_{\rm w} = 10$ km s^{-1}; [238]), implying CSM that is more strongly confined to the orbital plane than in V3890 Sgr.

Our estimate of $\dot{M}_{\rm w}$ is also significantly higher than the mass-loss rate estimated from

modelling V3890 Sgr's radio light curve in [95]: $\dot{M}_{\rm w} \approx 10^{-8}$ M$_\odot$ yr^{-1} (but we note their estimate depends crucially on the poorly known efficiencies of amplifying magnetic fields and accelerating relativistic electrons, and that it is possible to get good fits to the radio light curve with $\dot{M}_{\rm w} = 2 \times 10^{-7}$ M$_\odot$ yr^{-1}). The relatively dense environment of V3890 Sgr, and that this CSM appears relatively spherically distributed (as opposed to confined in an EDE) likely explains why its radio flux is so bright and radio images reach good S/N, even at a relatively large distance of 6.8 kpc. Its 5 GHz spectral radio luminosity at $d = 6.8$ kpc is 2.9×10^{21} erg s^{-1} Hz^{-1}, a factor of $\sim 4-5$ greater than RS Oph ([169], Molina et al. 2026, in preparation) and V745 Sco [23].

3.6.2 Efficiency of Magnetic Field Amplification and Lepton Acceleration

We can use the magnetic field estimates from §3.5.1 to constrain the efficiency with which the shock accelerates leptons (ϵ_e) and the fraction of the post-shock pressure in magnetic fields ($\epsilon_{\rm B}$). We remind the reader that B was estimated assuming equipartition with relativistic electrons, such that implicitly $\epsilon_{\rm B} = \epsilon_{\rm e}$, where $\epsilon_{\rm e}$ is the fraction of the post-shock pressure in relativistic electrons, $\epsilon_{\rm B}$ is defined such that $\frac{B^2}{8\pi} = \epsilon_{\rm B}\, \rho\, v_{\rm s}^2$, and ρ is the density of gas being shocked. These ϵ factors are commonly used in modelling radio emission from diverse astrophysical transients (e.g. [93, 246–248]). Table **??** lists B and $v_{\rm s}$ estimates from our VLBI images, and we estimate ρ from the spherical CSM component $\dot{M}_{\rm w}$ estimated in the previous sub-section. The resulting values of $\epsilon_{\rm B}$ are listed in Table 3.2.

Our estimates of $\epsilon_{\rm B}$ and $\epsilon_{\rm e}$ range from 3×10^{-4} to 2×10^{-3}, depending on the epoch and the assumed value of K_0. These equipartition parameters are smaller than what is often

taken or inferred in studies of supernovae and γ-ray bursts [24, 192, 246], which might be the result of the relatively low shock speeds in novae. For example, if the magnetic field is amplified via the non-resonant streaming instability [80], then $\epsilon_{\rm B}$ scales as $v_{\rm s}\epsilon_{\rm p}$, where $\epsilon_{\rm p}$ is the proton acceleration efficiency [see, e.g. 19, for a detailed implementation]. Moreover, estimates of $\epsilon_{\rm e}$ in supernova remnants, which have shock velocities similar to those seen in novae, find similarly low efficiencies [195, 249]. However, surprisingly, the efficiencies seem to increase between day 8 and 32 in V3890 Sgr, counter to expectations for a decelerating shock. This apparent increase might be attributed to shock expansion increasing the fraction of the emitting volume that is optically thin to radio (see Sections 3.6.3 and 3.6.4 for a more detailed discussion).

3.6.3 Lessons from Simultaneous Modelling of Radio and γ-ray Emission

V3890 Sgr achieved a peak γ-ray luminosity of $L_\gamma \approx 1.3 \times 10^{36}$ erg s^{-1} around the time of optical peak, assuming a distance of 6.8 kpc. The maximum possible L_γ is the calorimetric limit, in which accelerated protons lose all of their energy in proton-proton collisions such that $L_\gamma = \kappa L_{\rm p}$, where $\kappa \approx 0.1$ is the fraction of the proton energy that goes into $\gamma-$rays, and $L_{\rm p}$ is the cosmic ray (proton) luminosity (e.g. [21]). Taking $L_{\rm p} = \epsilon_{\rm p} L_{\rm s} \approx \epsilon_{\rm p} M_{\rm ej} v_{\rm s}^2 / t_{\rm age}$, where L_s is the shock luminosity, $M_{\rm ej}$ is the nova ejecta mass, and $t_{\rm age}$ is the nova age, we approximate:

$$L_\gamma \approx 2.3 \times 10^{35} \text{ erg s}^{-1} \times \left(\frac{\epsilon_{\rm p}}{10^{-2}}\right)\left(\frac{M_{\rm ej}}{10^{-6} M_\odot}\right)\left(\frac{v_{\rm s}}{1000 \text{ km s}^{-1}}\right)^2\left(\frac{t_{\rm age}}{\rm day}\right)^{-1}. \quad (3.6)$$

Thus, for $M_{\rm ej} \approx 10^{-6} M_\odot$ [95] and $v_{\rm s} \approx 5000$ km s^{-1}, we obtain the observed $L_\gamma \approx 1.3 \times 10^{36}$ erg s^{-1} at $t_{\rm age} = 4$ days.

Of course, even higher values of L_γ may be achievable at earlier times (the peak date of the γ-rays is uncertain) or with less conservative assumptions about the ejecta mass and acceleration efficiency. However, the fact remains that, to produce sufficient γ-ray flux, the density of the shocked gas must be very large, such that the pion production time-scale, $\tau_{\rm pp}$, is comparable to (or less than) $t_{\rm age}$. Taking $\tau_{\rm pp} \approx 260$ days $\times$ (10^8 cm$^{-3}/n_{\rm H}$) [19], we obtain a density, $n_{\rm H} \gtrsim 6.5 \times 10^9$ cm^{-3}, at $t_{\rm age} = 5$ days. Not only is this density much larger than that inferred in Section 3.6.1, it is almost certainly opaque to radio due to the large free-free optical depth. Note that a comparable density must be maintained until at least $t_{\rm age} \gtrsim 20$ days—well after the radio detection—since the γ-ray emission remains bright until that time.

In short, consistent with previous analysis in the context of classical novae (e.g. [75]), the γ-ray emission cannot arise from the same region as the radio. The most natural explanation is CSM characterized by an EDE. In this picture, a spherical outflow interacts with an aspherical environment: the interaction between the outflow and the dense equatorial medium produces a large γ-ray luminosity (but free-free absorption occludes any radio emission), while the interaction between the outflow and the lower-density red giant wind in the polar regions is responsible for the radio observations. This picture is consistent with the bipolar structure observed with VLBA at intermediate times (16 days $\lesssim t_{\rm age} \lesssim$ 32 days).

This picture is also supported by a comparison of radio and γ-ray luminosities of novae with evolved companions. While the peak 5 GHz radio luminosity scales with the density of the spherical wind component (§3.6.1), the γ-ray luminosity does not. V407 Cyg had denser spherical CSM than V3890 Sgr ($\dot{M}_{\rm w} = 10^{-6}$ M$_\odot$ yr^{-1}; [250]) but less luminous γ-

rays (§3.5.1), while RS Oph is characterized by lower $\dot{M}_{\rm w}$ and yet has more luminous γ-rays. We therefore predict that, of these three novae, RS Oph had the densest EDE and V407 Cyg had the least dense. This is consistent with expectations for mass transfer by wind Roche lobe overflow, where a larger fraction of the CSM is expected to be confined in the EDE for symbiotic binaries with smaller separations [164].

3.6.4 Origin of the Late-Time Diffuse Radio Emission

The late-time radio excess observed in V3890 Sgr around $t \simeq 45$–60 days cannot be explained by direct emission from the forward shock traced by our VLBI images. At these epochs, the angular extent of the diffuse radio emission detected by the EVN+e-MERLIN ($\sim 0.1''$, corresponding to physical scales $\sim 10^{16}$ cm at $d = 6.8$ kpc) is far larger than can be reached by ballistic nova ejecta expanding at the observed velocities ($\lesssim 5000$ km s^{-1}; §3.4.2). This disfavors an origin in freshly shocked ejecta or a simple density enhancement encountered by the forward shock.

Instead, we propose that the late-time radio emission arises from a *synchrotron halo*: non-thermal particles escaping from the γ-ray–producing shock and diffusing upstream, to interact with pre-existing CSM at a relatively large radius. In this picture, we focus on the shock in the equatorial region which, due to the large inferred post-shock density, is likely radiative; §3.6.3. Relativistic electrons and positrons—produced in proton-proton interactions within the dense, radiative, and relatively unmagnetized shell—leak out of the acceleration region, propagate into the unshocked CSM, and radiate synchrotron emission over much larger spatial scales. In Appendix B, we present a simple analytic model for this synchrotron halo, demonstrating that the observed radio luminosity, spectral properties, and spatial extent can be reproduced with physically reasonable parameters.

In this framework, the forward shock continues to accelerate hadrons and leptons at late times, particularly as indicated by the γ-ray re-brightening, but a fraction of the non-thermal particle population escapes upstream. Such escape is expected once the shock weakens and the surrounding medium becomes less confining, particularly for high-energy protons and secondary leptons. Moreover, if the observed γ-rays are produced predominantly through hadronic interactions, then charged pion decay naturally injects relativistic electron-positron pairs with Lorentz factors $\gamma \sim 10^2$–10^4, comparable to those required to produce GHz synchrotron emission in magnetic fields of order 10^{-4}–10^{-2} G.

As these particles stream or diffuse into the unshocked red giant wind, they encounter pre-existing magnetic fields carried by the wind itself. For plausible red giant surface fields of order $\sim$G and flux-freezing in the outflow, the magnetic field strength at radii $\sim 10^{15}$–10^{16} cm is expected to be $B \sim 10^{-3}$–10^{-2} G, comparable to or slightly below the magnetic fields we infer in the shocked region at earlier times (§3.5.1). Additional amplification may occur if escaping non-thermal ions drive plasma instabilities in the upstream medium (e.g. [80]) or if the latter gas was shocked and compressed by a previous recurrent nova eruption (§B.1.3).

Because the synchrotron cooling time of relativistic leptons in such fields is much longer than both the wind expansion time and the particle transport time, the emitting particles are firmly in the slow-cooling regime (§B.1.4). As a result, the radio luminosity reflects the cumulative injection and transport of non-thermal particles rather than local radiative losses. This naturally produces a low-surface-brightness, extended radio halo whose characteristic size is set by particle propagation rather than by ejecta dynamics.

A natural question raised by this scenario is why the diffuse radio halo (and corresponding bump in the radio light curve) appears contemporaneously with the second γ-ray peak, rather

than being dominated by particles accelerated during the earlier, more luminous γ-ray phase near optical maximum. Those early shocks undoubtedly produced large numbers of non-thermal particles, which in principle could also escape upstream and propagate to large radii.

If pairs were only produced during the first γ-ray peak, when the shock was still compact, then the delayed rise-time of the radio halo could in principle be attributed to the finite time required for the pairs to diffuse upstream into the red giant wind. However, it would then be a coincidence that the radio rebrightening occurred roughly contemporaneous with the second γ-ray peak. If the latter indicates ongoing shock interaction continuing to larger radii, the pairs released from this later shock phase may dominate the observed emission. In particular, particles injected at early times escape at relatively small radii, $r_0 \ll 10^{15}$ cm, and subsequently suffer substantial adiabatic energy losses as they propagate outward through the red giant wind. By the time such particles reach radii $\sim 10^{16}$ cm, their Lorentz factors have been reduced by factors of $\sim r_0/r$, shifting their synchrotron emission to frequencies well below the GHz band and rendering their contribution to the observed radio halo negligible.

The second γ-ray peak could mark the interaction of the nova ejecta with a denser circumstellar structure at $r \sim 10^{15}$ cm, such as a secondary density enhancement in the red giant wind or EDE inferred from the radio light curve. Shocks formed at these larger radii inject non-thermal particles with a much larger effective escape radius r_0. Because the subsequent adiabatic degradation from $r_0 \sim 10^{15}$ cm to $r \sim 10^{16}$ cm is modest, these particles retain sufficiently high Lorentz factors to radiate efficiently at GHz frequencies. As a result, the late-time shocks dominate the observable synchrotron halo, even if the total non-thermal energy injected at earlier times was larger.

3.7 Conclusion

We present VLBI radio imaging and *Fermi*/LAT GeV γ-ray monitoring of the 2019 eruption of the symbiotic recurrent nova V3890 Sgr. VLBI imaging spans 8–51 days following eruption, concurrent with the detected γ-rays. We conclude:

- The VLBI images start out asymmetric on day 8, with the eastern component brighter than the western component. However, the western component brightens with time, and by day 32, the radio emitting shell is quite circularly symmetric. We explain this evolution as bipolar expansion, with a density enhancement in the orbital plane oriented north–south and the western component absorbed by the EDE at early times (as in RS Oph; [237, 238]). In the EVN+e-MERLIN image from day 48, the shell appears brighter in the north–south direction, implying that at late times the shocks interacting with the denser EDE become visible at radio frequencies.

- We measure the expansion of the radio-emitting shell and compare it with radial velocities from optical spectroscopy. We thereby estimate an expansion parallax distance to V3890 Sgr of 6.8 kpc (§3.4.3). The radio images suggest significant deceleration of the shock between the first imaging epoch on day 8 and later epochs, from ∼6000 km s^{-1} to 3100 km s^{-1}.

- By comparing the flux recovered from our VLBI imaging with integrated flux from the VLA [95], we conclude that the VLBA is detecting most (>80 %) of the radio flux on days 8–32, confirming that the radio emission is characterized by high brightness temperatures only achievable with non-thermal emission ($> 10^7$ K).

- On day 51, the VLBA resolves out ∼ a third of the integrated flux, but the EVN+e-

MERLIN recovers this missing flux and finds it is distributed in a diffuse halo $\gtrsim 10^{16}$ cm across with peak $T_{\rm B} \approx 10^5$ K. The appearance of this radio halo is coincident with a second peak in the VLA radio light curve (Figure 3.3) and in the γ-ray light curve (Figure 3.7). The radio spectrum of this second peak and the brightness temperature of the diffuse flux significantly in excess of 10^4 K lead us to conclude that this halo is powered by synchrotron emission.

- We find the >100 MeV γ-rays peak at a flux of $(1.9 \pm 1.2) \times 10^{-7}$ phot s^{-1} cm^{-2} ($L_\gamma = 1.3 \times 10^{36}$ erg s^{-1} at 6.8 kpc) around the time of optical maximum. The γ-rays remain detectable for 23 days, and then reappear at 2.5σ significance around day 60, contemporaneous with the second peak in the radio light curve (§3.5.1).

- By modelling the simultaneous γ-ray and radio emission from V3890 Sgr, we conclude that radio emission and γ-rays must be originating from different portions of the shock: the high γ-ray luminosity requires a very dense medium for efficient pion production, while such a dense medium would free-free absorb radio emission. It is likely that the radio-emitting shock marks the ejecta's interaction with a spherical wind-like component of the CSM, while the γ-rays originate from interaction with an over-density of CSM in the orbital plane (§**??**).

- We estimate the density of the CSM from X-ray observations of the hot shocked gas [11], finding that the CSM can be parametrized as a spherical wind with $\dot{M}_{\rm w} = 2 \times 10^{-7}$ M$_\odot$ yr^{-1} (assuming $v_{\rm w} = 10$ km s^{-1}), plus denser material in the orbital plane. This is significantly denser than the CSM estimated in other symbiotic recurrent novae (§**??**).

- By combining our velocity, magnetic field, and CSM density measurements, we can estimate the fraction of the post-shock pressure in magnetic fields, and find $\epsilon_{\rm B} \approx$ few

$\times 10^{-4}$ to few $\times 10^{-3}$ (§??). We assume equipartition with relativistic electrons, so similar values of ϵ_e are implied.

- The $\sim 10^{16}$ cm synchrotron halo and late-time radio bump can be explained by relativistic leptons that escape the shocked shell (most of secondary origin) and interact with CSM upstream of the shock (§3.6.4).

Acknowledgements

Support for this work was provided by the NSF through the Grote Reber Fellowship Program administered by Associated Universities, Inc./National Radio Astronomy Observatory. Nova science at Michigan State is supported by NSF grant AST-2107070 and NASA grants 80NSSC23K0497, 80NSSC25K7334, and 80NSSC23K1247. RD and BDM were supported in part by NASA (grant number 80NSSC22K0807, 80NSSC24K0408), the Simons Foundation (grant PG013158), and Columbia University through the Research Stabilization Fund. The Flatiron Institute is supported by the Simons Foundation. KLP acknowledges support from the UK Space Agency. JLS acknowledges support from NASA grants 80NSSC25K0622 and 80NSSC25K7082.

The National Radio Astronomy Observatory and Green Bank Observatory are facilities of the U.S. National Science Foundation operated under cooperative agreement by Associated Universities, Inc. This work made use of the Swinburne University of Technology software correlator [251], developed as part of the Australian Major National Research Facilities Programme and operated under license. The European VLBI Network is a joint facility of independent European, African, Asian, and North American radio astronomy institutes. Scientific results from data presented in this publication are derived from the following EVN project code(s): RY008. e-MERLIN is a National Facility operated by the University of

Manchester at Jodrell Bank Observatory on behalf of STFC. The research leading to these results has received funding from the European Commission Horizon 2020 Research and Innovation Programme under grant agreement No. 730562 (RadioNet). e-VLBI research infrastructure in Europe is supported by the European Union's Seventh Framework Programme (FP7/2007-2013) under grant agreement number RI-261525 NEXPReS.

Data Availability

The radio images presented in this paper are available for download in fits format from Zenodo.

Chapter 4. Novae with Evolved Companions

In the previous chapters we investigated two recurrent symbiotic novae, V745 Sco and V3890 Sgr. Here we continue our investigation of novae with evolved companions, broadening our study to include 11 novae. We present radio observations (1 – 40 GHz) for 11 classical novae. These novae present a range of orbital periods as their companions include subgiants to Mira giants. Our brightness temperature measurements indicate that a large portion of these novae are dominated by synchrotron emission, though some show a mix of thermal and non-thermal radio emission. A high brightness temperature ($T_B > 5 \times 10^4$K) is found in 9 of the 11 novae. Radio and optical light curves are plotted along with spectral index evolution when possible, illustrating a combination of thermal and non-thermal emission in several novae. While there is a loose correlation between time to peak in the radio and optical decline time t_2, there is no such correlation between peak radio flux density and optical peak magnitude. Radio properties are also compared with γ-ray, and binary properties with radio luminosity showing a slight positive trend with orbital period. The novae with giant companions have high radio luminosity and γ-ray luminosity where the subgiant novae show a wider range of γ-ray and radio luminosity. By comparing consecutive eruptions of RS Oph, we distinguish a frequency dependent difference in radio decline, with the 2021 eruption having a more shallow decline from radio peak. RS Oph's double peak feature is also investigated as well as the evolution of its thermal and non thermal emission.

4.1 Introduction

Novae are thermonuclear eruptions that occur on the surfaces of white dwarfs in the accreted material from the binary companion [37, 98, 99]. The companion, which can range from a main sequence to a giant star, is stripped of hydrogen rich material which accumulates on

the surface of the white dwarf. This material builds up, compressing the bottom layer and increasing in temperature. Nuclear reactions increase, leading to a thermonuclear runaway which blows off the accreted material at velocities ranging from $500 - 5000$ km s^{-1} (see Refs.[101–103]). This eruption is seen as a sudden burst in luminosity [100]. The binary system survives this eruption and accretion can continue, leading to subsequent eruptions. Systems where we have observed more than one eruption are called recurrent novae. The majority of novae have recurrence times on timescales longer than the human lifespan and have only had one observed eruption. However, 10 recurrent novae have been observed in the Milky Way [3], with four of them being symbiotic binaries [61]. The prevalence of giant companions among recurrent novae is often explained by accretion fed by red giant winds reaching higher rates than accretion fed by a dwarf companion filling its Roche Lobe [105, 106].

Here we compile radio observations of 11 Galactic novae with evolved companions. The data were obtained with the Karl G. Jansky Very Large Array (VLA) as well as other telescopes like the Multi Element Remotely Linked Interferometer Network (MERLIN) and the Giant Metrewave Radio Telescope (GMRT). The observations span 40 years with eruptions ranging from 1982 – 2022. Our sample of novae have companions ranging from subgiants to a Mira giant. We split this set into two groups based on [50] with SG-novae being novae with subgiant companions and RG-novae being novae with giant companions. SG-novae having orbital periods on the order of days and RG-novae having orbital periods on the order of years.

The mass transfer rates and mechanisms for these two categories may differ, with wind fed accretion occurring more frequently in binaries with larger orbital periods. Roche Lobe overflow may be more common in novae with orbital periods < 3 years [63]. Wind fed Roche

Lobe overflow is tied to higher accretion rates and may be more common in recurrent novae with short recurrence times [2, 65].

Winds from the giant companion in RG-novae can be formed into structures called “circumstellar medium" or CSM. Interactions with this CSM can lead to observable radio emission. In SG-novae, the CSM is likely lower density than the CSM from RG-novae but very little is known about the environments of SG-novae.

In section 2 we describe the data used, where it came from, and how it was processed. In section 3 we discuss the radio properties of the novae, focusing on the radio light curve, brightness temperature, and spectral index evolution. In section 4 we analyze the multi-frequency properties of the novae looking at the radio, optical and gamma ray features. In section 5 we explain our conclusions and future directions of investigation.

4.2 Data

We compiled radio and optical data for RS Oph, V745 Sco, V723 Cas, U Sco V5589 Sgr, V1545 Sco, V1535 Sco, V392 Per, V3890 Sgr, and V1370 Aql. Table 4.1 lists the novae names, eruption dates, and other features. RS Oph, V745 Sco, and U Sco are recurrent novae with radio data of multiple eruptions. Table 4.2 lists the radio telescopes used to observe the novae, the date range of observations, peak flux density at 5 GHz, and the time to reach peak flux density. Radio observations for some novae did not occur close enough to the time of eruption to capture the rise to peak radio flux density. For these novae their time to max flux density and radio peak flux density is treated as a lower limit.

Table 4.1 Properties of Radio-Observed Novae with Evolved Companions

Name	Discovered (UT)	$V_{\rm peak}$ (mag)	t_2 (days)	$E(B-V)$ (mag)	v_1 (km s^{-1})	v_2 (km s^{-1})	Spectral Type	Distance[a] (kpc	$P_{\rm orb}$[b] (days)
V407 Cyg	2010 Mar 10[n]	7.1[v]	5.9[v]	0.6 ± 0.1[t]		3200 ± 345 [as]	Mira [ad]	$4.5^{+2.5}_{-1.8}$	15695[ad]
V3890 Sgr (2019)	2019 Aug 27[s]	7.2	6.4[t]	0.9 ± 0.3[t]		5300	M5 III [aa]	$6.0^{+1.3}_{-1.1}$ [b]	747.6[ap]
V1534 Sco	2014 Mar 26[p]	11.6[x]	5.6[x]	1.1[x]		4100 ± 100[x]	M6II [ac]	$8.6^{+1.7}_{-1.1}$	520 ± 120[ag]
RS Oph (1985)	1985 Jan 26[g]	4.8[t]	2.8[z]	0.7 ± 0.1[t]	2700[ad]	3700[e]	M0 − 2 III [f]	$2.7^{0.2}_{-0.1}$ [b]	453.6 ± 0.4[c]
RS Oph (2006)	2006 Feb 12[h]	"	"	"	"	"	"		
RS Oph (2021)	2021 Aug 8[i]	"	"	"	"	"	"	"	"
V745 Sco (1989)	1989 Jul 24[j]	9.4[t]	6.2[aj]	1.0 ± 0.2[t]		4450	M4 III [aa]	$8.2^{+1.4}_{-1.3}$ [b]	> 365 [ab]
V745 Sco (2014)	2014 Feb 6[k]	"	"	"		"	"	"	"
V1535 Sco	2015 Feb 11[q]	9.7[x]	13.9	1.0[x]	2300	4700	K−M[at]	$4.6^{+0.9}_{-0.6}$	39.6[au]
V392 Per	2018 Apr 29[r]	5.6[y]	3[y]	0.4 ± 0.1[y]	2800 [c]	4100 [c]	G9 III−IV [am]	$3.2^{+0.6}_{-0.4}$	3.4[am]
V1370 Aql	1982 Jan 27[an]	7.7 [u]	15[u]			2200 [ao]		$2.2^{+1.0}_{-0.5}$	2.0 [b]
V5589 Sgr	2012 Apr 21[o]	9.1[t]	4.5[t]	0.8 ± 0.2[t]		4800[al]		$7.5^{+0.9}_{-1.1}$	1.6[ak]
U Sco (1999)	1999 Feb 24[m]	7.5[u]	1[u]	0.1 ± 0.1[t]		5000[aj]	F8−K2 [af,ae]	7.5 ± 2.0	1.2[ah]
U Sco (2022)	2022 Jun 6[ar]	"	"	"		"	"	"	"
V723 Cas	1995 Aug 24[l]	7.1[u]	263[u]	0.5[t]		1750[ai]		$4.7^{+1.0}_{-0.7}$	0.7[ah]

[a]Distances are determined from *Gaia* EDR3 parallaxes, unless otherwise noted.

References: [b]this work [c][51]; [d][252]; [e][19]; [f] [253]; [g][254]; [h][255]; [i][256]; [j][126]; [k][127]; [l][257]; [m][258]; [n][259]; [o][260]; [p][261]; [q][262]; [r][263]; [s][264]; [t][3]; [u][265]; [v][158]; [w][45]; [x][266]; [y][221]; [z][267]; [aa][129]; [ab][268], [ac][269], [ad][270], [ae][271], [af][272] [ag][273] [ah][274];[ai][275];[aj][202]; [ak][87]; [al][175]; [am][276]; [an][277], [ao][278], [ap][211] [aq][279], [ar][280], [as][8], [at][281]; [au] Strader et al. in prep.

4.2.1 Optical Data

The optical data are publicly available data from the American Association of Variable Star Observers (AAVSO) or [265]. V band data were used for the optical light curves and the measured peak magnitude. V_{peak} and t_2 are mainly taken from the literature and references are given in Table 4.2, t_2 is the time it takes for the optical light curve to declines by two magnitudes from optical peak. Some novae exhibit multiple peaks and declines in the optical light curve. In these cases t_2 is taken as the last time the optical light curve declines by 2 magnitudes [265]. v_1 is the expansion velocity measured from the P Cygni absorption line a few days after optical peak. v_2 is the expansion velocity obtained through HWHM measurements of the H-α line observed after radio peak. Values for v_1 and v_2 are either found in literature or found using published spectra. Distance and extinction measurements are described in section 4.2.4.

Table 4.2 Overview of Radio Observations of Novae

Name	Telescope	Date Range	$t_{\max}$[e] (days)	$S_{\max}$[e] (mJy)	Reference
V407 Cyg	Jansky VLA	2010 Mar 27–2012 Apr 18	102.60	17.77	[250]
V3890 Sgr	MeerKAT/Jansky VLA	2019 Aug 30 - 2020 Feb 13	11.05	51.11	[95]
V1534 Sco	Jansky VLA	2014 Mar 31 - 2015 Dec 4	14.65	13.30 $\geq$	This work
RS Oph (2021)	GMRT/Merlin/VLA	2021 Aug 13 - 2023 Jul 6	10	67.6	This work
V745 Sco (2014)	GMRT/Jansky VLA	2014 Feb 8 - 2015 Feb 1	25.6	8.9	[137] & Tl
V1535 Sco	Jansky VLA	2015 Feb 14–2015 Jun 14	2.66	4.12	[94]
V392 Per	Jansky VLA	2018 Apr 30–2020 May 15	32.0	5.23	[51] & Thi
V1370 Aql	WSRT / VLA	1984 May 12 1987 Jan 24	73.5	20.20	[282]
V5589 Sgr	Jansky VLA	2012 Apr 23–2013 Aug 26	62.3	3.42	[175]
U Sco (2022)	VLA	2022 Jun 25–2022 Aug 24	32.53 $\geq$	$\geq$ 0.115	This work
V723 Cas	Merlin	1996 Dec 13–2001 Oct 26	1697.5	13.5	[283]

[e]Measured at C band (4–6 GHz).

Table 4.3 Overview of γ-ray Observations. [a] are 95 % upper limits

Nova	F_γ(max) 10^{-7} erg s^{-1} cm^{-2}	TS_{max}	Reference
V407 Cyg	13.9 ± 2.6	56.8	[8]
V3890 Sgr	0.0024 ± 0.002	19	*Molina et al. 2026*
V1354 Sco	< 0.4[a]	1.0	[138]
RS Oph (2021)	67 ± 15	99	[218]
V745 Sco	< 0.5 [a]	4.3	[138]
V1535 Sco	1.0 ± 0.3	17.2	[138]
V392 Per	10.5 ± 2.4	~ 133	[284]
V5589 Sgr	< 1.3[a]	8.1	[138]
U Sco (2022)	< 0.6[a]	2.0	[138]

4.2.2 Gamma-ray Data

>100 MeV γ-ray light curves, as observed by the Large Area Telescope (LAT) on the *Fermi Gamma Ray Space Telescope*, are from [138] for V745 Sco, V1534 Sco, V1535 Sco, V5589 Sgr and U Sco (see Appendix A) and are the result of 15 day binning. Details of their analysis can be found in [138]. The RS Oph data are from [218], the LAT light curve being the result of a varying bin process. More details of the analysis can be found in [218]. The V407 Cyg data are from [8], the LAT light curve uses one day binning. Detections for RS Oph and V407 Cyg are $> 3\sigma$ significance and non detections are $2 - 3\sigma$ significance. The V392 Per data are from [284]; upper limits are 2σ significance and detections are $> 3\sigma$ significance.

4.2.3 Radio Data

Data obtained with the historic VLA ($1980 - 2009$) were obtained in continuum mode typically in observing bands C (4.9 GHz), U (14.9 GHz) and K (22.4 GHz). Details about the observations are available in the NRAO data archive. Observations obtained with the Karl G. Jansky VLA (2010–present) were typically done in L band ($1 - 2$ GHz), C ($4 - 8$GHz), Ku ($12 - 18$ GHz), and Ka ($26.5 - 40$ GHz)—and in Q band ($40 - 50$GHz) for V407 Cyg. From

2010 – 2013 the VLA used 8-bit samplers producing two sub-bands of 1 GHz bandwidth which can be sampled with 2 MHz - wide channels. The VLA later transitioned to 3 bit samplers which can produce up to 8 GHz of bandwidth. Observations were all done in full Stokes mode. Data were edited, calibrated, and imaged in AIPS, CASA, and Difmap [140–142]. Further details on the observations and the calibrators used are available through the NRAO data archive. Flux densities $> 3\sigma$ are significant enough to be considered detections, those below this threshold are counted as non detections. For frequencies of 10 GHz or lower we use a calibration error of 5%, for frequencies over 10 GHz we assume 10% calibration error.

4.2.3.1 Notes on Radio Observations of Individual Sources

V1534 Sco was discovered on 2014 March 26. VLA observations began on 2014 March 31 and concluded on 2015 December 4 under program code 13B-057. Observations were done in L band, C band, Ka and Ku bands in B, A and D configurations.

RS Oph's 2021 eruption was discovered on 2021 August 8. VLA observations began on 2021 August 13 and ended on 2023 July 6 under program codes 21A-342, 21B-336, 21B-351, and 23A-342 in C, B, and A configuration. Details on the uGMRT observations are published in [173] and details on the MeerKAT and LOFAR observations can be found in [285]. The VLA data offers a greater range in frequency coverage (observations span 1.26 – 34.9 GHz)and time. All radio data of this eruption are listed in Table C.3 in Appendix C.

U Sco's 2022 eruption was discovered on 2022 June 6 and VLA observations started on 2022 June 25 and ended on 2022 August 24 under program codes 22A-500 in A and D configuration.

4.2.4 Distances

Distances for the novae discussed in this work are derived using a similar technique to the one described in [53]. This method uses a combination of several sources of distance information for each system. First, we use the Galactic mass model described in [7] as a prior on the distances, assuming the probability of a nova eruption scales linearly with stellar mass. This provides constraints on the most likely distance for a nova along a given sight line in the Galaxy. This prior is combined with constraints from another source of distance information, either in the form of a parallax, luminosity or 3D dust map.

When available, we utilize high-quality parallax measurements from Gaia DR3 [232, 233], which typically provide the most direct measurement of the distance towards a nova. Not all of the targets in this work have access to high-quality measurements, and we only include parallax measurements that are $\geq 3\sigma$. In addition, we further restrict this to systems with Gaia RUWE values of less than 1.4, to eliminate sources with poor astrometric solutions. In practice there are not any novae in this sample that have a high significance parallax and also have RUWE greater than 1.4, so every $> 3\sigma$ parallax is utilized.

When a suitable parallax measurement is not available, we instead use constraints on the peak V band magnitude from the light curves. Based on novae in M31, the peak absolute magnitudes of novae follow a normal distribution with a mean of -7.2 and a standard deviation of 0.8 [156]. When combined with the Galactic mass model prior described above, these luminosity constraints can provide reasonable estimates of the distance. We measure extinctions for these novae to constrain the extinction-corrected magnitudes, following the extinction measurement methods in [53]. This involves using equivalent width measurements of Diffuse Interstellar Bands (DIBs) when available, combined with the relationships between

$E(B-V)$ and these equivalent widths presented in [144]. Optical spectra for these measurements are obtained from the Astronomical Ring for Amateur Spectroscopy (ARAS; [286]), or from the CHIRON spectrograph on the Small and Medium Aperture Telescope System (SMARTS; [139]). When spectra of sufficient resolution ($R \geq 9000$) are not available, we use the observed $(B-V)$ colors and the intrinsic color calibrations from [53].

In general, this method can also be applied using these extinctions combined with 3D dust maps, which is often preferred if there is a need to avoid making assumptions about the nova luminosity. In this case we have also computed distances using the 3D dust maps from [287] when possible, followed by the [153] and [288] maps. Across this particular sample, the luminosities at peak or the parallaxes are available for every source, and provide tighter constraints on the resulting distances than the dust map measurements, so we adopt either parallaxes or luminosities in every case here. As a result, none of the final distances are estimated using dust maps.

There is one nova, V5589 Sgr, with a distance that is in tension with previously reported values from [175], where a distance of 4 kpc was adopted, compared to 7.5 kpc here. The value in [175] and the value here were both derived utilizing the peak V mag and extinction estimates. The difference in the resulting values is a result of somewhat different estimates for the peak V magnitude, plus the fact that the distance prior from the Galactic mass model in the direction of this nova would predict a distance closer to 8 kpc, placing the typical nova in this direction near the Galactic center.

4.3 Radio Properties

4.3.1 Radio Light Curves

Multi-frequency radio light curves for all eleven novae are plotted along with their corresponding optical light curves and when possible their spectral index evolution in Figures 4.1 – 4.11. The radio light curve is plotted on a log-log scale using L, C, Ku and Ka bands when available (for many novae, additional intermediate frequencies have been measured, but these clutter up a light curve and detract clarity, so only a subset are plotted here). Radio non-detections are taken as $3\sigma + S$ where S is the observed flux density, and are plotted as upside down triangles. Figures are sorted in descending order of orbital period.

Radio spectral evolution gives us insight into how the radio emission is evolving over time and for how long it remains optically thick. The spectral index is found by plotting flux density vs frequency in log-log space. The spectral index α is a way to assess how much flux density depends on frequency and is given by the relation $S_\nu \propto \nu^\alpha$. For more complex spectra that exhibit different behavior at high and low frequency, a broken power law is needed to fit the spectra. The broken power law requires a break frequency where the first line ends and the second begins. A range of frequencies were used to assess which gave the best fit to the data. When the broken power law was used, two α were given, α_{high} corresponds to the spectral index of the high frequencies and α_{low} corresponds to the spectral index of the low frequencies. In some cases, a single power law was adequate to fit the spectra. To determine which method provided a better fit, we performed a reduced χ^2 test. Fits to the spectra were done using Astropy's LevMarLSQFitter and were weighted by flux density errors and upper limits were not included in the fits. Spectral index plots, including these fits, are presented in Appendix A. The spectral index values and errors from

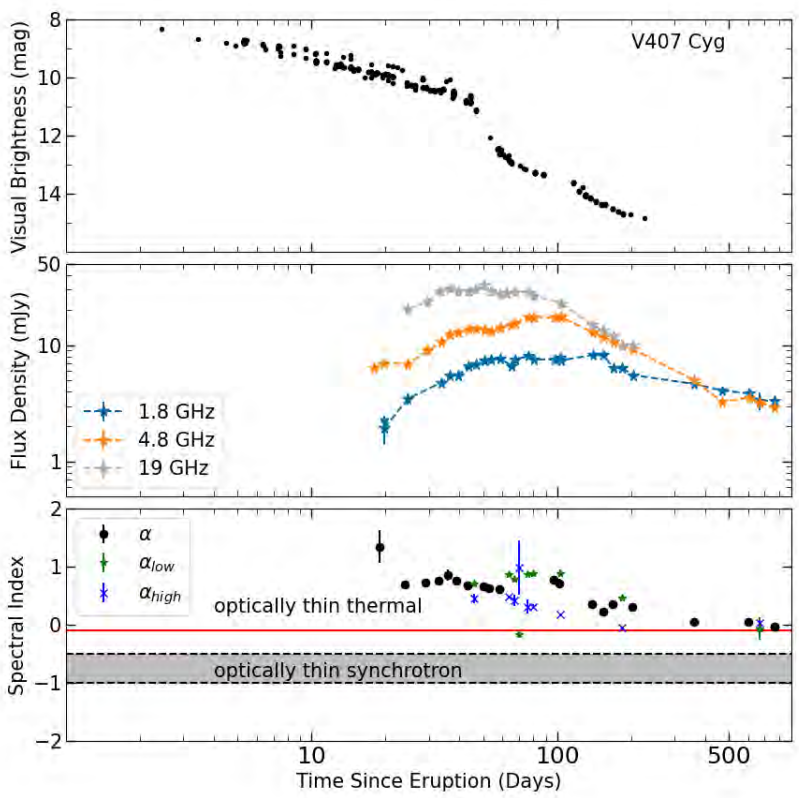

Figure 4.1 The evolution of the 2010 nova eruption of V407 Cyg. The top panel shows the optical light curve, which peaks at about 8 mag and declines to about 15 mag by day 110. The middle panel shows the multi-frequency radio light curve, which peaks at 33.03 mJy on day 50.6 and 19 GHz. The bottom panel shows the spectral index evolution. Spectral indices don't reach -0.1 until about day 200. Before that they are positive.

these plots are plotted in the bottom panels of Figures 4.1 – 4.11.

V407 Cyg's light curves are shown in Fig. 4.1. The optical light curve has a $t_2 \sim 16.4$ days and begins to decline at a faster rate around day 40, coinciding with the peak of the radio light curve. The radio emission is slowly evolving and remains optically thick for ∼100 days, which led [250] to conclude that the radio emission is dominated by thermal emission from the ionized CSM (a unique case amongst novae, likely driven by the very high density CSM around V407 Cyg).

The evolution of V3890 Sgr's 2019 eruption is shown in Fig. 4.2. The optical light curve starts high at a magnitude of ~ 7 remaining above 10 mag for ~ 10 days. At this time in the radio, the 5 GHz frequency is at its peak, with the 1.8 GHz frequency peaking a bit later (~ 15 days after discovery). Spectral index peaks on day 7.2 as the 5 GHz frequency band is rising to peak. The spectral index quickly declines to shallow values of $\sim 0 - 0.5$. The radio light curve evolution is indicative of synchrotron emission, [95] suggest this emission is produced through interactions between the nova ejecta and CSM. On day 45 we see a second small increase in flux density that is more noticeable at lower frequencies. The increase in flux density is slight, from 30.1 mJy to 30.4mJy in 1.8 GHz. This increase in flux may be caused by an increase in diffuse radio emission. As described in Ch.3 the radio emission and γ-ray emission are not coming from the same regions of the shock. In the shock where the γ-rays are being produced non thermal particles may be escaping the shock and diffusing upstream eventually interacting with CSM forming a synchrotron halo which can be see in the VLA light curve as a slight increase in flux density.

V1534 Sco's light curves and radio spectral evolution are shown in Fig. 4.3. The optical V band peak is 11.6 and declines with $t_2 = 5.6$ days. The peak of the optical light curve is not captured here. In the radio light curve the lower frequencies are at higher flux densities than the higher frequencies at all times. At 1.7 GHz on day 15.5 the flux density is 15.3 mJy, compared to the 35 GHz frequency on day 17.5 which only reaches 1.58 mJy. Spectral indices are negative until late times (day 260.9) indicative of synchrotron emission. On days 260.9 and 393.6 the spectral indices are in line with thermal emission.

RS Oph's light curves are shown in Fig. 4.4 for its most recent 2021 eruption. The optical light curve has a $t_2 = 2.77$ days. Around this time in the radio light curve 2.6 GHz and 5 GHz frequencies have already peaked and are slightly declining, while the 31.1 GHz

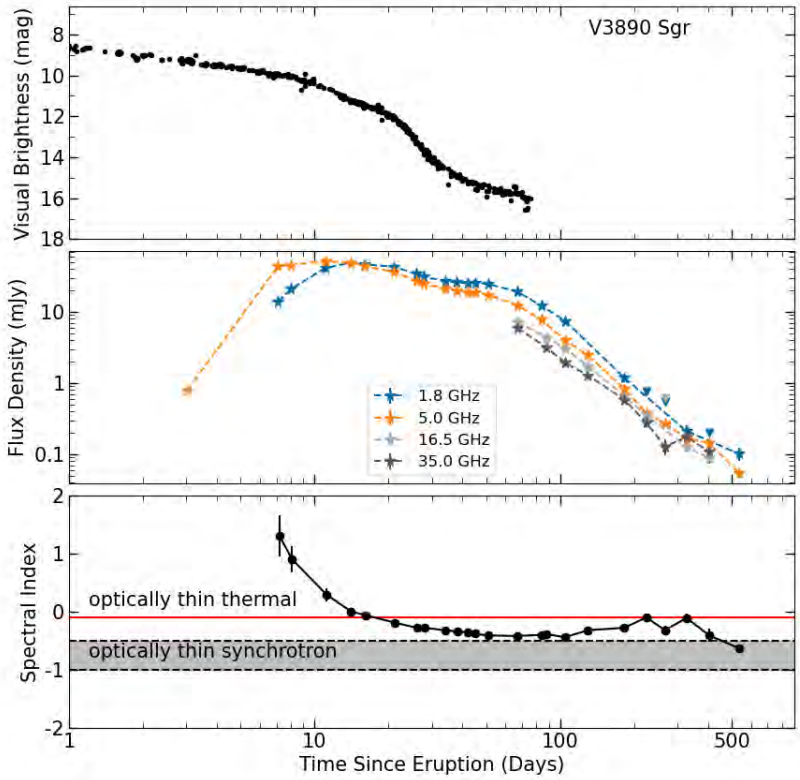

Figure 4.2 V3890 Sgr's optical and radio light curves are plotted above along with the spectral index evolution. The optical light curve peaks at about 7 mag and declines to about 16 mag by day 100. At 5 GHz the radio light curve peaks at a flux density of 50.11 mJy on day 11.05. Spectral indices start out steep $\sim$ 1 and flatten to about -0.5 by day 50. At the decline of the radio light curve there are some small peaks in spectral index to about -0.1.

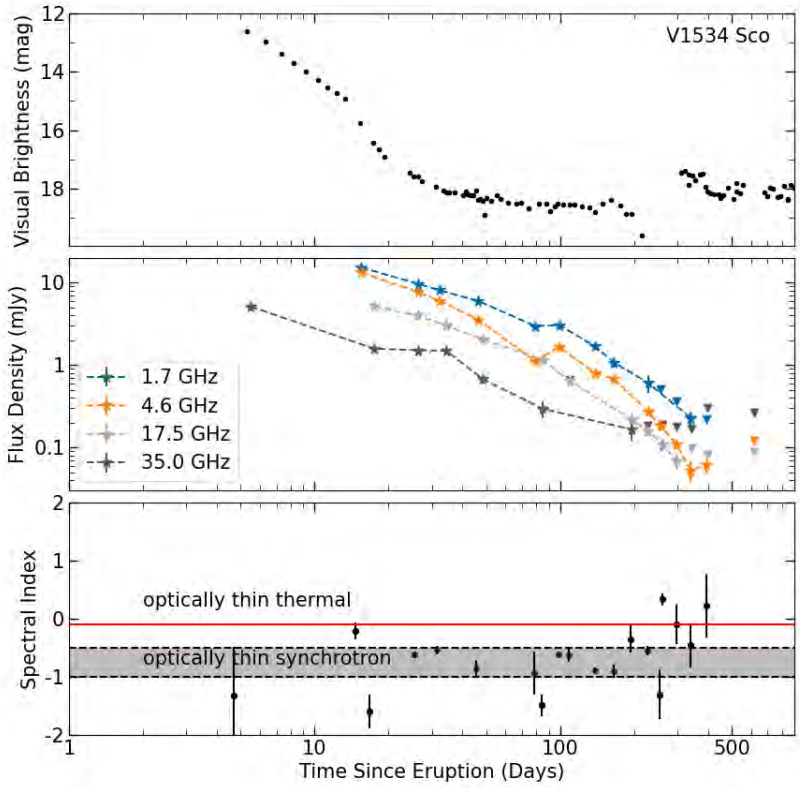

Figure 4.3 V1534 Sco's optical and radio light curves are shown here along with the spectral index evolution. Radio non detections are plotted as upside down triangles. The optical light curve starts at around 12.5 mag dropping to 18.5 mag on day 80. At 1.7 GHz the radio light curve starts at 15.3 mJy on day 15.5.

frequency is increasing (∼27 day). The high frequencies show two peaks, an initial low peak on day 10 (49.9 mJy at 34 GHz) and a larger increase in flux density on day 36 (103.5 mJy at 34 GHz). The lower frequencies show one peak on day 27.

RS Oph and V3890 Sgr stay bright in the radio to $\sim$ 100 days, however the evolution of their radio light curves show different frequency behaviour. In RS Oph lower frequencies are peaking at earlier times than the higher frequencies. In higher frequencies there are two peaks in RS Oph's radio light curve with the first peak being fainter than the second peak. In comparison, in V3890 Sgr's radio light curve the lower frequencies peak slightly earlier than the higher frequencies but they all decline at the same time. V3890 Sgr also shows two increases in flux density but its second peak is the smaller bump in flux density (only increasing to 30.4 mJy at 1.8 GHz) on day 45. This second bump in V3890 Sgr's radio light curve is more prominent in the lower frequencies. The spectral index values in RS Oph show a combination of thermal and non thermal emission. However, V3890 Sgr's spectral indices are indicative of synchrotron emission after $\sim$ 20 days.

V745 Sco's light curves and radio spectral evolution are plotted in Fig. 4.5. After the optical light curve has declined to about $\sim$ 15 mag, then the radio light curve reaches its peak in all frequencies by day 25.6. Unlike V3890 Sgr and RS Oph there is only one peak in the radio. By day 25.6 the spectral index values are around 0. To explain the radio behaviour [23] describe the CSM as having two distinct components. A dense CSM close to the binary and a less dense wind-like CSM farther away from the binary. The dense CSM could be an equatorial density enhancement or a red giant wind that has filled the region over the 25 years since the last eruption.

V1535 Sco's light curve is shown in Fig. 4.6. In the radio light curve the flux density at 4.6 GHz is 4.13 mJy on day 2.66. From here the light curve alternates between increasing

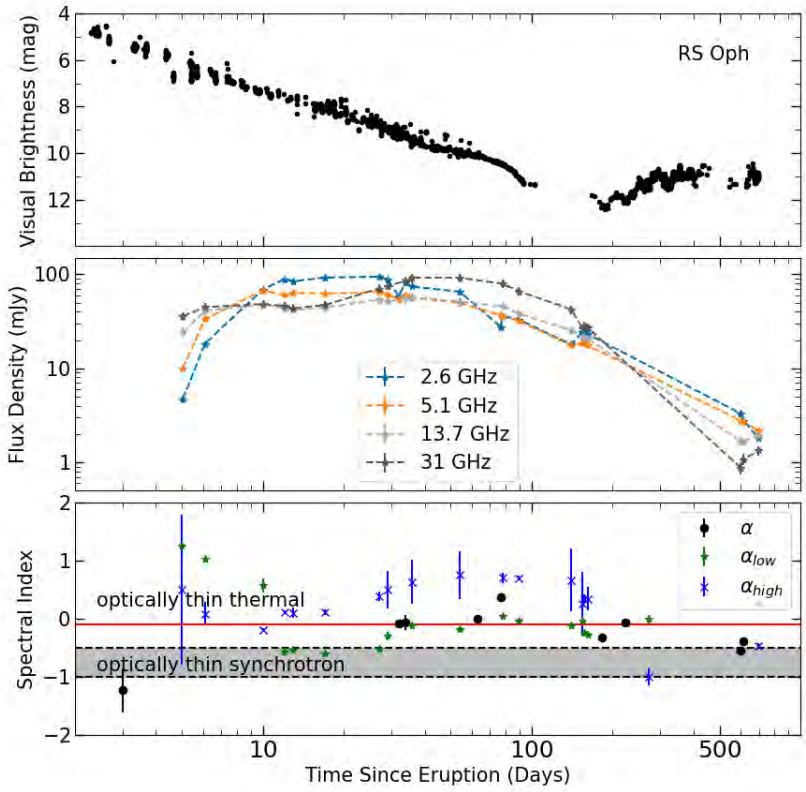

Figure 4.4 RS Oph's radio and optical light curves. The optical light curve peaks at 4.5 mag and declines with a $t_2 = 2.77$ days. In the radio light curve the 2.6 GHz band peaks at around 90 mJy on day 10 and the 31.1GHz band peaks at the same flux density around day 60. The spectral indices peak above 0.1 from day 27 –140.

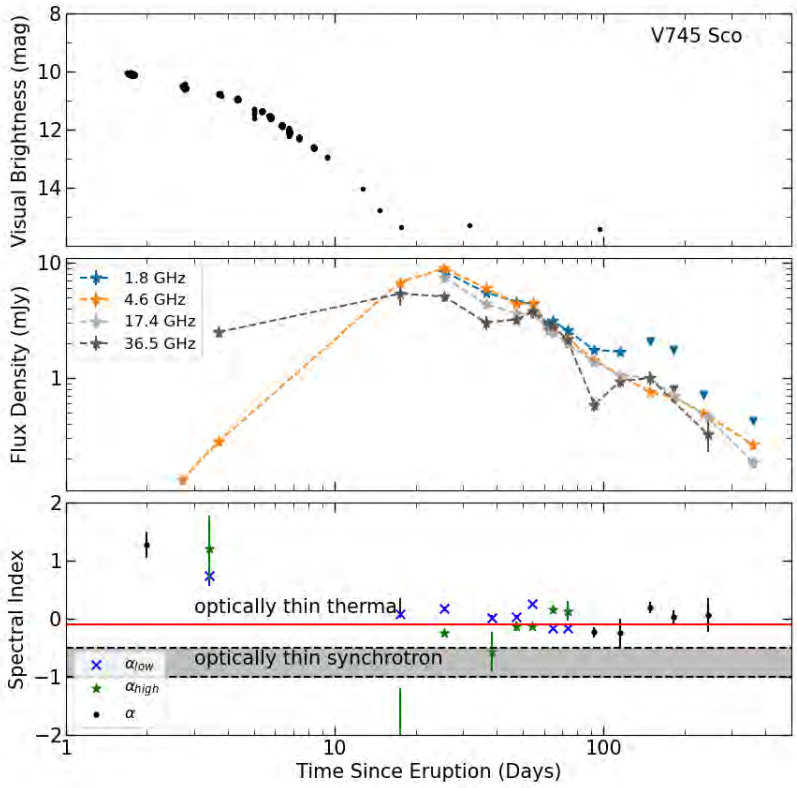

Figure 4.5 V745 Sco's optical and radio light curves are plotted along with the spectral index evolution. The optical light curve starts at about 8.5 mag and declines to about 15 mag by day 20. At 4.6 GHz the radio light curve peaks 25.6 days after eruption at about 8.93 mJy. After radio peak the spectral indices are rather flat, staying around -0.1.

and decreasing flux densities for the rest of the light curve. As the higher frequencies peak, the lower frequencies decrease in flux density. This odd behavior is reflected in the spectral index values, which also peak and decline over the course of their evolution. In [94] they describe a slow rise to peak likely the result of the emission being mainly thermal and tied to the size of the ejecta. They also posit that there are two emitting components in the ejecta and strong shocks early on from a dense wind. There is a possible second shock on day 50 where we see the spectral index values changing to be more in line with synchrotron emission. This second shock could be from collisions between multiple ejecta outflows or from a dense shell formed from previous eruptions [94]. The optical light curve peaks at 9.5 mag on day 2.71. V1535 Sco is a unique nova in our sample as it's orbital period (39.6 days) lies between the orbital period of the RG-novae (on the order of 100 of days) and SG-novae (on the order of days).

V392 Per's light curves are shown in Fig. 4.7. The optical light curve comes from AAVSO data and did not capture the peak of V band. Throughout the entire radio light curve the higher frequencies peak at higher flux densities than the lower frequencies. The 29.0 GHz frequency peaks at 14.42 mJy on day 32 and the 1.74 GHz frequency peaks at 3.89 mJy on day 32. All frequencies are peaking at the same time (day 32) and decline together. The novae from here on have subgiant companions. V392 Per has the largest orbital period of the SG-novae listed here, at 3.4 days.

Figure 4.8 shows the optical and radio light curves of V1370 Aql. The radio data is sparse and only in two frequencies (1.5 GHz and 4.9 GHz). The brightest flux density is at 20.2 mJy in 4.9 GHz. Detections end by day 152.5 in 1.5 GHz. The radio detections coincide with a second rise in the optical light curve around day 50. Due to there being no days where radio detections are found in two frequencies we could not plot spectral indices.

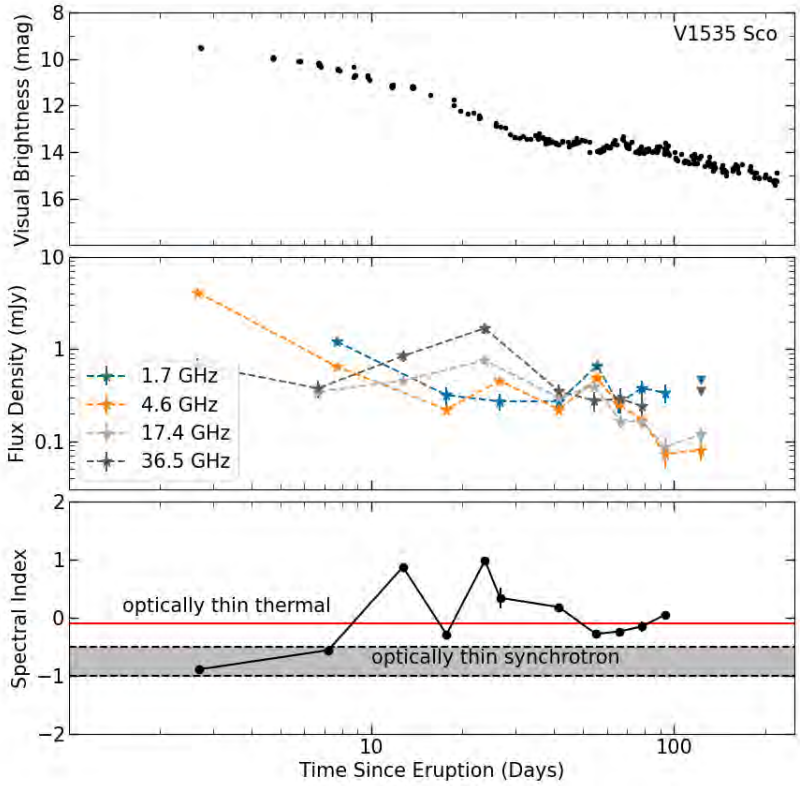

Figure 4.6 V1535 Sco's optical and radio light curves are plotted along with the spectral index evolution. Radio non detections are plotted as upside down triangles. The optical light curve starts at a peak of about 9.5 mag and declines with a $t_2 = 13.6$ days. The radio has multiple peaks and dips with the highest flux density being at 4.6 GHz at 4.13 mJy on day 2.7. The spectral indices start steep at -0.89 on day 2.7 and peak to 0.87 on day 12.7. Spectral indices then dip to -0.29 on day 17.7 and peak again to 0.98 on day 23.7. This fluctuating behavior is also seen in the radio light curve.

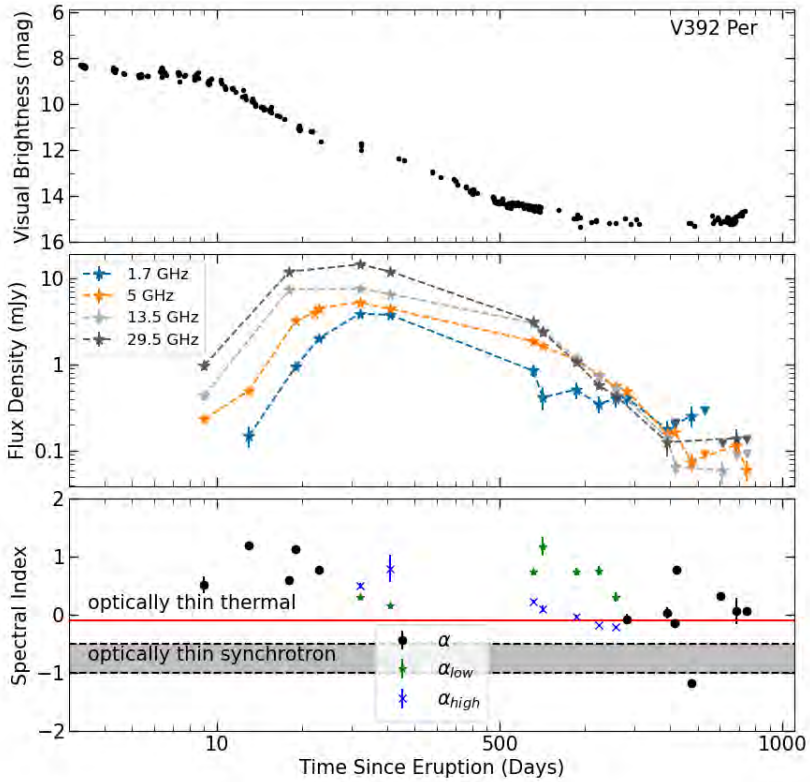

Figure 4.7 V392 Per's optical and radio light curves are plotted along with the spectral index evolution. The optical light curve peaks at 5.6 mag and declines with a $t_2 = 3$ days. At 29.50 GHz the radio light curve peaks at 14.42 mJy on day 32. The spectral indices are variable but tend to stay positive until the late decline of the radio light curve where they reach -0.1.

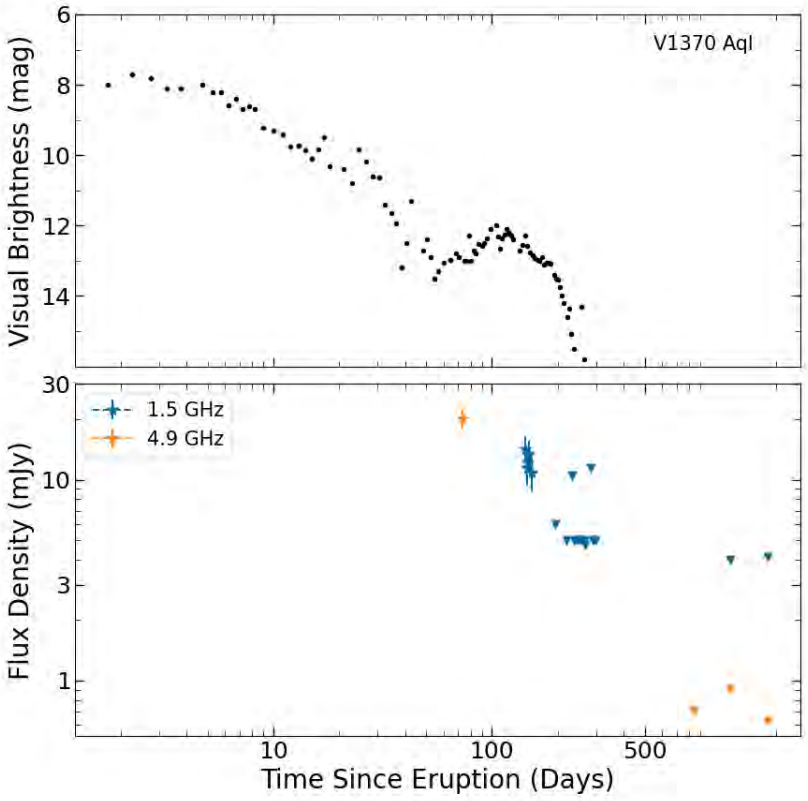

Figure 4.8 V1370 Aql's optical and radio light curves are shown here. The optical peaks at 7.7 mag and has a $t_2 = 15$ days. The radio data are very sparse, but demonstrate that this nova got bright at radio wavelengths (20.2 mJy at 5 GHz on day 73.5).

Fig. 4.9 shows V5589 Sgr's light curves. The optical light curve starts at ~ 10 mag and has a $t_2 = 4.5$ days. Radio detections do not start until day 46 but considering the non detection at 36.5 GHz frequency on day 2.5 and the 4.8 GHz frequency light curve it does appear we have captured the peak. The 36.5 GHz radio light curve peaks higher (at 5.96 mJy) than the 4.8 GHz frequency which peaks at 3.63 mJy. On day 46 the spectral index inverted (higher flux density at higher frequencies) and declines from 0.77 to -0.14 on day 90.3. On day 110 the spectral index is again positive (0.12) and then dips back down to negative values.

Fig. 4.10 shows U Sco's light curves for the 2022 eruption. The optical light curve has a peak optical magnitude of 7.8 and $t_2 = 1$ day, the fastest decline in the optical of the 11 novae. The radio light curve at 31.1 GHz peaks at 0.42 mJy the faintest radio peak of the nova sample. Lower frequencies are plotted in the radio light curve as they are all non detections. The spectral index values are steep on day 18.5 but are flatter by day 32.5.

V723 Cas's light curves are shown in Fig. 4.11. The optical light curve shows four peaks around day 100 – 400, and a very slowly evolving light curve characterized by $t_2 = 621$ days. The radio light curve does not start until day 477 with the 5 GHz frequency peaking on day 1221. There is unfortunately very limited coverage at other frequencies for this nova, but the overall picture is a slowly evolving radio light curve to match the slow optical evolution.

4.3.2 Comparing Consecutive Eruptions in the Radio

Of the 11 novae in our sample, three are recurrent novae with multiple eruptions observed at radio wavelengths (RS Oph, V745 Sco, and U Sco). While it has been demonstrated that consecutive eruptions of recurrent novae produce very similar optical light curves [3], less work has been done at radio wavelengths.

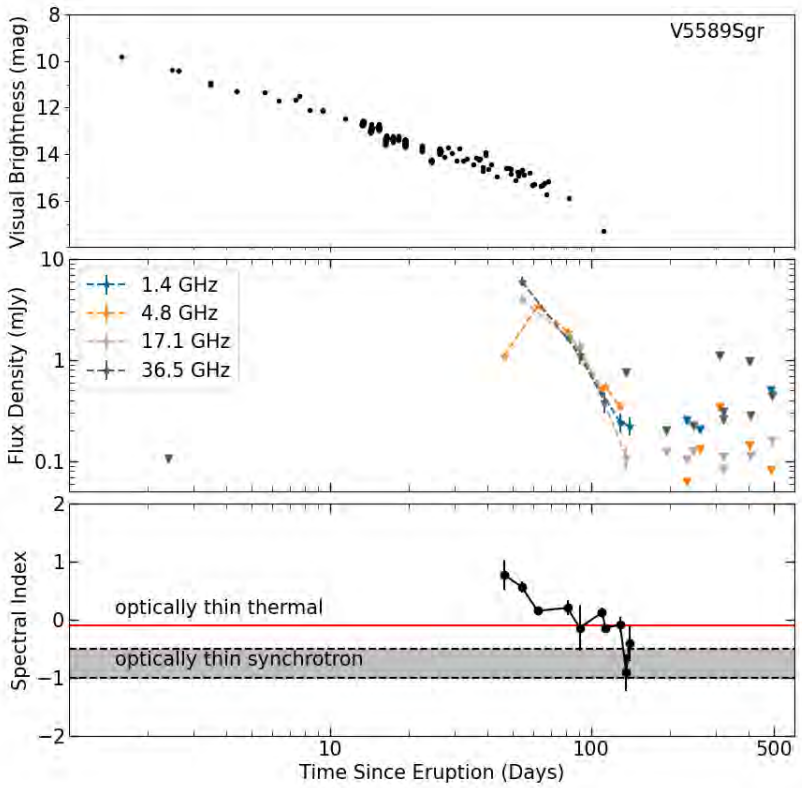

Figure 4.9 V5589 Sgr's optical and radio light curves are plotted along with the spectral index evolution. Radio non detections are plotted as upside down triangles. The optical light curve starts at about 10 mag and declines to about 17 mag by day 100. At 36.5 GHz the radio light curve peaks at 5.96 mJy on day 54.2. At around day 200 there are only non detections. The spectral index starts at 0.77 and flattens to about -0.1 by day 90.3.

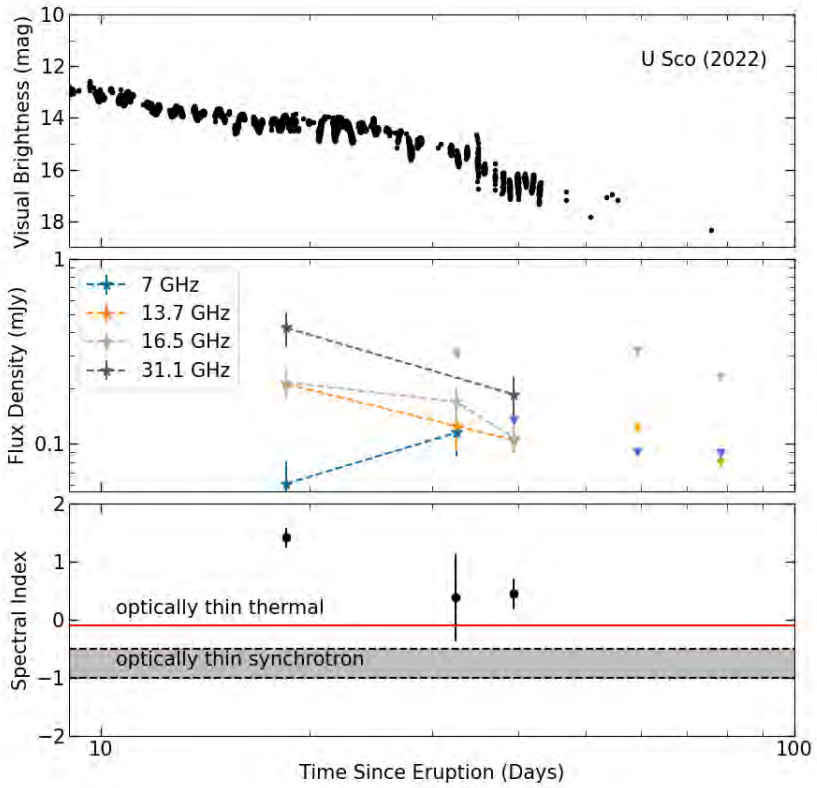

Figure 4.10 U Sco's optical and radio light curves for the 2022 eruption are plotted along with the spectral index evolution. The optical light curve peaks at about 8 mag with a $t_2 = 1$ day. At 31.1 GHz the radio light curve peaks at 0.42 mJy on day 18.50. The spectral indices start at 1.41 and decline to $\sim$0.4.

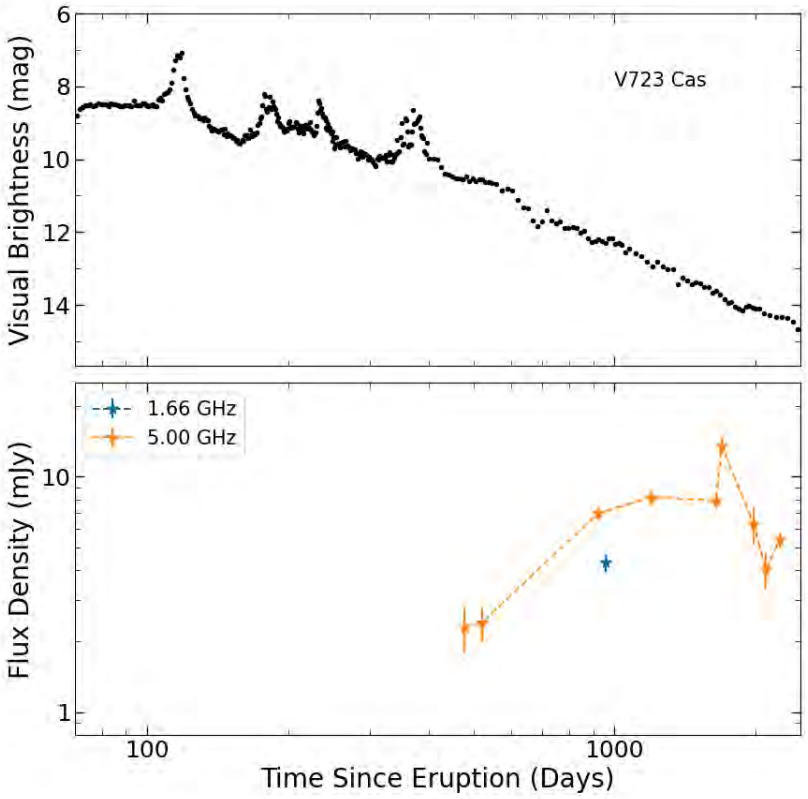

Figure 4.11 V723 Cas's radio and optical light curves are plotted above. The optical light curve starts at 9 mag and declines slowly. The radio light curve peaks at 13.5 mJy on day 1221 at 5 GHz. The rise to peak in the radio takes 1633 days.

V745 Sco's 1989 and 2014 eruptions were studied in [23] at 1.5 GHz and 4.9 GHz. The decline in the radio is similar in both frequencies with the 1989 eruption being $\sim 20\%$ fainter than the 2014 eruption, inconsistent with findings from [137]. We do not see a difference in behaviour for the two different frequencies. The 1989 radio decline does show slightly fainter flux densities than the 2014 eruption but they decline at similar rates, $t_{89} = -1.28 \pm 0.47$ and $t_{14} = -1.05 \pm 0.21$ at ~ 1.4 GHz. At 4.9 GHz the 2014 eruption declines with a rate of $t_{14} = -1.21 \pm 0.08$ and the 1989 eruption declines with a rate of $t_{89} = -1.47 \pm 0.19$ [23].

U Sco data of the 1999 and 2022 eruptions are limited. Observations for the 1999 eruption start 8 days after discovery and 2022 observations start 18.5 days after discovery. Within the time range of 30-40 days there are detections in both eruptions. The 1999 eruption only has detections at 8 GHz at this time, one on day 33 at a flux density of 0.14 mJy and the other on day 39 at a flux density of 0.10 mJy. In the 2022 eruption there is only one 7 GHz data point (0.12 mJy) at day 32 and a non detection at day 39.4 at 0.14 mJy, similar flux densities to the 1999 eruption.

We can compare RS Oph's radio behaviour across three observed eruptions: 1985, 2006 and 2021. Fig. 4.12 compares the 1.3–1.5 GHz light curves and power-law indices of the radio light curve decline. The 2006 data (frequencies 1.39 GHz, 1.28 GHz and 1.06 GHz) comes from [289] and (1.46 GHz data) [169]. The 2021 data at 1.36 GHz is from uGMRT observations. The 2021 eruption has a shallower power-law index ($t_{21} = -0.94$) than the 1985 eruption ($t_{85} = -1.51$), as does the 2006 power-law index ($t_{06} = -0.62$).

On day ~ 180 the 1985 light curve has a flux density of 7.0 mJy compared to the 2021 flux density of 13.1mJy. The peak of the 1985 radio light curve does appear to be captured but is not well constrained as there is only one point prior to the peak on day 29.6. Comparing peak radio flux densities across eruptions, the 2021 eruption peaks at the highest flux density

at 85.1 mJy on day 25, next is the 1985 eruption peaking at 63 mJy on day 41.5 and last the 2006 eruption which peaks at 57.6 mJy on day 13.9.

Fig. 4.13 compares all three eruptions in the $\sim$ 5 GHz frequency band. The 2021 outburst declines more slowly ($t_{21} = -1.21$) than the 1985 outburst($t_{85} = -1.34$). The 2021 eruption again shows the brightest flux densities. On day $\sim$ 157 the 1985 flux density is 10.0 mJy and the 2021 flux density is 19.8 mJy. The 2006 eruption has less radio data than the 2021 and 1985 eruptions which could explain the discrepancy in power-law indices ($t_{06} = -0.77$) . The difference in power-law indices between the 1985 and the 2021 eruptions is smaller at 5 GHz compared to the 1.5 GHz plot. Comparing the peak flux densities, the 2021 eruption peaks at 67.6 mJy on day 10, the 2006 eruption peaks lower at 53.3 mJy on day 13.9 and the 1985 eruption peaks at 61 mJy on day 41.5.

Fig. 4.14 compares the radio light curves of the 1985, 2006, and 2021 eruptions at 14 GHz. The 2021 and 1985 eruptions have very similar power-law indices(-1.53 for 1985 and -1.62 for 2021) indicating that the subsequent eruptions of RS Oph are very similar. At this frequency, the light curve flux densities are more comparable, suggesting that the differences seen in radio light curves is frequency dependent. On day $\sim$ 157 the 1985 flux density is 17.0 mJy and the 2021 flux density is 21.91 mJy. The peak flux densities also occur at more similar times, 2021 radio peak is 56.9 mJy on day 36 , 2006 radio peak is 55.8 mJy on day 41.6 and the 1985 radio peak is 68 mJy on day 38.7. At these higher frequencies, optical depth effects are less strong, indicating that perhaps the intrinsic eruption properties are similar in consecutive eruptions, but the absorbing screen is different—perhaps because the binary is caught in different locations in its orbit. In comparison, V745 Sco shows similar radio light curves at 1.4 GHz or 4.9 GHz for the 1989 and 2014 eruptions across the whole radio evolution. However, the 1989 eruption does show slightly fainter radio flux densities. At

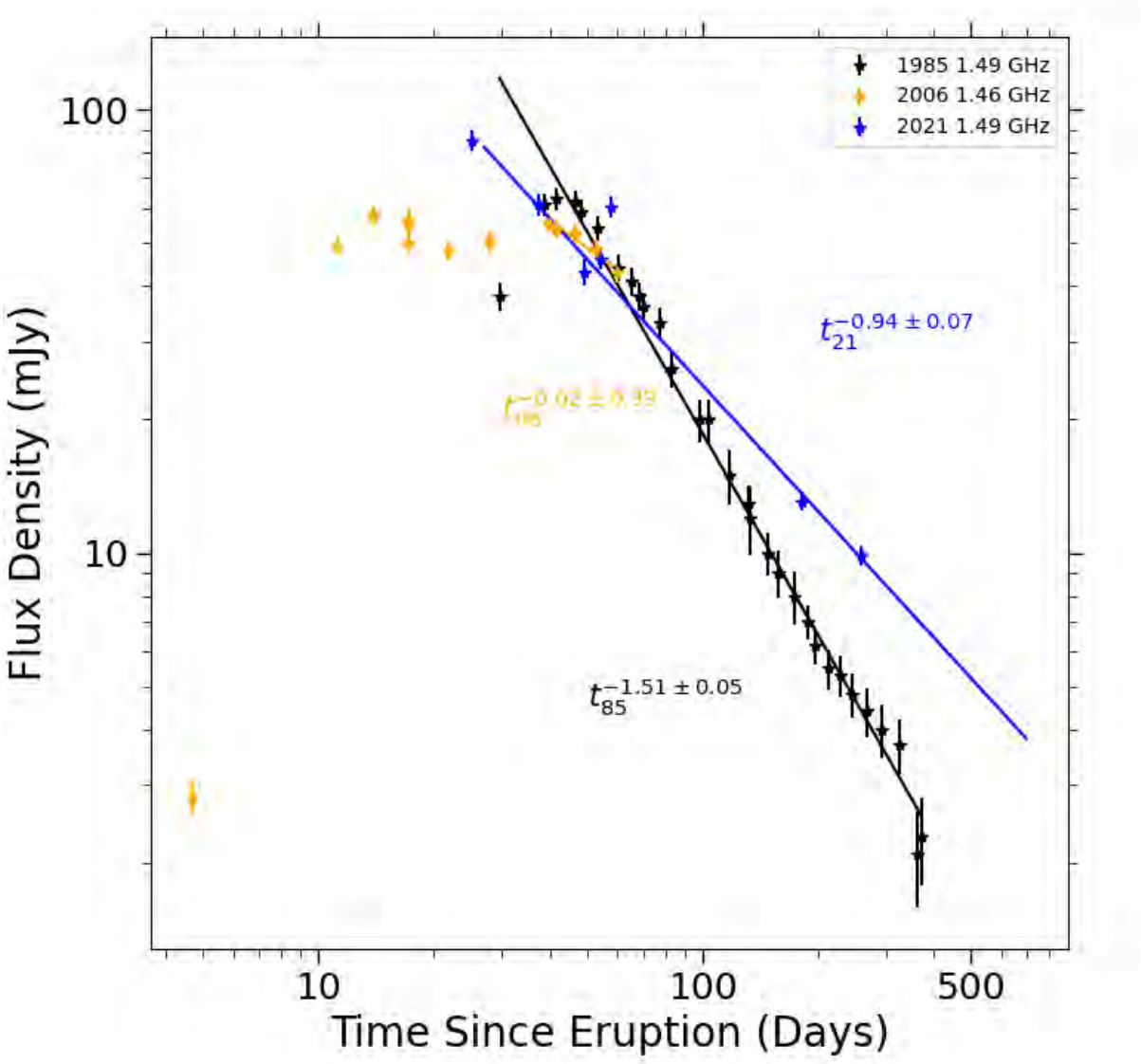

Figure 4.12 Comparison of 1.3–1.5 GHz light curves for RS Oph's three most recent eruptions (1985 in blue, 2006 in orange, and 2021 in blue). The power-law indices of the 2021, 2006, and 1985 light curve after radio peak are annotated in the plot.

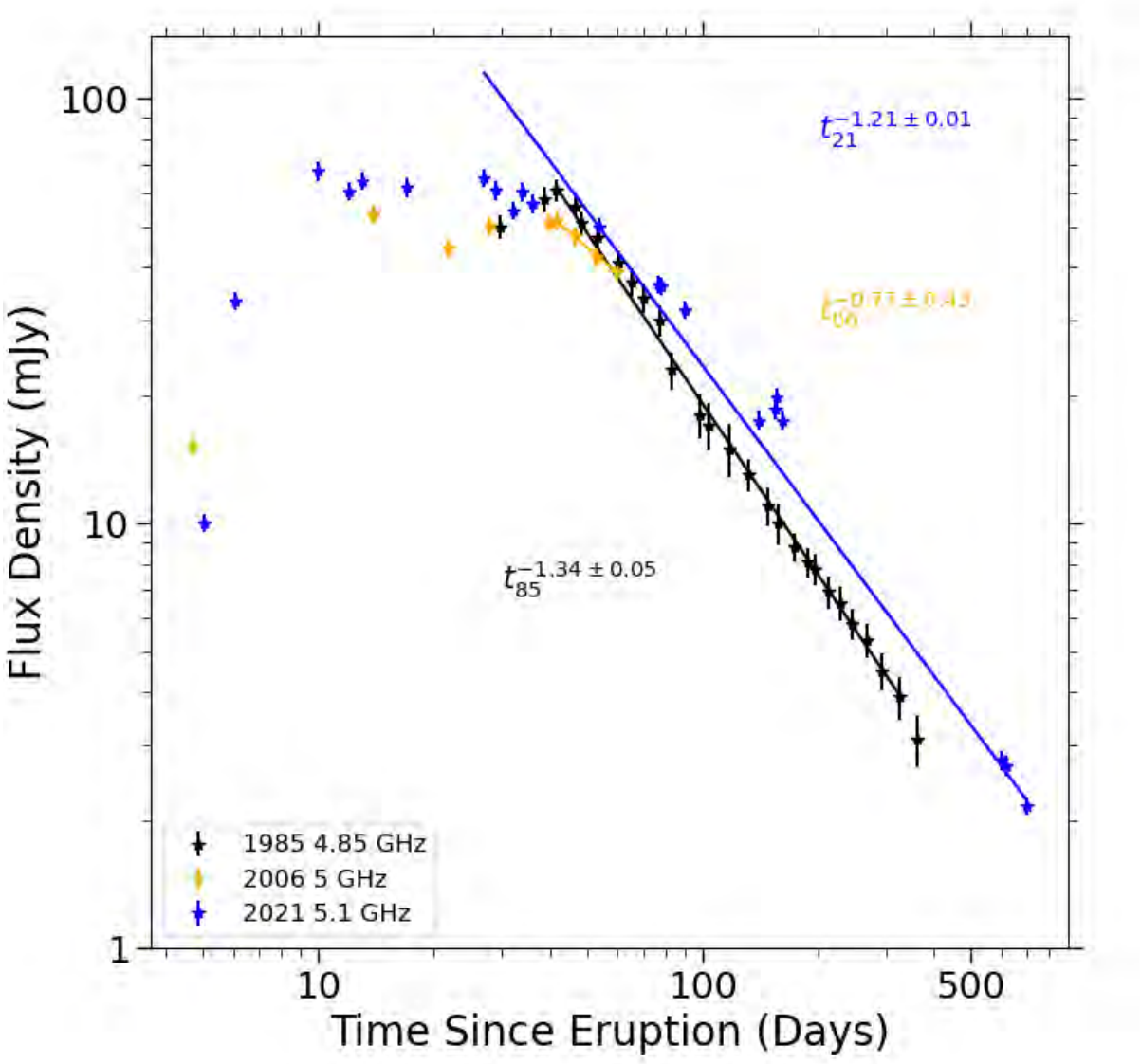

Figure 4.13 Comparison of 4.9–5.1 GHz light curves for RS Oph's three most recent eruptions (1985 in black, 2006 in orange, and 2021 in blue). The power-law indices of the 1985 (-1.34) and the 2021 eruption (-1.21) are more similar than the power-law index of the 2006 eruption (-0.77), but this could be because there is much less data from the 2006 eruption.

lower frequencies, RS Oph shows a growing discrepancy in flux densities over time. V745 Sco also does not show any frequency dependent distinctions across eruptions as RS Oph does.

[169] claim that RS Oph's 2006 eruption has two peaks in the radio light curve at 5GHz with the first peak starting on day 6.1 and the second on day 54. While not visible in all frequency bands during the 2021 eruption, we do see this double peak at higher frequencies (16.5 GHz and 34 GHz) as shown in Fig. 4.15. Through comparing multiple eruptions of three novae with evolved companions we see similarities in the declines of the radio flux densities. However, there are unique features to these eruptions like the frequency dependent behaviour we see in RS Oph.

4.4 Thermal Emission or Synchrotron?

In [51] they estimated that 25 % of novae with main sequence companions have radio light curves dominated by synchrotron emission at some time. While there have been numerous claims throughout the literature that novae with evolved companions have synchrotron dominated radio emission we set out to investigate this claim. Through brightness temperature estimates we determine what percentage of Galactic novae with evolved companions are dominated by synchrotron emission and if there is a connection with binary parameters.

4.4.1 Brightness Temperature

We estimate the radio brightness temperature (T_B) of all 11 novae over the course of their eruptions to determine if the radio emission is dominated by thermal or non-thermal emission. A brightness temperature exceeding 5×10^4K cannot be produced from photo-ionized gas and thus must be coming from non-thermal emission [174]. To calculate brightness temperature

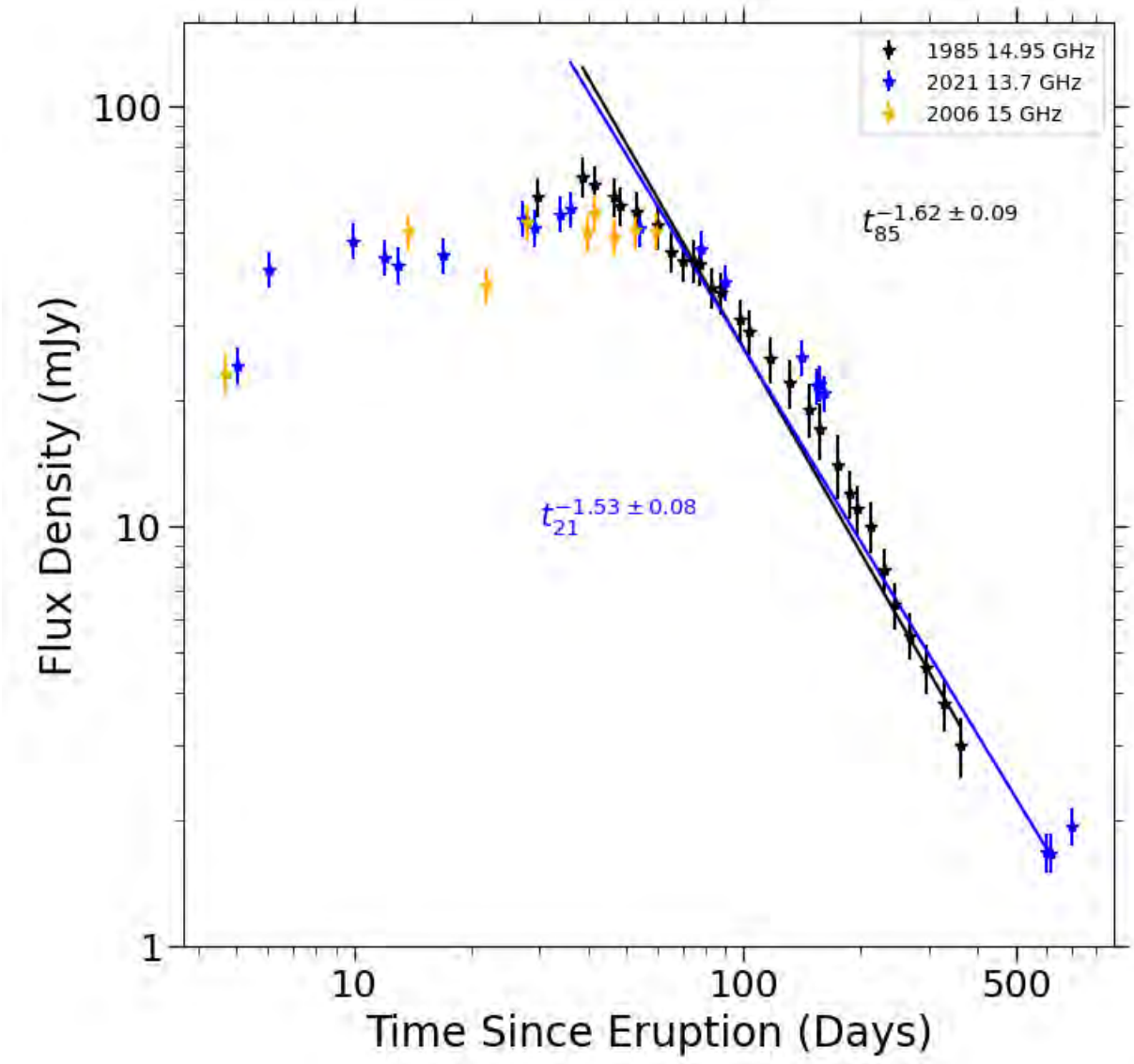

Figure 4.14 Comparison of ∼14 GHz light curves for RS Oph's three most recent eruptions (1985 in blue, 2006 in orange, and 2021 in blue). The 2006 data did not have enough points to measure the power-law index after radio peak. The power-law indices of the 1985 eruption (-1.62) and the 2021 eruption (-1.53) are similar.

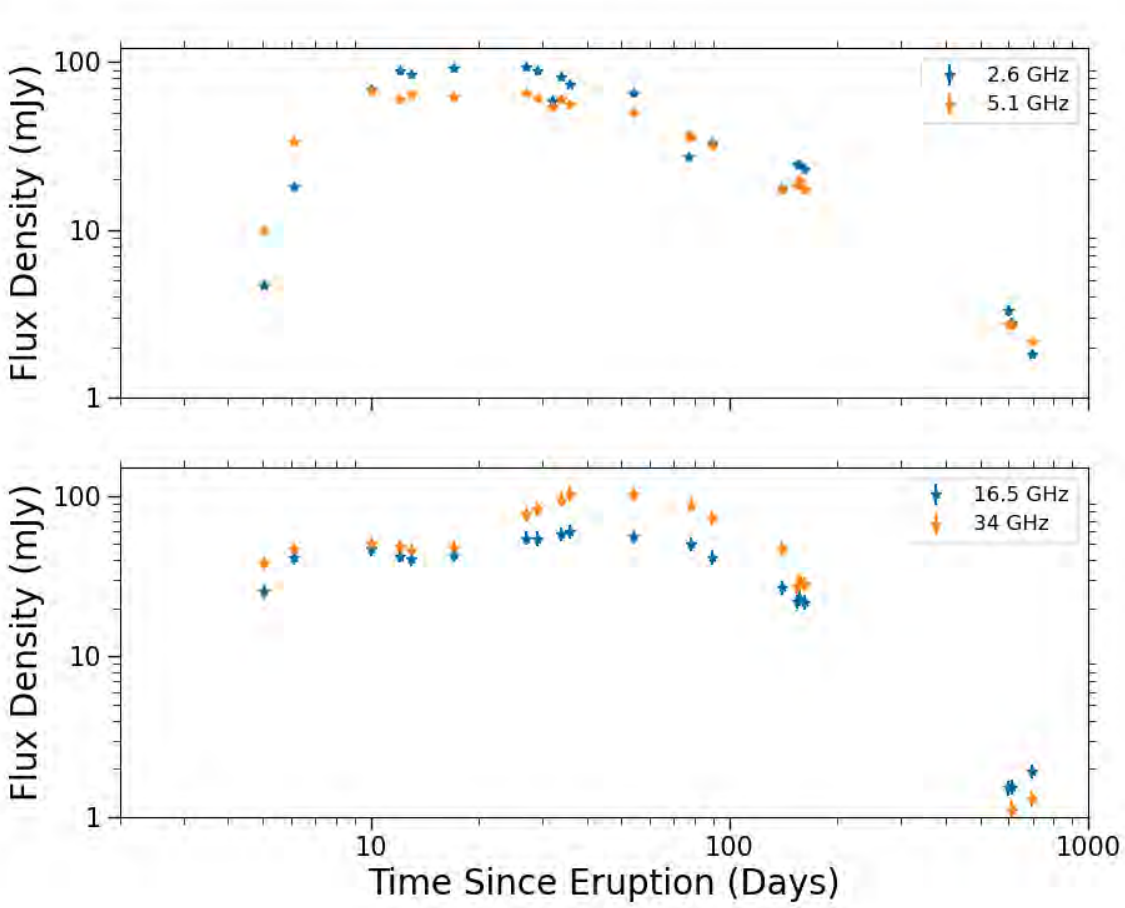

Figure 4.15 The radio light curves of RS Oph's 2021 eruption showing the frequency bands 16.5 GHz and 34 GHz in the bottom panel and 1.49 GHz and 5.1 GHz in the top panel. In the top panel there is only one peak on day 27. In the bottom panel we do see a double peak (on days 6.1 and 54). These peaks are most clearly seen in the 34 GHz frequency.

we used the equation:

$$T_B = 1765.8\,K \left(\frac{\nu}{\mathrm{GHz}}\right)^{-2} \left(\frac{S_\nu}{\mathrm{mJy}}\right) \left(\frac{\theta}{\mathrm{arcsec}}\right)^{-2} \tag{4.1}$$

where ν is the frequency band being used (1–2 GHz), S_ν is the corresponding flux density, and θ is the angular diameter of the emitting source, assuming the source is disc-shaped [167]. θ was estimated using the distances and range of velocities v_1 and v_2 listed in Table 4.1.

Although in some cases we have VLBI or VLA imaging that enables direct measurement of the diameter, this is often not possible. We can instead use our integrated radio flux density measurements to estimate brightness temperature, if we combine estimates of the distance to the nova, the velocity of the ejecta, and the amount of time the ejecta have been expanding to approximate the angular diameter. It is simplest to assume that the ejecta expand with a constant velocity, but estimating the diameter this way gives us an upper limit on the diameter of the ejecta, as we expect the ejecta to decelerate on impact with CSM. Lower frequency brightness temperature estimates are more constraining than higher frequency brightness temperature estimates, so where possible we use measurements obtained at 1.4–2.6 GHz.

The resulting brightness temperatures are plotted in Figures 4.16-4.17; the polygon shape comes from the range in velocity and the error in distance. In Figure 4.16 the brightness temperatures of novae with orbital periods $>$ 100 days are plotted. In Figure 4.17 the brightness temperatures of novae with orbital periods $<$ 100 days are plotted. V1535 Sco, with an orbital period of 39.6 days, has an order of magnitude difference with V392 Per and V745 Sco (3.41 days and 365 days, respectively) and is plotted with the subgiants.

Of the 11 novae considered here, nine show brightness temperatures that are higher than 5×10^4K for at least a portion of their evolution, indicating that 82% have strong contributions from synchrotron emission. All of the novae with giant companions have radio emission dominated by synchrotron emission. Of the novae with subgiant companions four of the six novae have synchrotron emission for at least some of their radio evolution. Only U Sco and V723 Cas remain below that threshold and have purely thermal emission. The completely thermal radio emission in V723 Cas is likely due to its slow evolution, with an ejecta velocity of 210 km s^{-1} [283]. The radio observations of V723 Cas do not start until 477 days after discovery so there may have been early synchrotron emission that was missed. U Sco, while it has a high ejecta velocity, is faint at radio wavelengths. The low density CSM could explain the lack of synchrotron emission. Some novae, like V1534 Sco, remain above 5×10^4K for the entire radio campaign. The highest brightness temperature reached here is by V3890 Sgr peaking at a value of 1.7×10^8K. In the case of V407 Cyg, the assumptions made while calculating brightness temperature are not accurate as the radio emission in this system does not originate from the ejecta. The nova has a Mira giant companion whose winds have been ionized. The radio emission is dominated by thermal emission from the CSM instead of from the ejecta [250].

[51] studies 36 novae with main sequence and sub-giant companions, intentionally excluding novae with giant companions. Of these 36 novae, only 9 (25 %) exhibited evidence for synchrotron emission through brightness temperature estimates. This is a significantly lower fraction compared to the sample of novae studied here, where 82 % (9 of the 11 novae) show evidence for synchrotron emission at some point in their light curve. This difference is likely caused by variations in the circumbinary environment: binaries including evolved stars are more likely to host dense CSM, which nova ejecta will interact with and create energetic

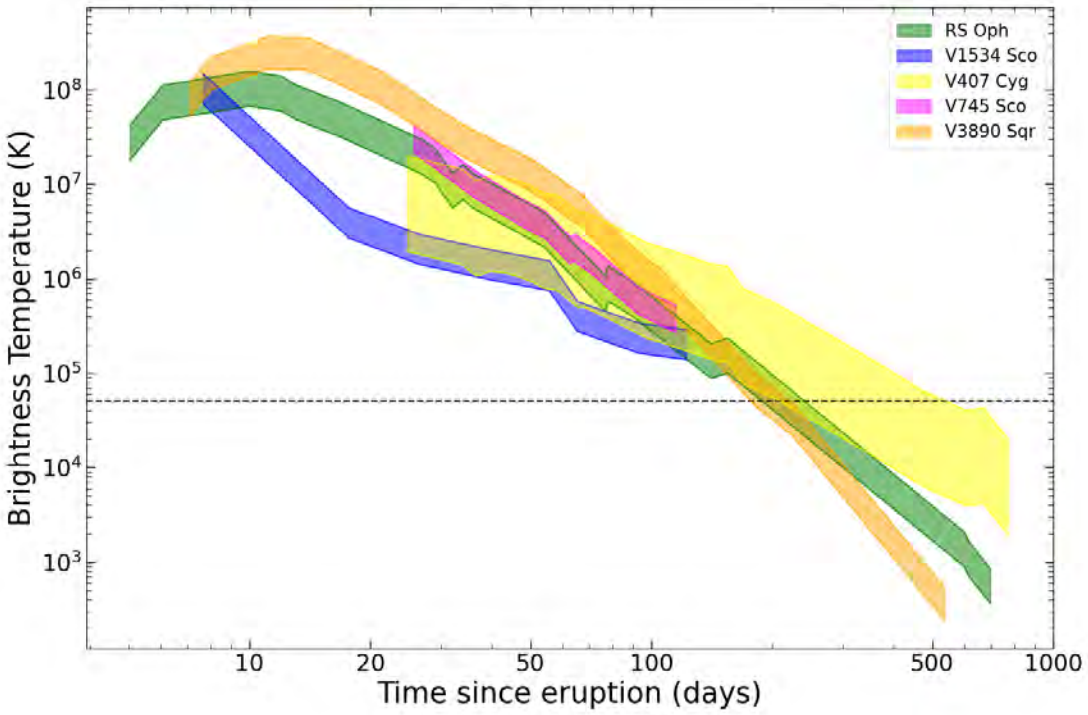

Figure 4.16 Compilation of brightness temperature estimates of the 5 novae with orbital periods greater than 100 days. Each colored polygon corresponds to a different nova. The dashed line is plotted at 5×10^4 K novae that exceed this line must have synchrotron emission.

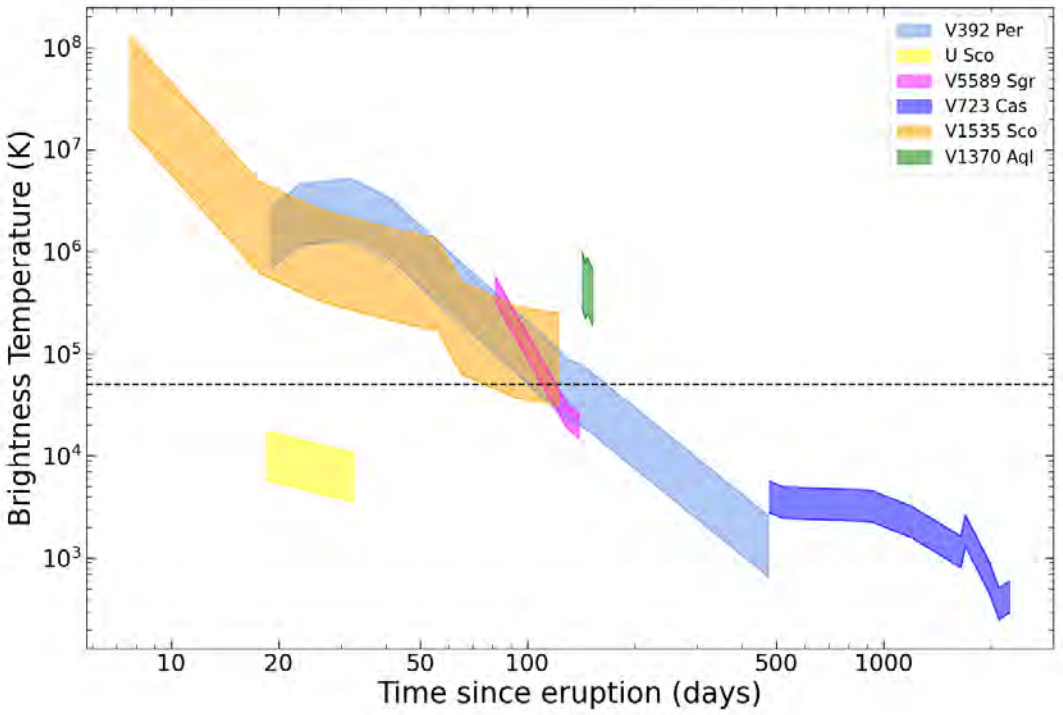

Figure 4.17 Compilation of brightness temperature estimates of the 6 novae with orbital periods shorter than 100 days. Each colored polygon corresponds to a different nova. The dashed line is plotted at 5×10^4 K novae that exceed this line must have synchrotron emission.

shocks. While novae with main-sequence companions are also thought to host shocks, these shocks are internal to the ejecta, implying that they are deeply embedded and radio emission will be free-free absorbed. Shock interaction with an external medium undergoes less significant absorption and is more likely to generate detectable synchrotron emission.

4.4.2 RS Oph: A Combination of Thermal and Synchrotron Radio Emission

Much has been written about the radio emission from RS Oph, and the clear role synchrotron radiation plays in it [173, 285, 290]. However, the radio light curve and spectral index evolution of RS Oph eruptions are clearly complex (Figure 4.4). Does thermal free-free emission also significantly contribute to RS Oph's radio luminosity?

As the VLA is sensitive to the integrated radio flux and the VLBI is only sensitive to high-surface-brightness synchrotron emission, we can compare VLA and VLBI light curves to ascertain the percentage of radio emission that is mainly thermal or non thermal. Fig. 4.18 compares the 1.5 GHz VLA and VLBI observations of the 2021 eruption from [238]. The VLA observation is clearly capturing more of the radio flux density and declines faster than the VLBI light curve indicating that thermal emission is an important contributor to the radio flux density.

Fig. 4.19 compares the 5GHz VLA and VLBI observations. Again the peak of the VLBI light curve ($\sim$ 45mJy) is much lower than the VLA light curve peak ($\sim$ 70mJy) and the VLA light curve declines faster ($t_{VLA} = -1.23$) than the VLBI light curve ($t_{VLBI} = -0.85$).

On the last VLBI observing epoch [238] note that the core flux density drops by $\sim$ 80 %, with the brightest region being the western lobe. On day $\sim$ 54 the VLA flux density at 5 GHz is 49.9mJy. The 5 GHz VLBI flux density on day $\sim$ 64 is 18mJy, about 0.36 of the

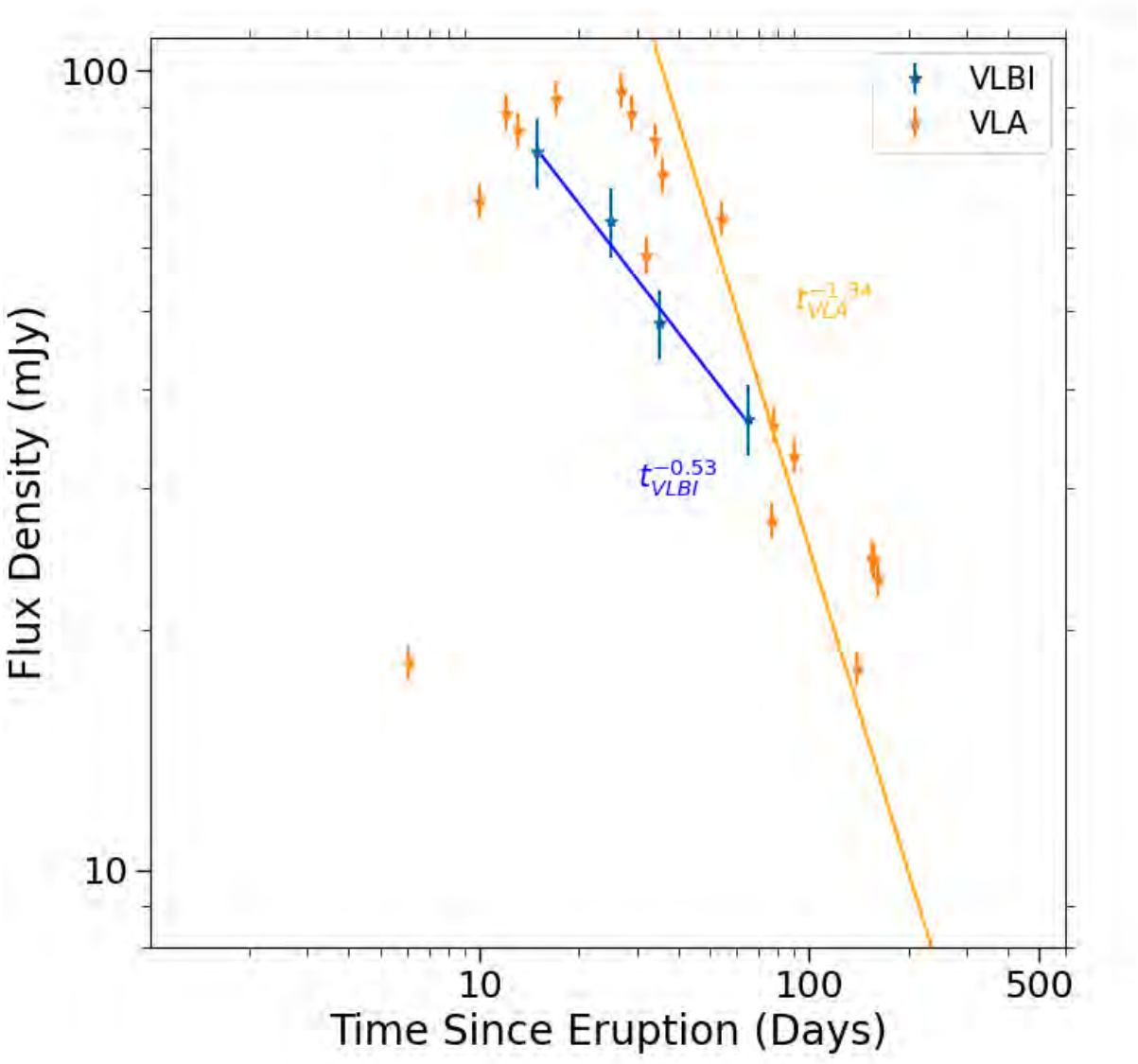

Figure 4.18 VLA and VLBI radio light curve of RS Oph's 2021 eruption in $\sim$ 1.5 GHz. The VLA light curve peaks at a higher value than the VLBI light curve and declines with a power-law index of -1.34. The VLBI light curve declines slower at a power-law index of -0.53.

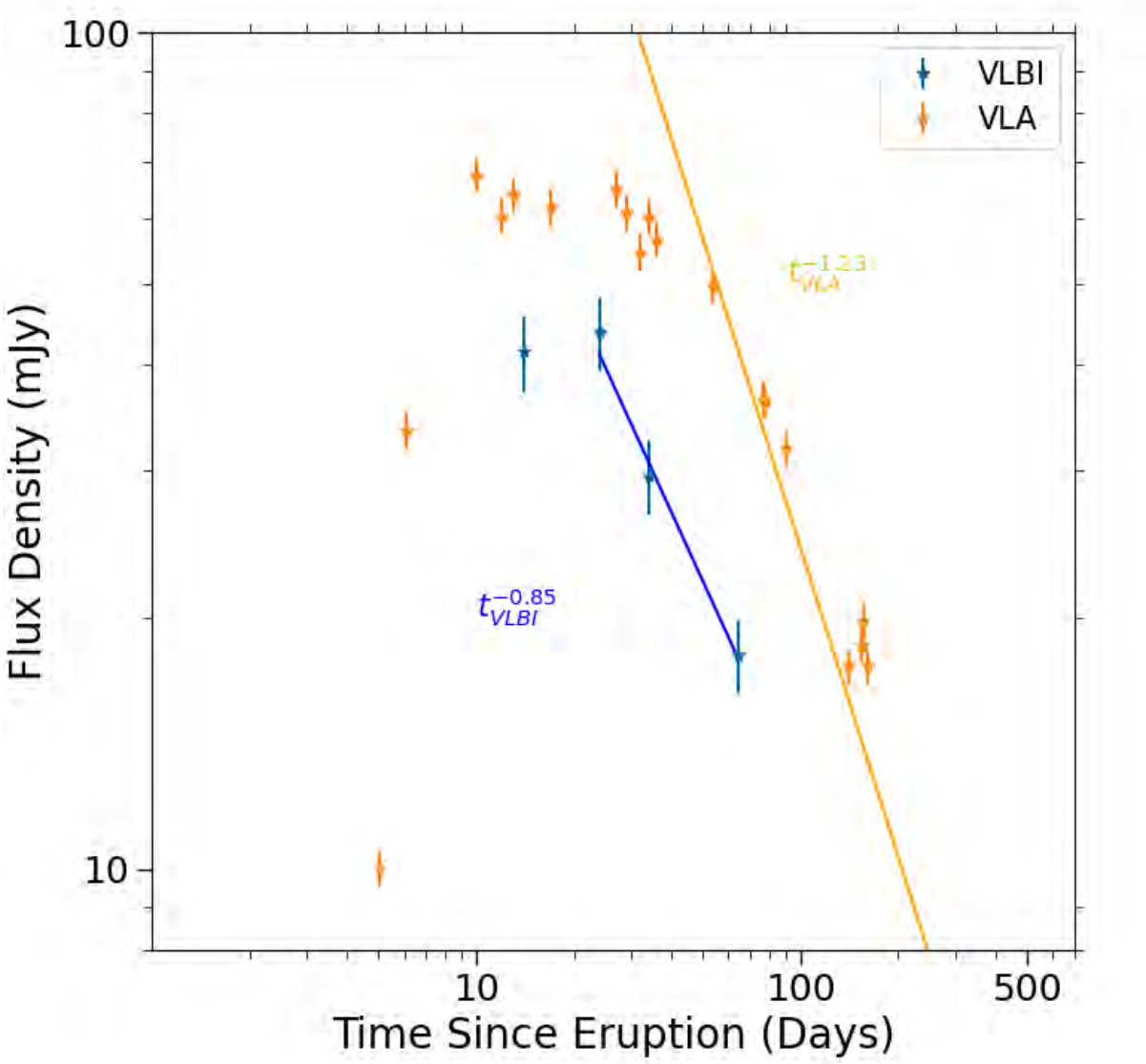

Figure 4.19 VLA and VLBI radio light curve of RS Oph's 2021 eruption in $\sim$ 5 GHz. The gap in flux density between the VLA and VLBI observations is more apparent in 5 GHz than in the 1.5 GHz plot.

VLA flux density. At the 1.5 GHz frequency the VLBI flux density is about 0.56 that of the VLA flux density.

The VLBI light curve declines with a shallower power-law index of -0.85 versus the faster decline of the VLA light curve at -1.23. The power-law index of the VLBI light curve is even shallower at 1.5 GHz with a decline of -0.53 compared to the VLA light curve ($t_{VLA} = -1.34$).

A significant fraction of the radio emission from the 2021 eruption of RS Oph must be coming from thermal emission that it is declining more rapidly than the synchrotron emission. RS Oph imaging has shown three components of the radio emission, a central core and two expanding lobes [238]. The synchrotron emission may be a result of these bi-polar lobes hitting up against CSM.

The VLA spectra include frequencies spanning from 2.6 - 34.9 GHz and required a broken power law to determine the spectral indices, except for on day 65. The spectra are concave on days 17, 25, and 35. The VLBI spectral index only include two frequencies (1.6 and 5 GHz) and so may not give a complete picture of how the spectra is evolving. On day 17 the VLA spectral indices are $\alpha_1 = -0.32$ and $\alpha_2 = 0.15$. Comparing that with the VLBI spectral index on day 15, $\alpha = -0.57$ almost twice as steep as α_1. On day 25, the VLA spectral indices are $\alpha_1 = -0.45$ and $\alpha_2 = 0.30$ while the VLBI spectral index is similar, $\alpha = -0.34$. On day 35 the VLA spectral indices are $\alpha_1 = -0.17$ and $\alpha_2 = 0.60$. The VLBI spectral index is again much steeper than α_1 at $\alpha = -0.43$. On day 65 the VLA spectral index is $\alpha = 0.25$ positive and shallow. However, the VLBI spectral index is $\alpha = -0.63$, again much steeper. These steep VLBI spectral indices are consistent with the VLBI capturing synchrotron emission.

4.5 Multi-wavelength nova properties

The maximum radio flux density and peak V band optical magnitude are plotted against one another Figure 4.20. Peak radio flux densities S_{max} at 5 GHz are listed in Table 4.2 along with time to 5 GHz radio peak t_{max}. S_{max} and t_{max} require the peak of the radio light curve to be captured. For U Sco and V1534 Sco, this was not the case and these values are plotted as upper limits, marked as upside down triangles.

Higher peak V band magnitudes possibly hint to a correlation with higher max radio flux density, though not for all novae. U Sco is a clear outlier with a low radio maximum, 0.12 mJy, but a V peak of about 7.5 mag. V1534 Sco shows opposite behaviour with a radio maximum of 13.3 mJy but a V band max of 11.6 mag. The highest radio and optical peak is measured in RS Oph with a radio peak of 67.6 mJy and an optical peak of about 4.8 mag. In [51] there is a distinct positive correlation between peak radio flux density and peak V-band magnitude for classical novae. This is not evident in Figure 4.20 Radio thermal emission and optical emission are the result of the same mechanisms and would show a stronger correlation, like that seen in [51]. However, radio synchrotron emission is produced through shocks and the lack a correlation, as shown in Figure 4.20, implies that these novae with evolved companions are dominated by synchrotron emission.

The time to peak in the radio is plotted against the time to decrease by two magnitudes in V band in Figure 4.21. About 73% of the novae have short t_2 (less than 10 days) much more than novae with main sequence companions [45]. V723 Cas and V1370 Aql take longer to decline by two magnitudes. V723 Cas also takes the most time to peak in the radio, almost 2000 days. 73% of the novae also take under 100 days to reach radio peak, with V407 Cyg taking 103 days, V723 Cas taking 1697 days, and V1370 Aql taking 142 days. Novae with

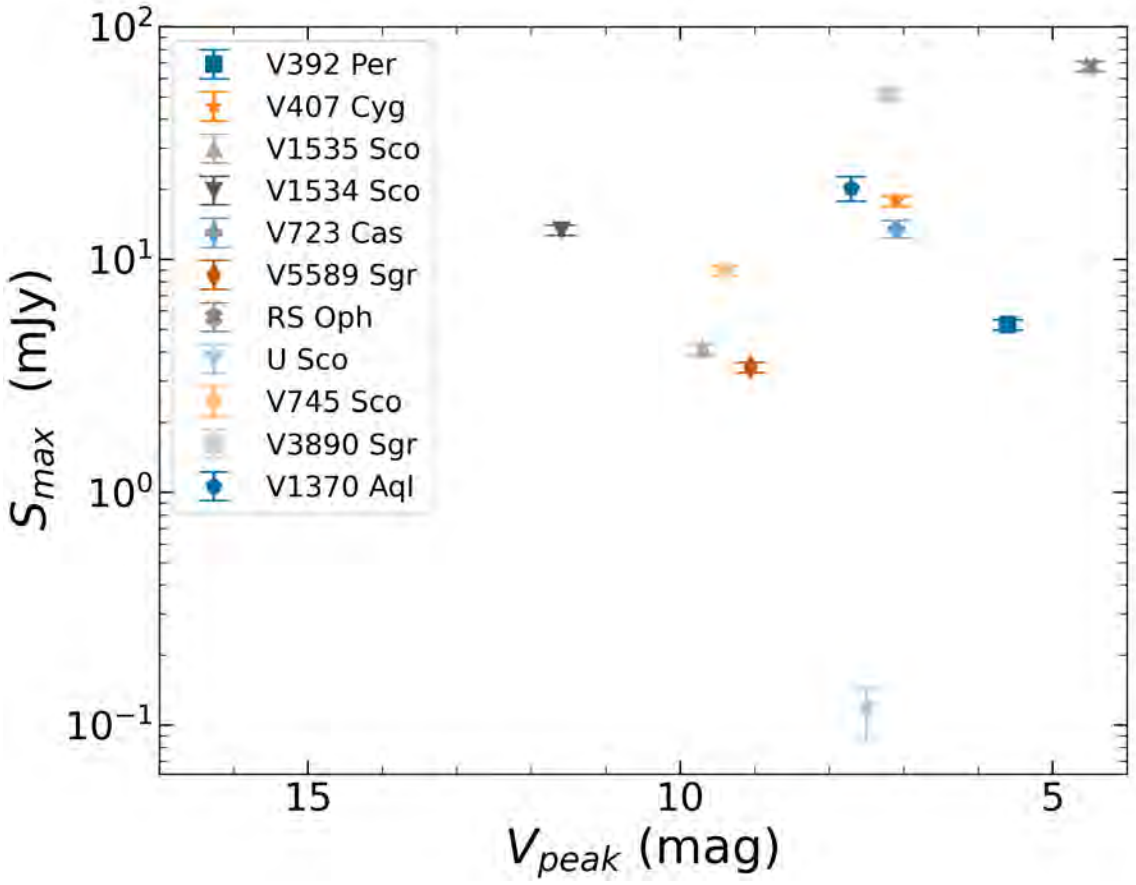

Figure 4.20 Peak radio flux density vs peak optical magnitude (V-band) of all 11 novae. The peak flux density in 5 GHz was used for all novae except for U Sco, where we had to use the 7 GHz band.

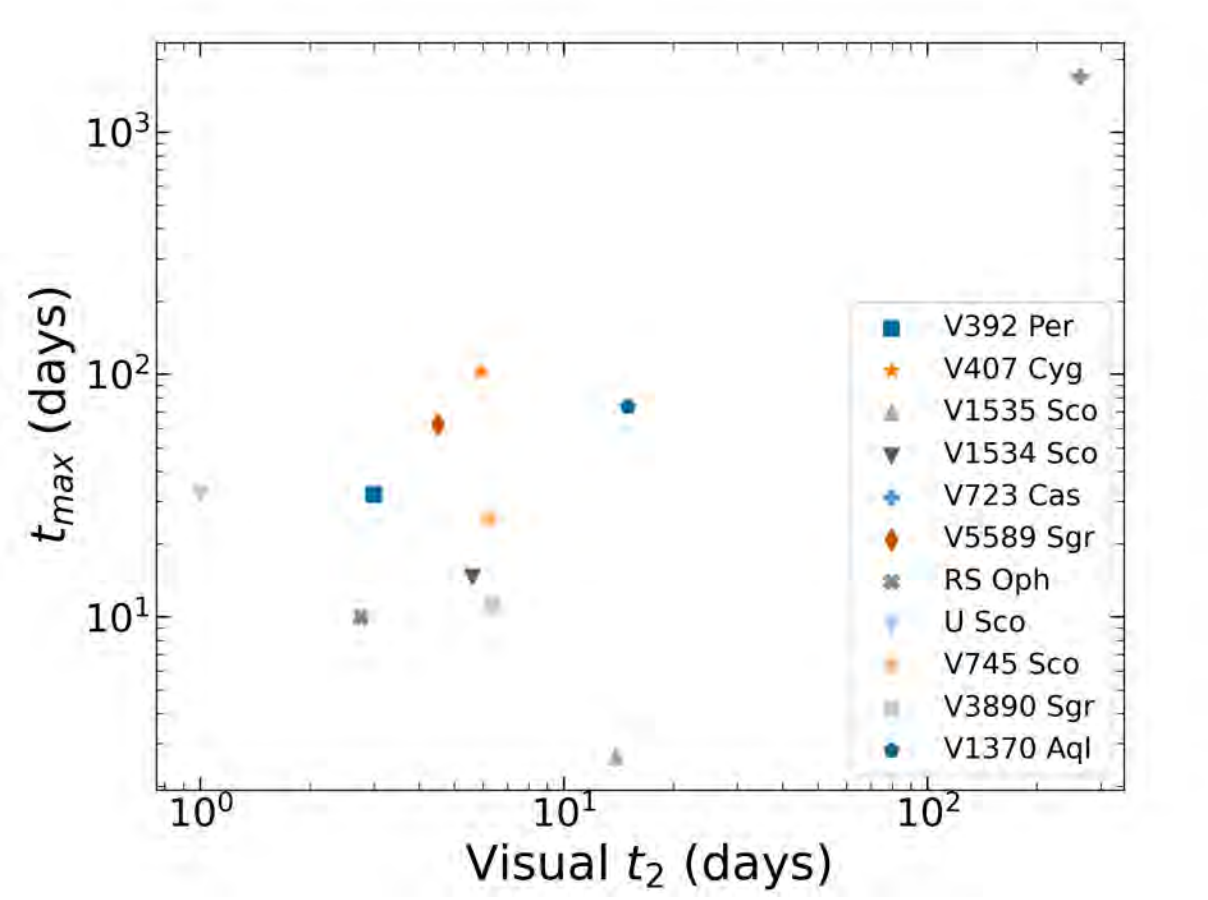

Figure 4.21 A comparison of the time elapsed between the start of eruption and radio peak at 5 GHz and the time for the optical light curve to decline by two magnitudes from peak. The two novae plotted as upside down triangles only have upper limits on peak radio flux density and time to radio peak.

main sequence companions have a greater range in time to radio peak ($10 < t_{max} < 2000$ days) with 26 taking over 100 days to peak[51].

Overall, time to radio peak is increasing with visual t_2 (excluding V1535 Sco). Compared with [51] there is a less noticeable positive correlation between time to radio maximum and optical t_2. This could be due to less novae in our sample or to the fact that the optical emission and thermal emission come from the same mechanisms and the synchrotron emission does not.

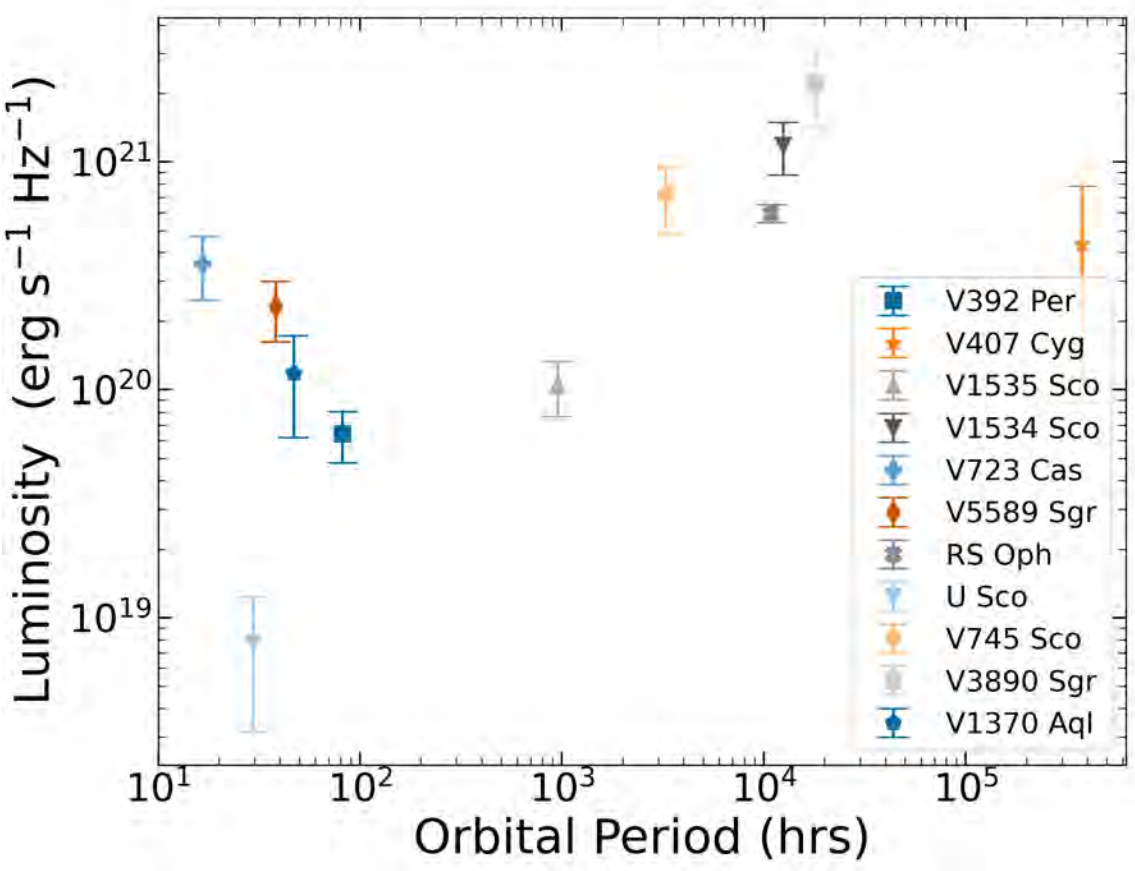

Figure 4.22 Peak radio luminosity for the 5 GHz band plotted against the binary orbital period in hours.

The peak 5 GHz radio luminosity is plotted against orbital period in Figure 4.22. There is a wide range of orbital periods from 16.6 hours – 376, 938 hours, implying donors that span evolutionary state from subgiant to AGB. We might expect the CSM environment of the nova, and the resulting radio emission, to depend on the evolutionary state of the companion star. U Sco is an outlier with a low orbital period and low radio luminosity. The novae with orbital periods ranging from 3×10^3 to $\sim 10^4$ hours have the highest radio luminosities. V407 Cyg has the largest orbital period but a radio luminosity similar to V723 Cas (with the shortest orbital period).

Time to maximum radio flux density is plotted against ejecta velocity (v_2) in Figure 4.23. 82% of the novae have velocities over 3000 km s^{-1}, with only V1370 Aql and V723 Cas having slower velocities. All velocities plotted in Figure 4.23 are v_2 values obtained through HWHM measurements of H-α lines observed after radio peak. These values and their references are listed in Table 4.1. In [51] a lower expansion velocity is correlated to a longer time to radio maximum. In Figure 4.23 we only see this trend in V723 Cas which has the slowest ejecta velocity and the longest time to radio peak. In the range of $3000 - 5500$ km s^{-1}, time to radio maximum increases with expansion velocity with the exception of V1535 Sco. A larger sample size may make a trend more apparent.

4.5.1 Radio vs Gamma-ray Properties

As done in [219] the shape of the γ-ray spectrum was assumed to follow the spectral shape of V906 Car. Novae generally do not vary much in γ-ray spectral shape and this nova was bright with a clear γ-ray spectra.

Figure 4.24 compares peak radio luminosity and γ-ray luminosity. The RG-novae are clustered at high radio luminosity ($> 3 \times 10^{20}$ erg s^{-1}Hz^{-1}) and high γ-ray luminosity ($> 10^{35}$ erg s^{-1}). V1535 Sco lies at the edge of this cluster (radio luminosity 1.0×10^{20} erg s^{-1}Hz^{-1} and γ-ray luminosity 3.2×10^{35} erg s^{-1}). The SG-novae show a larger range of γ-ray luminosities and radio luminosities suggesting a wider range of CSM structures.

Figure 4.25 shows the orbital period in hours plotted against γ-ray luminosity in erg s^{-1}. While some of the SG-novae have high γ-ray luminosity their orbital periods do not exceed 10^3 hours. The RG-novae have higher orbital periods and high γ-ray luminosity, not dipping below 10^{35} erg s^{-1}.

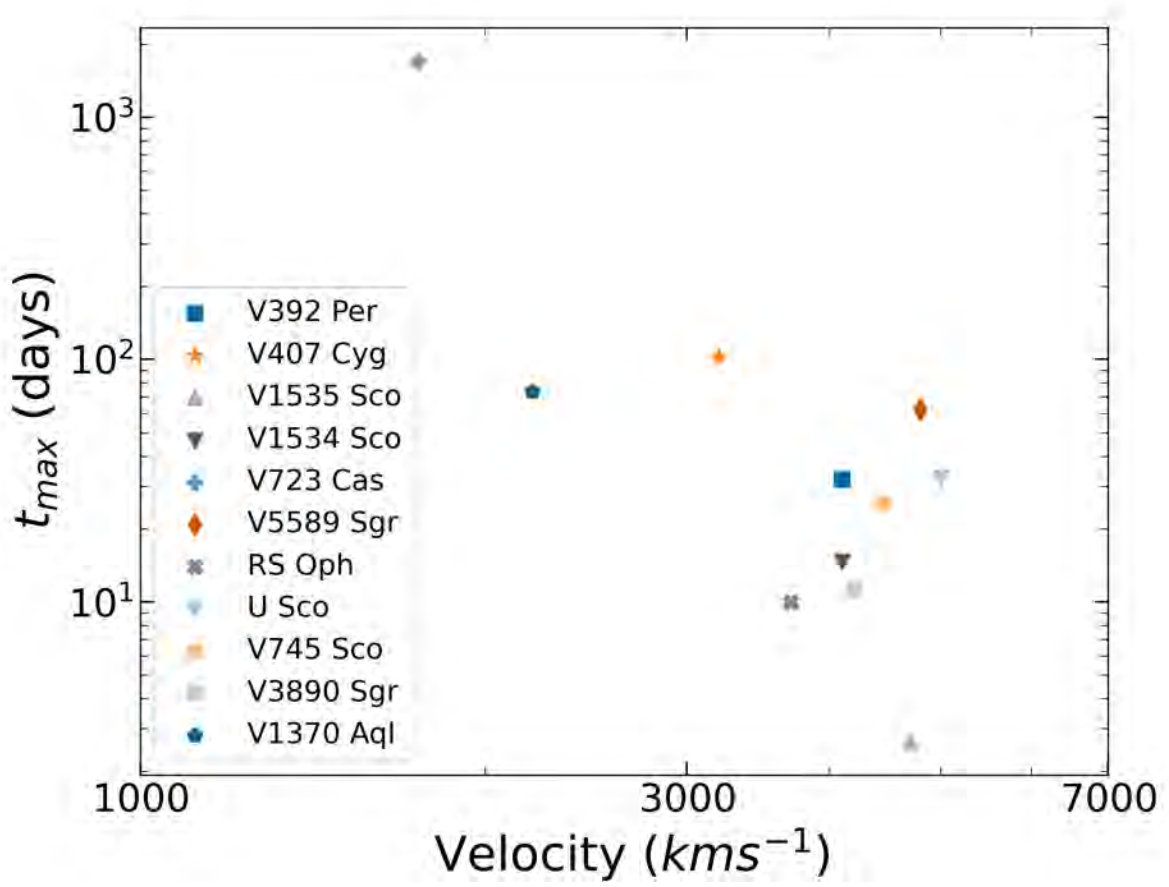

Figure 4.23 Time to peak radio flux density (days) plotted against ejecta velocity (v_2) (km s^{-1}). Of the 11 novae, nine cluster around a velocity ranging between 3500 – 5500 km s^{-1}. The slower novae are V723 Cas and V1370 Aql.

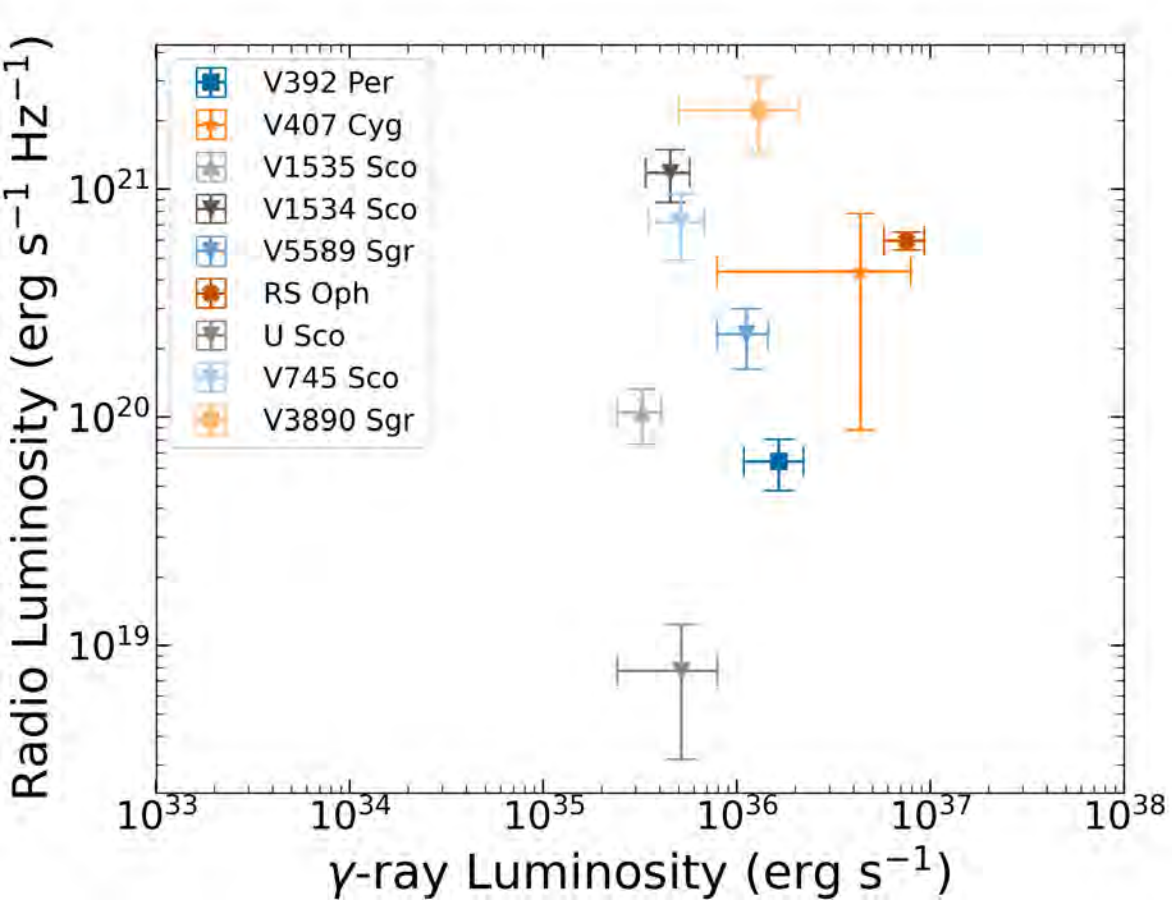

Figure 4.24 Radio and γ-ray luminosities of all novae listed in Table 4.3. The novae plotted here have high γ-ray luminosities ($> 10^{35}$ erg s^{-1}), with the exception of V5589 Sgr. Upper limits are plotted as left facing triangles, error on the γ-ray luminosity is from the error on the distance.

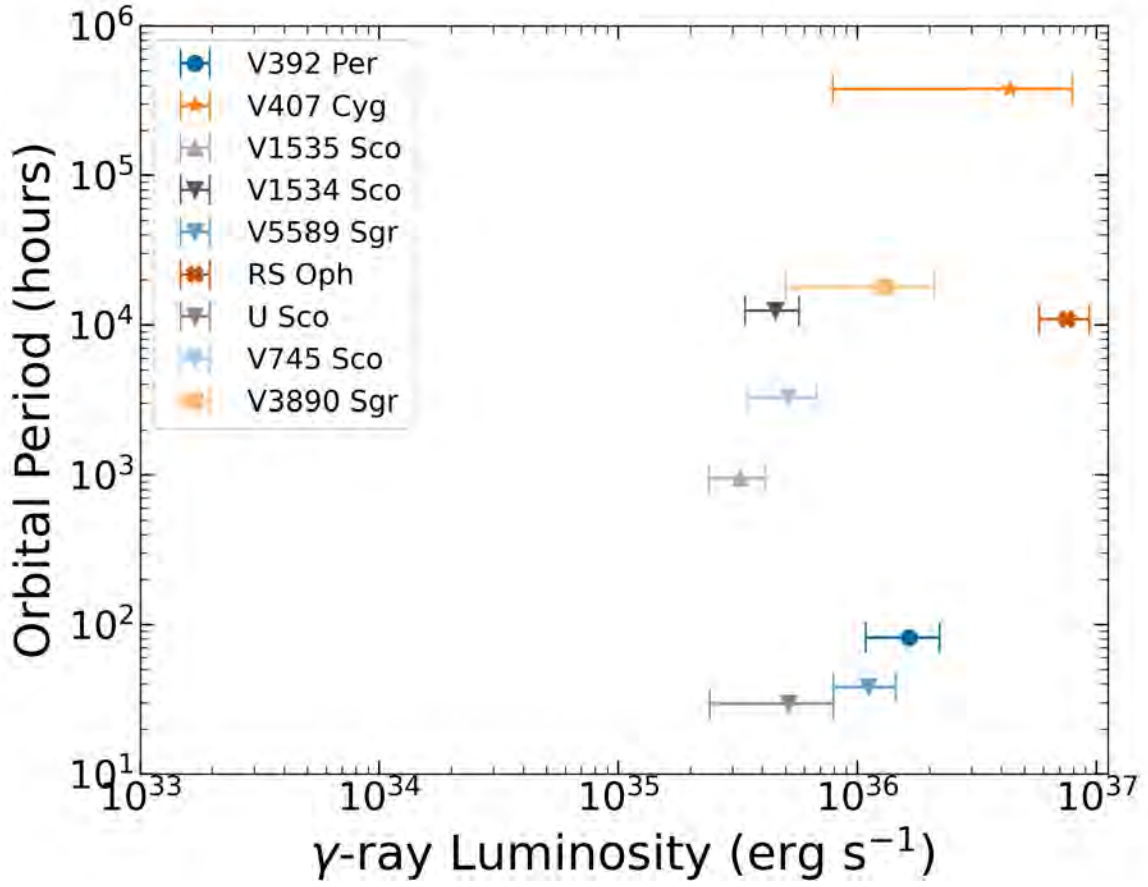

Figure 4.25 Orbital periods and γ-ray luminosities of all novae listed in Table 4.3, upper limits are plotted as upside down triangles. V5589 Sgr is the outlier here with both a low orbital period and a low γ-ray luminosity and given that this is an upper limit its value can be even lower.

4.6 Conclusions

We present multi-frequency radio light curves for 11 novae with evolved companions. The radio data span 40 years and binaries with orbital periods ranging from $P_{orb} = 0.7 - 15,695$ days. The optical properties of the nova eruptions vary with $V_{peak} = 4.8 - 11.6$ mag and $t_2 = 1 - 263$ days . Radio properties are also highly diverse with time to radio peak spanning $t_{max} = 2.7 - 1697.5$ days and peak radio flux density ranging from $3.4 - 67.6$ mJy, excluding upper limits. From this group of novae our key findings are:

- Of the 11 novae studied here 9 exhibit brightness temperatures greater than 5×10^4K indicating 82 % have synchrotron emission significantly higher than 9 % for novae with main sequence companions.

- Comparing radio and optical properties we see for a range of peak V band magnitudes the peak radio flux density does not vary much. This could be due to the radio emission being heavily synchrotron dominated and thus less tied to the optical emission. When comparing time to radio peak and visual t_2 we do see a very slight positive trend with novae that have larger t_2's taking longer to peak in the radio. This trend is more apparent with novae with main sequence companions as seen in [51]

- Comparing radio and γ-ray properties we see a clear distinction between the SG-novae and RG-novae with SG-novae having a wider range of radio and γ-ray luminosities.

- RS Oph shows two radio peaks at higher frequencies peaking on day 6.1 and 54 for 34 GHz. These double peaks are not evident at lower frequencies.

- Comparing consecutive eruptions in the radio, RS Oph shows brighter flux densities in the 2021 eruption compared to the 1985 eruption. The 2021 eruption declines

slower than the 1985 radio decline at lower frequencies ($\sim 1.3 - 5$ GHz) but at higher frequencies (~ 14 GHz) the eruptions are similar. The VLA VLBI analysis shows that the radio emission is a combination of thermal and non thermal emission. RS Oph's brightness temperature remains well above 5×10^4K until after ~ 100 days, this is also reflected in the VLA VLBI light curves.

In the future we will build on this work by calculating estimates for the CSM density and comparing those value to the radio and γ-ray analysis done here. Constraints on CSM density will give new insights into the environment around novae with subgiant companions. This along with a more thorough analysis of the γ-ray emission may further illustrate the structure of the CSM.

Chapter 5. Conclusions

This thesis is aimed at expanding our understanding of novae with evolved companions across wavelengths but with a focus on radio observations. In this work we have conducted a multi-wavelength study of two symbiotic recurrent novae, V745 Sco and V3890 Sgr, as well as a broader study on 11 novae.

In this chapter I summarize our finding and outline future directions.

5.1 V745 Sco

In chapter 2 we investigated the symbiotic recurrent nova V745 Sco in radio wavelengths. The distance to V745 Sco is estimated to be $8.2^{+1.2}_{-1.0}$ kpc constrained by the optical peak, dust extinction and a three dimensional map of the Milky Way in section 2.4. There is an apparent narrowing of the optical emission lines over the course of eruption, which is likely due to a rapid drop in line intensity and signal to noise. Thus Hα line FWZI /2 measurements are used as a lower limit on the shock velocity, with the exception of the first observations where the FWZI/2 is used to measure the maximum ejecta velocity of 4450 km s^{-1} (§2.5.3). V745 Sco is not detected in quiescence by VLASS (upper limits are <0.35 mJy (2018 Feb 11), <0.53 mJy (2020 Nov 6), and <0.38 mJy (2023 Jul 4)) consistent with low density CSM (§2.6.1).

Radio light curves of the 1989 and 2014 eruptions show very similar eruptions, although the 1989 eruption is ∼20% fainter than the 2014 eruption, in contrast with the claim of [137] (§2.6.2). The radio light curve is dominated by synchrotron emission, as shown by the brightness temperature. Using a simple [93] model we determine that a spherically symmetric wind like CSM is not able to explain the early time radio light curves. Instead, the CSM must be described as two components: a dense section that is close to the binary and a less

dense extended wind-like CSM further away from the binary. The close in CSM ($<$ several $\times 10^{14}$ cm) has a density of $\dot{M}_{in} = [5-10] \times 10^{-7}$ M$_\odot$ yr^{-1} and may be an equatorial density enhancement as described in [16] or a red giant wind that has only had 25 years to fill up the environment [73]. The farther away CSM can be described as $\dot{M}_{out} = 9 \times 10^{-10} - 7 \times 10^{-9}$ M$_\odot$ yr^{-1}, assuming $v_w = 10$ km s^{-1}, $\epsilon_e = 0.1$, and $\epsilon_B = 0.01 - 0.1$. The high ϵ values are necessary to explain the luminous late time synchrotron emission and the radio light curves' early peak (§2.7.1). Using only the CSM estimates we cannot rule out V745 Sco as a SN Ia progenitor for a significant fraction of SNe Ia (§2.7.2). As the dense CSM is confined to within 10^{14} cm of the binary it would be feasible to hide this CSM in a SN Ia, and the extended wind is lower density than most constraints on SN Ia CSM.

5.2 V3890 Sgr

In Chapter 3 we present VLBI radio imaging and *Fermi*/LAT GeV γ-ray monitoring of the 2019 eruption of the symbiotic recurrent nova V3890 Sgr. The VLBI imaging ranges from 8–51 after eruption illustrating a bipolar shape with a density enhancement in the orbital plane. The expansion parallax distance is estimated to be 6.8 kpc (in section 3.4.3) using optical spectroscopy to estimate radial velocities. A comparison of the VLBA and VLA observations show that the VLBA is detecting over 80% of the integrated radio flux on days 8-32. The VLBA loses about a third of the integrated flux on day 51, but this flux is captured in the EVN+eMERLIN observation. The flux is seen as a diffuse synchrotron emission halo $\gtrsim 10^{16}$ cm across. This radio halo appears at the same time as the second peak in the VLA radio light curve (Figure 3.3) and the second peak in γ-ray light curve (Figure 3.7).

The $>$100 MeV γ-rays peak at a flux of $(1.9 \pm 1.2) \times 10^{-7}$ phot s^{-1} cm^{-2} ($L_\gamma = 1.3 \times 10^{36}$ erg s^{-1} at 6.8 kpc) around the time of optical maximum. γ-rays are detected from around

optical peak to 23 days after. A second cluster of 2.5σ detections appears around day 60, in line with the second radio peak (§3.5.1). The radio emission and γ-rays are originating from different regions of the shock, as the high γ-ray luminosity requires a dense medium to efficiently produce pions. However, this dense medium would free-free absorb the radio emission. The radio-emitting shock is likely the ejecta colliding with a spherical wind-like component of the CSM, while the γ-rays originate from interaction with an over-density of CSM in the orbital plane (§3.6.3).

Estimates of the CSM density from X-ray observations of the hot shocked gas [11] show the CSM can be described as a spherical wind with $\dot{M}_{\rm w} = 2 \times 10^{-7}$ $\rm M_\odot$ $\rm yr^{-1}$ (assuming $v_{\rm w} = 10$ km $\rm s^{-1}$), with an equatorial density enhancement in the orbital plane. The CSM is considerably denser than what is estimated for other symbiotic recurrent novae (§**??**). The fraction of the post shock pressure in magnetic fields was estimated using the velocity, magnetic field and CSM density estimates. Assuming equipartition with relativistic electrons we find $\epsilon_{\rm B} \approx$ few $\times 10^{-4}$ to few $\times 10^{-3}$ (§**??**). The synchrotron halo is thought to be the result of relativistic leptons escaping the shock and interacting with CSM upstream. (§**??**).

5.3 Radio Study of Novae with Evolved Companions

Chapter 4 is a study of 11 novae with evolved companions ranging from subgiant companions to AGB companions. This chapter focuses on radio wavelengths but also includes optical observations and γ-rays. Of the 11 novae, 9 exhibit brightness temperatures greater than 5×10^4 K signalling synchrotron emission for at least a portion of the radio evolution. U Sco and V723 Cas are the only novae showing purely thermal emission. Comparing the radio and optical properties shows little correlation between time to radio peak and visual t_2 and no correlation between peak radio flux density and peak V band magnitude. This is

likely because the radio emission is, at least in part, non-thermal and not tied to the same mechanism that produces optical emission. The analysis of RS Oph does indeed show two peaks in the radio light curve, although only at higher frequencies. The 1985 and 2021 eruptions show similar radio declines only at higher frequencies and the VLA and VLBI comparison shows that, while RS Oph does display strong synchrotron emission, thermal emission is still an important contributor to the total radio emission.

5.4 Future Work

Future work will build on Chapter 4's characterization of the 11 novae with evolved companions and include estimating CSM densities and performing more in depth γ-ray analysis to further illuminate the structure of the CSM. To further examine the synchrotron emission coming from these novae, we will conduct an analysis on the flat non-thermal spectral indices in novae that show synchrotron emission in the attempt to distinguish a partially absorbed spectrum from a flat power law spectrum. Additionally, we will further investigate the mixed thermal and non thermal radio emission in more of these novae by using constraints from VLBI imaging for V3890 Sgr, V392 Per, V1535 Sco, and V407 Cyg.

The recurrent nova T CrB is predicted to erupt soon. It has been observed to go through a state of heightened activity before entering pre eruption optical dip has been observed in past eruptions as an indicator that the nova eruption will soon occur (for example its 1945 pre eruption dip prior to the 1946 eruption) [291]. The 2023 optical light curve has already significantly faded and if the nova performs on similar timescales as the last eruption this next eruption is imminent. T CrB's next eruption will be an extraordinary opportunity to study a very nearby (only 0.8 kpc away! [42]) nova at all wavelengths.

For V745 Sco we can extend our investigation by utilizing the simulations of [16] to model

a complex CSM with an equatorial density enhancement, like what we expect for V745 Sco, and use this to create the multi-frequency radio light curve. We can then compare this theoretical radio light curve to observation to test our model for V745 Sco's CSM and further decode the nature of the dense close in CSM.

BIBLIOGRAPHY

[1] L. Erdrich. *The Sentence*. HarperCollins, 2021.

[2] O. Yaron et al. "An Extended Grid of Nova Models. II. The Parameter Space of Nova Outbursts". In: *The Astrophysical Journal* 623 (Apr. 2005), pp. 398–410. DOI: 10.1086/428435.

[3] B. E. Schaefer. "Comprehensive Photometric Histories of All Known Galactic Recurrent Novae". In: *The Astrophysical Journal* 187 (Apr. 2010), pp. 275–373. DOI: 10.1088/0067-0049/187/2/275.

[4] A. Pagnotta and B. E. Schaefer. "Identifying and Quantifying Recurrent Novae Masquerading as Classical Novae". In: *The Astrophysical Journal* 788.2, 164 (June 2014), p. 164. DOI: 10.1088/0004-637X/788/2/164.

[5] D. M. Townsley and L. Bildsten. "Theoretical Modeling of the Thermal State of Accreting White Dwarfs Undergoing Classical Nova Cycles". In: *The Astrophysical Journal* 600 (Jan. 2004), pp. 390–403. DOI: 10.1086/379647.

[6] Y. Hillman et al. "Growing White Dwarfs to the Chandrasekhar Limit: The Parameter Space of the Single Degenerate SNIa Channel". In: *The Astrophysical Journal* 819.2, 168 (Mar. 2016), p. 168. DOI: 10.3847/0004-637X/819/2/168.

[7] A. Kawash et al. "The Galactic Nova Rate: Estimates from the ASAS-SN and Gaia Surveys". In: *The Astrophysical Journal* 937.2, 64 (Oct. 2022), p. 64. DOI: 10.3847/1538-4357/ac8d5e.

[8] A. A. Abdo, M. Ackermann, M. Ajello, et al. "Gamma-Ray Emission Concurrent with the Nova in the Symbiotic Binary V407 Cygni". In: *Science* 329 (Aug. 2010), pp. 817–821. DOI: 10.1126/science.1192537.

[9] J. Krautter. "The Super-soft Phase in Novae". In: *RS Ophiuchi (2006) and the Recurrent Nova Phenomenon*. Ed. by A. Evans et al. Vol. 401. Astronomical Society of the Pacific Conference Series. Dec. 2008, p. 139.

[10] N. Gehrels et al. "The Swift Gamma-Ray Burst Mission". In: *The Astrophysical Journal* 611.2 (Aug. 2004), pp. 1005–1020. DOI: 10.1086/422091.

[11] K. L. Page, A. P. Beardmore, and J. P. Osborne. "Neil Gehrels Swift Observatory studies of supersoft novae". In: *Advances in Space Research* 66.5 (Sept. 2020), pp. 1169–1192. DOI: 10.1016/j.asr.2019.08.003.

[12] M. M. Shara et al. "Non-equipartition of Energy, Masses of Nova Ejecta, and Type Ia Supernovae". In: *The Astrophysical Journal* 712.2 (Apr. 2010), pp. L143–L147. DOI: 10.1088/2041-8205/712/2/L143.

[13] R. D. Gehrz. "Infrared studies of classical novae". In: *Classical Novae*. Ed. by M. F. Bode and A. Evans. Cambridge Astrophysics. Cambridge University Press, 2008, pp. 167–193.

[14] A. Chong et al. "Revisiting the classics: on the statistics of dust formation in novae". In: *Monthly Notices of the Royal Astronomical Society* 541.2 (Aug. 2025), pp. 980–1001. DOI: 10.1093/mnras/staf1001.

[15] A. D. Scott et al. "A multiwavelength study of the classical nova V4169 Sagittarii." In: *Astronomy & Astrophysics* 296 (Apr. 1995), p. 439.

[16] S. Orlando, J. J. Drake, and M. Miceli. "Origin of asymmetries in X-ray emission lines from the blast wave of the 2014 outburst of nova V745 Sco". In: *Monthly Notices of the Royal Astronomical Society* 464.4 (Feb. 2017), pp. 5003–5017. DOI: 10.1093/mnras/stw2718.

[17] S. Orlando and J. J. Drake. "Modelling the 2010 blast wave of the symbiotic-like nova V407 Cygni". In: *Monthly Notices of the Royal Astronomical Society* 419.3 (Jan. 2012), pp. 2329–2337. DOI: 10.1111/j.1365-2966.2011.19880.x.

[18] B. D. Metzger et al. "Shocks in nova outflows - I. Thermal emission". In: *Monthly Notices of the Royal Astronomical Society* 442.1 (July 2014), pp. 713–731. DOI: 10.1093/mnras/stu844.

[19] R. Diesing et al. "Evidence for Multiple Shocks from the γ-Ray Emission of RS Ophiuchi". In: *The Astrophysical Journal* 947.2, 70 (Apr. 2023), p. 70. DOI: 10.3847/1538-4357/acc105.

[20] S. Mohamed et al. "3D Models of Symbiotic Binaries". In: *EAS Publications Series*. Vol. 71-72. EAS Publications Series. EDP, Dec. 2015, pp. 81–86. DOI: 10.1051/eas/1571015.

[21] B. D. Metzger et al. "Gamma-ray novae as probes of relativistic particle acceleration at non-relativistic shocks". In: *Monthly Notices of the Royal Astronomical Society* 450.3 (July 2015), pp. 2739–2748. DOI: 10.1093/mnras/stv742.

[22] D. Caprioli and A. Spitkovsky. "Simulations of Ion Acceleration at Non-relativistic Shocks. I. Acceleration Efficiency". In: *The Astrophysical Journal* 783.2, 91 (Mar. 2014), p. 91. DOI: 10.1088/0004-637X/783/2/91.

[23] I. Molina et al. "The symbiotic recurrent nova V745 Sco at radio wavelengths". In: *Monthly Notices of the Royal Astronomical Society* 534.2 (Nov. 2024), pp. 1227–1246. DOI: 10.1093/mnras/stae2093.

[24] L. Chomiuk et al. "A Deep Search for Prompt Radio Emission from Thermonuclear Supernovae with the Very Large Array". In: *The Astrophysical Journal* 821.2, 119 (Apr. 2016), p. 119. DOI: 10.3847/0004-637X/821/2/119.

[25] S. Mohamed, R. Booth, and P. Podsiadlowski. "The Asymmetric Outflow of RS Ophiuchi". In: *Binary Paths to Type Ia Supernovae Explosions*. Ed. by R. Di Stefano, M. Orio, and M. Moe. Vol. 281. IAU Symposium. Jan. 2013, pp. 195–198. DOI: 10.1017/S1743921312014998.

[26] R. A. Booth, S. Mohamed, and P. Podsiadlowski. "Modelling the circumstellar medium in RS Ophiuchi and its link to Type Ia supernovae". In: *Monthly Notices of the Royal Astronomical Society* 457.1 (Mar. 2016), pp. 822–835. DOI: 10.1093/mnras/stw001.

[27] F. Patat et al. "Connecting RS Ophiuchi to [some] type Ia supernovae". In: *Astronomy & Astrophysics* 530, A63 (June 2011), A63. DOI: 10.1051/0004-6361/201116865.

[28] D. Maoz, F. Mannucci, and G. Nelemans. "Observational Clues to the Progenitors of Type Ia Supernovae". In: *Annual Review of Astronomy and Astrophysics* 52 (Aug. 2014), pp. 107–170. DOI: 10.1146/annurev-astro-082812-141031.

[29] Z.-W. Liu, F. K. Röpke, and Z. Han. "Type Ia Supernova Explosions in Binary Systems: A Review". In: *Research in Astronomy and Astrophysics* 23.8, 082001 (Aug. 2023), p. 082001. DOI: 10.1088/1674-4527/acd89e.

[30] J. Whelan and J. Iben Icko. "Binaries and Supernovae of Type I". In: *The Astrophysical Journal* 186 (Dec. 1973), pp. 1007–1014. DOI: 10.1086/152565.

[31] K. J. Shen et al. "Sub-Chandrasekhar-mass White Dwarf Detonations Revisited". In: *The Astrophysical Journal* 854.1, 52 (Feb. 2018), p. 52. DOI: 10.3847/1538-4357/aaa8de.

[32] C. E. Harris et al. "Radio Observations of Six Young Type Ia Supernovae". In: *The Astrophysical Journal* 952.1, 24 (July 2023), p. 24. DOI: 10.3847/1538-4357/acd84f.

[33] T. J. Moriya et al. "Early excess emission in Type Ia supernovae from the interaction between supernova ejecta and their circumstellar wind". In: *Monthly Notices of the Royal Astronomical Society* 522.4 (July 2023), pp. 6035–6042. DOI: 10.1093/mnras/stad1386.

[34] E. C. Kool et al. “A radio-detected type Ia supernova with helium-rich circumstellar material”. In: *Nature* 617.7961 (May 2023), pp. 477–482. DOI: 10.1038/s41586-023-05916-w.

[35] S. Srivastav et al. “Unprecedented Early Flux Excess in the Hybrid 02es-like Type Ia Supernova 2022ywc Indicates Interaction with Circumstellar Material”. In: *The Astrophysical Journal* 956.2, L34 (Nov. 2023), p. L34. DOI: 10.3847/2041-8213/acffaf.

[36] J. Mikołajewska and M. M. Shara. “The Massive CO White Dwarf in the Symbiotic Recurrent Nova RS Ophiuchi”. In: *The Astrophysical Journal* 847.2, 99 (Nov. 2017), p. 99. DOI: 10.3847/1538-4357/aa87b6.

[37] L. Chomiuk, B. D. Metzger, and K. J. Shen. “New Insights into Classical Novae”. In: *Annual Review of Astronomy and Astrophysics* 59 (Sept. 2021), pp. 391–444. DOI: 10.1146/annurev-astro-112420-114502.

[38] C. C. Cheung et al. “Fermi-LAT Gamma-Ray Detections of Classical Novae V1369 Centauri 2013 and V5668 Sagittarii 2015”. In: *The Astrophysical Journal* 826.2, 142 (Aug. 2016), p. 142. DOI: 10.3847/0004-637X/826/2/142.

[39] J. L. Sokoloski et al. “An X-ray-emitting blast wave from the recurrent nova RS Ophiuchi”. In: *Nature* 442.7100 (July 2006), pp. 276–278. DOI: 10.1038/nature04893.

[40] M. Orio et al. “Chandra High Energy Transmission Gratings Spectra of V3890 Sgr”. In: *The Astrophysical Journal* 895.2, 80 (June 2020), p. 80. DOI: 10.3847/1538-4357/ab8c4d.

[41] J. Thwaites and J. Vandenbroucke. “IceCube search for neutrinos from novae”. In: *arXiv e-prints*, arXiv:2307.15372 (July 2023), arXiv:2307.15372. DOI: 10.48550/arXiv.2307.15372.

[42] C. A. L. Bailer-Jones et al. “Estimating Distance from Parallaxes. IV. Distances to 1.33 Billion Stars in Gaia Data Release 2”. In: *The Astrophysical Journal* 156.2, 58 (Aug. 2018), p. 58. DOI: 10.3847/1538-3881/aacb21.

[43] J. Thwaites and J. Vandenbroucke. “Search for GeV-PeV neutrinos from nova T Coronae Borealis with IceCube”. In: *arXiv e-prints*, arXiv:2507.07096 (July 2025), arXiv:2507.07096. DOI: 10.48550/arXiv.2507.07096.

[44] S. C. Williams et al. “On the Progenitors of Local Group Novae. II. The Red Giant Nova Rate of M31”. In: *The Astrophysical Journal* 817.2, 143 (Feb. 2016), p. 143. DOI: 10.3847/0004-637X/817/2/143.

[45] A. Özdönmez et al. "A new catalogue of Galactic novae: investigation of the MMRD relation and spatial distribution". In: *Monthly Notices of the Royal Astronomical Society* 476.3 (May 2018), pp. 4162–4186. DOI: 10.1093/mnras/sty432.

[46] S. L. Shapiro and S. A. Teukolsky. "Relativistic Stellar Dynamics on the Computer. IV. Collapse of a Star Cluster to a Black Hole". In: *The Astrophysical Journal* 307 (Aug. 1986), p. 575. DOI: 10.1086/164445.

[47] D. Koester and G. Chanmugam. "REVIEW: Physics of white dwarf stars". In: *Reports on Progress in Physics* 53.7 (July 1990), pp. 837–915. DOI: 10.1088/0034-4885/53/7/001.

[48] F. Hoyle and W. A. Fowler. "Nucleosynthesis in Supernovae." In: *The Astrophysical Journal* 132 (Nov. 1960), p. 565. DOI: 10.1086/146963.

[49] W. Hillebrandt et al. "Towards an understanding of Type Ia supernovae from a synthesis of theory and observations". In: *Frontiers of Physics* 8.2 (Apr. 2013), pp. 116–143. DOI: 10.1007/s11467-013-0303-2.

[50] M. J. Darnley et al. "On the Progenitors of Galactic Novae". In: *The Astrophysical Journal* 746.1, 61 (Feb. 2012), p. 61. DOI: 10.1088/0004-637X/746/1/61.

[51] L. Chomiuk et al. "Classical Novae at Radio Wavelengths". In: *The Astrophysical Journal* 257.2, 49 (Dec. 2021), p. 49. DOI: 10.3847/1538-4365/ac24ab.

[52] G. J. Schwarz et al. "Swift X-Ray Observations of Classical Novae. II. The Super Soft Source Sample". In: *The Astrophysical Journal* 197.2, 31 (Dec. 2011), p. 31. DOI: 10.1088/0067-0049/197/2/31.

[53] P. Craig et al. "What determines the γ-ray luminosities of classical novae?" In: *Monthly Notices of the Royal Astronomical Society* (Dec. 2025). DOI: 10.1093/mnras/staf2270.

[54] K. L. Page et al. "The 2021 outburst of the recurrent nova RS Ophiuchi observed in X-rays by the Neil Gehrels Swift Observatory: a comparative study". In: *Monthly Notices of the Royal Astronomical Society* 514.2 (Aug. 2022), pp. 1557–1574. DOI: 10.1093/mnras/stac1295.

[55] M. P. Rupen, A. J. Mioduszewski, and J. L. Sokoloski. "An Expanding Shell and Synchrotron Jet in RS Ophiuchi". In: *The Astrophysical Journal* 688.1 (Nov. 2008), pp. 559–567. DOI: 10.1086/525555.

[56] A. Azzollini et al. "Multi-wavelength spectroscopic study of shock-driven phenomena in explosive outbursts in symbiotic-like recurrent novae with an emphasis on RS Ophiuchi". In: *Astronomy & Astrophysics* 674, A139 (June 2023), A139. DOI: 10.1051/0004-6361/202245185.

[57] U. Kolb. "A model for the intrinsic population of cataclysmic variables". In: *Astronomy & Astrophysics* 271 (Apr. 1993), p. 149.

[58] R. C. Smith. "Cataclysmic Variables". In: *arXiv e-prints*, astro-ph/0701654 (Jan. 2007), astro–ph/0701654. DOI: 10.48550/arXiv.astro-ph/0701654.

[59] B. Warner. *Cataclysmic variable stars*. Vol. 28. Cambridge University Press, 1995.

[60] M. M. Shara. "Recent Progress in Understanding the Eruptions of Classical Novae". In: *Publications of the Astronomical Society of the Pacific* 101 (Jan. 1989), p. 5. DOI: 10.1086/132400.

[61] S. J. Kenyon. *The symbiotic stars*. Cambridge University Press, 1986.

[62] E. R. Seaquist and A. R. Taylor. "The Collective Radio Properties of Symbiotic Stars". In: *The Astrophysical Journal* 349 (Jan. 1990), p. 313. DOI: 10.1086/168315.

[63] J. Mikolajewska. "Symbiotic Novae". In: *arXiv e-prints*, arXiv:1011.5657 (Nov. 2010), arXiv:1011.5657. DOI: 10.48550/arXiv.1011.5657.

[64] E. R. Seaquist, A. R. Taylor, and S. Button. "A Radio Survey of Symbiotic Stars". In: *The Astrophysical Journal* 284 (Sept. 1984), p. 202. DOI: 10.1086/162399.

[65] S. Mohamed and P. Podsiadlowski. "Wind Roche-Lobe Overflow: a New Mass-Transfer Mode for Wide Binaries". In: *15th European Workshop on White Dwarfs*. Ed. by R. Napiwotzki and M. R. Burleigh. Vol. 372. Astronomical Society of the Pacific Conference Series. Sept. 2007, p. 397.

[66] A. E. Wright and M. J. Barlow. "The radio and infrared spectrum of early type stars undergoing mass loss." In: *Monthly Notices of the Royal Astronomical Society* 170 (Jan. 1975), pp. 41–51. DOI: 10.1093/mnras/170.1.41.

[67] N. Panagia and M. Felli. "The spectrum of the free-free radiation from extended envelopes." In: *Astronomy & Astrophysics* 39 (Feb. 1975), pp. 1–5.

[68] E. R. Seaquist, M. Krogulec, and A. R. Taylor. "A Highly Sensitive Radio Survey of Symbiotic Stars at 3.6 Centimeters". In: *The Astrophysical Journal* 410 (June 1993), p. 260. DOI: 10.1086/172742.

[69] C. Iliadis. *Nuclear physics of stars*. Wiley-VCH, 2015. DOI: 10.1002/9783527692668.

[70] F. H. Shu. *The physics of astrophysics. Volume II: Gas dynamics.* 1992.

[71] J. K. Truelove and C. F. McKee. "Evolution of Nonradiative Supernova Remnants". In: *The Astrophysical Journal* 120.2 (Feb. 1999), pp. 299–326. DOI: 10.1086/313176.

[72] X. Tang and R. A. Chevalier. "Shock evolution in non-radiative supernova remnants". In: *Monthly Notices of the Royal Astronomical Society* 465.4 (Mar. 2017), pp. 3793–3802. DOI: 10.1093/mnras/stw2978.

[73] L. Delgado and M. Hernanz. "Early multiwavelength analysis of the recurrent nova V745 Sco". In: *Monthly Notices of the Royal Astronomical Society* 490.3 (Dec. 2019), pp. 3691–3704. DOI: 10.1093/mnras/stz2765.

[74] A. R. Taylor et al. "The unusual radio outburst of Nova Vulpeculae 1984 No 2." In: *Astronomy & Astrophysics* 183 (Sept. 1987), pp. 38–46.

[75] A. Vlasov, I. Vurm, and B. D. Metzger. "Shocks in nova outflows - II. Synchrotron radio emission". In: *Monthly Notices of the Royal Astronomical Society* 463.1 (Nov. 2016), pp. 394–412. DOI: 10.1093/mnras/stw1949.

[76] M. Livio et al. "The common envelope phase in the outbursts of classical novae". In: *The Astrophysical Journal* 356 (June 1990), pp. 250–254. DOI: 10.1086/168836.

[77] H. M. Lloyd, T. J. O'Brien, and M. F. Bode. "Shaping of nova remnants by binary motion". In: *Monthly Notices of the Royal Astronomical Society* 284.1 (Jan. 1997), pp. 137–147. DOI: 10.1093/mnras/284.1.137.

[78] R. D. Blandford and J. P. Ostriker. "Particle acceleration by astrophysical shocks." In: *The Astrophysical Journal* 221 (Apr. 1978), pp. L29–L32. DOI: 10.1086/182658.

[79] A. R. Bell. "The acceleration of cosmic rays in shock fronts - I." In: *Monthly Notices of the Royal Astronomical Society* 182 (Jan. 1978), pp. 147–156. DOI: 10.1093/mnras/182.2.147.

[80] A. R. Bell. "Turbulent amplification of magnetic field and diffusive shock acceleration of cosmic rays". In: *Monthly Notices of the Royal Astronomical Society* 353.2 (Sept. 2004), pp. 550–558. DOI: 10.1111/j.1365-2966.2004.08097.x.

[81] K. Nomoto. "Accreting white dwarf models for type I supernovae. I - Presupernova evolution and triggering mechanisms". In: *The Astrophysical Journal* 253 (Feb. 1982), pp. 798–810. DOI: 10.1086/159682.

[82] W. M. Wolf et al. "Hydrogen Burning on Accreting White Dwarfs: Stability, Recurrent Novae, and the Post-nova Supersoft Phase". In: *The Astrophysical Journal* 777, 136 (Nov. 2013), p. 136. DOI: 10.1088/0004-637X/777/2/136.

[83] K. Mukai, M. Orio, and M. Della Valle. "Novae as a Class of Transient X-Ray Sources". In: *The Astrophysical Journal* 677 (Apr. 2008), pp. 1248–1252. DOI: 10.1086/529362.

[84] M. Ackermann et al. "Fermi establishes classical novae as a distinct class of gamma-ray sources". In: *Science* 345.6196 (Aug. 2014), pp. 554–558. DOI: 10.1126/science.1253947.

[85] G. Pojmański. "The All Sky Automated Survey (ASAS-3) System - Its Operation and Preliminary Data". In: *IAU Colloquium 183: Small Telescope Astronomy on Global Scales*. Ed. by B. Paczynski, W.-P. Chen, and C. Lemme. Vol. 246. Astronomical Society of the Pacific Conference Series. Jan. 2001, p. 53.

[86] A. Udalski, M. K. Szymański, and G. Szymański. "OGLE-IV: Fourth Phase of the Optical Gravitational Lensing Experiment". In: *ACTA Astronomica* 65.1 (Mar. 2015), pp. 1–38. DOI: 10.48550/arXiv.1504.05966.

[87] P. Mróz et al. "OGLE Atlas of Classical Novae. I. Galactic Bulge Objects". In: *The Astrophysical Journal* 219.2, 26 (Aug. 2015), p. 26. DOI: 10.1088/0067-0049/219/2/26.

[88] K. Sokolovsky, S. Korotkiy, and A. Lebedev. "The New Milky Way: A Wide-Field Survey of Optical Transients near the Galactic plane". In: *Stellar Novae: Past and Future Decades*. Ed. by P. A. Woudt and V. A. R. M. Ribeiro. Vol. 490. Astronomical Society of the Pacific Conference Series. Dec. 2014, p. 395. DOI: 10.48550/arXiv.1303.3268.

[89] B. Shappee et al. "All Sky Automated Survey for SuperNovae (ASAS-SN or "Assassin")". In: *American Astronomical Society Meeting Abstracts #223*. Vol. 223. American Astronomical Society Meeting Abstracts. Jan. 2014, 236.03, p. 236.03.

[90] C. S. Kochanek et al. "The All-Sky Automated Survey for Supernovae (ASAS-SN) Light Curve Server v1.0". In: *Publications of the Astronomical Society of the Pacific* 129.980 (Oct. 2017), p. 104502. DOI: 10.1088/1538-3873/aa80d9.

[91] B. F. Burke and F. Graham-Smith. *An Introduction to Radio Astronomy*. Cambridge University Press, 2014.

[92] T. Nelson et al. "The 2011 Outburst of Recurrent Nova T Pyx: Radio Observations Reveal the Ejecta Mass and Hint at Complex Mass Loss". In: *The Astrophysical Journal* 785, 78 (Apr. 2014), p. 78. DOI: 10.1088/0004-637X/785/1/78.

[93] R. A. Chevalier. "The radio and X-ray emission from type II supernovae." In: *The Astrophysical Journal* 259 (Aug. 1982), pp. 302–310. DOI: 10.1086/160167.

[94] J. D. Linford et al. "The Peculiar Multiwavelength Evolution Of V1535 Sco". In: *The Astrophysical Journal* 842.2, 73 (June 2017), p. 73. DOI: 10.3847/1538-4357/aa7512.

[95] M. M. Nyamai et al. "Synchrotron emission from double-peaked radio light curves of the symbiotic recurrent nova V3890 Sagitarii". In: *Monthly Notices of the Royal Astronomical Society* 523.2 (Aug. 2023), pp. 1661–1675. DOI: 10.1093/mnras/stad1534.

[96] A. R. Taylor et al. "Radio images of the expanding ejecta of nova QU Vulpeculae 1984". In: *Nature* 335 (Sept. 1988), pp. 235–238. DOI: 10.1038/335235a0.

[97] L. Chomiuk et al. "Binary orbits as the driver of γ-ray emission and mass ejection in classical novae". In: *Nature* 514 (Oct. 2014), pp. 339–342. DOI: 10.1038/nature13773.

[98] J. S. Gallagher and S. Starrfield. "Theory and observations of classical novae." In: *Annual Review of Astronomy and Astrophysics* 16 (Jan. 1978), pp. 171–214. DOI: 10.1146/annurev.aa.16.090178.001131.

[99] M. F. Bode and A. Evans. *Classical Novae*. Cambridge: Cambridge University Press, Apr. 2008. DOI: 10.1017/CBO9780511536168.

[100] S. Starrfield, C. Iliadis, and W. R. Hix. "The Thermonuclear Runaway and the Classical Nova Outburst". In: *Publications of the Astronomical Society of the Pacific* 128.963 (May 2016), p. 051001. DOI: 10.1088/1538-3873/128/963/051001.

[101] J. Casanova et al. "Kelvin-Helmholtz instabilities as the source of inhomogeneous mixing in nova explosions". In: *Nature* 478.7370 (Oct. 2011), pp. 490–492. DOI: 10.1038/nature10520.

[102] M. M. Shara et al. "The Masses and Accretion Rates of White Dwarfs in Classical and Recurrent Novae". In: *The Astrophysical Journal* 860.2, 110 (June 2018), p. 110. DOI: 10.3847/1538-4357/aabfbd.

[103] K. V. Sokolovsky et al. "X-ray spectroscopy of the γ-ray brightest nova V906 Car (ASASSN-18fv)". In: *Monthly Notices of the Royal Astronomical Society* 497.3 (Sept. 2020), pp. 2569–2585. DOI: 10.1093/mnras/staa2104.

[104] M. J. Darnley et al. "M31N 2008-12a - The Remarkable Recurrent Nova in M31: Panchromatic Observations of the 2015 Eruption." In: *The Astrophysical Journal* 833.2, 149 (Dec. 2016), p. 149. DOI: 10.3847/1538-4357/833/2/149.

[105] H.-L. Chen et al. "Modelling nova populations in galaxies". In: *Monthly Notices of the Royal Astronomical Society* 458.3 (May 2016), pp. 2916–2927. DOI: 10.1093/mnras/stw458.

[106] A. J. Kemp et al. "Population synthesis of accreting white dwarfs: rates and evolutionary pathways of H and He novae". In: *Monthly Notices of the Royal Astronomical Society* 504.4 (July 2021), pp. 6117–6143. DOI: 10.1093/mnras/stab1160.

[107] R. F. Webbink. "Double white dwarfs as progenitors of R Coronae Borealis stars and type I supernovae." In: *The Astrophysical Journal* 277 (Feb. 1984), pp. 355–360. DOI: 10.1086/161701.

[108] R. D. Gehrz et al. "Nucleosynthesis in Classical Novae and Its Contribution to the Interstellar Medium". In: *Publications of the Astronomical Society of the Pacific* 110 (Jan. 1998), pp. 3–26. DOI: 10.1086/316107.

[109] K. L. Page et al. "Swift detection of the super-swift switch-on of the super-soft phase in nova V745 Sco (2014)". In: *Monthly Notices of the Royal Astronomical Society* 454.3 (Dec. 2015), pp. 3108–3120. DOI: 10.1093/mnras/stv2144.

[110] J. P. Osborne, K. L. Page, A. P. Beardmore, et al. "The Supersoft X-ray Phase of Nova RS Ophiuchi 2006". In: *The Astrophysical Journal* 727, 124 (Feb. 2011), p. 124. DOI: 10.1088/0004-637X/727/2/124.

[111] J. Gutierrez et al. "The Final Evolution of ONeMg Electron-Degenerate Cores". In: *The Astrophysical Journal* 459 (Mar. 1996), p. 701. DOI: 10.1086/176934.

[112] B. Wang. "The single-degenerate model for the progenitors of accretion-induced collapse events". In: *Monthly Notices of the Royal Astronomical Society* 481.1 (Nov. 2018), pp. 439–446. DOI: 10.1093/mnras/sty2278.

[113] A. J. Ruiter et al. "On the formation of neutron stars via accretion-induced collapse in binaries". In: *Monthly Notices of the Royal Astronomical Society* 484.1 (Mar. 2019), pp. 698–711. DOI: 10.1093/mnras/stz001.

[114] R. D. Gehrz and N. J. Woolf. "Mass Loss from M Stars". In: *The Astrophysical Journal* 165 (May 1971), p. 285. DOI: 10.1086/150897.

[115] R. P. Kudritzki and D. Reimers. "On the absolute scale of mass-loss in red giants. II. Circumstellar absorption lines in the spectrum of alpha Sco B and mass-loss of alpha Sco A." In: *Astronomy & Astrophysics* 70 (Nov. 1978), pp. 227–239.

[116] W. M. Wood-Vasey and J. L. Sokoloski. "Novae as a Mechanism for Producing Cavities around the Progenitors of SN 2002ic and Other Type Ia Supernovae". In: *The Astrophysical Journal* 645.1 (July 2006), pp. L53–L56. DOI: 10.1086/506179.

[117] M. J. Darnley et al. "A recurrent nova super-remnant in the Andromeda galaxy". In: *Nature* 565.7740 (Jan. 2019), pp. 460–463. DOI: 10.1038/s41586-018-0825-4.

[118] M. M. Shara et al. "Introducing the Condor Array Telescope - IV. A possible nova super-remnant surrounding the putative recurrent nova KT Eridani". In: *Monthly Notices of the Royal Astronomical Society* 529.1 (Mar. 2024), pp. 224–235. DOI: 10.1093/mnras/stad3612.

[119] N. Panagia et al. "A Search for Radio Emission from Type Ia Supernovae". In: *The Astrophysical Journal* 646.1 (July 2006), pp. 369–377. DOI: 10.1086/504710.

[120] P. Lundqvist et al. "The Deepest Radio Observations of Nearby SNe Ia: Constraining Progenitor Types and Optimizing Future Surveys". In: *The Astrophysical Journal* 890.2, 159 (Feb. 2020), p. 159. DOI: 10.3847/1538-4357/ab6dc6.

[121] B. R. Russell and S. Immler. "Swift X-Ray Upper Limits on Type Ia Supernova Environments". In: *The Astrophysical Journal* 748.2, L29 (Apr. 2012), p. L29. DOI: 10.1088/2041-8205/748/2/L29.

[122] D. J. Sand et al. "Circumstellar Medium Constraints on the Environment of Two Nearby Type Ia Supernovae: SN 2017cbv and SN 2020nlb". In: *The Astrophysical Journal* 922.1, 21 (Nov. 2021), p. 21. DOI: 10.3847/1538-4357/ac20da.

[123] F. Patat et al. "Detection of Circumstellar Material in a Normal Type Ia Supernova". In: *Science* 317.5840 (Aug. 2007), p. 924. DOI: 10.1126/science.1143005.

[124] K. Maguire et al. "A statistical analysis of circumstellar material in Type Ia supernovae". In: *Monthly Notices of the Royal Astronomical Society* 436.1 (Nov. 2013), pp. 222–240. DOI: 10.1093/mnras/stt1586.

[125] L. Plaut. "Estimates of 140 variable stars on Franklin-Adams plates centred at l=325^o, b=-2^o, taken by the late Dr. van Gent". In: *Annalen van de Sterrewacht te Leiden* 21 (Jan. 1958), pp. 217–252.

[126] W. Liller. "V745 Scorpii". In: *International Astronomical Union Circular Central Bureau for Astronomical Telegrams* 4820 (July 1989), p. 1.

[127] E. O. Waagen. "Outburst of the recurrent nova V745 Sco". In: *AAVSO Alert Notice* 496 (Feb. 2014), p. 1.

[128] H. W. Duerbeck. "V745 Sco - a new member of the elusive group of recurrent novae." In: *The Messenger* 58 (Dec. 1989), pp. 34–35.

[129] T. E. Harrison, J. J. Johnson, and J. Spyromilio. "Infrared Observations of the Recurrent Novae V745 SCO and V3890 SGR". In: *The Astrophysical Journal* 105 (Jan. 1993), p. 320. DOI: 10.1086/116429.

[130] P. Mróz et al. "Recurrent and symbiotic novae in data from the Optical Gravitational Lensing Experiment". In: *Monthly Notices of the Royal Astronomical Society* 443.1 (Sept. 2014), pp. 784–790. DOI: 10.1093/mnras/stu1181.

[131] A. Udalski. "The Optical Gravitational Lensing Experiment. Real Time Data Analysis Systems in the OGLE-III Survey". In: *ACTA Astronomica* 53 (Dec. 2003), pp. 291–305. DOI: 10.48550/arXiv.astro-ph/0401123.

[132] B. K. Kloppenborg. *Observations from the AAVSO International Database, https://www.aavso.org*. 2023.

[133] K. Sekiguchi et al. "The 1989 outburst of the recurrent nova V745 Sco." In: *Monthly Notices of the Royal Astronomical Society* 246 (Sept. 1990), pp. 78–83.

[134] M. Orio et al. "A NuSTAR observation of the fast symbiotic nova V745 Sco in outburst." In: *Monthly Notices of the Royal Astronomical Society* 448 (Mar. 2015), pp. L35–L39. DOI: 10.1093/mnrasl/slu195.

[135] J. J. Drake et al. "Collimation and Asymmetry of the Hot Blast Wave from the Recurrent Nova V745 Sco". In: *The Astrophysical Journal* 825.2, 95 (July 2016), p. 95. DOI: 10.3847/0004-637X/825/2/95.

[136] D. P. K. Banerjee et al. "Near-IR Studies of Recurrent Nova V745 Scorpii during its 2014 Outburst". In: *The Astrophysical Journal* 785.1, L11 (Apr. 2014), p. L11. DOI: 10.1088/2041-8205/785/1/L11.

[137] N. G. Kantharia et al. "Insights into the evolution of symbiotic recurrent novae from radio synchrotron emission: V745 Scorpii and RS Ophiuchi". In: *Monthly Notices of the Royal Astronomical Society* 456 (Feb. 2016), pp. L49–L53. DOI: 10.1093/mnrasl/slv154.

[138] A. Franckowiak et al. "Search for gamma-ray emission from Galactic novae with the Fermi -LAT". In: *Astronomy & Astrophysics* 609, A120 (Feb. 2018), A120. DOI: 10.1051/0004-6361/201731516.

[139] F. M. Walter et al. "The Stony Brook/SMARTS Atlas of (mostly) Southern Novae". In: *Publications of the Astronomical Society of the Pacific* 124 (Oct. 2012), pp. 1057–1072. DOI: 10.1086/668404.

[140] E. W. Greisen. "AIPS, the VLA, and the VLBA". In: *Information Handling in Astronomy - Historical Vistas*. Ed. by A. Heck. Vol. 285. Springer, Dordrecht, 2003, p. 109. DOI: 10.1007/0-306-48080-8_7.

[141] J. P. McMullin et al. "CASA Architecture and Applications". In: *Astronomical Data Analysis Software and Systems XVI*. Ed. by R. A. Shaw, F. Hill, and D. J. Bell. Vol. 376. Astronomical Society of the Pacific Conference Series. Oct. 2007, p. 127.

[142] M. C. Shepherd. "Difmap: an Interactive Program for Synthesis Imaging". In: *Astronomical Data Analysis Software and Systems VI*. Ed. by G. Hunt and H. Payne. Vol. 125. Astronomical Society of the Pacific Conference Series. Jan. 1997, p. 77.

[143] B. E. Schaefer. "Orbital Periods for Three Recurrent Novae". In: *The Astrophysical Journal* 697.1 (May 2009), pp. 721–729. DOI: 10.1088/0004-637X/697/1/721.

[144] S. D. Friedman et al. "Studies of Diffuse Interstellar Bands V. Pairwise Correlations of Eight Strong DIBs and Neutral Hydrogen, Molecular Hydrogen, and Color Excess". In: *The Astrophysical Journal* 727.1, 33 (Jan. 2011), p. 33. DOI: 10.1088/0004-637X/727/1/33.

[145] E. F. Schlafly and D. P. Finkbeiner. "Measuring Reddening with Sloan Digital Sky Survey Stellar Spectra and Recalibrating SFD". In: *The Astrophysical Journal* 737.2, 103 (Aug. 2011), p. 103. DOI: 10.1088/0004-637X/737/2/103.

[146] A. Bahramian et al. "Limits on thermal variations in a dozen quiescent neutron stars over a decade". In: *Monthly Notices of the Royal Astronomical Society* 452.4 (Oct. 2015), pp. 3475–3488. DOI: 10.1093/mnras/stv1585.

[147] B. .-. Chen et al. "Three-dimensional interstellar dust reddening maps of the Galactic plane". In: *Monthly Notices of the Royal Astronomical Society* 483.4 (Mar. 2019), pp. 4277–4289. DOI: 10.1093/mnras/sty3341.

[148] S. Wang and X. Chen. "The Optical to Mid-infrared Extinction Law Based on the APOGEE, Gaia DR2, Pan-STARRS1, SDSS, APASS, 2MASS, and WISE Surveys". In: *The Astrophysical Journal* 877.2, 116 (June 2019), p. 116. DOI: 10.3847/1538-4357/ab1c61.

[149] L. Li et al. "Three-dimensional Structure of the Milky Way Dust: Modeling of LAMOST Data". In: *The Astrophysical Journal* 858.2, 75 (May 2018), p. 75. DOI: 10.3847/1538-4357/aabaef.

[150] A. Kawash et al. "Galactic Extinction: How Many Novae Does It Hide and How Does It Affect the Galactic Nova Rate?" In: *The Astrophysical Journal* 922.1, 25 (Nov. 2021), p. 25. DOI: 10.3847/1538-4357/ac1f1a.

[151] A. C. Robin et al. "A synthetic view on structure and evolution of the Milky Way". In: *Astronomy & Astrophysics* 409 (Oct. 2003), pp. 523–540. DOI: 10.1051/0004-6361:20031117.

[152] J. Bovy et al. "On Galactic Density Modeling in the Presence of Dust Extinction". In: *The Astrophysical Journal* 818.2, 130 (Feb. 2016), p. 130. DOI: 10.3847/0004-637X/818/2/130.

[153] G. M. Green et al. "A 3D Dust Map Based on Gaia, Pan-STARRS 1, and 2MASS". In: *The Astrophysical Journal* 887.1, 93 (Dec. 2019), p. 93. DOI: 10.3847/1538-4357/ab5362.

[154] D. J. Marshall et al. "Modelling the Galactic interstellar extinction distribution in three dimensions". In: *Astronomy & Astrophysics* 453.2 (July 2006), pp. 635–651. DOI: 10.1051/0004-6361:20053842.

[155] R. Drimmel, A. Cabrera-Lavers, and M. López-Corredoira. "A three-dimensional Galactic extinction model". In: *Astronomy & Astrophysics* 409 (Oct. 2003), pp. 205–215. DOI: 10.1051/0004-6361:20031070.

[156] A. W. Shafter. "The Galactic Nova Rate Revisited". In: *The Astrophysical Journal* 834.2, 196 (Jan. 2017), p. 196. DOI: 10.3847/1538-4357/834/2/196.

[157] E. Aydi et al. "Revisiting the classics: on the evolutionary origin of the 'Fe II' and 'He/N' spectral classes of novae". In: *Monthly Notices of the Royal Astronomical Society* 527.3 (Jan. 2024), pp. 9303–9321. DOI: 10.1093/mnras/stad3342.

[158] U. Munari et al. "Properties, evolution and morpho-kinematical modelling of the very fast nova V2672 Oph (Nova Oph 2009), a clone of U Sco". In: *Monthly Notices of the Royal Astronomical Society* 410.1 (Jan. 2011), pp. 525–534. DOI: 10.1111/j.1365-2966.2010.17462.x.

[159] R. K. Zamanov et al. "Hα spectroscopy of the recurrent nova RS Oph during the 2021 outburst". In: *Bulgarian Astronomical Journal* 37 (July 2022), p. 24. DOI: 10.48550/arXiv.2109.11306.

[160] E. Aydi et al. "Early Spectral Evolution of Classical Novae: Consistent Evidence for Multiple Distinct Outflows". In: *The Astrophysical Journal* 905.1, 62 (Dec. 2020), p. 62. DOI: 10.3847/1538-4357/abc3bb.

[161] V. Tatischeff and M. Hernanz. "Evidence for Nonlinear Diffusive Shock Acceleration of Cosmic Rays in the 2006 Outburst of the Recurrent Nova RS Ophiuchi". In: *The Astrophysical Journal* 663.2 (July 2007), pp. L101–L104. DOI: 10.1086/520049.

[162] U. Munari and D. P. K. Banerjee. "Infrared spectroscopy of the remnant of Nova Sco 2014: a symbiotic star with too little circumstellar matter to decelerate the ejecta". In: *Monthly Notices of the Royal Astronomical Society* 475.1 (Mar. 2018), pp. 508–513. DOI: 10.1093/mnras/stx3192.

[163] D. L. DePoy et al. "A Novel Double Imaging Camera (ANDICAM)". In: *Instrument Design and Performance for Optical/Infrared Ground-based Telescopes*. Ed. by M. Iye and A. F. M. Moorwood. Vol. 4841. Society of Photo-Optical Instrumentation Engineers (SPIE) Conference Series. Mar. 2003, pp. 827–838. DOI: 10.1117/12.459907.

[164] S. Mohamed and P. Podsiadlowski. "Mass Transfer in Mira-type Binaries". In: *Baltic Astronomy* 21 (Jan. 2012), pp. 88–96. DOI: 10.1515/astro-2017-0362.

[165] D. Reimers. "Observational evidence for mass-loss from K giants, G and K supergiants." In: *Astronomy & Astrophysics* 57 (May 1977), pp. 395–400.

[166] R. M. Hjellming et al. "Radio emission from nova shells". In: *The Astrophysical Journal* 84 (Oct. 1979), pp. 1619–1631. DOI: 10.1086/112585.

[167] E. R. Seaquist and M. F. Bode. In: *Classical Novae, 2nd Edition. Cambridge Astrophysics Series, No. 43, Cambridge: Cambridge University Press*. Ed. by M. F. Bode & A. Evans. 2008, p. 141.

[168] T. Finzell et al. "A Detailed Observational Analysis of V1324 Sco, the Most Gamma-Ray-luminous Classical Nova to Date". In: *The Astrophysical Journal* 852.2, 108 (Jan. 2018), p. 108. DOI: 10.3847/1538-4357/aaa12a.

[169] S. P. S. Eyres et al. "Double radio peak and non-thermal collimated ejecta in RS Ophiuchi following the 2006 outburst". In: *Monthly Notices of the Royal Astronomical Society* 395.3 (May 2009), pp. 1533–1540. DOI: 10.1111/j.1365-2966.2009.14633.x.

[170] J. H. S. Weston et al. "Non-thermal radio emission from colliding flows in classical nova V1723 Aql". In: *Monthly Notices of the Royal Astronomical Society* 457 (Mar. 2016), pp. 887–901. DOI: 10.1093/mnras/stv3019.

[171] K. V. Sokolovsky et al. "The multiwavelength view of shocks in the fastest nova V1674 Her". In: *Monthly Notices of the Royal Astronomical Society* 521.4 (June 2023), pp. 5453–5472. DOI: 10.1093/mnras/stad887.

[172] K. W. Weiler et al. "Radio Emission from Supernovae and Gamma-Ray Bursters". In: *Annual Review of Astronomy and Astrophysics* 40 (Jan. 2002), pp. 387–438. DOI: 10.1146/annurev.astro.40.060401.093744.

[173] A. J. Nayana et al. "Shock-driven synchrotron radio emission from the 2021 outburst of RS Ophiuchi". In: *Monthly Notices of the Royal Astronomical Society* 528.4 (Mar. 2024), pp. 5528–5536. DOI: 10.1093/mnras/stae201.

[174] T. Cunningham, W. M. Wolf, and L. Bildsten. "Photoionization Heating of Nova Ejecta by the Post-outburst Supersoft Source". In: *The Astrophysical Journal* 803.2, 76 (Apr. 2015), p. 76. DOI: 10.1088/0004-637X/803/2/76.

[175] J. H. S. Weston et al. "Shock-powered radio emission from V5589 Sagittarii (Nova Sgr 2012 #1)". In: *Monthly Notices of the Royal Astronomical Society* 460 (Aug. 2016), pp. 2687–2697. DOI: 10.1093/mnras/stw1161.

[176] R. D. Blandford and A. Königl. "Relativistic jets as compact radio sources." In: *The Astrophysical Journal* 232 (Aug. 1979), pp. 34–48. DOI: 10.1086/157262.

[177] V. L. Ginzburg and S. I. Syrovatskii. "Cosmic Magnetobremsstrahlung (synchrotron Radiation)". In: *Annual Review of Astronomy and Astrophysics* 3 (Jan. 1965), p. 297. DOI: 10.1146/annurev.aa.03.090165.001501.

[178] G. B. Rybicki and A. P. Lightman. *Radiative Processes in Astrophysics*. 1979.

[179] J. M. Pittard et al. "Radio emission models of colliding-wind binary systems. Inclusion of IC cooling". In: *Astronomy & Astrophysics* 446.3 (Feb. 2006), pp. 1001–1019. DOI: 10.1051/0004-6361:20053649.

[180] S. Van Loo, M. C. Runacres, and R. Blomme. "Non-thermal radio emission from single hot stars". In: *Astronomy & Astrophysics* 418 (May 2004), pp. 717–725. DOI: 10.1051/0004-6361:20034480.

[181] C. Erba and R. Ignace. "Radio Spectral Energy Distributions for Single Massive Star Winds with Free-Free and Synchrotron Emission". In: *The Astrophysical Journal* 932.1, 12 (June 2022), p. 12. DOI: 10.3847/1538-4357/ac6c90.

[182] K. I. Kellermann. "The radio source 1934-63". In: *Australian Journal of Physics* 19 (Apr. 1966), p. 195. DOI: 10.1071/PH660195.

[183] A. L. Roy et al. "The Compact Radio Sources in the Nucleus of NGC 1068". In: *The Astrophysical Journal* 504.1 (Sept. 1998), pp. 147–157. DOI: 10.1086/306071.

[184] D. A. Green. "A revised catalogue of 294 Galactic supernova remnants". In: *Journal of Astrophysics and Astronomy* 40.4, 36 (Aug. 2019), p. 36. DOI: 10.1007/s12036-019-9601-6.

[185] R. P. Fender. "Powerful jets from black hole X-ray binaries in low/hard X-ray states". In: *Monthly Notices of the Royal Astronomical Society* 322.1 (Mar. 2001), pp. 31–42. DOI: 10.1046/j.1365-8711.2001.04080.x.

[186] N. M. Nagar et al. "Radio sources in low-luminosity active galactic nuclei. III. "AGNs" in a distance-limited sample of "LLAGNs"". In: *Astronomy & Astrophysics* 392 (Sept. 2002), pp. 53–82. DOI: 10.1051/0004-6361:20020874.

[187] A. Konigl. "Relativistic jets as X-ray and gamma-ray sources." In: *The Astrophysical Journal* 243 (Feb. 1981), pp. 700–709. DOI: 10.1086/158638.

[188] D. Caprioli. "Particle Acceleration at Shocks: An Introduction". In: *arXiv e-prints*, arXiv:2307.00284 (June 2023), arXiv:2307.00284. DOI: 10.48550/arXiv.2307.00284.

[189] P. H. Hauschildt et al. "Spherically Symmetric, Expanding, Non–LTE Model Atmospheres for Novae during Their Early Stages". In: *The Astrophysical Journal* 393 (July 1992), p. 307. DOI: 10.1086/171507.

[190] R. A. Chevalier. "Synchrotron Self-Absorption in Radio Supernovae". In: *The Astrophysical Journal* 499.2 (May 1998), pp. 810–819. DOI: 10.1086/305676.

[191] A. G. Pacholczyk. *Radio astrophysics. Nonthermal processes in galactic and extragalactic sources*. 1970.

[192] R. A. Chevalier and C. Fransson. "Circumstellar Emission from Type Ib and Ic Supernovae". In: *The Astrophysical Journal* 651.1 (Nov. 2006), pp. 381–391. DOI: 10.1086/507606.

[193] R. A. Chevalier. "The interaction of the radiation from a type II supernova with a circumstellar shell." In: *The Astrophysical Journal* 251 (Dec. 1981), pp. 259–265. DOI: 10.1086/159460.

[194] D. Caprioli and A. Spitkovsky. "Simulations of Ion Acceleration at Non-relativistic Shocks. II. Magnetic Field Amplification". In: *The Astrophysical Journal* 794.1, 46 (Oct. 2014), p. 46. DOI: 10.1088/0004-637X/794/1/46.

[195] S. K. Sarbadhicary et al. "Supernova remnants in the Local Group - I. A model for the radio luminosity function and visibility times of supernova remnants". In: *Monthly Notices of the Royal Astronomical Society* 464.2 (Jan. 2017), pp. 2326–2340. DOI: 10.1093/mnras/stw2566.

[196] L. Chomiuk et al. "EVLA Observations Constrain the Environment and Progenitor System of Type Ia Supernova 2011fe". In: *The Astrophysical Journal* 750.2, 164 (May 2012), p. 164. DOI: 10.1088/0004-637X/750/2/164.

[197] M. A. Pérez-Torres et al. "Constraints on the Progenitor System and the Environs of SN 2014J from Deep Radio Observations". In: *The Astrophysical Journal* 792.1, 38 (Sept. 2014), p. 38. DOI: 10.1088/0004-637X/792/1/38.

[198] M. A. Tucker et al. "Nebular spectra of 111 Type Ia supernovae disfavour single-degenerate progenitors". In: *Monthly Notices of the Royal Astronomical Society* 493.1 (Mar. 2020), pp. 1044–1062. DOI: 10.1093/mnras/stz3390.

[199] K.-C. Pan, P. M. Ricker, and R. E. Taam. "Impact of Type Ia Supernova Ejecta on Binary Companions in the Single-degenerate Scenario". In: *The Astrophysical Journal* 750.2, 151 (May 2012), p. 151. DOI: 10.1088/0004-637X/750/2/151.

[200] P. Boehner, T. Plewa, and N. Langer. "Imprints of the ejecta-companion interaction in Type Ia supernovae: main-sequence, subgiant, and red giant companions". In: *Monthly*

Notices of the Royal Astronomical Society 465.2 (Feb. 2017), pp. 2060–2075. DOI: 10.1093/mnras/stw2737.

[201] J. Botyánszki, D. Kasen, and T. Plewa. "Multidimensional Models of Type Ia Supernova Nebular Spectra: Strong Emission Lines from Stripped Companion Gas Rule Out Classic Single-degenerate Systems". In: *The Astrophysical Journal* 852.1, L6 (Jan. 2018), p. L6. DOI: 10.3847/2041-8213/aaa07b.

[202] G. C. Anupama et al. "The 2010 outburst and pre-outburst optical spectrum of the recurrent nova U Scorpii". In: *Astronomy & Astrophysics* 559, A121 (Nov. 2013), A121. DOI: 10.1051/0004-6361/201321262.

[203] M. J. Darnley et al. "A remarkable recurrent nova in M 31: The optical observations". In: *Astronomy & Astrophysics* 563, L9 (Mar. 2014), p. L9. DOI: 10.1051/0004-6361/201423411.

[204] J. Basu et al. "Survival of the Accretion Disk in LMC Recurrent Nova 1968-12a: UV–X-Ray Case Study of the 2024 Eruption". In: *The Astrophysical Journal* 994.2, 229 (Dec. 2025), p. 229. DOI: 10.3847/1538-4357/ae13e1.

[205] M. J. Darnley. "Accrete, Accrete, Accrete... Bang! (and repeat): The remarkable Recurrent Novae". In: *The Golden Age of Cataclysmic Variables and Related Objects V*. Vol. 2-7. Feb. 2021, 44, p. 44. DOI: 10.22323/1.368.0044.

[206] J. Strader et al. "SOAR spectroscopic confirmation of a new eruption of the recurrent nova V3890 Sgr". In: *The Astronomer's Telegram* 13047 (Aug. 2019), p. 1.

[207] D. A. H. Buckley et al. "V3890 Sagittarii". In: *International Astronomical Union Circular Central Bureau for Astronomical Telegrams* 5019 (May 1990), p. 1.

[208] G. C. Anupama and S. Sethi. "Spectroscopy of the Recurrent Nova V3890-SAGITTARII 18-DAYS after the 1990 Outburst". In: *Monthly Notices of the Royal Astronomical Society* 269 (July 1994), p. 105. DOI: 10.1093/mnras/269.1.105.

[209] W. Wenzel. "On the Amplitude of the Recurrent Nova V3890 Sagittarii". In: *Information Bulletin on Variable Stars* 3517 (Sept. 1990), p. 1.

[210] L. T. P. Miller. "V3890 Sagittarii Brightness Update". In: *The Journal of the American Association of Variable Star Observers* 20.2 (Oct. 1991), pp. 182–184.

[211] J. Mikołajewska et al. "The symbiotic recurrent nova V3890 Sgr: binary parameters and pre-outburst activity". In: *Monthly Notices of the Royal Astronomical Society* 504.2 (June 2021), pp. 2122–2132. DOI: 10.1093/mnras/stab1058.

[212] S. Buson, P. Jean, and C. C. Cheung. "Fermi-LAT Gamma-ray Detection of Symbiotic Recurrent Nova V3890 Sgr". In: *The Astronomer's Telegram* 13114 (Sept. 2019), p. 1.

[213] M. M. Nyamai et al. "Radio detection of the recurrent nova V3890 Sgr with MeerKAT at 1.28 GHz". In: *The Astronomer's Telegram* 13089 (Sept. 2019), p. 1.

[214] E. Polisensky et al. "VLITE/VLA Detection of Nova V3890 Sgr Reveals Sub-GHz Turnover". In: *The Astronomer's Telegram* 13185 (Oct. 2019), p. 1.

[215] A. Evans et al. "Infrared spectroscopy of the 2019 eruption of the recurrent nova V3890 Sgr: Separation into equatorial and polar winds revealed". In: *Monthly Notices of the Royal Astronomical Society* 517.4 (Dec. 2022), pp. 6077–6090. DOI: 10.1093/mnras/stac2363.

[216] B. Kaminsky et al. "The recurrent nova V3890 Sgr: a near-infrared and optical study of the red giant component and its environment". In: *Monthly Notices of the Royal Astronomical Society* 517.4 (Dec. 2022), pp. 6064–6076. DOI: 10.1093/mnras/stac2199.

[217] J. .-. Ness et al. "The super-soft source phase of the recurrent nova V3890 Sgr". In: *Astronomy & Astrophysics* 658, A169 (Feb. 2022), A169. DOI: 10.1051/0004-6361/202142037.

[218] C. C. Cheung et al. "Fermi LAT Gamma-ray Detection of the Recurrent Nova RS Ophiuchi during its 2021 Outburst". In: *The Astrophysical Journal* 935.1, 44 (Aug. 2022), p. 44. DOI: 10.3847/1538-4357/ac7eb7.

[219] P. Craig et al. "What determines the γ-ray luminosities of classical novae?" In: *Monthly Notices of the Royal Astronomical Society* (Dec. 2025). DOI: 10.1093/mnras/staf2270.

[220] T. Nelson et al. "NuSTAR Detection of X-Rays Concurrent with Gamma-Rays in the Nova V5855 Sgr". In: *The Astrophysical Journal* 872.1, 86 (Feb. 2019), p. 86. DOI: 10.3847/1538-4357/aafb6d.

[221] A. C. Gordon et al. "Surveying the X-Ray Behavior of Novae as They Emit γ-Rays". In: *The Astrophysical Journal* 910.2, 134 (Apr. 2021), p. 134. DOI: 10.3847/1538-4357/abe547.

[222] E. Steinberg and B. D. Metzger. "The multidimensional structure of radiative shocks: suppressed thermal X-rays and relativistic ion acceleration". In: *Monthly Notices of the Royal Astronomical Society* 479.1 (Sept. 2018), pp. 687–702. DOI: 10.1093/mnras/sty1641.

[223] B. D. Metzger, L. Lancaster, and R. Diesing. "Suppression of Shock X-Ray Emission in Novae from Turbulent Mixing with Cool Gas". In: *The Astrophysical Journal* 988.2, 211 (Aug. 2025), p. 211. DOI: 10.3847/1538-4357/ade711.

[224] S. Mitrani et al. "X-Ray Observations of Nova Sco 2023: Spectroscopic Evidence of Charge Exchange". In: *The Astrophysical Journal* 989.2, 166 (Aug. 2025), p. 166. DOI: 10.3847/1538-4357/adf1a3.

[225] T. Nelson et al. "X-Ray Emission from an Asymmetric Blast Wave and a Massive White Dwarf in the Gamma-Ray Emitting Nova V407 Cyg". In: *The Astrophysical Journal* 748, 43 (Mar. 2012), p. 43. DOI: 10.1088/0004-637X/748/1/43.

[226] S. Orlando, J. J. Drake, and J. M. Laming. "Three-dimensional modeling of the asymmetric blast wave from the 2006 outburst of RS Ophiuchi: Early X-ray emission". In: *Astronomy & Astrophysics* 493.3 (Jan. 2009), pp. 1049–1059. DOI: 10.1051/0004-6361:200810109.

[227] S. Orlando et al. "Predicting the X-ray signatures of the imminent T Coronae Borealis outburst through 3D hydrodynamic modeling". In: *Astronomy & Astrophysics* 704, A144 (Dec. 2025), A144. DOI: 10.1051/0004-6361/202556617.

[228] M. C. Shepherd. "Difmap: an Interactive Program for Synthesis Imaging". In: *Astronomical Data Analysis Software and Systems VI*. Ed. by G. Hunt and H. Payne. Vol. 125. Astronomical Society of the Pacific Conference Series. Jan. 1997, p. 77.

[229] S. Abdollahi et al. "Incremental Fermi Large Area Telescope Fourth Source Catalog". In: *apjs* 260.2, 53 (June 2022), p. 53. DOI: 10.3847/1538-4365/ac6751.

[230] K. V. Sokolovsky et al. "Swift X-ray detection during the optical peak of the recurrent nova V3890 Sgr". In: *The Astronomer's Telegram* 13050 (Aug. 2019), p. 1.

[231] K. L. Page et al. "Swift detection of super-soft X-ray emission from V3890 Sgr". In: *The Astronomer's Telegram* 13084 (Sept. 2019), p. 1.

[232] Gaia Collaboration et al. "The Gaia mission". In: *Astronomy & Astrophysics* 595, A1 (Nov. 2016), A1. DOI: 10.1051/0004-6361/201629272.

[233] Gaia Collaboration et al. "Gaia Data Release 3. Summary of the content and survey properties". In: *Astronomy & Astrophysics* 674, A1 (June 2023), A1. DOI: 10.1051/0004-6361/202243940.

[234] R. Walder, D. Folini, and S. N. Shore. "3D simulations of RS Ophiuchi: from accretion to nova blast". In: *Astronomy & Astrophysics* 484.1 (June 2008), pp. L9–L12. DOI: 10.1051/0004-6361:200809703.

[235] S. Mohamed, R. Booth, and P. Podsiadlowski. "The Asymmetric Outflow of RS Ophiuchi". In: *Binary Paths to Type Ia Supernovae Explosions*. Ed. by R. Di Stefano, M. Orio, and M. Moe. Vol. 281. IAU Symposium. Jan. 2013, pp. 195–198. DOI: 10.1017/S1743921312014998.

[236] R. A. Booth, S. Mohamed, and P. Podsiadlowski. "Simulations of RS Oph and the CSM in Type Ia Supernovae". In: *Supernova Environmental Impacts*. Ed. by A. Ray and R. A. McCray. Vol. 296. IAU Symposium. Jan. 2014, pp. 382–383. DOI: 10.1017/S1743921313009939.

[237] U. Munari et al. "Radio interferometric imaging of RS Oph bipolar ejecta for the 2021 nova outburst". In: *Astronomy & Astrophysics* 666, L6 (Oct. 2022), p. L6. DOI: 10.1051/0004-6361/202244821.

[238] R. Lico et al. "High-resolution imaging of the evolving bipolar outflows in symbiotic novae: The case of the RS Ophiuchi 2021 nova outburst". In: *Astronomy & Astrophysics* 692, A107 (Dec. 2024), A107. DOI: 10.1051/0004-6361/202451364.

[239] M. Giroletti et al. "Very long baseline interferometry imaging of the advancing ejecta in the first gamma-ray nova V407 Cygni". In: *Astronomy & Astrophysics* 638, A130 (June 2020), A130. DOI: 10.1051/0004-6361/202038142.

[240] J. Wrobel and R. Walker. "Synthesis Imaging in Radio Astronomy II". In: *Synthesis Imaging in Radio Astronomy II*. Vol. 180. Astronomical Society of the Pacific Conference Series. Astronomical Society of the Pacific Conference Series, Jan. 1999. Chap. Lecture 9: Sensitivity, pp. 171–185.

[241] R. Beck and M. Krause. "Revised equipartition and minimum energy formula for magnetic field strength estimates from radio synchrotron observations". In: *Astronomische Nachrichten* 326.6 (July 2005), pp. 414–427. DOI: 10.1002/asna.200510366.

[242] E. Aydi et al. "Direct evidence for shock-powered optical emission in a nova". In: *Nature Astronomy* 4 (Apr. 2020), pp. 776–780. DOI: 10.1038/s41550-020-1070-y.

[243] V. A. Acciari et al. "Proton acceleration in thermonuclear nova explosions revealed by gamma rays". In: *Nature Astronomy* 6 (Apr. 2022), pp. 689–697. DOI: 10.1038/s41550-022-01640-z.

[244] M. Orio et al. "The RS Oph Outburst of 2021 Monitored in X-Rays with NICER". In: *The Astrophysical Journal* 955.1, 37 (Sept. 2023), p. 37. DOI: 10.3847/1538-4357/ace9bd.

[245] M. Lacy et al. "The Karl G. Jansky Very Large Array Sky Survey (VLASS). Science Case and Survey Design". In: *Publications of the Astronomical Society of the Pacific* 132.1009, 035001 (Mar. 2020), p. 035001. DOI: 10.1088/1538-3873/ab63eb.

[246] P. Chandra and D. A. Frail. "A Radio-selected Sample of Gamma-Ray Burst Afterglows". In: *The Astrophysical Journal* 746.2, 156 (Feb. 2012), p. 156. DOI: 10.1088/0004-637X/746/2/156.

[247] R. Margutti and R. Chornock. "First Multimessenger Observations of a Neutron Star Merger". In: *Annual Review of Astronomy and Astrophysics* 59 (Sept. 2021), pp. 155–202. DOI: 10.1146/annurev-astro-112420-030742.

[248] M. F. Bietenholz et al. "The Radio Luminosity-risetime Function of Core-collapse Supernovae". In: *The Astrophysical Journal* 908.1, 75 (Feb. 2021), p. 75. DOI: 10.3847/1538-4357/abccd9.

[249] G. Morlino and D. Caprioli. "Strong evidence for hadron acceleration in Tycho's supernova remnant". In: *Astronomy & Astrophysics* 538, A81 (Feb. 2012), A81. DOI: 10.1051/0004-6361/201117855.

[250] L. Chomiuk et al. "The Radio Light Curve of the Gamma-Ray Nova in V407 Cyg: Thermal Emission from the Ionized Symbiotic Envelope, Devoured from within by the Nova Blast". In: *The Astrophysical Journal* 761, 173 (Dec. 2012), p. 173. DOI: 10.1088/0004-637X/761/2/173.

[251] A. T. Deller et al. "DiFX-2: A More Flexible, Efficient, Robust, and Powerful Software Correlator". In: *Publications of the Astronomical Society of the Pacific* 123.901 (Mar. 2011), p. 275. DOI: 10.1086/658907.

[252] E. Brandi et al. "Spectroscopic orbits and variations of RS Ophiuchi". In: *Astronomy & Astrophysics* 497.3 (Apr. 2009), pp. 815–825. DOI: 10.1051/0004-6361/200811417.

[253] G. C. Anupama and J. Mikołajewska. "Recurrent novae at quiescence: systems with giant secondaries". In: *Astronomy & Astrophysics* 344 (Apr. 1999), pp. 177–187. DOI: 10.48550/arXiv.astro-ph/9812432.

[254] W. Morrison. "RS Ophiuchi". In: *International Astronomical Union Circular Central Bureau for Astronomical Telegrams* 4030 (Jan. 1985), p. 2.

[255] H. Narumi et al. "RS Ophiuchi". In: *International Astronomical Union Circular Central Bureau for Astronomical Telegrams* 8671 (Feb. 2006), p. 2.

[256] K. Geary and A. Amorim. "RS Oph". In: *Central Bureau Electronic Telegrams* 5013 (Aug. 2021), p. 1.

[257] K. Hirosawa et al. "Nova Cassiopeiae 1995". In: *International Astronomical Union Circular Central Bureau for Astronomical Telegrams* 6213 (Aug. 1995), p. 1.

[258] P. Schmeer et al. "U Scorpii". In: *International Astronomical Union Circular Central Bureau for Astronomical Telegrams* 7113 (Feb. 1999).

[259] K. Nishiyama et al. "V407 Cygni". In: *International Astronomical Union Circular Central Bureau for Astronomical Telegrams* 9130 (Mar. 2010), p. 1.

[260] S. Korotkiy et al. "Nova Sagittarii 2012 = PNV J17452791-2305213." In: *Central Bureau Electronic Telegrams* 3089 (Apr. 2012), p. 1.

[261] K. Nishiyama et al. "V1534 Scorpii = Nova Scorpii 2014 = Tcp J17154683-3128303". In: *International Astronomical Union Circular Central Bureau for Astronomical Telegrams* 9273 (July 2015), p. 2.

[262] K. Nishiyama et al. "V5667 Sagittarii = N Sgr 2015 (No. 1) = Pnv J18142514-2554343". In: *International Astronomical Union Circular Central Bureau for Astronomical Telegrams* 9274 (July 2015), p. 3.

[263] I. Endoh, M. Soma, and Y. Nakamura. "V392 PERSEI = TCP J04432130+4721280". In: *Central Bureau Electronic Telegrams* 4515 (Apr. 2018), p. 1.

[264] A. Pereira and E. O. Waagen. "V3890 Sgr". In: *Central Bureau Electronic Telegrams* 4660 (Sept. 2019), p. 1.

[265] R. J. Strope, B. E. Schaefer, and A. A. Henden. "Catalog of 93 Nova Light Curves: Classification and Properties". In: *The Astrophysical Journal* 140 (July 2010), pp. 34–62. DOI: 10.1088/0004-6256/140/1/34.

[266] U. Munari, F. .-. Hambsch, and A. Frigo. "Photometric evolution of seven recent novae and the double-component characterizing the light curve of those emitting in gamma rays". In: *Monthly Notices of the Royal Astronomical Society* 469.4 (Aug. 2017), pp. 4341–4358. DOI: 10.1093/mnras/stx1116.

[267] R. Pandey et al. "Study of 2021 outburst of the recurrent nova RS Ophiuchi: Photoionization and morphokinematic modelling". In: *Monthly Notices of the Royal Astronomical Society* 515.3 (Sept. 2022), pp. 4655–4668. DOI: 10.1093/mnras/stac2079.

[268] D. P. K. Banerjee et al. "Near-infrared studies of the 2010 outburst of the recurrent nova U Scorpii". In: *Monthly Notices of the Royal Astronomical Society* 408 (Oct. 2010), pp. L71–L75. DOI: 10.1111/j.1745-3933.2010.00932.x.

[269] U. Munari and D. P. K. Banerjee. "Infrared spectroscopy of the remnant of Nova Sco 2014: a symbiotic star with too little circumstellar matter to decelerate the ejecta". In: *Monthly Notices of the Royal Astronomical Society* 475.1 (Mar. 2018), pp. 508–513. DOI: 10.1093/mnras/stx3192.

[270] U. Munari, R. Margoni, and R. Stagni. "The extreme, possible symbiotic Mira V407 CYG and its relevance to the OH/IR sources." In: *Monthly Notices of the Royal Astronomical Society* 242 (Feb. 1990), pp. 653–659. DOI: 10.1093/mnras/242.4.653.

[271] G. C. Anupama and G. C. Dewangan. "The 1999 Outburst of the Recurrent Nova U Scorpii". In: *The Astrophysical Journal* 119 (Mar. 2000), pp. 1359–1364. DOI: 10.1086/301249.

[272] H. M. Johnston and S. R. Kulkarni. "Spectroscopy of the Recurrent Nova U Scorpii". In: *The Astrophysical Journal* 396 (Sept. 1992), p. 267. DOI: 10.1086/171714.

[273] B. E. Schaefer. "Discovery of 13 New Orbital Periods for Classical Novae". In: *Research Notes of the American Astronomical Society* 5.6, 150 (June 2021), p. 150. DOI: 10.3847/2515-5172/ac0d5b.

[274] H. Ritter and U. Kolb. "Catalogue of cataclysmic binaries, low-mass X-ray binaries and related objects (Seventh edition)". In: *Astronomy & Astrophysics* 404 (June 2003), pp. 301–303. DOI: 10.1051/0004-6361:20030330.

[275] T. Iijima. "Spectral evolution of the slowest classical nova V723 Cassiopeiae in the decline stage". In: *Astronomy & Astrophysics* 451.2 (May 2006), pp. 563–580. DOI: 10.1051/0004-6361:20053984.

[276] U. Munari, S. Moretti, and A. Maitan. "The sustained post-outburst brightness of Nova Per 2018, the evolved companion, and the long orbital period". In: *Astronomy & Astrophysics* 639, L10 (July 2020), p. L10. DOI: 10.1051/0004-6361/202038403.

[277] H. Kosai et al. "Nova Aquilae 1982". In: *International Astronomical Union Circular Central Bureau for Astronomical Telegrams* 3661 (Feb. 1982).

[278] L. Rosino, T. Iijima, and S. Ortolani. "Light curve and spectral evolution of Nova Aquilae 1982." In: *Monthly Notices of the Royal Astronomical Society* 205 (Dec. 1983), pp. 1069–1083. DOI: 10.1093/mnras/205.4.1069.

[279] K. H. Hinkle et al. "Infrared Spectroscopy of Symbiotic Stars. IX. D-type Symbiotic Novae". In: *The Astrophysical Journal* 770.1, 28 (June 2013), p. 28. DOI: 10.1088/0004-637X/770/1/28.

[280] A. Pearce et al. "U Scorpii". In: *Central Bureau Electronic Telegrams* 5129 (June 2022), p. 1.

[281] M. K. Srivastava et al. "Near-infrared studies during maximum and early decline of Nova Cephei 2014 and Nova Scorpii 2015". In: *Monthly Notices of the Royal Astronomical Society* 454.2 (Dec. 2015), pp. 1297–1309. DOI: 10.1093/mnras/stv2094.

[282] M. F. Bode, E. R. Seaquist, and A. Evans. "Radio survey of classical novae". In: *Monthly Notices of the Royal Astronomical Society* 228 (Sept. 1987), pp. 217–227. DOI: 10.1093/mnras/228.2.217.

[283] I. Heywood et al. "V723 Cas (Nova Cassiopeiae 1995): MERLIN observations from 1996 to 2001". In: *Monthly Notices of the Royal Astronomical Society* 362 (Sept. 2005), pp. 469–474. DOI: 10.1111/j.1365-2966.2005.09328.x.

[284] A. Albert et al. "γ-Ray Emission from Classical Nova V392 Per: Measurements from Fermi and HAWC". In: *The Astrophysical Journal* 940.2, 141 (Dec. 2022), p. 141. DOI: 10.3847/1538-4357/ac966a.

[285] I. de Ruiter et al. "Low-frequency radio observations of recurrent nova RS Ophiuchi with MeerKAT and LOFAR". In: *Monthly Notices of the Royal Astronomical Society* 523.1 (July 2023), pp. 132–148. DOI: 10.1093/mnras/stad1418.

[286] F. Teyssier. "Eruptive stars monitoring and the ARAS database". In: *Contributions of the Astronomical Observatory Skalnate Pleso* 49 (May 2019), pp. 217–227.

[287] C. Zucker et al. "A Deep, High-angular-resolution 3D Dust Map of the Southern Galactic Plane". In: *The Astrophysical Journal* 992.1, 39 (Nov. 2025), p. 39. DOI: 10.3847/1538-4357/adfbe6.

[288] B. .-. Chen et al. "Three-dimensional interstellar dust reddening maps of the Galactic plane". In: *Monthly Notices of the Royal Astronomical Society* 483.4 (Mar. 2019), pp. 4277–4289. DOI: 10.1093/mnras/sty3341.

[289] N. G. Kantharia et al. "Giant Metrewave Radio Telescope Observations of the 2006 Outburst of the Nova RS Ophiuchi: First Detection of Emission at Radio Frequencies 1.4 GHz". In: *The Astrophysical Journal* 667 (Nov. 2007), pp. L171–L174. DOI: 10.1086/522201.

[290] K. Sokolovsky et al. "VLA observations of the 2021 eruption of RS Oph". In: *The Astronomer's Telegram* 14886 (Aug. 2021), p. 1.

[291] U. Munari, S. Dallaporta, and G. Cherini. "The 2015 super-active state of recurrent nova T CrB and the long term evolution after the 1946 outburst". In: 47 (Aug. 2016), pp. 7–15. DOI: 10.1016/j.newast.2016.01.002.

[292] C. C. Cheung, P. Jean, and S. N. Shore. "Fermi-LAT Gamma-ray Observations of Recurrent Nova V745 Sco". In: *The Astronomer's Telegram* 5879 (Feb. 2014), p. 1.

[293] E. S. Weibel. "Spontaneously Growing Transverse Waves in a Plasma Due to an Anisotropic Velocity Distribution". In: *Physical Review Letters* 2.3 (Feb. 1959), pp. 83–84. DOI: 10.1103/PhysRevLett.2.83.

[294] J. Skilling. "Cosmic ray streaming. I - Effect of Alfven waves on particles". In: *MNRAS* 172 (Sept. 1975), pp. 557–566. URL: http://adsabs.harvard.edu/abs/1975MNRAS.172..557S.

[295] M. A. J. Snijders et al. “Nova Aquilae 1982”. In: *Monthly Notices of the Royal Astronomical Society* 228 (Sept. 1987), pp. 329–376. DOI: 10.1093/mnras/228.2.329.

[296] R. M. Hjellming et al. “Radio observations of the 1985 outburst of RS Ophiuchi”. In: *The Astrophysical Journal* 305 (June 1986), pp. L71–L75. DOI: 10.1086/184687.

APPENDIX A.

Is the shock in V745 Sco radiative due to efficient particle acceleration?

A.1 Is the shock in V745 Sco radiative due to efficient particle acceleration?

Here we further explore the question proposed in §2.5.3: is the rapid decline in Hα line widths (Figure 2.8) merely an observational effect driven by dropping densities and fading lines, or does it imply dramatic energy loss from the shock due to acceleration of relativistic particles, as suggested by [73]?

If the blast wave is losing energy due to efficient particle acceleration, this population of relativistic particles may have observable signatures in the form of GeV γ-rays. Marginal γ-ray detections had 2.5 and 2.4σ significance on 2014 Feb 6 (the day of eruption discovery) and Feb 7 (day 1), with >100 MeV fluxes of 1.8×10^{-7} phot cm^{-2} s^{-1} [138, 292]. However, these marginal detections occur before the steep drop in FWZI, which begins around day 10 (Figure 2.6). A more relevant constraint may be the sliding time window analysis of [138], which found a 95 per cent upper limit on the >100 MeV flux of $< 0.5 \times 10^{-7}$ phot cm^{-2} s^{-1} over a time window covering 3–18 days following eruption. Assuming the same γ-ray spectrum as V906 Car (the highest S/N *Fermi*/LAT observation of a nova; [242]) and a distance of 8.2 kpc, this translates to a γ-ray luminosity of $< 5.2 \times 10^{35}$ erg s^{-1} and a γ-ray fluence over this time period of $< 6.7 \times 10^{41}$ erg. Assuming that 20–30 per cent of the energy in relativistic particles is radiated as GeV γ-rays [21], this implies that $< 3.3 \times 10^{42}$ erg is transferred to relativistic particles during day 3–18. This is comparable to the kinetic energy of the ejecta assuming $M_{ej} = 10^{-7}$ M$_\odot$ ($KE \approx 5 \times 10^{42}$ erg), but much less than the KE for $M_{ej} = 10^{-6}$ M$_\odot$ ($KE \approx 5 \times 10^{43}$ erg). The *Fermi*/LAT constraints therefore imply

that the shock in V745 Sco could be radiative if the ejecta mass is very small (as suggested by [109]), but not if M_{ej} is closer to 10^{-6} $M_\odot$.

The temperature of the hot shocked X-ray gas observed by *Swift*/XRT over the course of V745 Sco's 2014 eruption shows a decline in temperature which tracks the narrowing of the Hα FWZI [73], with relatively constant temperature for the first few days of eruption followed by a rapid decline. This does not need to imply deceleration of the blast (as suggested by Delgado & Hernanz), but could instead reflect adiabatic expansion and cooling of the shocked gas, if the interaction with CSM significantly weakens.

A radiative shock is not supported by the evolution of the X-ray absorbing column (N_H; Figure 4 of [73]), which shows that N_H levels reach the ISM value just ∼16 days into eruption, around the time when the Hα FWZI steeply declines. This rapid decline in N_H and CSM density is further supported by our radio observations, which show all light curves peaking around this time near simultaneously—which must imply a sudden drop in the absorbing column (§2.7.1). Both our radio observations and the analysis of [73] imply a dense CSM characterized by $\dot{M}_{in} \approx 5 \times 10^{-7}$ $M_\odot$ yr^{-1} (assuming $v_w = 10$ km s^{-1}) out to a radius $\sim [1-9] \times 10^{14}$ cm, and a much lower density CSM characterized by $\dot{M}_{out} \lesssim 10^{-9}$ $M_\odot$ yr^{-1} at larger radii. If the shock was losing much of its energy to relativistic particles (as in the radiative shock scenario suggested by [73]), it would lose energy as a fraction of the shock luminosity, which can be written as $L_s = 1.48 \times 10^{-24} R^2 n_s v_s^3$ [21], where n_s is the number density of particles in the shock (all quantities in cgs units). We estimate the shock luminosity as a function of time in Figure A.1, using $v_s = FWZI/2$, $R(t)$ as the integral under $v_s(t)$, and n_s derived as 4× the swept-up CSM density ($\dot{M}_{in} = 5 \times 10^{-7}$ $M_\odot$ yr^{-1} and $\dot{M}_{out} = 10^{-9}$ $M_\odot$ yr^{-1}). Figure A.1 shows that we expect the shock luminosity (and attendant energy loss through relativistic particles) to be much higher at early times, when

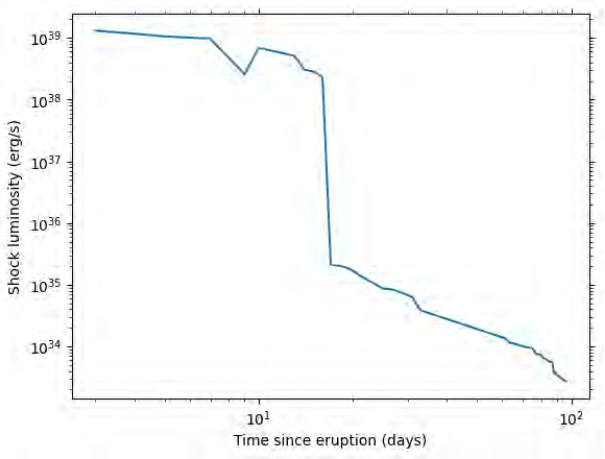

Figure A.1 The estimated shock luminosity as a function of time over the course of V745 Sco's 2014 eruption. The sudden drop around day 16 is caused by the shock breaking out of relatively dense CSM into a much lower density environment.

the shock is interacting with denser CSM, and to plummet after day 16.

This is the opposite of what is required to explain the declining Hα FWZI (Figure 2.8) through a radiative shock—the observed FWZI is quite constant during the first 10 days of eruption, and then rapidly declines between days 10–100. In other words—V745 Sco shows a temporal coincidence between the narrowing of the Hα emission line profile and a sudden drop in the CSM density which is the opposite of what is expected if the shock was decelerating due to rapid particle acceleration. On the other hand, this temporal coincidence is expected if the narrowing of the lines is primarily an observational effect dictated by a drop in density (§2.5.3).For these reasons, we do not treat the line width measurements as accurate tracers of the shock velocity, and instead employ a model for an adiabatic shock [72] in modelling the shock kinematics and interpreting the radio light curve.

APPENDIX B.

A synchrotron halo model for the late-time radio emission.

B.1 A Synchrotron Halo Model for the Late-Time Radio Emission

In this Appendix we outline a simple analytic model for the diffuse radio halo proposed in § **??**. The goal is not to provide a detailed numerical treatment, but rather to demonstrate that the observed radio luminosity, characteristic size, and spectral properties follow naturally from non-thermal particles escaping the γ-ray–producing shock into the red giant wind.

B.1.1 Injection and Transport of Escaping Pairs

The late-time γ-ray luminosity is $L_\gamma \sim 10^{35.5}$ erg s^{-1} (Figure 3.7). If the γ-rays originate from hadronic interactions, a comparable power is injected into relativistic $e^\pm$ pairs through charged pion decay. We therefore parametrize the power injected into escaping pairs as

$$L_\pm = \xi_\pm L_\gamma, \tag{B.1}$$

with $\xi_\pm \sim \mathcal{O}(1)$.

Pairs escape the dense acceleration region at a characteristic radius

$$r_0 \sim 10^{15} \text{ cm}, \tag{B.2}$$

motivated by the VLBI size at $t \sim 50$ days (Table 3.1) and the timing of the second radio peak (Figure 3.3). We take the injected pairs to have characteristic Lorentz factors $\gamma_{\pm,0} \sim 10^2$–10^4, in the range expected if the observed $E_\gamma \sim 1$–10 GeV emission arises from neutral pion

decay following inelastic *pp* collisions. The corresponding parent proton energies ($E_{\rm p} \sim 10$–100 GeV) imply secondary $e^{\pm}$ from charged pion decay with energies $E_{\pm} \sim 0.1$–10 GeV, consistent with this range of Lorentz factors.

After escape, particles stream or diffuse outward with an effective radial speed $v_{\pm}$. To populate the halo out to $\sim 10^{16}$ cm within ~ 50 days requires $v_{\pm} \gtrsim 0.1c$. In steady state, conservation of particle flux gives a pair density profile

$$n_{\pm}(r) = \frac{\dot{N}_{\pm}}{4\pi r^2 v_{\pm}} = \frac{L_{\pm}}{4\pi r^2 v_{\pm} \gamma_{\pm,0} m_{\rm e} c^2}. \tag{B.3}$$

B.1.2 Red Giant Wind Density and Magnetic Field

We assume a steady red giant wind with mass-loss rate $\dot{M}_{\rm w}$ and velocity $v_{\rm w}$, yielding a density profile

$$\rho(r) = \frac{\dot{M}_{\rm w}}{4\pi v_{\rm w} r^2}. \tag{B.4}$$

We adopt $\dot{M}_{\rm w} \simeq 2 \times 10^{-7}\, M_{\odot}\,{\rm yr}^{-1}$ and $v_{\rm w} \simeq 10$ km s^{-1}, consistent with the X-ray constraints (Table 3.3).

We assume the wind carries a magnetic field that is approximately frozen into the flow. Beyond the Alfvén radius, a convenient scaling is

$$B(r) = B_{*} \left(\frac{R_{*}}{r} \right), \tag{B.5}$$

where B_{*} is the red-giant surface field at radius R_{*}. For $B_{*} \sim 1$–10 G and $R_{*} \sim 1$ AU, this yields $B \sim 10^{-3}$–10^{-2} G at $r \sim 10^{15}$–10^{16} cm, comparable to the magnetic field strengths

inferred in the shocked region (Table 3.2).

B.1.3 Magnetic Field Amplification

The magnetic field calculated in the previous section assumes that the red giant wind has reached $r \sim 10^{16}$ cm since the previous (1990) nova eruption. Depending on the wind velocity, this may not be the case. However, we argue that $B \sim 10^{-3} - 10^{-2}$ is still a reasonable estimate. Not only can the post-shock region of the previous nova outburst contribute to the magnetic field at large radii, but escaping particles (ions and pairs) drive magnetic field amplification via streaming instabilities [80, 293, 294]. Assuming energy equipartition between the escaping pairs and the amplified field, we obtain,

$$\frac{B^2(r)}{8\pi} \sim u_{\pm}(r) \simeq \frac{L_{\pm}}{4\pi r^2 v_{\pm}}. \tag{B.6}$$

Taking $v_{\pm} = 0.1c$, we find $B \sim 10^{-3}$ G for $L_{\pm} = L_{\gamma} = 10^{35}$ erg s^{-1} and $r = 10^{16}$ cm.

B.1.4 Slow cooling, characteristic frequency, and adiabatic losses

At the field strengths relevant here, synchrotron cooling is extremely slow compared to the transport/expansion time-scale. We therefore assume that pairs cool predominantly adiabatically as they propagate outward, so that

$$\gamma_{\pm}(r) \simeq \gamma_{\pm,0} \left(\frac{r_0}{r}\right). \tag{B.7}$$

The characteristic synchrotron frequency at radius r is

$$\nu_{\rm syn}(r) \simeq 6\ {\rm GHz} \left(\frac{B_*}{1\,{\rm G}}\right) \left(\frac{R_*}{1\,{\rm AU}}\right) \times \left(\frac{\gamma_{\pm,0}}{10^4}\right)^2 \left(\frac{r_0}{10^{16}\,{\rm cm}}\right)^2 \left(\frac{r}{10^{16}\,{\rm cm}}\right)^{-3}. \tag{B.8}$$

so that GHz emission naturally arises at $r \sim 10^{16}$ cm for fiducial parameters.

The synchrotron cooling time is

$$t_{\rm syn}(r) \simeq 1.1 \times 10^4\ {\rm yr} \left(\frac{B_*}{1\,{\rm G}}\right)^{-2} \left(\frac{R_*}{1\,{\rm AU}}\right)^{-2} \times \left(\frac{\gamma_{\pm,0}}{10^4}\right)^{-1} \left(\frac{r_0}{10^{16}\,{\rm cm}}\right)^{-1} \left(\frac{r}{10^{16}\,{\rm cm}}\right)^{3}. \tag{B.9}$$

while the transport/adiabatic time-scale is $t_{\rm ad}(r) \sim r/v_\pm$. For the parameter space of interest, $t_{\rm ad} \ll t_{\rm syn}$ at all relevant radii, confirming that the pairs are in the slow-cooling regime.

B.1.5 Radio luminosity and predicted flux density

A useful way to estimate the synchrotron output in the slow-cooling regime is to consider the energy contained in pairs within a logarithmic radial interval at radius r. The residence time in a shell of width $d\ln r$ is $\sim r/v_\pm$, so the energy content is

$$\frac{dE_\pm}{d\ln r}(r) \ \simeq\ \left(\frac{r}{v_\pm}\right) \dot{N}_\pm\, \gamma_\pm(r)\, m_{\rm e}c^2, \qquad \dot{N}_\pm = \frac{L_\pm}{\gamma_{\pm,0} m_{\rm e}c^2}. \tag{B.10}$$

Using $\gamma_{\pm}(r) = \gamma_{\pm,0}(r_0/r)$, the dependence on r and $\gamma_{\pm,0}$ cancels, giving

$$\begin{aligned}\frac{dE_{\pm}}{d\ln r} &\simeq \frac{L_{\pm} r_0}{v_{\pm}} \\ &\simeq 3.3\times10^{39}\left(\frac{L_{\pm}}{10^{35}\ \mathrm{erg\,s^{-1}}}\right)\left(\frac{r_0}{10^{16}\ \mathrm{cm}}\right) \\ &\quad\times\left(\frac{v_{\pm}}{0.1c}\right)^{-1}\ \mathrm{erg}.\end{aligned} \tag{B.11}$$

In the slow-cooling regime, the synchrotron power radiated from this interval is

$$\frac{dL_{\rm syn}}{d\ln r} \;\simeq\; \frac{1}{t_{\rm syn}(r)}\frac{dE_{\pm}}{d\ln r}. \tag{B.12}$$

A convenient estimate of the spectral luminosity near the characteristic frequency emitted at radius r is then

$$L_{\nu}(r) \;\sim\; \frac{1}{\nu_{\rm syn}(r)}\frac{dL_{\rm syn}}{d\ln r} \;\sim\; \frac{1}{t_{\rm syn}(r)\,\nu_{\rm syn}(r)}\frac{dE_{\pm}}{d\ln r}. \tag{B.13}$$

Substituting the expressions above and evaluating at the radius contributing to GHz emission (i.e. $r \sim 10^{16}$ cm for fiducial parameters) yields

$$\begin{aligned}L_{\nu} \simeq 1.5\times10^{19}&\left(\frac{L_{\pm}}{10^{35}\ \mathrm{erg\,s^{-1}}}\right)\left(\frac{B_*}{1\ \mathrm{G}}\right)\left(\frac{R_*}{1\ \mathrm{AU}}\right) \\ &\times\left(\frac{\gamma_{\pm,0}}{10^4}\right)^{-1}\left(\frac{r_0}{10^{16}\ \mathrm{cm}}\right)\left(\frac{v_{\pm}}{0.1c}\right)^{-1}\ \mathrm{erg\,s^{-1}\,Hz^{-1}}.\end{aligned} \tag{B.14}$$

The corresponding flux density is

$$F_\nu \simeq 0.28 \left(\frac{L_\pm}{10^{35}\ \mathrm{erg\,s^{-1}}}\right)\left(\frac{B_*}{1\ \mathrm{G}}\right)\left(\frac{R_*}{1\ \mathrm{AU}}\right) \times \left(\frac{\gamma_{\pm,0}}{10^4}\right)^{-1}\left(\frac{r_0}{10^{16}\ \mathrm{cm}}\right)\left(\frac{v_\pm}{0.1c}\right)^{-1} \times \left(\frac{d}{6.8\ \mathrm{kpc}}\right)^{-2}\ \mathrm{mJy}. \tag{B.15}$$

For $\xi_\pm \sim 1$ and $L_\gamma \sim 10^{35.5}$ erg s^{-1} (Figure **??**), this predicts $F_\nu \sim 0.1$–1 mJy for plausible values of $(B_*, R_*, \gamma_{\pm,0}, v_\pm)$. This is of the same order as the observed diffuse component dominating the second radio bump in the integrated light curve (Figure **??**), up to order-unity factors associated with the breadth of the synchrotron spectrum and the mapping between observing frequency and emission radius.

Finally, because $\nu_{\rm syn} \propto r^{-3}$ under the scalings adopted above, a broad range of radii contributes across a decade in observing frequency. This naturally produces a shallow, approximately power-law radio spectrum and a low-surface-brightness halo whose characteristic extent is set by particle transport.

Although non-thermal particles are produced throughout the eruption, the contribution of a given population to the observed GHz radio halo depends sensitively on the radius r_0 at which the particles escape the dense shock region. For particles injected at early times ($r_0 \ll 10^{15}$ cm), adiabatic losses reduce their Lorentz factors as $\gamma_\pm(r) \propto r_0/r$, so that by the time they reach radii $\sim 10^{16}$ cm their characteristic synchrotron frequencies lie well below the GHz band. In contrast, particles injected at later times, when the shock forms at $r_0 \sim 10^{15}$ cm, experience only modest adiabatic degradation and retain sufficient energy to emit efficiently at radio frequencies.

This effect is explicitly reflected in the scalings derived below: while the characteristic

synchrotron frequency depends on both r_0 and r (equation (B.8)), the normalization of the radio luminosity or flux scales linearly with r_0 (equation (B.15)). As a result, late-time injection at larger radii naturally dominates the observable synchrotron halo, even if earlier shocks were more luminous in γ-rays.

APPENDIX C.

Novae with Evolved Companions Data Tables

C.1 Novae with Evolved Companions Data Tables

C.2 Spectral Index Plots

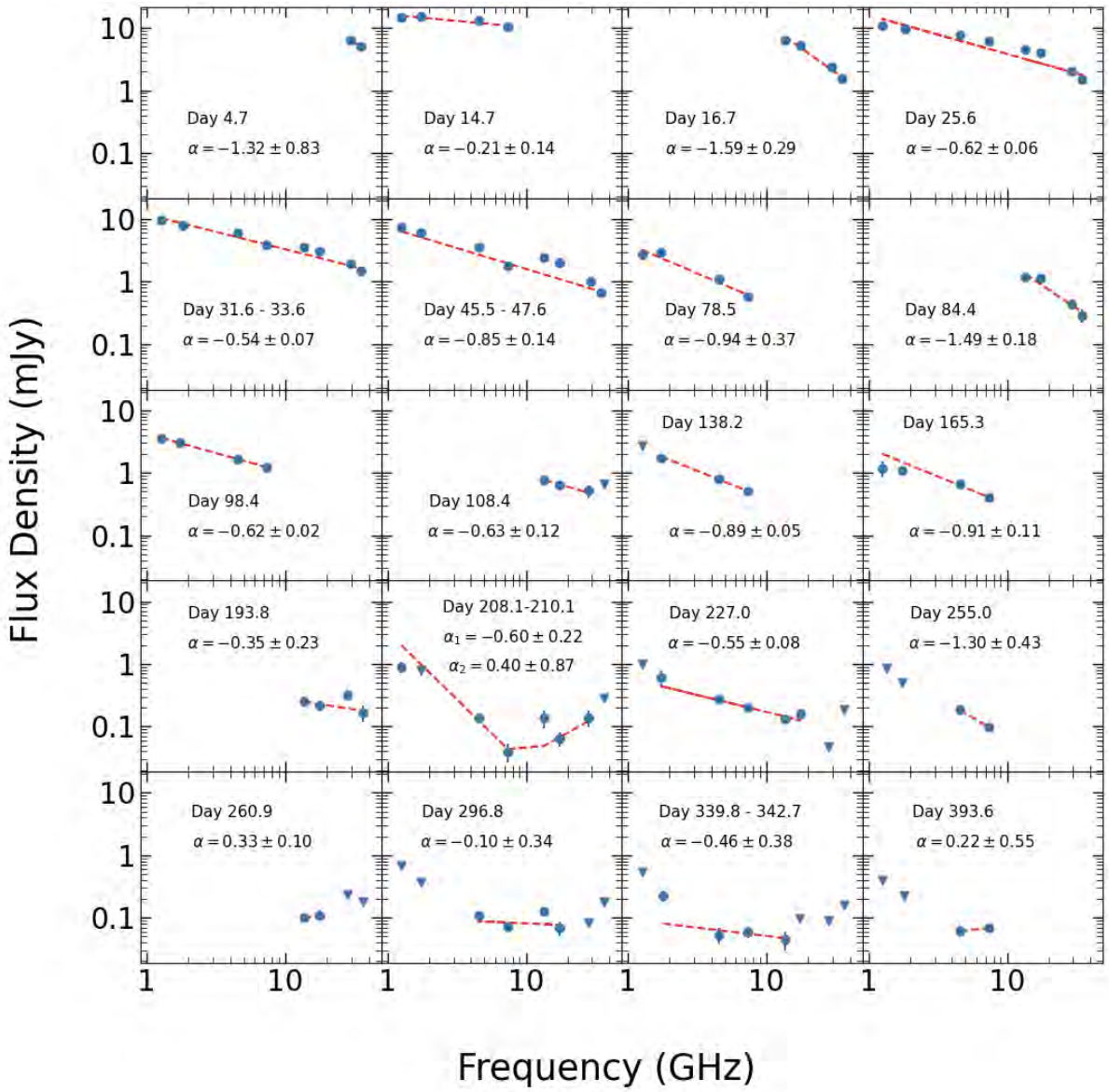

Figure C.1 V1534 Sco Spectral Index. Day 210.05 and Day 339.75 on the plot required extra weights on the most left point to achieve reasonable alpha values.

Table C.1 V392 Per γ-ray data

MJD	Photon Flux photons $s^{-1}cm^{-2}$	Error
58238.5	1.05E-06	2.44E-07
58239.5	4.53E-07	1.06E-07
58240.5	1.81E-07	7.37E-08
58241.5	8.08E-08	5 .82E-08
58242.5	1.26E-07	7.44E-08
58243.5	1.72E-07	8.12E-08
58244.5	3.04E-07	-99
58245.5	1.44E-07	7.38E-08
58246.5	2.11E-07	-99
58247.5	2.09E-07	-99
58248.5	1.86E-07	-99

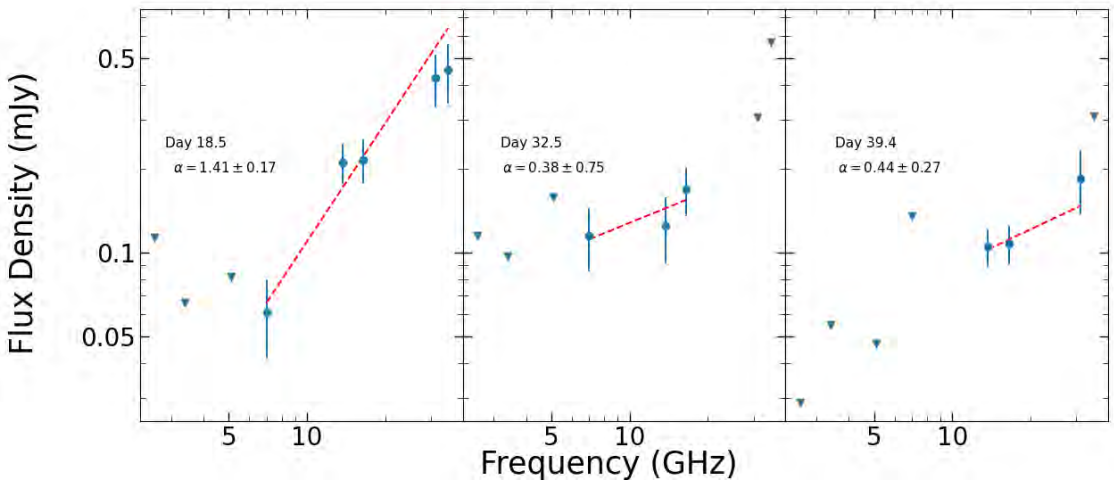

Figure C.2 Spectral index plots of Usco's 2022 eruption. Non detections are plotted as upside down triangles.

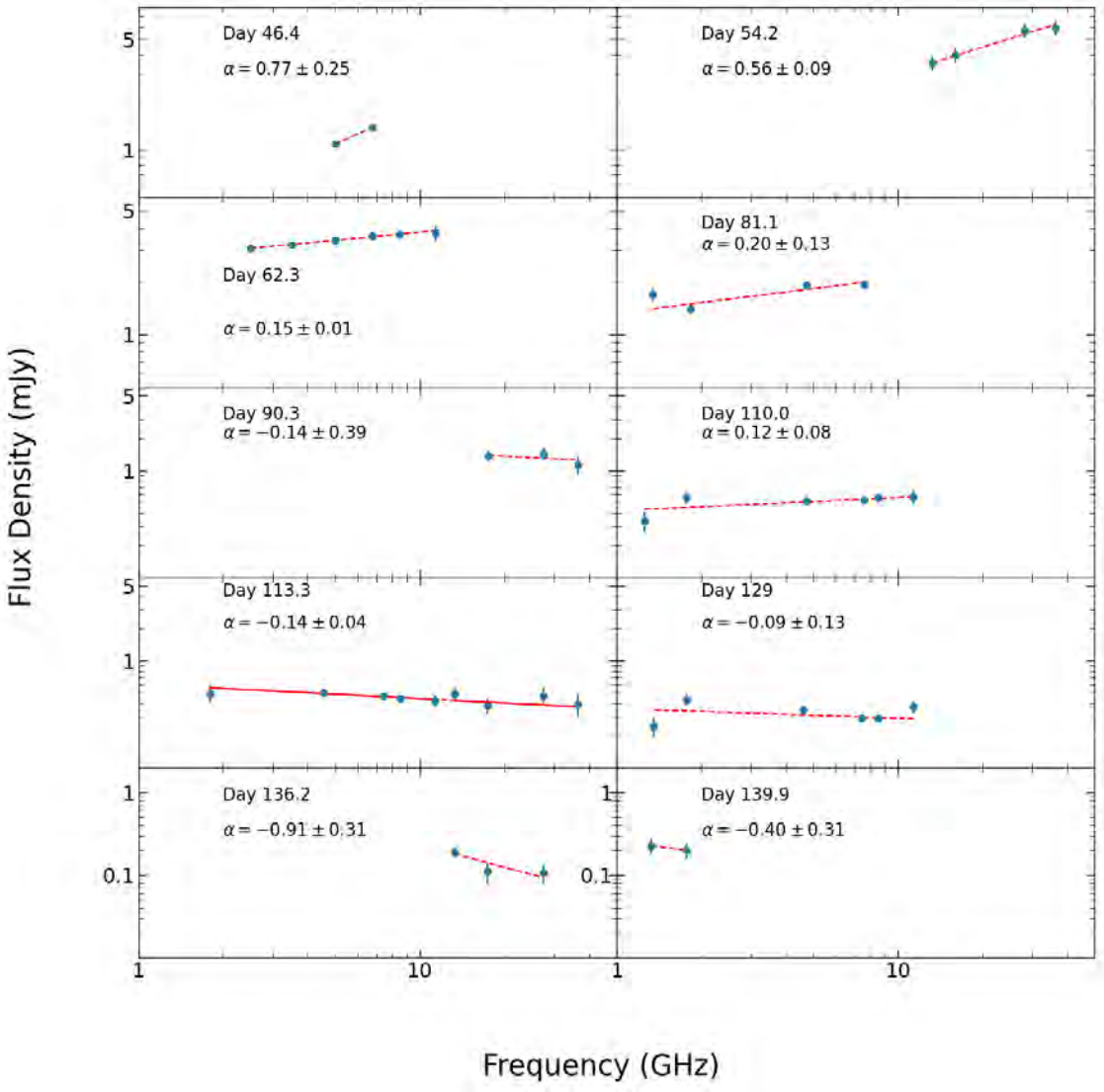

Figure C.3 V5589 Sgr Spectral Index

Table C.2 Radio Observations of V1370 Aql. We take the time of discovery, 1982 Jan 27, as t_0. The data were published by [295] at 1.41 GHz. The VLA data are published in [282]

UT Obs Date	MJD	$t - t_0$	0.6 GHz S_ν	1.5 GHz S_ν	4.9 GHz S_ν	14.9 GHz S_ν	Telescope
		Days	mJy	mJy	mJy	mJy	
1982 Mar 28	45055	59	8.4 ± 2.0				WSRT
1982 Apr 10	45069.5	73			20.2 ± 2.0		WSRT
1982 Jun 18	45138.5	142		14.2 ± 2.0			WSRT
1982 Jun 20	45140.5	144		12.2 ± 2.0			WSRT
1982 Jun 21	45141.5	145		11.5 ± 2.0			WSRT
1982 Jun 23	45143.5	147		13.4 ± 2.0			WSRT
1982 Jun 28	45148.5	152		10.9 ± 2.0			WSRT
1982 Aug 9	45190.5	194		3.0 ± 2.0			WSRT
1982 Sep 3	45215.5	219		< 2.0			WSRT
1982 Sep 15	45227.5	231		4.5 ± 2.0			WSRT
1982 Sep 21	45233.5	237		< 2.0			WSRT
1982 Sep 27	45239.5	243		< 2.0			WSRT
1982 Oct 2	45244.5	248		< 2.0			WSRT
1982 Oct 10	45252.5	256		< 2.0			WSRT
1982 Oct 18	45260.5	264		< 2.0			WSRT
1982 Oct 21	45263.5	267		2.0 ± 2.0			WSRT
1982 Nov 7	45280.5	284		5.4 ± 2.0			WSRT
1982 Nov 11	45284.5	288		< 2.0			WSRT
1982 Nov 13	45286.5	290		< 2.0			WSRT
1982 Nov 21	45294.5	298		< 2.0			WSRT
1984 May 12	45832.5	836			<0.4		VLA
1985 Jun 14	46230.5	1234		$< 1.6 \pm 0.5$	$< 0.4 \pm 0.1$		VLA
1987 Jan 24	46819.5	1823		$< 1.9 \pm 0.5$	$< 0.3 \pm 0.1$	$< 0.7 \pm 0.2$	VLA

Table C.3 Radio Observations of RS Oph. We take the time of discovery, 1982 Jan 27, as t_0. Data were published in [a] [296], [b] [169], [c] [289], [d] [285], [e] [173] and [f] this work.

UT Obs Date	MJD	$t - t_0$	Frequency	Flux Density	Error	Telescope
		Days	(GHz)	(mJy)	(mJy)	
1985 Feb 24	46120.1	29.59	1.49	38	2.76	VLA[a]
1985 Feb 24	46120.1	29.59	4.85	50	3.20	VLA[a]
1985 Feb 24	46120.1	29.59	14.94	61	6.42	VLA[a]
1985 Feb 24	46120.1	29.59	22.46	65	7.16	VLA[a]
1985 Mar 5	46129.2	38.70	1.49	61	3.65	VLA[a]
1985 Mar 5	46129.2	38.70	4.85	58	4.17	VLA[a]
1985 Mar 5	46129.2	38.70	14.94	68	7.43	VLA[a]
1985 Mar 5	46129.2	38.70	22.46	75	8.08	VLA[a]
1985 Mar 7	46132.0	41.49	1.49	63	3.73	VLA[a]
1985 Mar 7	46132.0	41.49	4.85	61	3.65	VLA[a]
1985 Mar 7	46132.0	41.49	14.94	65	7.16	VLA[a]
1985 Mar 13	46137.0	46.52	1.49	62	3.69	VLA[a]
1985 Mar 13	46137.0	46.52	4.85	56	3.44	VLA[a]
1985 Mar 13	46137.0	46.52	14.94	61	6.42	VLA[a]
1985 Mar 13	46137.0	46.52	22.46	71	7.71	VLA[a]
1985 Mar 14	46139.0	48.49	1.49	59	3.56	VLA[a]
1985 Mar 14	46139.0	48.49	4.85	51	3.24	VLA[a]
1985 Mar 14	46139.0	48.49	14.94	58	6.14	VLA[a]
1985 Mar 14	46139.0	48.49	22.46	72	7.80	VLA[a]
1985 Mar 19	46144.0	53.46	1.49	54	3.36	VLA[a]
1985 Mar 19	46144.0	53.46	4.85	47	3.09	VLA[a]
1985 Mar 19	46144.0	53.46	14.94	56	6.35	VLA[a]
1985 Mar 19	46144.0	53.46	22.46	66	7.25	VLA[a]
1985 Mar 27	46151.0	60.52	1.49	44	2.97	VLA[a]
1985 Mar 27	46151.0	60.52	4.85	41	2.86	VLA[a]
1985 Mar 27	46151.0	60.52	14.94	52	6.56	VLA[a]
1985 Mar 27	46151.0	60.52	22.46	60	6.71	VLA[a]
1985 Mar 31	46155.9	65.39	1.49	41	2.86	VLA[a]
1985 Mar 31	46155.9	65.39	4.85	37	2.72	VLA[a]
1985 Mar 31	46155.9	65.39	14.94	45	4.92	VLA[a]
1985 Mar 31	46155.9	65.39	22.46	56	6.35	VLA[a]
1985 Apr 3	46158.9	68.36	1.49	38	2.76	VLA[a]
1985 Apr 5	46160.9	70.35	1.49	36	2.69	VLA[a]
1985 Apr 5	46160.9	70.35	4.85	34	2.62	VLA[a]
1985 Apr 5	46160.9	70.35	14.94	43	4.74	VLA[a]
1985 Apr 5	46160.9	70.35	22.46	51	5.92	VLA[a]
1985 Apr 10	46165.0	74.52	14.94	43	5.24	VLA[a]
1985 Apr 12	46167.9	77.35	1.49	33	2.59	VLA[a]
1985 Apr 12	46167.9	77.35	4.85	30	2.50	VLA[a]
1985 Apr 12	46167.9	77.35	14.94	42	4.65	VLA[a]
1985 Apr 12	46167.9	77.35	22.46	47	5.58	VLA[a]
1985 Apr 18	46173.8	83.29	1.49	26	2.39	VLA[a]
1985 Apr 18	46173.8	83.29	4.85	23	2.31	VLA[a]
1985 Apr 18	46173.8	83.29	14.94	37	4.21	VLA[a]
1985 Apr 22	46178.0	87.48	14.94	36	4.12	VLA[a]

Table C.4 Radio Observations of RS Oph continued

UT Obs Date	MJD	$t - t_0$	Frequency	Flux Density	Error	Telescope
		Days	(GHz)	(mJy)	(mJy)	
1985 Apr 22	46178.0	87.48	22.46	43	5.24	VLA[a]
1985 May 3	46188.8	98.31	1.49	20	2.24	VLA[a]
1985 May 3	46188.8	98.31	4.85	18	2.19	VLA[a]
1985 May 3	46188.8	98.31	14.94	31	3.69	VLA[a]
1985 May 8	46193.8	103.33	1.49	20	2.24	VLA[a]
1985 May 8	46193.8	103.33	4.85	17	2.17	VLA[a]
1985 May 8	46193.8	103.33	14.94	29	3.52	VLA[a]
1985 May 8	46193.8	103.33	22.46	39	4.92	VLA[a]
1985 May 22	46207.9	117.40	1.49	15	2.14	VLA[a]
1985 May 22	46207.9	117.40	4.85	15	2.14	VLA[a]
1985 May 22	46207.9	117.40	14.94	25	3.20	VLA[a]
1985 May 22	46207.9	117.40	22.46	34	4.53	VLA[a]
1985 Jun 5	46221.9	131.38	1.49	13	1.19	VLA[a]
1985 Jun 5	46221.9	131.38	4.85	13	1.19	VLA[a]
1985 Jun 5	46221.9	131.38	14.94	22	2.97	VLA[a]
1985 Jun 5	46221.9	131.38	22.46	30	4.24	VLA[a]
1985 Jun 7	46223.9	133.42	1.49	12	2.09	VLA[a]
1985 Jun 22	46238.7	148.23	1.49	10	1.12	VLA[a]
1985 Jun 22	46238.7	148.23	4.85	11	1.14	VLA[a]
1985 Jun 22	46238.7	148.23	14.94	19	2.76	VLA[a]
1985 Jun 22	46238.7	148.23	22.46	25	3.91	VLA[a]
1985 Jul 1	46247.7	157.21	1.49	9	1.10	VLA[a]
1985 Jul 1	46247.7	157.21	4.85	10	1.12	VLA[a]
1985 Jul 1	46247.7	157.219	14.94	17	2.62	VLA[a]
1985 Jul 1	46247.7	157.21	22.46	22	2.97	VLA[a]
1985 Jul 18	46264.7	174.17	1.49	8	1.08	VLA[a]
1985 Jul 18	46264.7	174.17	4.85	8.8	0.67	VLA[a]
1985 Jul 18	46264.7	174.17	14.94	14	2.44	VLA[a]
1985 Jul 18	46264.7	174.17	22.46	18	2.69	VLA[a]
1985 Jul 31	46277.6	187.14	1.49	7	0.61	VLA[a]
1985 Jul 31	46277.6	187.14	4.85	8.1	0.64	VLA[a]
1985 Jul 31	46277.6	187.14	14.94	12	1.56	VLA[a]
1985 Jul 31	46277.6	187.14	22.46	14	2.44	VLA[a]
1985 Aug 9	46286.7	196.21	1.49	6.2	0.59	VLA[a]
1985 Aug 9	46286.7	196.21	4.85	7.8	0.63	VLA[a]
1985 Aug 9	46286.7	196.21	14.94	11	1.49	VLA[a]
1985 Aug 9	46286.7	196.21	22.46	13	2.39	VLA[a]
1985 Aug 25	46302.8	212.25	1.49	5.5	0.57	VLA[a]
1985 Aug 25	46302.8	212.25	4.85	6.9	0.61	VLA[a]
1985 Aug 25	46302.8	212.25	14.94	10	1.41	VLA[a]
1985 Aug 25	46302.8	212.25	22.46	11	2.28	VLA[a]
1985 Sep 11	46319.7	229.17	1.49	5.3	0.57	VLA[a]
1985 Sep 11	46319.7	229.17	4.85	6.5	0.60	VLA[a]
1985 Sep 11	46319.7	229.17	14.94	7.9	0.93	VLA[a]

Table C.5 Radio Observations of RS Oph continued

UT Obs Date	MJD	$t - t_0$	Frequency	Flux Density	Error	Telescope
		Days	(GHz)	(mJy)	(mJy)	
1985 Sep 27	46335.5	245.04	1.49	4.8	0.55	VLA[a]
1985 Sep 27	46335.5	245.04	4.85	5.8	0.49	VLA[a]
1985 Sep 27	46335.5	245.04	14.94	6.5	0.82	VLA[a]
1985 Oct 19	46357.5	267.04	1.49	4.4	0.55	VLA[a]
1985 Oct 19	46357.5	267.04	4.85	5.3	0.48	VLA[a]
1985 Oct 19	46357.5	267.04	14.94	5.5	0.68	VLA[a]
1985 Nov 15	46384.5	293.99	1.49	4.0	0.54	VLA[a]
1985 Nov 15	46384.5	293.99	4.85	4.5	0.46	VLA[a]
1985 Nov 15	46384.5	293.99	14.94	4.6	0.61	VLA[a]
1985 Dec 18	46417.2	326.72	1.49	3.7	0.53	VLA[a]
1985 Dec 18	46417.2	326.72	4.85	3.9	0.45	VLA[a]
1985 Dec 18	46417.2	326.72	14.94	3.8	0.55	VLA[a]
1985 Jan 21	46451.1	360.65	1.49	2.1	0.51	VLA[a]
1985 Jan 21	46451.1	360.65	4.85	3.1	0.43	VLA[a]
1985 Jan 21	46451.1	360.65	14.94	3.0	0.50	VLA[a]
1985 Jan 31	46461.1	370.64	1.49	2.3	0.51	VLA[a]
2006 Feb 17	53783.33	4.50	6	14.2	2.12	MERLIN[b]
2006 Feb 17	53783.52	4.70	1.46	2.8	0.24	VLA[b]
2006 Feb 17	53783.52	4.70	4.89	15.2	0.79	VLA[b]
2006 Feb 17	53783.52	4.70	14.96	23.2	2.40	VLA[b]
2006 Feb 17	53783.52	4.70	22.48	26.2	2.67	VLA[b]
2006 Feb 18	53784.32	5.50	6	33.0	2.59	MERLIN[b]
2006 Feb 20	53786.32	7.46	6	41.2	2.21	MERLIN[b]
2006 Feb 26	53792.71	13.88	1.46	57.6	2.90	VLA[b]
2006 Feb 26	53792.71	13.88	4.89	53.3	2.67	VLA[b]
2006 Feb 26	53792.71	13.88	14.96	50.5	5.07	VLA[b]
2006 Feb 26	53792.71	13.88	22.48	61.1	6.15	VLA[b]
2006 Mar 1	53795.16	16.34	30	55.0	8.14	OCRA-p[b]
2006 Mar 1	53795.12	16.52	6	37.9	2.19	MERLIN[b]
2006 Mar 2	53796.12	17.47	6	35.8	1.92	MERLIN[b]
2006 Mar 6	53800.68	21.85	1.46	48.2	2.43	VLA[b]
2006 Mar 6	53800.68	21.85	4.89	44.5	2.23	VLA[b]
2006 Mar 6	53800.68	21.85	6	43.0	5.44	MERLIN[b]
2006 Mar 6	53800.68	21.85	14.96	37.4	3.79	VLA[b]
2006 Mar 6	53800.68	21.85	22.48	36.4	3.75	VLA[b]
2006 Mar 8	53802.18	23.36	30	53.0	8.01	OCRA-p[b]
2006 Mar 9	53803.11	24.28	30	74.0	10.19	OCRA-p[b]
2006 Mar 13	53806.68	27.85	1.46	50.4	2.55	VLA[b]
2006 Mar 13	53806.68	27.85	4.89	50.3	2.52	VLA[b]
2006 Mar 13	53806.68	27.85	14.96	52.9	5.32	VLA[b]
2006 Mar 13	53806.68	27.85	22.48	69.4	6.98	VLA[b]
2006 Mar 14	53807.33	28.50	6	45.0	5.48	MERLIN[b]

Table C.6 Radio Observations of RS Oph continued

UT Obs Date	MJD	$t - t_0$	Frequency	Flux Density	Error	Telescope
		Days	(GHz)	(mJy)	(mJy)	
2006 Mar 23	53817.23	38.41	30	103.0	13.04	OCRA-p[b]
2006 Mar 23	53818.45	39.62	1.46	55.5	2.79	VLA[b]
2006 Mar 23	53818.45	39.62	4.89	51.2	2.57	VLA[b]
2006 Mar 23	53818.45	39.62	14.96	49.9	5.04	VLA[b]
2006 Mar 23	53818.45	39.62	22.48	78.1	7.83	VLA[b]
2006 Mar 24	53819.45	40.62	6	50.0	5.59	MERLIN[b]
2006 Mar 25	53820.45	41.62	1.46	53.8	2.71	VLA[b]
2006 Mar 25	53820.45	41.62	4.89	51.7	2.59	VLA[b]
2006 Mar 25	53820.45	41.62	14.96	55.8	5.62	VLA[b]
2006 Mar 25	53820.45	41.62	22.48	78.5	7.89	VLA[b]
2006 Mar 30	53825.40	46.57	1.46	52.9	2.65	VLA[b]
2006 Mar 30	53825.40	46.57	4.89	47.4	2.38	VLA[b]
2006 Mar 30	53825.40	46.57	14.96	48.8	4.92	VLA[b]
2006 Mar 30	53825.40	46.57	22.48	65.4	6.57	VLA[b]
2006 Apr 3	53828.54	49.71	6	40.0	5.39	MERLIN[b]
2006 Apr 6	53831.54	52.71	1.46	48.6	2.45	VLA[b]
2006 Apr 6	53831.54	52.71	4.89	42.4	2.13	VLA[b]
2006 Apr 6	53831.54	52.71	14.96	50.9	5.14	VLA[b]
2006 Apr 6	53831.54	52.71	22.48	66.0	6.60	VLA[b]
2006 Apr 13	53838.57	59.74	1.46	42.8	2.16	VLA[b]
2006 Apr 13	53838.57	59.74	4.89	39.3	1.98	VLA[b]
2006 Apr 13	53838.57	59.74	14.96	50.5	5.10	VLA[b]
2006 Apr 13	53838.57	59.74	22.48	79.9	8.17	VLA[b]
2006 Feb 24	53790.05	11.22	1.28	49.5	2.55	GMRT[c]
2006 Mar 2	53796.02	17.19	1.06	55.4	2.80	GMRT[c]
2006 Mar 2	53796.02	17.19	1.39	56.8	2.90	GMRT[c]
2006 Mar 2	53796.02	17.19	1.28	50.0	2.5	GMRT[c]
2006 Mar 5	53799.09	20.26	0.61	48.4	2.59	GMRT[c]
2006 Mar 13	53807.98	29.15	0.61	48.9	2.55	GMRT[c]
2006 Mar 13	53807.98	29.15	0.24	< 13.0		GMRT[c]
2006 Mar 22	53816.98	38.15	0.325	43.7	2.32	GMRT[c]
2006 Mar 29	53823.90	45.07	0.24	54.2	3.07	GMRT[c]
2006 Mar 29	53823.90	45.07	0.61	47.9	2.44	GMRT[c]
2006 Apr 7	53832.07	53.24	0.325	57.0	3.0	GMRT[c]
2006 May 16	53871.82	92.99	0.24	30.5	1.60	GMRT[c]
2006 May 16	53871.82	92.99	0.61	21.0	1.19	GMRT[c]
2006 Jun 2	53888.83	110	0.15	< 9.0		GMRT[c]
2006 Jun 13	53899.69	120.86	0.61	15.3	0.78	GMRT[c]
2006 Jun 15	53901.95	123.12	0.325	17.2	2.38	GMRT[c]
2006 Jun 26	53912.90	134.07	0.325	18.0	2.55	GMRT[c]
2006 Jun 29	53915.75	136.92	0.61	15.3	0.78	GMRT[c]
2006 Jul 10	53926.71	147.88	0.61	10.5	0.60	GMRT[c]
2006 Jul 16	53932.77	153.94	0.61	18.2	1.00	GMRT[c]

Table C.7 Radio Observations of RS Oph continued

UT Obs Date	MJD	$t - t_0$	Frequency	Flux Density	Error	Telescope
		Days	(GHz)	(mJy)	(mJy)	
2006 Jul 29	53945.60	166.77	0.61	10.9	0.64	GMRT[c]
2006 Aug 01	53948.58	169.75	0.325	20.6	4.90	GMRT[c]
2006 Aug 24	53971.67	192.84	0.61	10.1	0.55	GMRT[c]
2006 Sep 07	53985.72	206.89	0.61	5.5	0.34	GMRT[c]
2006 Sep 15	53993.49	214.66	0.61	5.8	0.37	GMRT[c]
2006 Sep 22	54000.69	221.86	0.61	< 6.01		GMRT[c]
2006 Sep 26	54004.44	225.61	0.325	< 12.69		GMRT[c]
2006 Nov 24	54063.26	284.43	0.325	6.3	1.56	GMRT[c]
2007 Jan 30	54130.23	351.40	0.61	3.9	0.24	GMRT[c]
2021 Aug 11	59437.0	2.5	1.28	0.35	0.05	MeerKAT [d]
2021 Aug 11	59437.7	3.2	1.28	0.28	0.05	MeerKAT [d]
2021 Aug 11	59437.8	3.3	0.82	0.49	0.07	MeerKAT [d]
2021 Aug 12	59438.6	4.1	1.28	0.59	0.09	MeerKAT [d]
2021 Aug 13	59439.6	5.1	1.28	1.7	0.18	MeerKAT [d]
2021 Aug 14	59440.6	6.1	0.82	1.4	0.16	MeerKAT [d]
2021 Aug 14	59440.6	6.1	1.28	8.6	0.87	MeerKAT [d]
2021 Aug 15	59441.8	7.3	0.82	9.8	1.00	MeerKAT [d]
2021 Aug 15	59441.8	7.3	1.28	32.9	3.30	MeerKAT [d]
2021 Aug 16	59442.8	8.3	1.28	52.4	5.30	MeerKAT [d]
2021 Aug 17	59443.6	9.1	1.28	64.5	6.50	MeerKAT [d]
2021 Aug 18	59444.8	10.3	0.82	54.5	5.50	MeerKAT [d]
2021 Aug 18	59444.9	10.4	1.28	70.5	7.10	MeerKAT [d]
2021 Aug 23	59449.7	15.2	1.28	87.4	8.78	MeerKAT [d]
2021 Aug 23	59449.8	15.3	0.82	85.0	8.50	MeerKAT [d]
2021 Sep 01	59458.6	24.1	1.28	76.1	7.62	MeerKAT [d]
2021 Sep 01	59458.6	24.1	0.82	78.7	7.90	MeerKAT [d]
2021 Sep 01	59458.7	24.2	0.15	39.9	5.70	LOFAR [d]
2021 Sep 11	59468.6	34.1	0.82	73.5	7.40	MeerKAT [d]
2021 Sep 11	59468.7	34.2	1.28	70.8	7.10	MeerKAT [d]
2021 Sep 11	59468.7	34.2	0.15	64.4	7.60	LOFAR [d]
2021 Sep 26	59483.6	49.1	1.28	66.8	6.70	MeerKAT [d]
2021 Sep 26	59483.6	49.1	0.82	72.0	7.20	MeerKAT [d]
2021 Sep 26	59483.6	49.1	0.05	< 87.18		LOFAR [d]
2021 Sep 26	59483.7	49.2	0.15	49.8	7.40	LOFAR [d]
2021 Oct 11	59498.6	64.1	0.82	59.2	5.94	MeerKAT [d]
2021 Oct 11	59498.7	64.2	1.28	53.6	5.40	MeerKAT [d]
2021 Oct 12	59499.6	65.1	0.15	52.0	6.50	LOFAR [d]
2022 Mar 17	59655	220.5	0.05	< 66.66		LOFAR [d]
2022 Mar 17	59655.2	220.7	1.28	11.6	1.20	MeerKAT [d]
2022 Mar 17	59655.3	220.8	0.82	12.2	1.24	MeerKAT [d]
2022 Mar 19	59657.2	222.7	0.15	12.7	3.40	LOFAR [d]
2022 Mar 19	59657.2	222.7	1.28	11.5	1.20	MeerKAT [d]
2022 Mar 19	59657.2	222.7	0.82	11.9	1.20	MeerKAT [d]

Table C.8 Radio Observations of RS Oph continued

UT Obs Date	MJD	$t - t_0$	Frequency	Flux Density	Error	Telescope
		Days	(GHz)	(mJy)	(mJy)	
2021 Sep 02	59459.53	25.03	1.36	85.10	4.43	uGMRT[e]
2021 Sep 14	59471.73	37.23	1.37	61.00	3.43	uGMRT[e]
2021 Sep 26	59483.69	49.19	1.36	43.10	2.86	uGMRT[e]
2021 Sep 31	59488.67	54.17	1.36	45.90	2.31	uGMRT[e]
2021 Oct 05	59492.34	57.84	1.36	60.40	3.10	uGMRT[e]
2022 Feb 05	59615.26	180.76	1.36	13.10	0.66	uGMRT[e]
2022 Apr 25	59694.03	259.53	1.36	9.90	0.50	uGMRT[e]
2021 Aug 31	59457.67	23.17	0.69	77.50	4.35	uGMRT[e]
2021 Sep 17	59474.67	40.17	0.69	78.00	4.10	uGMRT[e]
2021 Sep 21	59478.72	44.22	0.69	63.00	3.35	uGMRT[e]
2021 Oct 01	59488.58	54.08	0.69	72.10	4.51	uGMRT[e]
2021 Oct 08	59495.41	60.91	0.69	58.90	3.35	uGMRT[e]
2021 Nov 15	59533.42	98.92	0.69	43.30	2.30	uGMRT[e]
2021 Nov 26	59544.25	109.75	0.69	23.90	1.57	uGMRT[e]
2021 Dec 06	59554.15	119.65	0.69	26.90	1.89	uGMRT[e]
2021 Dec 18	59566.21	131.71	0.69	25.00	1.25	uGMRT[e]
2021 Dec 31	59579.26	144.76	0.69	21.30	1.37	uGMRT[e]
2022 Jan 10	59589.08	154.58	0.69	16.50	1.09	uGMRT[e]
2022 Feb 08	59618.19	183.69	0.69	16.49	0.94	uGMRT[e]
2022 Mar 01	59639.04	204.54	0.69	13.36	0.73	uGMRT[e]
2022 Mar 28	59666.95	232.45	0.69	11.55	0.61	uGMRT[e]
2022 Apr 24	59693.98	259.48	0.69	10.14	0.52	uGMRT[e]
2021 Sep 05	59462.51	28.01	0.40	73.10	9.24	uGMRT[e]
2021 Sep 16	59473.7	39.20	0.40	71.70	4.72	uGMRT[e]
2021 Sep 21	59478.38	43.88	0.40	85.10	10.47	uGMRT[e]
2021 Sep 30	59487.62	53.12	0.40	80.00	4.20	uGMRT[e]
2021 Oct 03	59490.42	55.92	0.40	75.80	9.44	uGMRT[e]
2021 Nov 15	59533.49	98.99	0.40	48.30	3.72	uGMRT[e]
2021 Nov 26	59544.33	109.83	0.40	38.43	1.94	uGMRT[e]
2021 Dec 07	59555.46	120.96	0.40	37.15	1.91	uGMRT[e]
2021 Dec 18	59566.46	131.96	0.40	29.68	1.68	uGMRT[e]
2021 Dec 31	59579.34	144.84	0.40	28.06	1.51	uGMRT[e]
2022 Jan 10	59589.32	154.82	0.40	23.91	1.23	uGMRT[e]
2022 Feb 08	59618.31	183.81	0.40	18.40	1.09	uGMRT[e]
2022 Mar 01	59639.12	204.62	0.40	14.46	0.79	uGMRT[e]
2022 Mar 29	59667.04	232.54	0.40	13.12	0.71	uGMRT[e]
2022 Mar 22	59721.85	287.35	0.40	8.93	0.94	uGMRT[e]
2021 Sep 30	59487.53	53.03	0.15	33.20	6.72	uGMRT[e]
2021 Oct 03	59490.34	55.84	0.15	31.40	4.88	uGMRT[e]
2021 Oct 08	59495.38	60.88	0.15	48.90	8.30	uGMRT[e]
2022 May 22	59721.91	287.41	0.15	26.80	3.41	uGMRT[e]
2021 Aug 13	59439.04	5.04	2.6	4.7	0.27	VLA[f]
2021 Aug 13	59439.04	5.04	3.4	5.3	0.28	VLA[f]
2021 Aug 13	59439.04	5.04	5.1	10	0.50	VLA[f]

Table C.9 Radio Observations of RS Oph continued

UT Obs Date	MJD	$t - t_0$	Frequency	Flux Density	Error	Telescope
		Days	(GHz)	(mJy)	(mJy)	
2021 Aug 13	59439.04	5.04	7.0	15.6	0.78	VLA[f]
2021 Aug 13	59439.04	5.04	13.7	24.1	2.41	VLA[f]
2021 Aug 13	59439.04	5.04	16.5	24.1	2.56	VLA[f]
2021 Aug 13	59439.04	5.04	31.1	24.1	3.60	VLA[f]
2021 Aug 13	59439.04	5.04	34.9	24.1	3.84	VLA[f]
2021 Aug 14	59440.08	6.08	2.6	18.2	0.92	VLA[f]
2021 Aug 14	59440.08	6.08	3.4	23.4	1.17	VLA[f]
2021 Aug 14	59440.08	6.08	5.1	33.5	1.67	VLA[f]
2021 Aug 14	59440.08	6.08	7	39.7	1.98	VLA[f]
2021 Aug 14	59440.08	6.08	13.7	40.9	4.09	VLA[f]
2021 Aug 14	59440.08	6.08	16.5	41.6	4.16	VLA[f]
2021 Aug 14	59440.08	6.08	31.1	44.8	4.48	VLA[f]
2021 Aug 14	59440.08	6.08	34.9	46.7	4.67	VLA[f]
2021 Aug 18	59443.99	9.99	2.6	68.9	3.47	VLA[f]
2021 Aug 18	59443.99	9.99	3.4	73.9	3.70	VLA[f]
2021 Aug 18	59443.99	9.99	5.1	67.6	3.38	VLA[f]
2021 Aug 18	59443.99	9.99	7	58.7	2.93	VLA[f]
2021 Aug 18	59443.99	9.99	13.7	47.8	4.79	VLA[f]
2021 Aug 18	59443.99	9.99	16.5	46.8	4.68	VLA[f]
2021 Aug 18	59443.99	9.99	31.1	48.1	4.82	VLA[f]
2021 Aug 18	59443.99	9.99	34.9	49.9	5.00	VLA[f]
2021 Aug 20	59446.01	12.01	2.6	88.7	4.44	VLA[f]
2021 Aug 20	59446.01	12.01	3.4	78.3	3.91	VLA[f]
2021 Aug 20	59446.01	12.01	5.1	60.5	3.02	VLA[f]
2021 Aug 20	59446.01	12.01	7	50.9	2.54	VLA[f]
2021 Aug 20	59446.01	12.01	13.7	43.7	4.37	VLA[f]
2021 Aug 20	59446.01	12.01	16.5	42.4	4.24	VLA[f]
2021 Aug 20	59446.01	12.01	31.1	46.1	4.61	VLA[f]
2021 Aug 20	59446.01	12.01	34.9	48.5	4.85	VLA[f]
2021 Aug 21	59446.99	12.99	2.6	84.4	4.24	VLA[f]
2021 Aug 21	59446.99	12.99	3.4	82.0	4.10	VLA[f]
2021 Aug 21	59446.99	12.99	5.1	64.0	3.20	VLA[f]
2021 Aug 21	59446.99	12.99	7	51.9	2.59	VLA[f]
2021 Aug 21	59446.99	12.99	13.7	41.9	4.19	VLA[f]
2021 Aug 21	59446.99	12.99	16.5	40.8	4.08	VLA[f]
2021 Aug 21	59446.99	12.99	31.1	43.7	4.37	VLA[f]
2021 Aug 21	59446.99	12.99	34.9	46.0	4.60	VLA[f]
2021 Aug 25	59451.01	17.01	2.6	92.5	4.63	VLA[f]
2021 Aug 25	59451.01	17.01	3.4	83.1	4.16	VLA[f]
2021 Aug 25	59451.01	17.01	5.1	61.8	3.09	VLA[f]
2021 Aug 25	59451.01	17.01	7	52.3	2.62	VLA[f]
2021 Aug 25	59451.01	17.01	13.7	44.1	4.41	VLA[f]

Table C.10 Radio Observations of RS Oph continued

UT Obs Date	MJD	$t - t_0$	Frequency	Flux Density	Error	Telescope
		Days	(GHz)	(mJy)	(mJy)	
2021 Aug 25	59451.01	17.01	16.5	42.9	4.29	VLA[f]
2021 Aug 25	59451.01	17.01	31.1	47.1	4.71	VLA[f]
2021 Aug 25	59451.01	17.01	34.9	48.1	4.81	VLA[f]
2021 Sep 4	59461.01	27.01	2.6	94.5	4.73	VLA[f]
2021 Sep 4	59461.01	27.01	3.4	85.8	4.29	VLA[f]
2021 Sep 4	59461.01	27.01	5.1	65.1	3.26	VLA[f]
2021 Sep 4	59461.01	27.01	7	57.6	2.88	VLA[f]
2021 Sep 4	59461.01	27.01	13.7	54.1	5.41	VLA[f]
2021 Sep 4	59461.01	27.01	16.5	54.5	5.45	VLA[f]
2021 Sep 4	59461.01	27.01	31.1	70.8	7.08	VLA[f]
2021 Sep 4	59461.01	27.01	34.9	77.0	7.71	VLA[f]
2021 Sep 6	59463.02	29.02	2.6	88.6	4.44	VLA[f]
2021 Sep 6	59463.02	29.02	3.4	80.6	4.03	VLA[f]
2021 Sep 6	59463.02	29.02	5.1	60.8	3.04	VLA[f]
2021 Sep 6	59463.02	29.02	7	56.0	2.80	VLA[f]
2021 Sep 6	59463.02	29.02	13.7	51.5	5.15	VLA[f]
2021 Sep 6	59463.02	29.02	16.5	54.3	5.43	VLA[f]
2021 Sep 6	59463.02	29.02	31.1	75.2	7.52	VLA[f]
2021 Sep 6	59463.02	29.02	34.9	82.8	8.29	VLA[f]
2021 Sep 9	59466.04	32.04	2.6	58.9	2.95	VLA[f]
2021 Sep 9	59466.04	32.04	3.4	58.4	2.92	VLA[f]
2021 Sep 9	59466.04	32.04	5.1	54.5	2.73	VLA[f]
2021 Sep 9	59466.04	32.04	7	54.4	2.72	VLA[f]
2021 Sep 10	59467.99	33.99	2.6	82.0	4.10	VLA[f]
2021 Sep 10	59467.99	33.99	3.4	75.0	3.76	VLA[f]
2021 Sep 10	59467.99	33.99	5.1	60.3	3.01	VLA[f]
2021 Sep 10	59467.99	33.99	7	55.8	2.79	VLA[f]
2021 Sep 10	59467.99	33.99	13.7	55.5	5.55	VLA[f]
2021 Sep 10	59467.99	33.99	16.5	57.7	5.77	VLA[f]
2021 Sep 10	59467.99	33.99	31.1	85.3	8.53	VLA[f]
2021 Sep 10	59467.99	33.99	34.9	94.9	9.49	VLA[f]
2021 Sep 13	59470.01	36.01	2.6	74.2	3.72	VLA[f]
2021 Sep 13	59470.01	36.01	3.4	68.0	3.40	VLA[f]
2021 Sep 13	59470.01	36.01	5.1	56.6	2.83	VLA[f]
2021 Sep 13	59470.01	36.01	7	54.5	2.72	VLA[f]
2021 Sep 13	59470.01	36.01	13.7	56.9	5.69	VLA[f]
2021 Sep 13	59470.01	36.01	16.5	60.3	6.03	VLA[f]
2021 Sep 13	59470.01	36.01	31.1	92.4	9.24	VLA[f]
2021 Sep 13	59470.01	36.01	34.9	103.52	10.35	VLA[f]

Table C.11 Radio Observations of RS Oph continued

UT Obs Date	MJD	$t - t_0$	Frequency	Flux Density	Error	Telescope
		Days	(GHz)	(mJy)	(mJy)	
2021 Sep 30	59487.96	53.96	2.6	65.4	3.27	VLA[f]
2021 Sep 30	59487.96	53.96	3.4	60.8	3.04	VLA[f]
2021 Sep 30	59487.96	53.96	5.1	49.9	2.49	VLA[f]
2021 Sep 30	59487.96	53.96	7	46.1	2.31	VLA[f]
2021 Sep 30	59487.96	53.96	13.7	51.3	5.13	VLA[f]
2021 Sep 30	59487.96	53.96	16.5	55.6	5.56	VLA[f]
2021 Sep 30	59487.96	53.96	31.1	92.1	9.21	VLA[f]
2021 Sep 30	59487.96	53.96	34.9	103.3	10.33	VLA[f]
2021 Oct 23	59510.94	76.94	2.6	27.4	1.38	VLA[f]
2021 Oct 23	59510.94	76.94	3.4	31.0	1.55	VLA[f]
2021 Oct 23	59510.94	76.94	5.1	36.5	1.82	VLA[f]
2021 Oct 23	59510.94	76.94	7	38.6	1.93	VLA[f]
2021 Oct 24	59511.92	77.92	2.6	36.1	1.81	VLA[f]
2021 Oct 24	59511.92	77.92	3.4	36.5	1.83	VLA[f]
2021 Oct 24	59511.92	77.92	5.1	36.2	1.81	VLA[f]
2021 Oct 24	59511.92	77.92	7	38.2	1.91	VLA[f]
2021 Oct 24	59511.92	77.92	13.7	45.8	4.58	VLA[f]
2021 Oct 24	59511.92	77.92	16.5	50.3	5.03	VLA[f]
2021 Oct 24	59511.92	77.92	31.1	79.5	7.95	VLA[f]
2021 Oct 24	59511.92	77.92	34.9	88.4	8.84	VLA[f]
2021 Nov 5	59523.82	89.82	2.6	33.0	1.65	VLA[f]
2021 Nov 5	59523.82	89.82	3.4	32.5	1.63	VLA[f]
2021 Nov 5	59523.82	89.82	5.1	31.8	1.59	VLA[f]
2021 Nov 5	59523.82	89.82	7	32.1	1.60	VLA[f]
2021 Nov 5	59523.82	89.82	13.7	38.1	3.81	VLA[f]
2021 Nov 5	59523.82	89.82	16.5	41.5	4.15	VLA[f]
2021 Nov 5	59523.82	89.82	31.1	66.1	6.61	VLA[f]
2021 Nov 5	59523.82	89.82	34.9	73.0	7.30	VLA[f]
2021 Dec 26	59574.76	140.76	2.6	17.9	0.92	VLA[f]
2021 Dec 26	59574.76	140.76	3.4	17.7	0.91	VLA[f]
2021 Dec 26	59574.76	140.76	5.1	17.5	0.88	VLA[f]
2021 Dec 26	59574.76	140.76	7	19.5	0.98	VLA[f]
2021 Dec 26	59574.76	140.76	13.7	25.2	2.53	VLA[f]
2021 Dec 26	59574.76	140.76	16.5	27.0	2.70	VLA[f]
2021 Dec 26	59574.76	140.76	31.1	42.2	4.24	VLA[f]
2021 Dec 26	59574.76	140.76	34.9	47.1	4.73	VLA[f]
2022 Jan 9	59588.66	154.66	2.6	24.6	1.24	VLA[f]
2022 Jan 9	59588.66	154.66	3.4	22.7	1.14	VLA[f]
2022 Jan 9	59588.66	154.66	5.1	18.6	0.93	VLA[f]
2022 Jan 9	59588.66	154.66	7	18.6	0.93	VLA[f]
2022 Jan 9	59588.66	154.66	13.7	21.6	2.16	VLA[f]
2022 Jan 9	59588.66	154.66	16.5	22.2	2.22	VLA[f]

Table C.12 Radio Observations of RS Oph continued

UT Obs Date	MJD	$t - t_0$	Frequency	Flux Density	Error	Telescope
		Days	(GHz)	(mJy)	(mJy)	
2022 Jan 9	59588.66	154.66	31.1	26.5	2.65	VLA[f]
2022 Jan 9	59588.66	154.66	34.9	27.5	2.75	VLA[f]
2022 Jan 11	59590.61	156.61	2.6	24.4	1.24	VLA[f]
2022 Jan 11	59590.61	156.61	3.4	22.6	1.14	VLA[f]
2022 Jan 11	59590.61	156.61	5.1	19.8	1.00	VLA[f]
2022 Jan 11	59590.61	156.61	7	19.2	0.96	VLA[f]
2022 Jan 11	59590.61	156.61	13.7	21.9	2.19	VLA[f]
2022 Jan 11	59590.61	156.61	16.5	23.0	2.30	VLA[f]
2022 Jan 11	59590.61	156.61	31.1	28.3	2.84	VLA[f]
2022 Jan 11	59590.61	156.61	34.9	29.7	2.98	VLA[f]
2022 Jan 16	59595.61	161.61	2.6	23.2	1.17	VLA[f]
2022 Jan 16	59595.61	161.61	3.4	20.7	1.05	VLA[f]
2022 Jan 16	59595.61	161.61	5.1	17.5	0.88	VLA[f]
2022 Jan 16	59595.61	161.61	7	17.9	0.90	VLA[f]
2022 Jan 16	59595.61	161.61	13.7	20.7	2.07	VLA[f]
2022 Jan 16	59595.61	161.61	16.5	21.9	2.19	VLA[f]
2022 Jan 16	59595.61	161.61	31.1	27.1	2.71	VLA[f]
2022 Jan 16	59595.61	161.61	34.9	28.4	2.84	VLA[f]
2023 Mar 31	60034.47	600.47	2.6	3.3	0.24	VLA[f]
2023 Mar 31	60034.47	600.47	3.4	3.3	0.21	VLA[f]
2023 Mar 31	60034.47	600.47	5.1	2.8	0.15	VLA[f]
2023 Mar 31	60034.47	600.47	7	2.3	0.13	VLA[f]
2023 Mar 31	60034.47	600.47	13.7	1.7	0.17	VLA[f]
2023 Mar 31	60034.47	600.47	16.5	1.5	0.16	VLA[f]
2023 Mar 31	60034.47	600.47	31.1	0.9	0.13	VLA[f]
2023 Mar 31	60034.47	600.47	34.9	0.9	0.14	VLA[f]
2023 Apr 15	60049.34	615.34	2.6	2.8	0.22	VLA[f]
2023 Apr 15	60049.34	615.34	3.4	2.8	0.16	VLA[f]
2023 Apr 15	60049.34	615.34	5.1	2.7	0.14	VLA[f]
2023 Apr 15	60049.34	615.34	7	2.4	0.13	VLA[f]
2023 Apr 15	60049.34	615.34	13.7	1.7	0.17	VLA[f]
2023 Apr 15	60049.34	615.34	16.5	1.5	0.16	VLA[f]
2023 Apr 15	60049.34	615.34	31.1	1.1	0.15	VLA[f]
2023 Apr 15	60049.34	615.34	34.9	1.1	0.16	VLA[f]
2023 Jul 6	60131.12	697.12	2.6	1.8	0.09	VLA[f]
2023 Jul 6	60131.12	697.12	3.4	2.0	0.10	VLA[f]
2023 Jul 6	60131.12	697.12	5.1	2.2	0.11	VLA[f]
2023 Jul 6	60131.12	697.12	7	2.3	0.12	VLA[f]
2023 Jul 6	60131.12	697.12	13.7	1.9	0.19	VLA[f]
2023 Jul 6	60131.12	697.12	16.5	1.9	0.19	VLA[f]
2023 Jul 6	60131.12	697.12	31.1	1.3	0.15	VLA[f]
2023 Jul 6	60131.12	697.12	34.9	1.3	0.15	VLA[f]

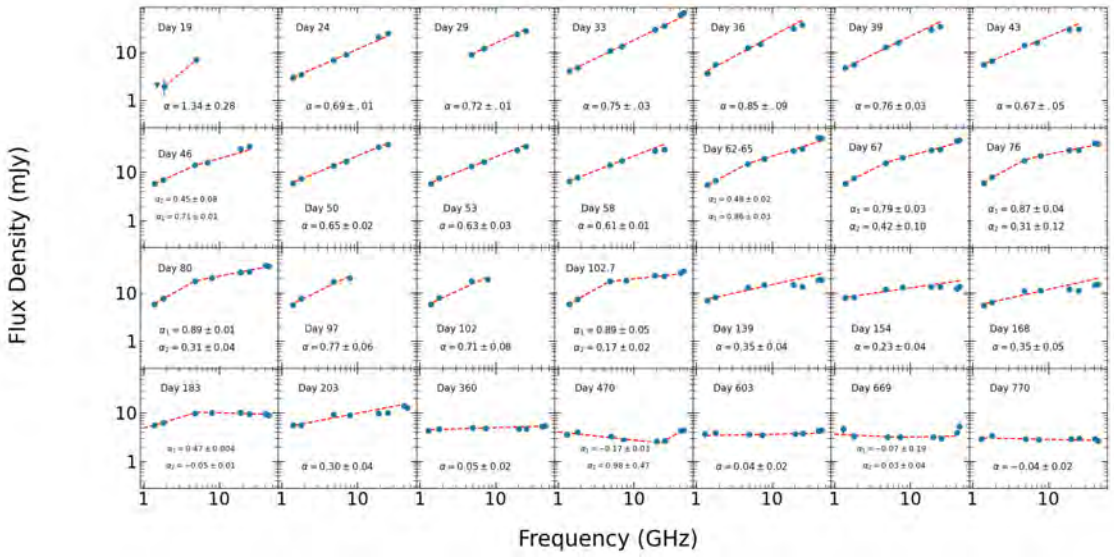

Figure C.4 V407 Cyg Spectral Index

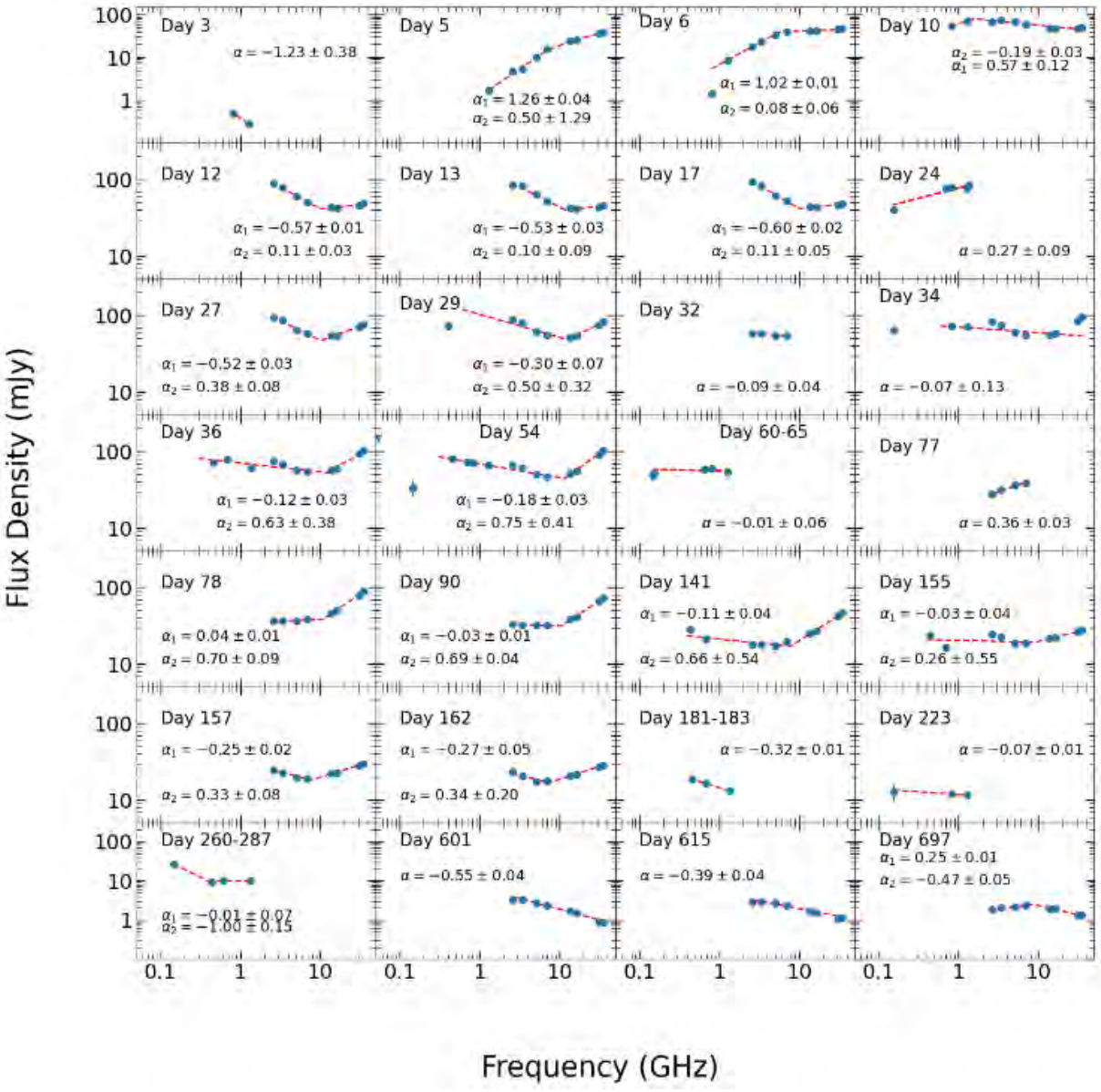

Figure C.5 RS Oph spectral index plot over the course of the 2021 eruption.

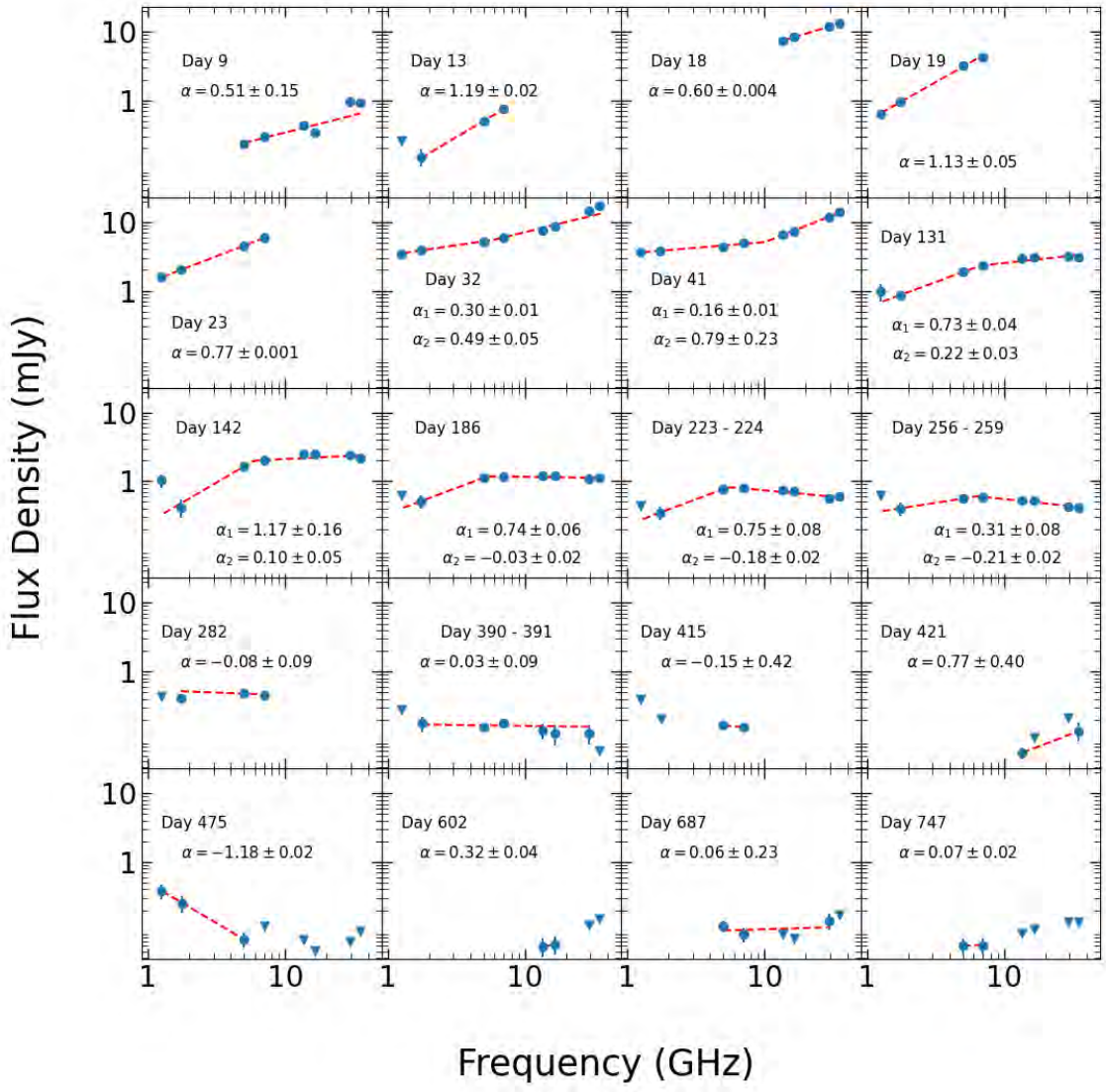

Figure C.6 V392 Per Spectral Index

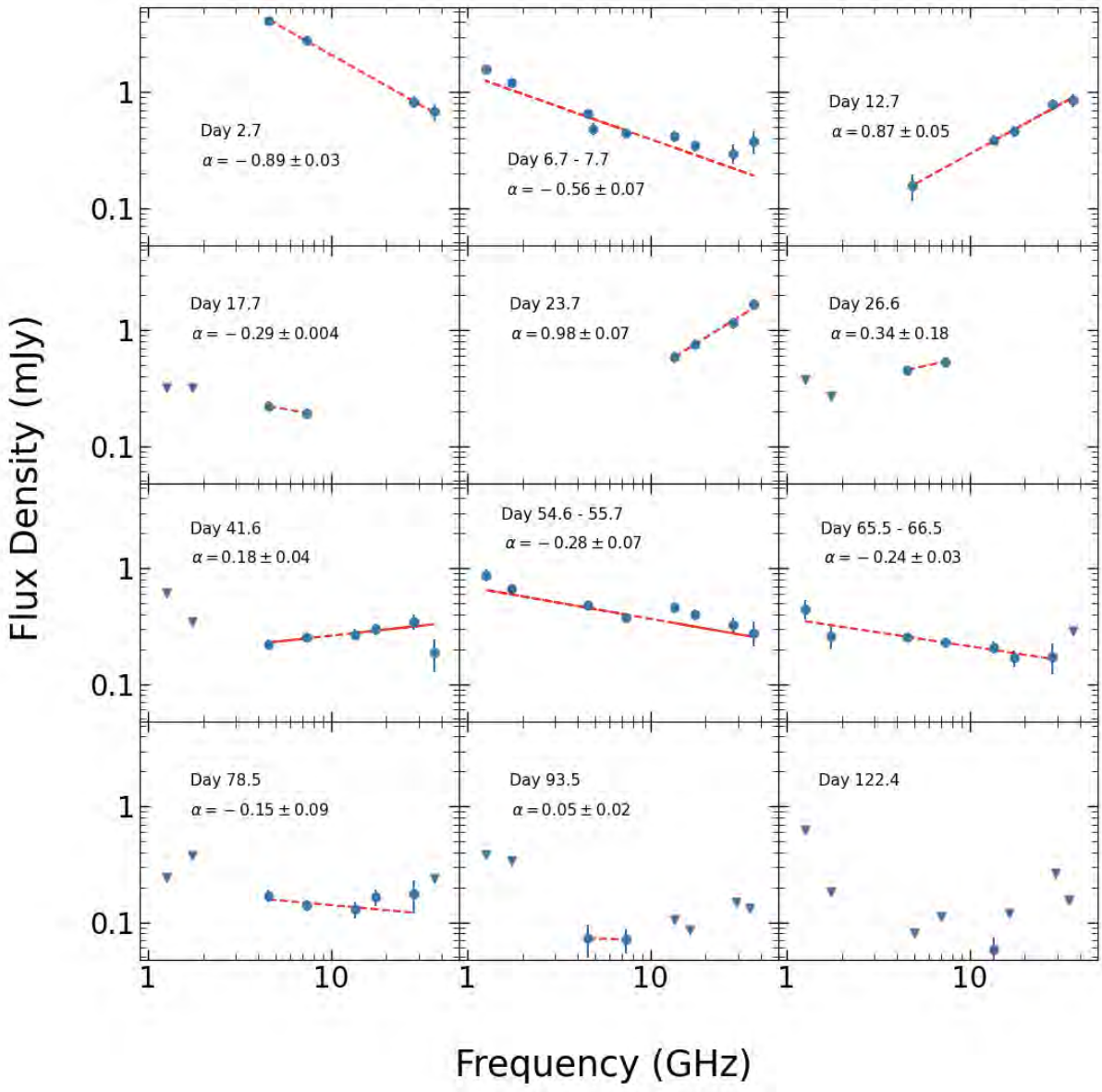

Figure C.7 V1535 Sco spectral indices spanning 2.7 to 122.4 days after discovery of the 2015 eruption.